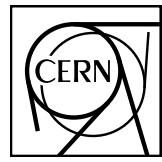


EUROPEAN ORGANIZATION FOR NUCLEAR RESEARCH



ALICE-ANA-2018-xxx
March 21, 2019

ΛK and $\Xi^- K^\pm$ Femtoscopy in Pb-Pb Collisions at $\sqrt{s_{NN}} = 2.76$ TeV from the LHC ALICE Experiment

Jesse T. Buxton¹

1. Department of Physics, The Ohio State University, Columbus, Ohio, USA

Email: jesse.thomas.buxton@cern.ch

Abstract

I present the first femtoscopic analysis of ΛK correlations in Pb-Pb collisions at $\sqrt{s_{NN}} = 2.76$ TeV measured by the ALICE experiment at the Large Hadron Collider (LHC). All pair combinations of Λ and $\bar{\Lambda}$ with K^+ , K^- and K_S^0 are analyzed. The femtoscopic correlations result from strong final-state interactions, and are fit with a parametrization allowing us to both characterize the emission source and measure the scattering parameters for the particle pairs. We observe a large difference in the ΛK^+ and ΛK^- correlations in pairs with low relative momenta ($k^* \lesssim 100$ MeV/c). This might suggest an effect arising from different quark-antiquark interactions within the pairs ($s\bar{s}$ in ΛK^+ and $u\bar{u}$ in ΛK^-), or from different net strangeness for each system. To gain further insight into this hypothesis, we are currently conducting a $\Xi^- K^\pm$ femtoscopic analysis, for which I present preliminary results.

Contents

1	Introduction	7
2	Data Sample and Software	7
2.1	Data Sample	7
2.2	Software	7
3	Data Selection	7
3.1	Event Selection and Mixing	7
3.2	K^\pm Track Selection	8
3.3	V0 Selection	8
3.4	General V0 Reconstruction	8
3.4.1	Λ Reconstruction	11
3.4.2	K_S^0 Reconstruction	13
3.5	V0 Purity Estimation	15
3.6	V0 Purity Background Estimation	15
3.7	Ξ Reconstruction	16
3.8	Pair Selection	18
4	Correlation Functions	22
4.1	Typical Correlation Function Construction	22
4.2	Stavinskiy Correlation Function Construction	24
5	Fitting	27
5.1	Model: ΛK_S^0 , ΛK^\pm , $\Xi^- K_S^0$	27
5.2	Model: $\Xi^- K^\pm$	27
5.3	Momentum Resolution Corrections	28
5.4	Residual Correlations	33
5.5	Non-Flat Background	41
5.6	LednickyFitter	45
5.7	Coulomb Fitter	47
6	Systematic Errors	48
6.1	Systematic Errors: ΛK_S^0	48
6.1.1	Particle and Pair Cuts	48

6.1.2	Non-Flat Background	49
6.1.3	Fit Range	49
6.2	Systematic Errors: ΛK^\pm	49
6.2.1	Particle and Pair Cuts	49
6.2.2	Non-Flat Background	49
6.2.3	Fit Range	49
6.3	Systematic Errors: ΞK^\pm	49
6.3.1	Particle and Pair Cuts	49
7	Results and Discussion	51
7.1	Results: ΛK_S^0 and ΛK^\pm	51
7.1.1	3 Residual Correlations Included in Fit	52
7.1.2	10 Residual Correlations Included in Fit	59
7.1.3	No Residual Correlations Included in Fit	66
7.1.4	Fit Method Comparisons	72
7.1.5	Discussion of m_T -Scaling	77
7.2	Results: ΞK^\pm	82
8	To Do	83
9	Additional Figures	88
9.1	Residuals	88
9.1.1	ΛK^+ Residuals	88
9.1.2	ΛK^- Residuals	94
9.1.3	ΛK_S^0 Residuals	100
9.2	Spherical Harmonics	106

List of Figures

1	V0 Reconstruction	10
2	K_S^0 contamination in $\Lambda(\bar{\Lambda})$ collection	13
3	$\Lambda(\bar{\Lambda})$ contamination in K_S^0 collection	14
4	$V0(\Lambda, \bar{\Lambda}, K_S^0)$ Purities	16
5	V0 Purity Background Estimation	17
6	Ξ Reconstruction	17
7	$\Xi^-(\bar{\Xi}^+)$ Purity	18
8	Average Separation of $\Lambda(\bar{\Lambda})$ and K_S^0 Daughters	20
9	Average Separation of $\Lambda(\bar{\Lambda})$ Daughter and K^\pm	20
10	Average Separation of Ξ Daughters and K^\pm	21
11	ΛK Correlation Functions	23
12	Correlation Functions: ΛK^+ vs ΛK^- for 0-10% Centrality	23
13	ΛK Stavinskiy Correlation Functions (Correct)	25
14	ΛK Stavinskiy Correlation Functions (Correct and Incorrect)	26
15	Momentum Resolution: Sample k_{True}^* vs. k_{Rec}^*	29
16	Particle Contaminations Visible in k_{True}^* vs. k_{Rec}^*	30
17	Momentum Resolution Corrections: Methods Comparison	32
18	Residual Contributions Cartoon	33
19	Sample Transform Matrices for ΛK^+ Analysis	34
20	Sample Transform Matrices for $\bar{\Lambda} K^+$ Analysis	35
21	Reconstruction Efficiencies	36
22	$\Sigma^0 K^+$ Transform	39
23	ΛK^{*0} Transform	40
24	Compare Non-Femtoscopic Backgrounds	41
25	Backgrounds with THERMINATOR, K_S^0 Tweak	42
26	Backgrounds with THERMINATOR	43
27	Correlation with background decomposition (THERM)	44
28	Background reduction methods with THERMINATOR	45
29	Extracted Scattering Parameters: 3 Residuals in Fit	52
30	m_T Scaling of Radii: 3 Residuals in Fit	52
31	$\Lambda(\bar{\Lambda}) K_S^0$ Fits with 3 Residuals	53
32	$\Lambda K^+(\bar{\Lambda} K^-)$ Fits with 3 Residuals	54

33	$\Lambda K^- (\bar{\Lambda} K^+)$ Fits with 3 Residuals	55
34	$\Lambda (\bar{\Lambda}) K_S^0$ Fits showing 3 Residuals	56
35	$\Lambda K^+ (\bar{\Lambda} K^-)$ and $\Lambda K^- (\bar{\Lambda} K^+)$ Fits with 3 Residuals	57
36	Extracted Scattering Parameters: 3 Residuals in Fit	59
37	m_T Scaling of Radii: 10 Residuals in Fit	59
38	$\Lambda K_S^0 (\bar{\Lambda} K_S^0)$ Fits with 10 Residuals	60
39	$\Lambda K^+ (\bar{\Lambda} K^-)$ Fits with 10 Residuals	61
40	$\Lambda K^- (\bar{\Lambda} K^+)$ Fits with 10 Residuals	62
41	$\Lambda (\bar{\Lambda}) K_S^0$ Fits showing 10 Residuals	63
42	$\Lambda K^+ (\bar{\Lambda} K^-)$ and $\Lambda K^- (\bar{\Lambda} K^+)$ Fits with 10 Residuals	64
43	Extracted Scattering Parameters: No Residuals in Fit	66
44	m_T Scaling of Radii: No Residuals in Fit	67
45	$\Lambda K_S^0 (\bar{\Lambda} K_S^0)$ Fits with No Residuals	68
46	$\Lambda K^+ (\bar{\Lambda} K^-)$ Fits, with NO residual correlations included, with No Residuals	69
47	$\Lambda K^- (\bar{\Lambda} K^+)$ Fits with No Residuals	70
48	Compare Fit Parameters: Background treatment	72
49	Compare Fit Parameters: Number of residuals	73
50	Compare Fit Parameters: Free vs fixed λ	74
51	Compare Fit Parameters: Shared vs unique λ	75
52	Compare Fit Parameters: Shared vs. Separate Radii	76
53	m_T Scaling of Radii: 3 Residuals in Fit (with individual m_T highlighted)	77
54	$\Lambda K^+ C_{00}$ and $\Re C_{11}$ Spherical Harmonic Components (0-10%)	79
55	Short Overall	80
56	Short Caption	81
57	Short Caption	81
58	ΞK^\pm Results	82
59	ΞK^\pm Data with Coulomb-Only Bands, 0-10% Centrality	83
60	Effect of Strong Force Inclusion on Coulomb-Only Curve for ΞK^\pm systems	84
61	ΞK^\pm Global Coulomb-Only Fit (Set 1)	85
62	ΞK^\pm Global Coulomb-Only Fit (Set 2)	86
63	$\Xi^- K^+$ Coulomb-Only Fit	86
64	$\Xi^- K^-$ Coulomb-Only Fit	87
65	Residuals: $\Sigma^0 K^+$ to ΛK^+ (0-10% Centrality)	88

66	Residuals: $\Xi^0 K^+$ to ΛK^+ (0-10% Centrality)	89
67	Residuals: $\Xi^- K^+$ to ΛK^+ (0-10% Centrality)	89
68	Residuals: $\Sigma^{*+} K^+$ to ΛK^+ (0-10% Centrality)	90
69	Residuals: $\Sigma^{*-} K^+$ to ΛK^+ (0-10% Centrality)	90
70	Residuals: $\Sigma^{*0} K^+$ to ΛK^+ (0-10% Centrality)	91
71	Residuals: ΛK^{*0} to ΛK^+ (0-10% Centrality)	91
72	Residuals: $\Sigma^0 K^{*0}$ to ΛK^+ (0-10% Centrality)	92
73	Residuals: $\Xi^0 K^{*0}$ to ΛK^+ (0-10% Centrality)	92
74	Residuals: $\Xi^- K^{*0}$ to ΛK^+ (0-10% Centrality)	93
75	Residuals: $\Sigma^0 K^-$ to ΛK^- (0-10% Centrality)	94
76	Residuals: $\Xi^0 K^-$ to ΛK^- (0-10% Centrality)	95
77	Residuals: $\Xi^- K^-$ to ΛK^- (0-10% Centrality)	95
78	Residuals: $\Sigma^{*+} K^-$ to ΛK^- (0-10% Centrality)	96
79	Residuals: $\Sigma^{*-} K^-$ to ΛK^- (0-10% Centrality)	96
80	Residuals: $\Sigma^{*0} K^-$ to ΛK^- (0-10% Centrality)	97
81	Residuals: $\Lambda \bar{K}^{*0}$ to ΛK^- (0-10% Centrality)	97
82	Residuals: $\Sigma^0 \bar{K}^{*0}$ to ΛK^- (0-10% Centrality)	98
83	Residuals: $\Xi^0 \bar{K}^{*0}$ to ΛK^- (0-10% Centrality)	98
84	Residuals: $\Xi^- \bar{K}^{*0}$ to ΛK^- (0-10% Centrality)	99
85	Residuals: $\Sigma^0 K_S^0$ to ΛK_S^0 (0-10% Centrality)	100
86	Residuals: $\Xi^0 K_S^0$ to ΛK_S^0 (0-10% Centrality)	101
87	Residuals: $\Xi^- K_S^0$ to ΛK_S^0 (0-10% Centrality)	101
88	Residuals: $\Sigma^{*+} K_S^0$ to ΛK_S^0 (0-10% Centrality)	102
89	Residuals: $\Sigma^{*-} K_S^0$ to ΛK_S^0 (0-10% Centrality)	102
90	Residuals: $\Sigma^{*0} K_S^0$ to ΛK_S^0 (0-10% Centrality)	103
91	Residuals: ΛK^{*0} to ΛK_S^0 (0-10% Centrality)	103
92	Residuals: $\Sigma^0 K^{*0}$ to ΛK_S^0 (0-10% Centrality)	104
93	Residuals: $\Xi^0 K^{*0}$ to ΛK_S^0 (0-10% Centrality)	104
94	Residuals: $\Xi^- K^{*0}$ to ΛK_S^0 (0-10% Centrality)	105
95	ΛK^+ C_{00} and $\Re C_{11}$ Spherical Harmonic Components	106
96	ΛK^+ First Six Components of Spherical Harmonic Decomposition (0-10%)	107
97	ΛK^- C_{00} and $\Re C_{11}$ Spherical Harmonic Components	108
98	ΛK^- First Six Components of Spherical Harmonic Decomposition (0-10%)	109

99	$\Lambda K_S^0 C_{00}$ and $\Re C_{11}$ Spherical Harmonic Components	110
100	ΛK_S^0 First Six Components of Spherical Harmonic Decomposition (0-10%)	111

10 1 Introduction

11 We present results from a femtoscopic analysis of ΛK and $\Xi^- K^\pm$ correlations in Pb-Pb collisions at
 12 $\sqrt{s_{NN}} = 2.76$ TeV by the ALICE experiment at the LHC. All pair combinations of Λ and $\bar{\Lambda}$ with K^+ ,
 13 K^- and K_S^0 are analyzed. The femtoscopic correlations are the result of strong final-state interactions,
 14 and are fit with a parametrization based on a model by R. Lednicky and V. L. Lyuboshitz [1]. This
 15 allows us to both characterize the emission source and measure the scattering parameters for the particle
 16 pairs. We observe a large difference in the $\Lambda K^+(\bar{\Lambda} K^-)$ and $\Lambda K^-(\bar{\Lambda} K^+)$ correlations in pairs with low
 17 relative momenta ($k^* \lesssim 100$ MeV). The results suggest an effect arising from different quark-antiquark
 18 interactions in the pairs, i.e. $s\bar{s}$ in $\Lambda K^+(\bar{\Lambda} K^-)$ and $u\bar{u}$ in $\Lambda K^-(\bar{\Lambda} K^+)$, or from different net strangeness for
 19 each system. To gain further insight into this hypothesis, we currently are conducting a ΞK femtoscopic
 20 analysis.

21 2 Data Sample and Software

22 2.1 Data Sample

23 The analysis used “pass 2” reconstructed Pb-Pb data from LHC11h (AOD145). The runlist was selected
 24 from runs with global quality tag “1” in the ALICE Run Condition Table. Approximately 40 million
 25 combined central, semi-central, and minimum bias events were analyzed. Runs from both positive (++)
 26 and negative (--) magnetic field polarity settings were used.

27 Run list: 170593, 170572, 170388, 170387, 170315, 170313, 170312, 170311, 170309, 170308, 170306,
 28 170270, 170269, 170268, 170230, 170228, 170207, 170204, 170203, 170193, 170163, 170159, 170155,
 29 170091, 170089, 170088, 170085, 170084, 170083, 170081, 170040, 170027, 169965, 169923, 169859,
 30 169858, 169855, 169846, 169838, 169837, 169835, 169591, 169590, 169588, 169587, 169586, 169557,
 31 169555, 169554, 169553, 169550, 169515, 169512, 169506, 169504, 169498, 169475, 169420, 169419,
 32 169418, 169417, 169415, 169411, 169238, 169167, 169160, 169156, 169148, 169145, 169144, 169138,
 33 169099, 169094, 169091, 169045, 169044, 169040, 169035, 168992, 168988, 168826, 168777, 168514,
 34 168512, 168511, 168467, 168464, 168460, 168458, 168362, 168361, 168342, 168341, 168325, 168322,
 35 168311, 168310, 168315, 168108, 168107, 168105, 168076, 168069, 167988, 167987, 167985, 167920,
 36 167915

37 Analysis was also performed on the LHC12a17a_fix (AOD149) Monte Carlo HIJING events for certain
 38 checks. THERMINATOR2 was also used for certain aspects, such as generation of transform matrices
 39 describing feed-down contributions, estimation of λ parameters, and non-femtoscopic background
 40 modeling.

41 2.2 Software

42 The analysis was performed on the PWGCF analysis train using AliRoot v5-09-29-1 and AliPhysics
 43 vAN-20180505-1.

44 The main classes utilized include: AliFemtoVertexMultAnalysis, AliFemtoEventCutEstimators, AliFemto
 45 toESDTrackCutNSigmaFilter, AliFemtoV0TrackCutNSigmaFilter, AliFemtoXiTrackCut, AliFemtoV0PairCut,
 46 AliFemtoV0TrackPairCut, AliFemtoXiTrackPairCut, and AliFemtoAnalysisLambdaKaon. All of these
 47 classes are contained in /AliPhysics/PWGCF/FEMTOSCOPY/AliFemto and .../AliFemtoUser.

48 3 Data Selection

49 3.1 Event Selection and Mixing

50 The events used in this study were selected with the class AliFemtoEventCutEstimators according to the
 51 following criteria:

- 52 – Triggers
- 53 – minimum bias (kMB)
- 54 – central (kCentral)
- 55 – semi-central (kSemiCentral)
- 56 – z-position of reconstructed event vertex must be within 10 cm of the center of the ALICE detector
- 57 – the event must contain at least one particle of each type from the pair of interest

58 The event mixing was handled by the AliFemtoVertexMultAnalysis class, which only mixes events with
59 like vertex position and centrality. The following criteria were used for event mixing:

- 60 – Number of events to mix = 5
- 61 – Vertex position bin width = 2 cm
- 62 – Centrality bin width = 5

63 The AliFemtoEventReaderAODChain class is used to read the events. Event flattening is not currently
64 used. FilterBit(7). The centrality is determined by the “V0M” method of AliCentrality, set by calling
65 AliFemtoEventReaderAOD::SetUseMultiplicity(kCentrality). We utilize the SetPrimaryVertexCorrec-
66 tionTPCPoints switch, which causes the reader to shift all TPC points to be relative to the event vertex.

67 4 K \pm Track Selection

68 Charged kaons are identified using the AliFemtoESDTrackCutNSigmaFilter class. The single-particle
69 selection criteria used to select charged kaon candidates are summarized in Tables 1 and ???. K \pm track
70 detection utilized both TPC and TOF detectors, and tracks within the range $0.14 < p_T < 1.5$ GeV/c were
71 accepted. As we are interested in primary particles originating from the primary vertex, to reduce the
72 number of secondaries (for instance, charged particles produced in the detector material, particles from
73 weak decays, etc.) in our sample, we established a maximum cut on the distance-of-closest-approach
74 (DCA) of the track the the primary vertex. This restriction is realized by imposing a DCA cut in both the
75 transverse and beam directions.

76 PID was performed using both the TPC and TOF detectors via the $N\sigma$ method. Additionally, we include
77 methods to reduce the contamination in our K \pm samples from electrons and pions. The specifics for these
78 cuts are contained in Table 1.

79 The purity of the K \pm collections was estimated using the HIJING MC data, for which the true identity
80 of each reconstructed K \pm particle is known. Therefore, the purity may be estimated as:

$$Purity(K^\pm) = \frac{N_{true}}{N_{reconstructed}} \quad (1)$$

81 Purity(K $^+$) \approx Purity(K $^-$) \approx 97%

K $^\pm$ selection

Kinematic range	
$ \eta $	< 0.8
p_T	$0.14 < p_T < 1.5 \text{ GeV}/c$
Track quality and selection	
FilterBit	7
Number of clusters in the TPC	> 80
χ^2/N_{DOF} for (ITS, TPC) clusters	< (3.0, 4.0)
DCA to primary vertex (XY, Z)	< (2.4, 3.0) cm
Remove particles with any kink labels	true
$N\sigma$ to primary vertex	< 3.0
K$^\pm$ identification	
PID Probabilities	
K	> 0.2
(π , μ , p)	< (0.1, 0.8, 0.1)
Most probable particle type (fMostProbable =)	Kaon (3)
TPC and TOF N σ Cuts	
$p < 0.4 \text{ GeV}/c$	$N_{\sigma K, \text{TPC}} < 2$
$0.4 < p < 0.45 \text{ GeV}/c$	$N_{\sigma K, \text{TPC}} < 1$
$0.45 < p < 0.80 \text{ GeV}/c$	$N_{\sigma K, \text{TPC}} < 3$ $N_{\sigma K, \text{TOF}} < 2$
$0.80 < p < 1.0 \text{ GeV}/c$	$N_{\sigma K, \text{TPC}} < 3$ $N_{\sigma K, \text{TOF}} < 1.5$
$p > 1.0 \text{ GeV}/c$	$N_{\sigma K, \text{TPC}} < 3$ $N_{\sigma K, \text{TOF}} < 1$

Table 1: K $^\pm$ selection

K\pm selection - Misidentification Cuts			
Electron Rejection: Reject if			$N_{\sigma e^-, \text{TPC}} < 3$
Pion Rejection: Reject if:			
$p < 0.65 \text{ GeV}/c$	TOF and TPC available		$N_{\sigma\pi, \text{TPC}} < 3$ $N_{\sigma\pi, \text{TOF}} < 3$
	Only TPC available	$p < 0.5 \text{ GeV}/c$	$N_{\sigma\pi, \text{TPC}} < 3$
		$0.5 < p < 0.65 \text{ GeV}/c$	$N_{\sigma\pi, \text{TPC}} < 2$
$0.65 < p < 1.5 \text{ GeV}/c$			$N_{\sigma\pi, \text{TPC}} < 5$ $N_{\sigma\pi, \text{TOF}} < 3$
$p > 1.5 \text{ GeV}/c$			$N_{\sigma\pi, \text{TPC}} < 5$ $N_{\sigma\pi, \text{TOF}} < 2$

Table 2: K \pm selection - misidentification cuts

82 **4.1 V0 Selection**83 **4.2 General V0 Reconstruction**

84 $\Lambda(\bar{\Lambda})$ and K_S^0 particles are electrically neutral, and cannot be directly detected, but must instead be re-
 85 constructed through detection of their decay products, or daughters. This process is illustrated in Figure
 86 1, and the main cuts used are shown in Tables 2 and 3. In general, particles which are topologically
 87 reconstructed in this fashion are called V0 particles. The decay channel $\Lambda \rightarrow p\pi^-$ was used for the
 88 identification of Λ hyperons (and, similarly the charge-conjugate decay for the $\bar{\Lambda}$ identification), and K_S^0
 89 $\rightarrow \pi^+\pi^-$ for the identification of K_S^0 mesons. The class AliFemtoV0TrackCutNSigmaFilter (which is an
 90 extension of AliFemtoV0TrackCut) is used to reconstruct the V0s.

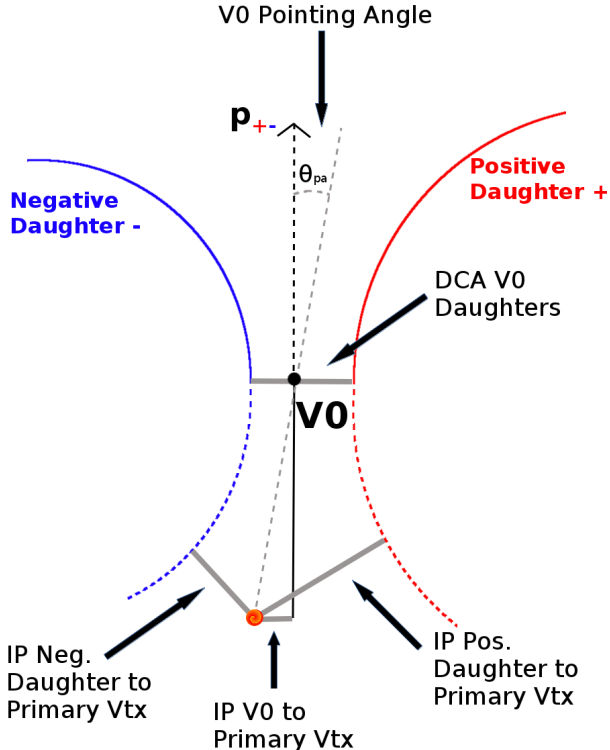


Fig. 1: V0 Reconstruction

91 To construct a V0 particle, the charged daughter tracks must first be found. Aside from typical kinematic
 92 and PID cuts (using TPC and TOF detectors), the daughter tracks are also exposed to a minimum cut
 93 on their impact parameter with respect to the primary vertex. The daughters of a V0 particle should
 94 not originate from the primary vertex, but rather from the decay vertex of the V0, hence the minimum
 95 cut imposition. The decay vertex of the V0 is assumed to be the point of closest approach between the
 96 daughter tracks. To help ensure quality, a maximum value cut is demanded on the distance-of-closest-
 97 approach between the daughters (DCA V0 Daughters). The positive and negative daughter tracks are
 98 combined to form the V0 candidate, the momentum of which is simply the sum of the momenta of the
 99 daughters (calculated at the DCA).

100 A minimum transverse momentum cut on the V0 candidate is introduced to reduce contamination from
 101 fake candidates. Opposite to that of the daughter tracks, the V0 candidate is exposed to a maximum cut
 102 on its impact parameter with respect to the primary vertex. In this case, we do want our V0 candidates
 103 to be primary, hence the maximum cut imposition. To further strengthen our selection of primary V0
 104 candidates, we impose a selection on the pointing angle, θ_{pa} , between the V0 momentum and the vector
 105 pointing from the primary vertex to the secondary V0 decay vertex. We want the V0 candidate's momen-
 106 tum to point back to the primary decay vertex, and therefore a small θ_{pa} ; we achieve this by appointing a

minimum value on $\cos(\theta_{\text{pa}})$ (“Cosine of pointing angle” in Tables 2 and 3).

On occasion, $\Lambda(\bar{\Lambda})$ particles are misidentified as K_S^0 , and vice versa. To attempt to remove these contaminations without throwing away good candidates, we impose a set of misidentification cuts. The intent of these cuts is to judge whether a candidate is more likely a $\Lambda(\bar{\Lambda})$ or a K_S^0 , and are implemented as described below. For a given V0, we calculate the mass assuming different identities (Λ , $\bar{\Lambda}$, K_S^0) of the candidate; the mass assuming K_S^0 hypothesis ($m_{\text{inv}, K_S^0 \text{ hyp.}}$) is calculated assuming $\pi^+\pi^-$ daughters, the mass assuming Λ hypothesis ($m_{\text{inv}, \Lambda \text{ hyp.}}$) is calculated assuming $p\pi^-$ daughters, and the mass assuming $\bar{\Lambda}$ hypothesis ($m_{\text{inv}, \bar{\Lambda} \text{ hyp.}}$) is calculated assuming $\bar{p}\pi^+$ daughters. In addition to the notation just introduced, in the following, m_{PDG, K_S^0} and $m_{\text{PDG}, \Lambda(\bar{\Lambda})}$ denote the particle masses of the K_S^0 and $\Lambda(\bar{\Lambda})$, respectively, as recorded by the Particle Data Group [2].

For $\Lambda(\bar{\Lambda})$ selection, a candidate is assumed to be misidentified and is rejected if all of the following criteria are satisfied:

1. $|m_{\text{inv}, K_S^0 \text{ hyp.}} - m_{\text{PDG}, K_S^0}| < 9.0 \text{ MeV}/c^2$
2. The daughter particles pass daughter cuts intended for K_S^0 reconstruction
 - (a) Λ selection
 - i. p daughter passes π^+ cuts intended for K_S^0 reconstruction
 - ii. π^- daughter passes π^- cuts intended for K_S^0 reconstruction.
 - (b) $\bar{\Lambda}$ selection
 - i. π^+ daughter passes π^+ cuts intended for K_S^0 reconstruction
 - ii. \bar{p} daughter passes π^- cuts intended for K_S^0 reconstruction.
3. $|m_{\text{inv}, K_S^0 \text{ hyp.}} - m_{\text{PDG}, K_S^0}| < |m_{\text{inv}, \Lambda(\bar{\Lambda}) \text{ hyp.}} - m_{\text{PDG}, \Lambda(\bar{\Lambda})}|$

Similarly, for K_S^0 selection, a candidate is rejected if all of the following criteria are satisfied for the Λ case, or for the $\bar{\Lambda}$ case:

1. $|m_{\text{inv}, \Lambda(\bar{\Lambda}) \text{ hyp.}} - m_{\text{PDG}, \Lambda(\bar{\Lambda})}| < 9.0 \text{ MeV}/c^2$
2. The daughter particles pass daughter cuts intended for $\Lambda(\bar{\Lambda})$ reconstruction
 - (a) π^+ daughter passes $p(\pi^+)$ daughter cut intended for $\Lambda(\bar{\Lambda})$ reconstruction
 - (b) π^- daughter passes $\pi^-(\bar{p})$
3. $|m_{\text{inv}, \Lambda(\bar{\Lambda}) \text{ hyp.}} - m_{\text{PDG}, \Lambda(\bar{\Lambda})}| < |m_{\text{inv}, K_S^0 \text{ hyp.}} - m_{\text{PDG}, K_S^0}|$

At this stage, we have a collection of V0 candidates satisfying all of the aforementioned cuts. However, this collection is still polluted by fake V0s, for which the daughter particles happen to pass all of our cuts, but which do not actually originate from a V0. Although the two daughter particles appear to reconstruct a V0 candidate, they are lacking one critical requirement: the system invariant mass does not match that of our desired V0 species (these can be seen outside of the mass peaks in Fig. 4). Therefore, as our final single-particle cut, we require the invariant mass of the V0 candidate to fall within the mass peak of our desired species. Note, however, that some fake V0s still make it past this final cut, as their invariant mass also happens to fall within our acceptance window.

143 Occasionally, we encounter a situation where two V0 candidates share a common daughter. Not both of
 144 these candidates can be real V0s, and including both could introduce an artificial signal into our data.
 145 To avoid any auto-correlation effects, for each event, we impose a single-particle shared daughter cut on
 146 each collection of V0 candidates. This cut iterates through the V0 collection to ensure that no daughter is
 147 claimed by more than one V0 candidate. If a shared daughter is found between two V0 candidates, that
 148 candidate with a smaller DCA to primary vertex is kept while the other is excluded from the analysis.
 149 Note, this single-particle shared daughter cut is unique from the pair shared daughter cut discussed in
 150 Sec. 3.8, the latter of which ensure there is no daughter sharing between the particles in a given pair.
 151 The specific cuts used to reconstruct our $\Lambda(\bar{\Lambda})$ and K_S^0 populations, along with plots showing the effect
 152 of the misidentification cuts, are shown in the following sections.

153 4.2.1 Λ Reconstruction

154 The following cuts, in addition to the misidentification and shared daughter cuts presented in Sec. 3.4,
 155 were used to select good $\Lambda(\bar{\Lambda})$ candidates:

Λ reconstruction	
$ \eta $	< 0.8
p_T	> 0.4 GeV/c
$ m_{\text{inv}} - m_{\text{PDG}} $	< 3.8 MeV
DCA to prim. vertex	< 0.5 cm
Cosine of pointing angle	> 0.9993
OnFlyStatus	false
Decay Length	< 60 cm
Shared Daughter Cut	true
Misidentification Cut	true
Daughter Cuts (π and p)	
$ \eta $	< 0.8
Number of clusters in the TPC	> 80
Daughter status	kTPC τ cut
DCA πp Daughters	< 0.4 cm
π-specific cuts	
p_T	> 0.16 GeV/c
DCA to prim vertex	> 0.3 cm
TPC and TOF Nσ Cuts	
$p < 0.5 \text{ GeV}/c$	$N\sigma_{\text{TPC}} < 3$
$p > 0.5 \text{ GeV}/c$	if TOF & TPC available else
	$N\sigma_{\text{TPC}} < 3 \& N\sigma_{\text{TOF}} < 3$ $N\sigma_{\text{TOF}} < 3$
p-specific cuts	
p_T	> $0.5(p) [0.3(\bar{p})] \text{ GeV}/c$
DCA to prim vertex	> 0.1 cm
TPC and TOF Nσ Cuts	
$p < 0.8 \text{ GeV}/c$	$N\sigma_{\text{TPC}} < 3$
$p > 0.8 \text{ GeV}/c$	if TOF & TPC available else
	$N\sigma_{\text{TPC}} < 3 \& N\sigma_{\text{TOF}} < 3$ $N\sigma_{\text{TOF}} < 3$

Table 3: Λ reconstruction

156 Figure 2a shows the mass assuming K_S^0 hypothesis for the Λ collection, i.e. assume the daughters are
 157 $\pi^+ \pi^-$ instead of $p^+ \pi^-$. Figure 2b is a similar plot, but is for the $\bar{\Lambda}$ collection, i.e. assume the daughters
 158 are $\pi^+ \pi^-$ instead of $\pi^+ \bar{p}^-$. The K_S^0 contamination is visible, although not profound, in both, in the slight

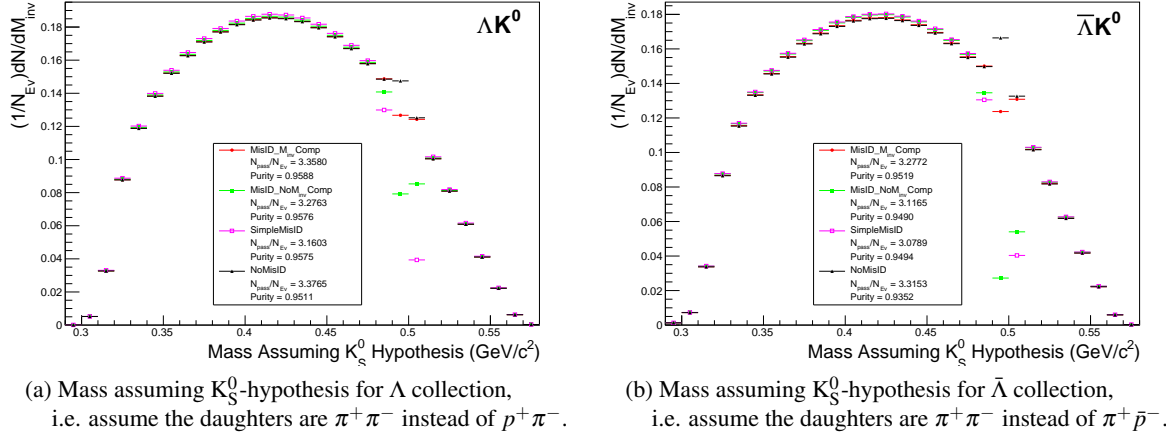


Fig. 2: Mass assuming K_S^0 -hypothesis for V0 candidates passing all Λ (2a) and $\bar{\Lambda}$ (2b) cuts. The “NoMisID” distribution (black triangles) uses the V0 finder without any attempt to remove misidentified K_S^0 . The slight peak in the “NoMisID” distribution around $m_{\text{inv}} = 0.5 \text{ GeV}/c^2$ contains misidentified K_S^0 particles in our $\Lambda(\bar{\Lambda})$ collection. “SimpleMisID” (pink squares) simply cuts out the entire peak, which throws away some good Λ and $\bar{\Lambda}$ particles. “MisID_NoM_{inv}Comp” (green squares) uses the misidentification cut outlined in the text, but does not utilize the final invariant mass comparison step. “MisID_M_{inv}Comp” (red circles) utilizes the full misidentification methods, and is currently used for this analysis. “ $N_{\text{pass}}/N_{\text{ev}}$ ” is the total number of $\Lambda(\bar{\Lambda})$ particles found, normalized by the total number of events. The purity of the collection is also listed.

peaks around $m_{\text{inv}} = 0.497 \text{ GeV}/c^2$. If one simply cuts out the entire peak, good Λ particles will be lost. Ideally, the Λ selection and K_S^0 misidentification cuts are selected such that the peak is removed from this plot while leaving the underlying distribution continuous. To attempt to remove these K_S^0 contaminations without throwing away good Λ and $\bar{\Lambda}$ particles, the misidentification cuts introduced in Sec. 3.4 were imposed.

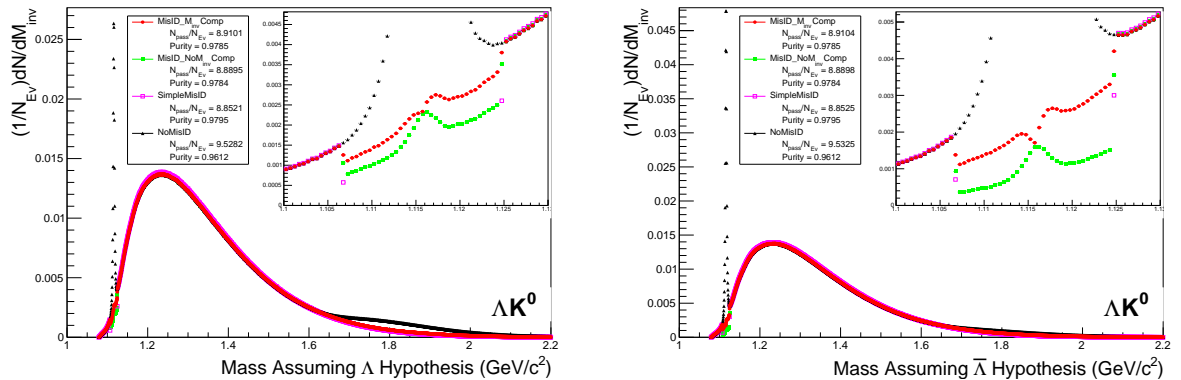
4.2.2 K_S^0 Reconstruction

The following cuts, in addition to the misidentification and shared daughter cuts presented in Sec. 3.4, were used to select good K_S^0 candidates:

As can be seen in Figure 3, some misidentified Λ and $\bar{\Lambda}$ particles contaminate our K_S^0 sample. Figure 3a shows the mass assuming Λ -hypothesis for the K_S^0 collection, i.e. assume the daughters are $p^+\pi^-$ instead of $\pi^+\pi^-$. Figure 3b is similar, but shows the mass assuming $\bar{\Lambda}$ -hypothesis for the collection, i.e. assume the daughters are $\pi^+\bar{p}^-$ instead of $\pi^+\pi^-$. The Λ contamination can be seen in 3a, and the $\bar{\Lambda}$ contamination in 3b, in the peaks around $m_{\text{inv}} = 1.115 \text{ GeV}/c^2$. Additionally, the $\bar{\Lambda}$ contamination is visible in Figure 3a, and the Λ contamination visible in Figure 3b, in the region of excess around $1.65 < m_{\text{inv}} < 2.1 \text{ GeV}/c^2$. This is confirmed as the number of misidentified Λ particles in the sharp peak of Figure 3a (misidentified $\bar{\Lambda}$ particles in the sharp peak of Figure 3b) approximately equals the excess found in the $1.65 < m_{\text{inv}} < 2.1 \text{ GeV}/c^2$ region of Figure 3a (Figure 3b).

The peaks around $m_{\text{inv}} = 1.115 \text{ GeV}/c^2$ in Figure 3 contain both misidentified $\Lambda(\bar{\Lambda})$ particles and good K_S^0 . If one simply cuts out the entire peak, some good K_S^0 particles will be lost. Ideally, the K_S^0 selection and $\Lambda(\bar{\Lambda})$ misidentification cuts can be selected such that the peak is removed from this plot while leaving the underlying distribution continuous. To attempt to remove these Λ and $\bar{\Lambda}$ contaminations without throwing away good K_S^0 particles, the misidentification cuts introduced in Sec. 3.4 were imposed.

K_S^0 reconstruction		
$ \eta $	< 0.8	
p_T	> 0.2 GeV/c	
$m_{PDG} - 13.677 \text{ MeV} < m_{\text{inv}} < m_{PDG} + 2.0323 \text{ MeV}$		
DCA to prim. vertex	< 0.3 cm	
Cosine of pointing angle	> 0.9993	
OnFlyStatus	false	
Decay Length	< 30 cm	
Shared Daughter Cut	true	
Misidentification Cut	true	
π^\pm Daughter Cuts		
$ \eta $	< 0.8	
Number of clusters in TPC	> 80	
Daughter Status	kTPCrefit	
DCA $\pi^+\pi^-$ Daughters	< 0.3 cm	
p_T	> 0.15 GeV/c	
DCA to prim vertex	> 0.3 cm	
TPC and TOF N σ Cuts		
$p < 0.5 \text{ GeV}/c$	$N\sigma_{\text{TPC}} < 3$	
$p > 0.5 \text{ GeV}/c$	if TOF & TPC available else	$N\sigma_{\text{TPC}} < 3 \& N\sigma_{\text{TOF}} < 3$ $N\sigma_{\text{TOF}} < 3$

Table 4: K_S^0 reconstruction

 (a) Mass assuming Λ -hypothesis for K_S^0 collection, i.e. assume the daughters are $p^+\pi^-$ instead of $\pi^+\pi^-$.

 (b) Mass assuming $\bar{\Lambda}$ -hypothesis for K_S^0 collection, i.e. assume the daughters are $\pi^+\bar{p}^-$ instead of $\pi^+\pi^-$.

Fig. 3: Mass assuming Λ -hypothesis (3a) and $\bar{\Lambda}$ -hypothesis (3b) for K_S^0 collection. The “NoMisID” distribution (black triangles) uses the V0 finder without any attempt to remove misidentified Λ and $\bar{\Lambda}$. The peak in the “NoMisID” distribution around $m_{\text{inv}} = 1.115 \text{ GeV}/c^2$ contains misidentified Λ (3a) and $\bar{\Lambda}$ (3b) particles in our K_S^0 collection. “SimpleMisID” (pink squares) simply cuts out the entire peak, which throws away some good K_S^0 particles. “MisID_NoM_{inv}Comp” (green squares) uses the misidentification cut outlined in the text, but does not utilize the final invariant mass comparison step. “MisID_M_{inv}Comp” (red circles) utilizes the full misidentification methods, and is currently used for this analysis. “N_{pass}/N_{ev}” is the total number of K_S^0 particles found, normalized by the total number of events. The purity of the collection is also listed. Also note, the relative excess of the “NoMisID” distribution around $1.65 < m_{\text{inv}} < 2.1 \text{ GeV}/c^2$ shows misidentified $\bar{\Lambda}$ (3a) and Λ (3b) particles in our K_S^0 collection.

181 4.3 V0 Purity Estimation

182 In order to obtain a true and reliable signal, one must ensure good purity of the V0 collection. The purity
 183 of the collection is calculated as:

$$Purity = \frac{Signal}{Signal + Background} \quad (2)$$

184 To access both the signal and background, the invariant mass distribution (m_{inv}) of all V0 candidates
 185 must be constructed immediately before the final invariant mass cut, as shown in Fig. 4 for Λ , $\bar{\Lambda}$ and K_S^0
 186 candidates in the 0-10% centrality bin. Fig. 4a presents the $p\pi^-$ invariant mass distribution showing the
 187 Λ peak, Fig. 4b presents the $\bar{p}\pi^+$ invariant mass distribution showing the $\bar{\Lambda}$ peak, and Fig. 4c presents
 188 the $\pi^+\pi^-$ invariant mass distribution showing the K_S^0 peak.

189 It is vital that this distribution be constructed immediately before the final m_{inv} cut, otherwise it would be
 190 impossible to estimate the background. These distributions are used to calculate the collections' purities
 191 (defined in Eq. 2). As shown in Figure 4, the background is fit (with a polynomial) outside of the peak
 192 region of interest to obtain an estimate for the background within the region. Within the m_{inv} cut limits,
 193 the background is assumed to be the region below the fit while the signal is that above the fit. The Λ and
 194 $\bar{\Lambda}$ purities were found to be $\approx 95\%$, and the K_S^0 purity was found to be $\approx 98\%$.

195 4.4 V0 Purity Background Estimation

196 As previously stated, the backgrounds in the m_{inv} distributions are modeled by a polynomial which is
 197 fit outside of the final cut region in an attempt to estimate the background within the cut region. As
 198 this estimate of the background under the mass peak is vital for our estimate of our V0 purity, it is
 199 important for us to ensure that our estimate is accurate. More specifically, it is necessary that we ensure
 200 the background is well described by a polynomial fit within the cut region.

201 To better understand our background, we studied V0 candidates reconstructed with daughters from dif-
 202 ferent events. These mixed-event V0s certainly do not represent real, physical V0s (a single V0 cannot
 203 have daughters living in two different events!), but, rather, represent a large portion of the background
 204 creeping into our analysis.

205 The standard AliFemto framework is not equipped to handle this situation, as most are not interested in
 206 these fake-V0s. Therefore, we built a new class, `AliFemtoV0PurityBgdEstimator`, to handle our needs.
 207 In addition to finding fake-V0s using mixed-event daughters, we also used our new class to find real-V0s
 208 using same-event daughters. The purpose here was to compare our new class to the established V0 finder
 209 used in standard AliFemto analyses.

210 Figure 5 shows the results of our study. In the figures, the black points, marked “Data”, correspond
 211 to V0s found using the standard V0-finder, and to the V0s used in my analyses. The red and blue
 212 points utilize our personal V0-finder (i.e. `AliFemtoV0PurityBgdEstimator`). The red points show real
 213 V0s reconstructed using same-event daughters, and the blue points show fake-V0s reconstructed using
 214 mixed-event daughters. Both the red and blue points have been scaled by different factors (listed in the
 215 legends) to nicely align all three data on a single plot.

216 Figure 5 shows that our personal V0-finder does a good, but not perfect, job of matching the shape of the
 217 m_{inv} plots obtained from the data. The scale factor listed in the legend reveals that we are only finding
 218 $1/3 - 1/2$ of the V0s found by the standard V0-finder. These two points are not of concern, as our purpose
 219 here was to gain a sense of the broad shape of the background. It is revealed in Fig. 5, when studying
 220 the red and blue points, that the background distribution within the mass peak region is simply a smooth
 221 connection of the backgrounds outside of the cut region, as we assumed. Therefore, our method of fitting
 222 the background outside of the cut region, fitting with a smooth polynomial, and extrapolating to the cut

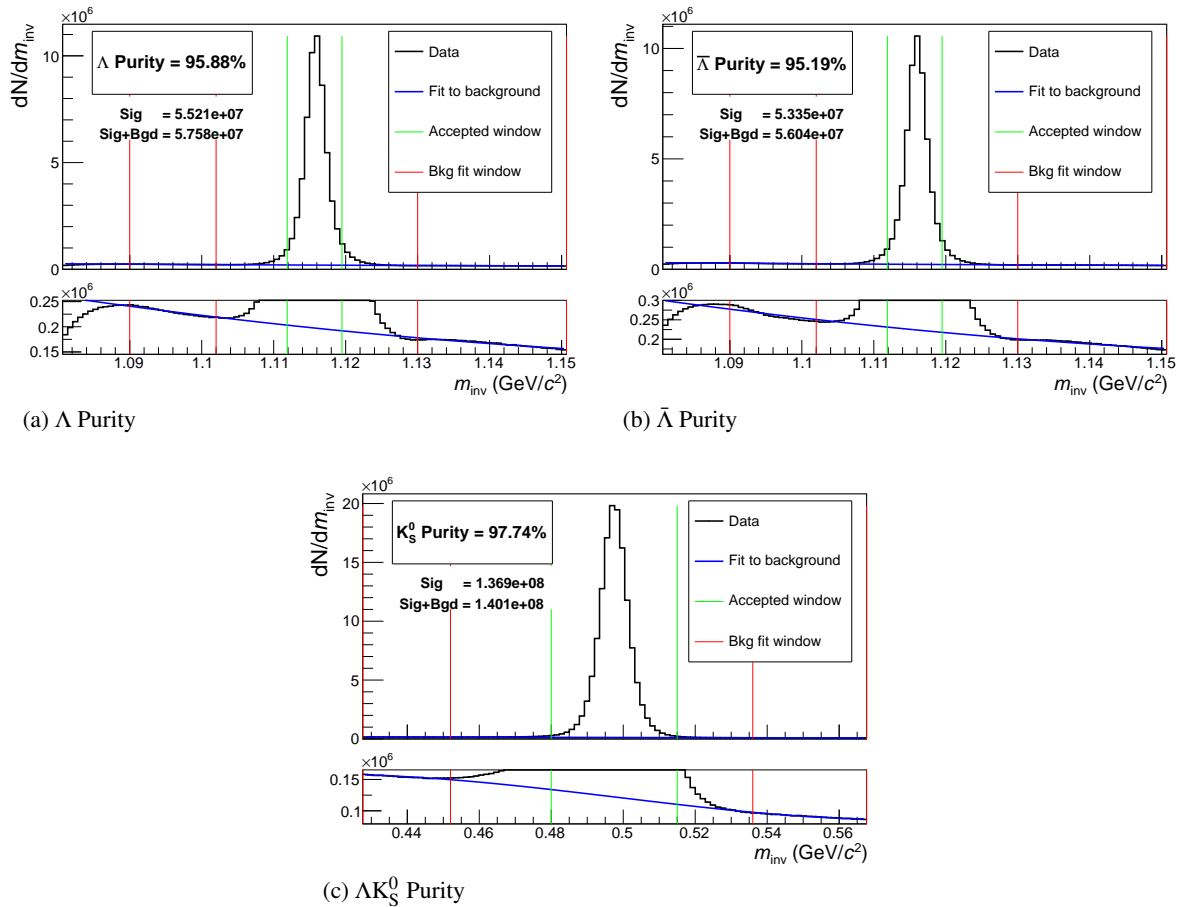


Fig. 4: Invariant mass (m_{inv}) distribution for all Λ (a), $\bar{\Lambda}$ (b), and K_S^0 (c) candidates immediately before the final invariant mass cut. The bottom figures are zoomed to show the background with fit. The vertical green lines represent the m_{inv} cuts used in the analyses, the red vertical lines delineate the regions over which the background was fit, and the blue line shows the background fit. These distributions are used to calculate the collection purities, $\text{Purity}(\Lambda) \approx \text{Purity}(\bar{\Lambda}) \approx 95\%$, and $\text{Purity}(K_S^0) \approx 98\%$.

region is justified.

4.5 Ξ Reconstruction

Our motivation for studying $\Xi^- K^\pm$ systems is to attempt to better understand the striking difference in the ΛK^+ and ΛK^- data at low k^* (Figure 12).

The reconstruction of Ξ particles is one level above V0 reconstruction. V0 particles are topologically reconstructed by searching for the charged daughters' tracks into which they decay. With Ξ particles, we search for the V0 particle and charged daughter into which the Ξ decays. In the case of Ξ^- , we search for the Λ (V0) and π^- (track) daughters. We will refer to this π as the “bachelor π ”.

The following cuts were used to select good Ξ^- ($\bar{\Xi}^+$) candidates:

1. Shared Daughter Cut for Ξ Collection

- Iterate through Ξ collection to ensure that no daughter is used in more than one Ξ candidate
- Remove any candidate in which the bachelor π is also a daughter of the Λ (implemented in AliFemtoXITrackPairCut class)

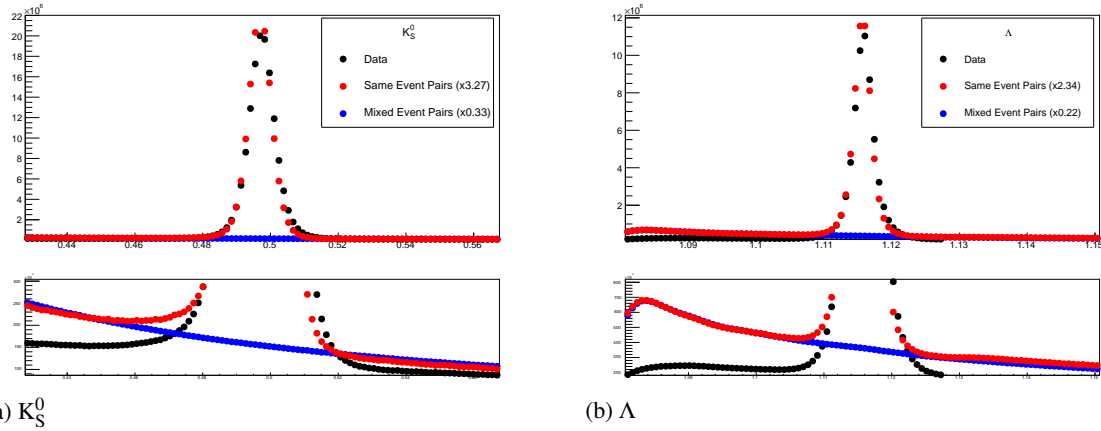


Fig. 5: V0 Purity Background Estimation. The black points, marked “Data”, correspond to real V0s found using the standard V0-finder (i.e. the V0s used in my analyses). The red points, marked “Same Event Pairs”, show real V0s reconstructed with our personal V0-finder in AliFemtoVOPurityBgdEstimator. These data are scaled by a factor (listed in the legend) to match their *Signal + Background* value in the cut region with that of the data. The blue points, marked “Mixed Event Pairs”, show fake-V0s reconstructed with our personal V0-finder using mixed-event daughters. The blue points are scaled by a factor (listed in the legend) to closely match the red points in the side-band region.

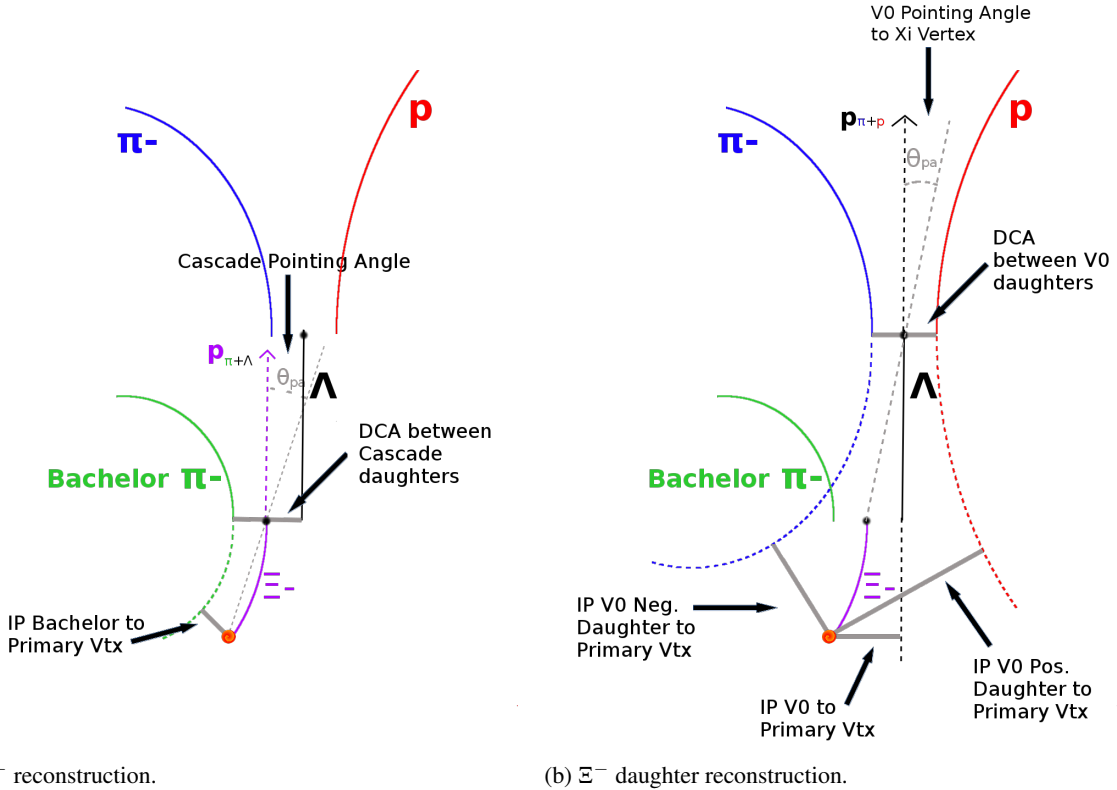


Fig. 6: (Left) Ξ^- reconstruction (DCA to primary vertex for Ξ^- not shown). (Right) Ξ^- daughter reconstruction.

236 The purity of our Ξ and $\bar{\Xi}$ collections are calculated just as those of our V0 collections 3.3. Figure 7,
237 which is used to calculate the purity, shows the m_{inv} distribution of our $\Xi(\bar{\Xi})$ candidates just before the
238 final m_{inv} cut. Currently, we have $\text{Purity}(\Xi^-) \approx 90\%$ and $\text{Purity}(\bar{\Xi}^+) \approx 92\%$.

Ξ reconstruction					
$ \eta $	< 0.8				
p_T	> 0.8 GeV/c				
$ m_{\text{inv}} - m_{\text{PDG}} $	< 3.0 MeV				
DCA to prim. vertex	< 0.3 cm				
Cosine of pointing angle	> 0.9992				
Λ daughter cuts					
DCA to prim. vertex	> 0.2 cm				
Cosine of pointing angle	> 0.0				
Cosine of pointing angle to Ξ decay vertex	> 0.9993				
OnFlyStatus	false				
All other Λ and corresponding (π and p) daughter cuts are same as in primary Λ selection, and can be found in Sec. 3.4.1					
Bachelor π cuts					
$ \eta $	< 0.8				
p_T	> 0.0 GeV/c				
DCA to prim. vertex	> 0.1 cm				
Number of clusters in the TPC	> 70				
Daughter status	kTPC π fit				
TPC and TOF $N\sigma$ Cuts					
$p < 0.5 \text{ GeV}/c$	$N\sigma_{\text{TPC}} < 3$				
$p > 0.5 \text{ GeV}/c$	<table border="1"> <tr> <td>if TOF & TPC available</td> <td>$N\sigma_{\text{TPC}} < 3 \& N\sigma_{\text{TOF}} < 3$</td> </tr> <tr> <td>else</td> <td>$N\sigma_{\text{TOF}} < 3$</td> </tr> </table>	if TOF & TPC available	$N\sigma_{\text{TPC}} < 3 \& N\sigma_{\text{TOF}} < 3$	else	$N\sigma_{\text{TOF}} < 3$
if TOF & TPC available	$N\sigma_{\text{TPC}} < 3 \& N\sigma_{\text{TOF}} < 3$				
else	$N\sigma_{\text{TOF}} < 3$				

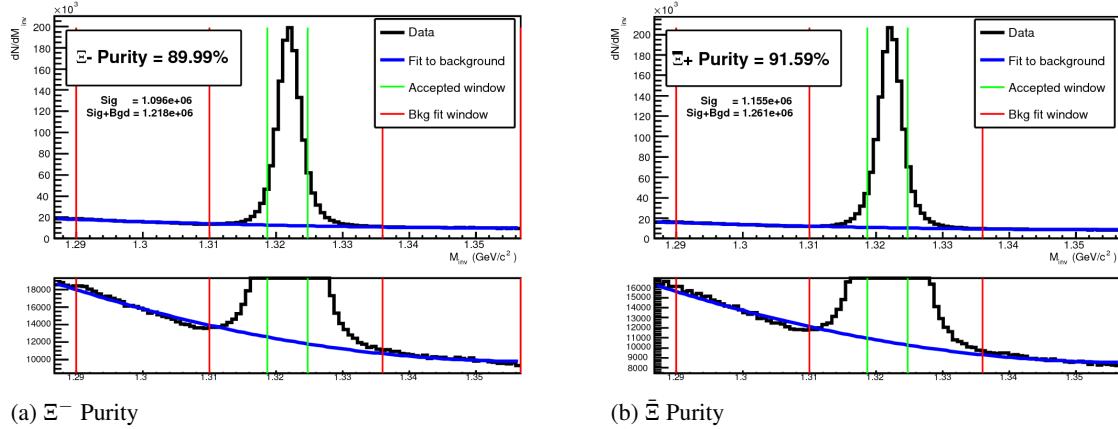
Table 5: Ξ reconstruction

Fig. 7: Invariant mass (m_{inv}) distribution for all Ξ^- (a) and $\bar{\Xi}^+$ (b) candidates immediately before the final invariant mass cut. The bottom figures are zoomed to show the background with fit. The vertical green lines represent the m_{inv} cuts used in the analyses, the red vertical lines delineate the regions over which the background was fit, and the blue line shows the background fit. These distributions are used to calculate the collection purities, $\text{Purity}(\Xi^-) \approx 90\%$ and $\text{Purity}(\bar{\Xi}^+) \approx 92\%$.

4.6 Pair Selection

The femtoscopic analysis of two-particle correlation functions relies on the proper formation of particle pairs. As such, it is important to obtain true particle pairs in the analysis. In particular, contamination from pairs constructed with split or merged tracks, and pairs sharing daughters, can introduce artificial signals into the correlation function, obscuring the actual physics. In an effort to remove contamination,

244 we impose two main pair cuts: a shared daughter cut, and an average separation cut.

245 The purpose of the shared daughter cut is to ensure the first particle in the pair is unique from the second.
 246 For pairs formed of two V0s (e.g. ΛK_S^0), this cut is implemented by removing all pairs which share
 247 a daughter. For example, in the ΛK_S^0 analysis, if the Λ and K_S^0 in a potential pair claim the same π^-
 248 daughter, the pair is excluded from the analysis. For a pair formed of a single V0 and a charged track
 249 (e.g. ΛK^\pm), the cut removes all pairs in which the charged track is also claimed as a daughter of the V0.
 250 This mistake could only occur if, for instance, either a K^\pm is misidentified as a π or p and used in the V0
 251 reconstruction, or a π or p is misidentified as a K^\pm in the K^\pm selection. In the case of a pair formed from
 252 a charged Ξ and a charged track (e.g. $\Xi^- K^\pm$), the cut removes all pairs in which the charged track is also
 253 claimed as a daughter of the Ξ , be it the bachelor- π daughter directly, or a daughter of the Λ daughter (a
 254 granddaughter of the Ξ). In the $\Xi^- K^\pm$ analysis, as in the ΛK^\pm case, this could only occur if there was
 255 misidentification of a K^\pm as a π or p, or vice versa.

256 The purpose of the average separation cut is to remove splitting and merging effects, and it is employed
 257 in the following way. To calculate the average separation between two tracks, the spatial separation is
 258 determined at several points throughout the TPC (every 20 cm radially from 85 cm to 245 cm), and the
 259 results averaged. For that ΛK_S^0 analysis, which involves two V0 particles, a minimum average separation
 260 cut of 6 cm between the like-charge daughters in the pairs was imposed (for example, between the p
 261 daughter of the Λ and the π^+ daughter of the K_S^0). For the ΛK^\pm analyses, a minimum average separation
 262 cut of 8 cm was enforced between the K^\pm and the Λ daughter sharing the same charge (for example,
 263 in the ΛK^+ analysis, between the p daughter of the Λ and the K^+). Finally, for the $\Xi^- K^\pm$ analysis, a
 264 minimum average separation cut of 8 cm was enforced between any daughter of the Ξ sharing the same
 265 charge as the K^\pm in the pair (for example, in the $\Xi^- K^-$ analysis, between the π^- granddaughter which
 266 decayed from the Λ daughter and the K^- , and between the bachelor- π^- daughter and the K^-).

267 The motivation for the values used in these cuts can be seen in Figures 8, 9, and 10, in which average sep-
 268 aration correlation functions are presented. The average separation correlation functions are formed just
 269 as for our relative-momentum correlation functions, but we instead bin in average separation. Looking at
 270 these average separation correlation functions for like-charge tracks, at lowest average separation we see
 271 an enhancement due to track splitting, followed by (at slightly higher average separation) a suppression
 272 due to track merging. When the average separation correlation function stabilizes to unity, these effects
 273 are no longer abundant, and we choose our cut value. Splitting and merging effects between oppositely
 274 charged tracks was found to be negligible, therefore no cuts on unlike-charge tracks were imposed. To
 275 summarize:

276 Average Separation Cuts ($\overline{\Delta r}$)

277 (a) ΛK_S^0 Analyses

- 278 – $\overline{\Delta r} > 6.0$ cm for like-charge sign daughters
- 279 – No cut for unlike-charge daughters

280 (b) ΛK^\pm Analyses

- 281 – $\overline{\Delta r} > 8.0$ cm for daughter of $\Lambda(\bar{\Lambda})$ sharing charge sign of K^\pm
- 282 – No cut for unlike-charge

283 (c) $\Xi^- K^\pm$ Analyses

- 284 – $\overline{\Delta r} > 8.0$ cm for any daughter of Ξ sharing charge sign of K^\pm
- 285 – No cut for unlike-charge

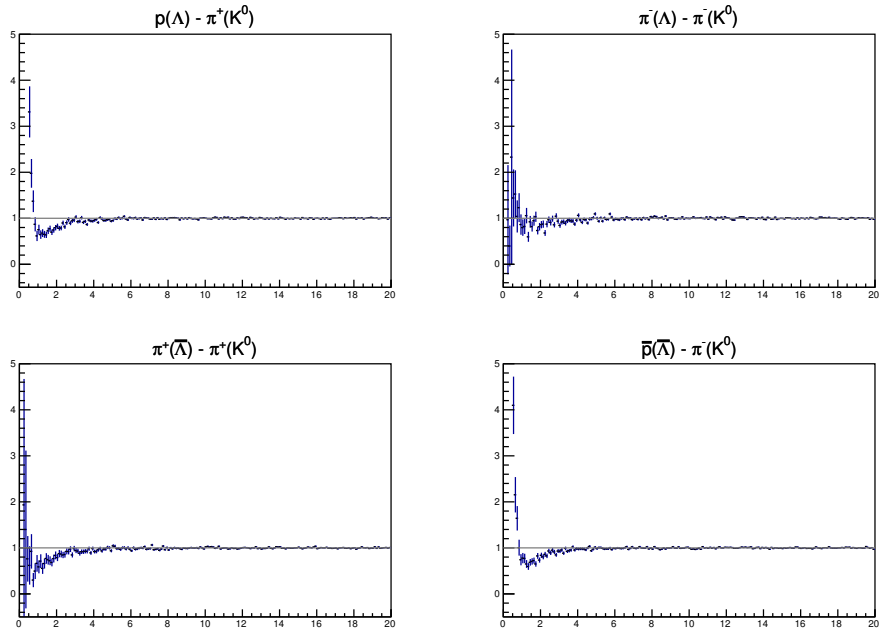


Fig. 8: Average separation (cm) correlation functions of $\Lambda(\bar{\Lambda})$ and K_S^0 Daughters. Only like-sign daughter pairs are shown (the distributions for unlike-signs were found to be flat). The title of each subfigure shows the daughter pair, as well as the mother of each daughter (in “()”), ex. top left is p from Λ with π^+ from K_S^0 .

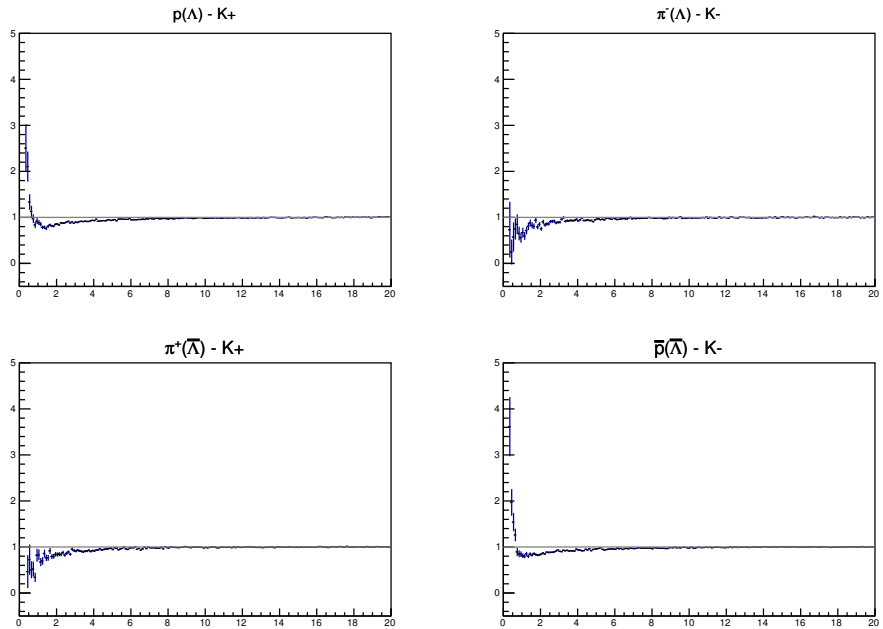


Fig. 9: Average separation (cm) correlation functions of $\Lambda(\bar{\Lambda})$ Daughter and K^\pm . Only like-sign pairs are shown (unlike-signs were flat). In the subfigure titles, the particles in “()” represent the mothers, ex. top left is p from Λ with K^+ .

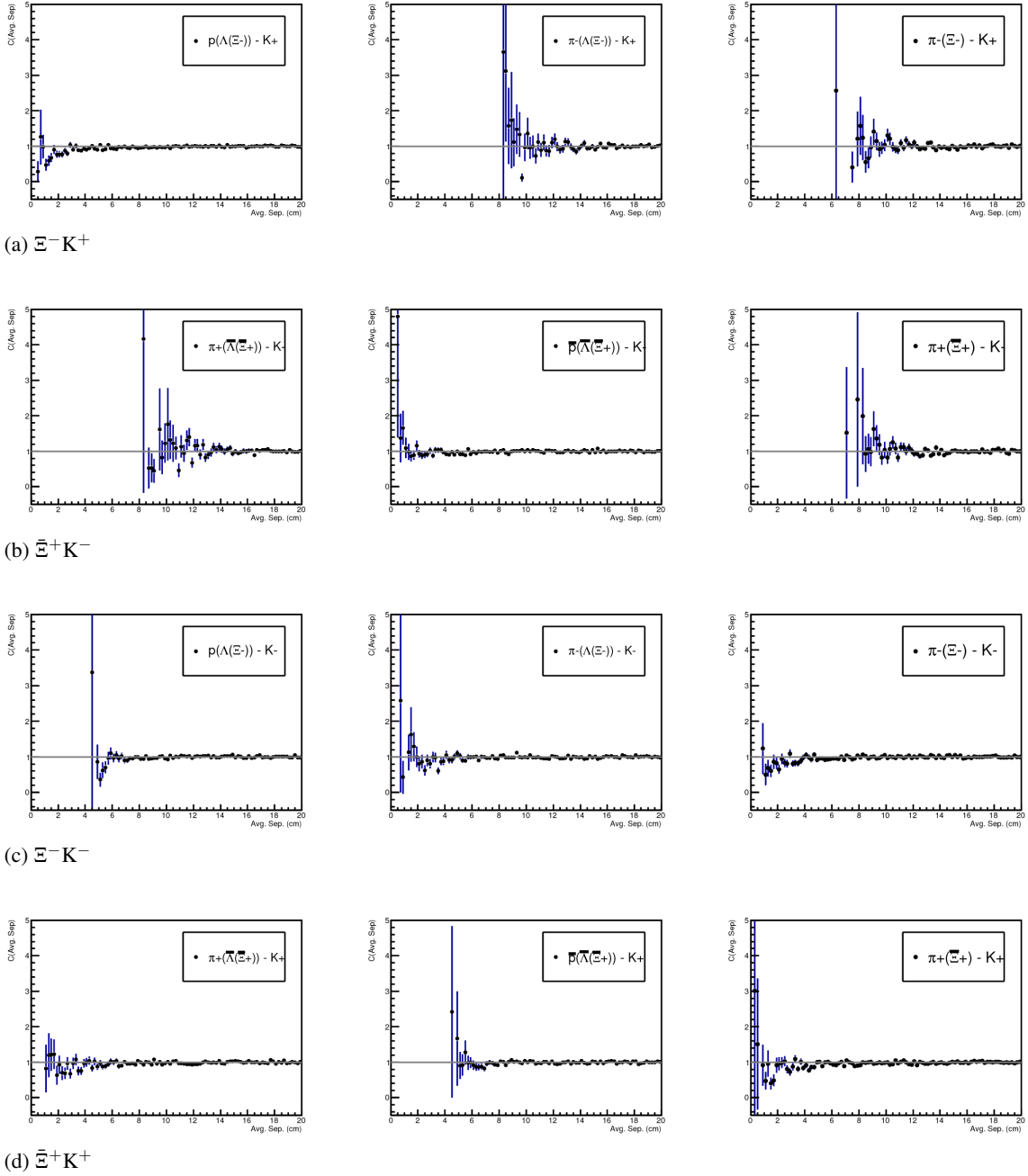


Fig. 10: Average separation (cm) correlation functions of Ξ Daughter and K^\pm . In the subfigure titles, the particles in “()” represent the mothers, ex. top left is p from Λ from Ξ^- with K^+ .

286 **5 Correlation Functions**

287 This analysis studies the momentum correlations of both ΛK and $\Xi^- K^\pm$ pairs using the two-particle
 288 correlation function, defined as $C(k^*) = A(k^*)/B(k^*)$, where $A(k^*)$ is the signal distribution, $B(k^*)$ is the
 289 reference (or background) distribution, and k^* is the momentum of one of the particles in the pair rest
 290 frame. In practice, $A(k^*)$ is constructed by binning in k^* pairs from the same event. Ideally, $B(k^*)$ is
 291 similar to $A(k^*)$ in all respects excluding the presence of femtoscopic correlations [3]; as such, $B(k^*)$
 292 is used to divide out the phase-space effects, leaving only the femtoscopic effects in the correlation
 293 function.

294 This analysis presents correlation functions for three centrality bins (0-10%, 10-30%, and 30-50%), and
 295 is currently pair transverse momentum ($k_T = 0.5|\mathbf{p}_{T,1} + \mathbf{p}_{T,2}|$) integrated (i.e. not binned in k_T). The
 296 correlation functions are constructed separately for the two magnetic field configurations, and, after
 297 assuring consistency, are combined using a weighted average:

$$C_{combined}(k^*) = \frac{\sum_i w_i C_i(k^*)}{\sum_i w_i} \quad (3)$$

298 where the sum runs over the correlation functions to be combined, and the weight, w_i , is the number of
 299 numerator pairs in $C_i(k^*)$. Here, the sum is over the two field configurations (++ and - -).

300 **5.1 Typical Correlation Function Construction**

301 In practice, $B(k^*)$ is typically obtained by forming mixed-event pairs, i.e. particles from a given event
 302 are paired with particles from $N_{mix}(= 5)$ other events, and these pairs are then binned in k^* . In forming
 303 the background distribution, it is important to mix only similar events; mixing events with different
 304 phase-spaces can result in an unreliable background distribution, and can introduce artificial signals in
 305 the correlation function. Therefore, in this analysis, we bin our events both in primary vertex location (2
 306 cm bin width) and in centrality (5% bin width), and we only mix events within a given bin; i.e. we only
 307 mix events of like centrality and of like primary vertex location. Also note, a vertex correction is also
 308 applied to each event, which essentially recenters the the primary vertices to $z = 0$.

309 Figures 11a, 11b, 11c show the correlation functions for all centralities studied for $\Lambda K^+(\bar{\Lambda} K^-)$, $\Lambda K^-(\bar{\Lambda} K^+)$,
 310 and $\Lambda(\bar{\Lambda}) K_S^0$, respectively. All were normalized in the range $0.32 < k^* < 0.4$ GeV/c. It is interesting to
 311 note that the average of the $\Lambda K^+(\bar{\Lambda} K^-)$ and $\Lambda K^-(\bar{\Lambda} K^+)$ correlation functions is consistent with our
 312 $\Lambda K_S^0(\bar{\Lambda} K_S^0)$ measurement.

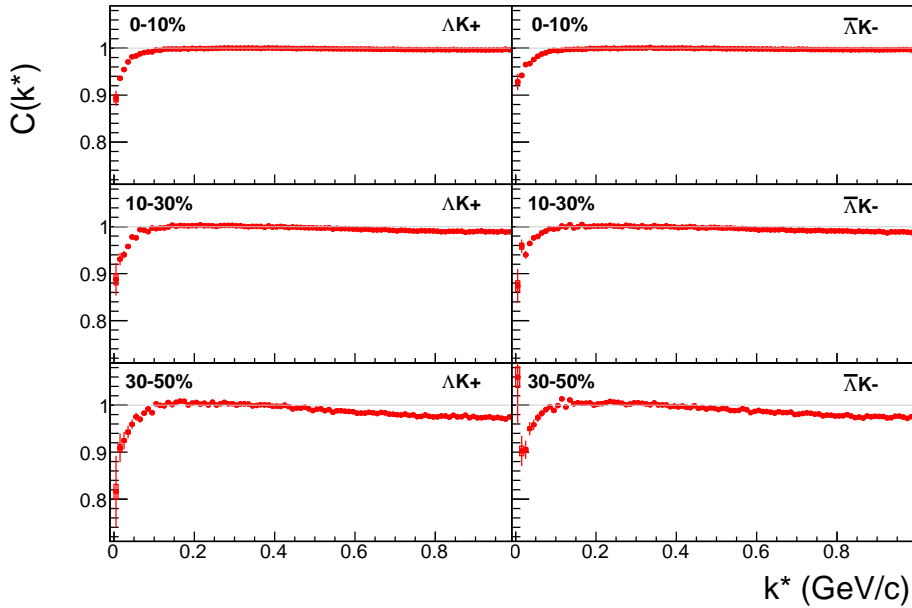


Fig. 11: ΛK^+ (left) and $\bar{\Lambda} K^-$ (right) correlations for 0-10% (top), 10-30% (middle), and 30-50% (bottom) centralities.

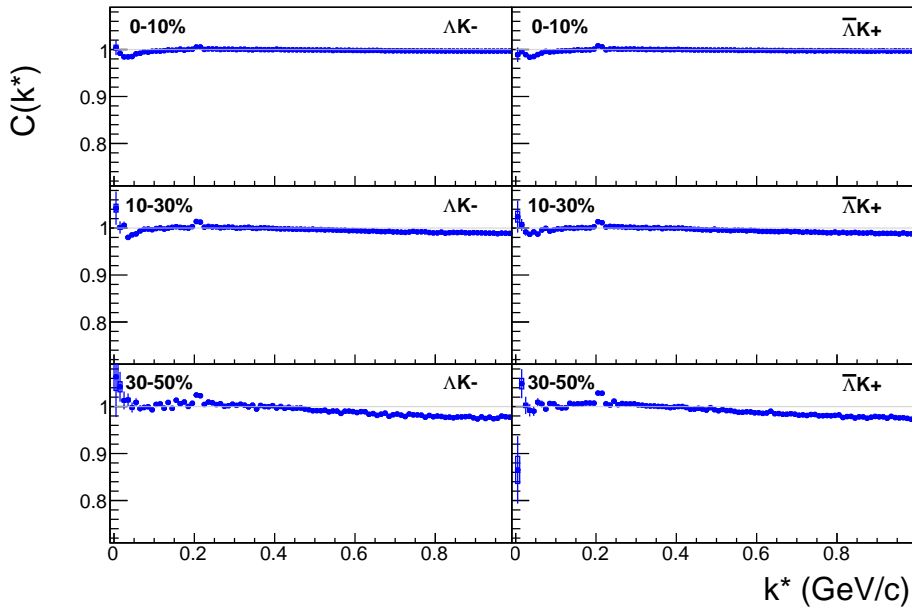


Fig. 12: ΛK^- (left) and $\bar{\Lambda} K^+$ (right) correlations for 0-10% (top), 10-30% (middle), and 30-50% (bottom) centralities. The peak at $k^* \approx 0.2$ GeV/c is due to the Ω^- (and, to a much smaller extent, the $\Xi(1690)$) resonances.

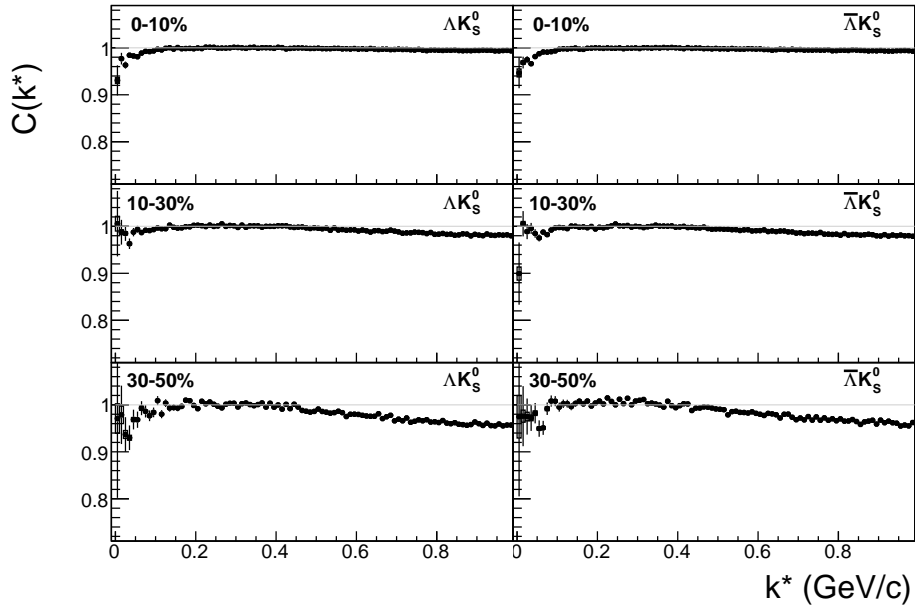


Fig. 13: ΛK_s^0 (left) and $\bar{\Lambda} K_s^0$ (right) correlations for 0-10% (top), 10-30% (middle), and 30-50% (bottom) centralities.

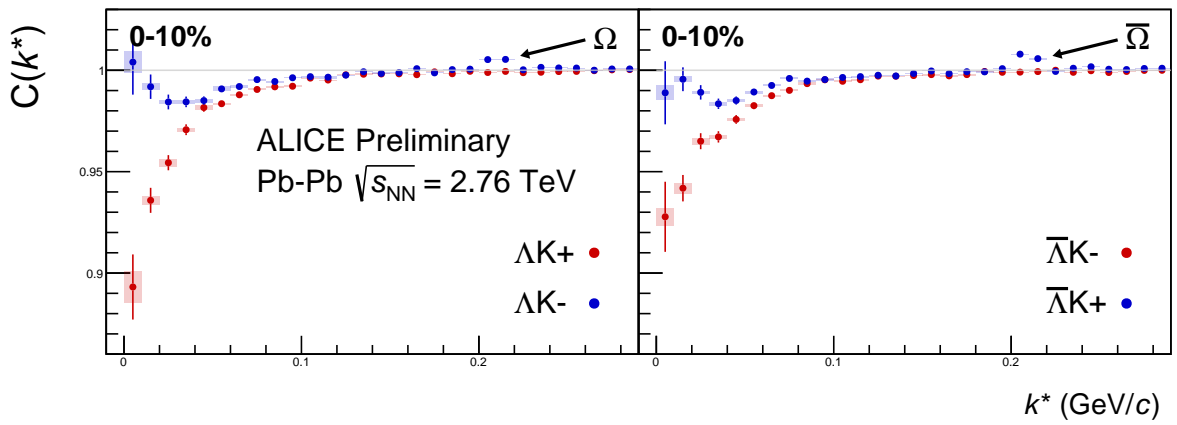


Fig. 14: Correlation Functions: ΛK^+ vs ΛK^- ($\bar{\Lambda} K^+$ vs $\bar{\Lambda} K^-$) for 0-10% centrality. The peak in ΛK^- ($\bar{\Lambda} K^+$) at $k^* \approx 0.2$ GeV/c is due to the Ω^- (and, to a much smaller extent, the $\Xi(1690)$ resonance. The lines represent the statistical errors, while boxes represent systematic errors.

313 5.2 Stavinskiy Correlation Function Construction

314 The purpose of the Stavinskiy method is to rid the correlation functions of the non-femtoscopic back-
315 ground. More specifically, this method is intended to handle background contributions from elliptic
316 flow, and other sources having reflection symmetry in the transverse plane. With the Stavinskiy method,
317 mixed-event pairs are not used for the background ($B(k^*)$); instead, same-event pseudo-pairs, formed
318 by rotating one particle in a real pair by 180° in the transverse plane, are used as a background. This
319 rotation rids the pairs of any femtoscopic correlation, while maintaining correlations due to elliptic flow
320 (and other suitably symmetric contributors).

321 The results of correctly implementing such a procedure are shown in Figure 13. The figure shows the
322 Stavinskiy method does a very good job of ridding the ΛK^\pm correlations of their non-femtoscopic back-
323 grounds. We also see the procedure does not work as well on the ΛK_S^0 system.

324 Now, one must be somewhat careful when applying this Stavinskiy method. We found that, in order to
325 obtain correct results, we had to run our pseudo-pairs through the same pair cuts used in our analyses.
326 In an ideal world, our pair cut would only remove truly bad pairs results from splitting, merging, etc. In
327 the real world, the pair cut always throws out some of the good with the bad. For the pseudo-pairs to
328 form a reliable background, they too must experience the pair cut, and the loss of “good” pseudo-pairs.
329 We found this issue affected mainly our ΛK^+ & $\bar{\Lambda} K^-$ analysis, as can be seen in Figure 14, which shows
330 both a correct implementation of the Stavinskiy method, and an incorrect implementation lacking the
331 additional pair cut on the pseudo-pairs.

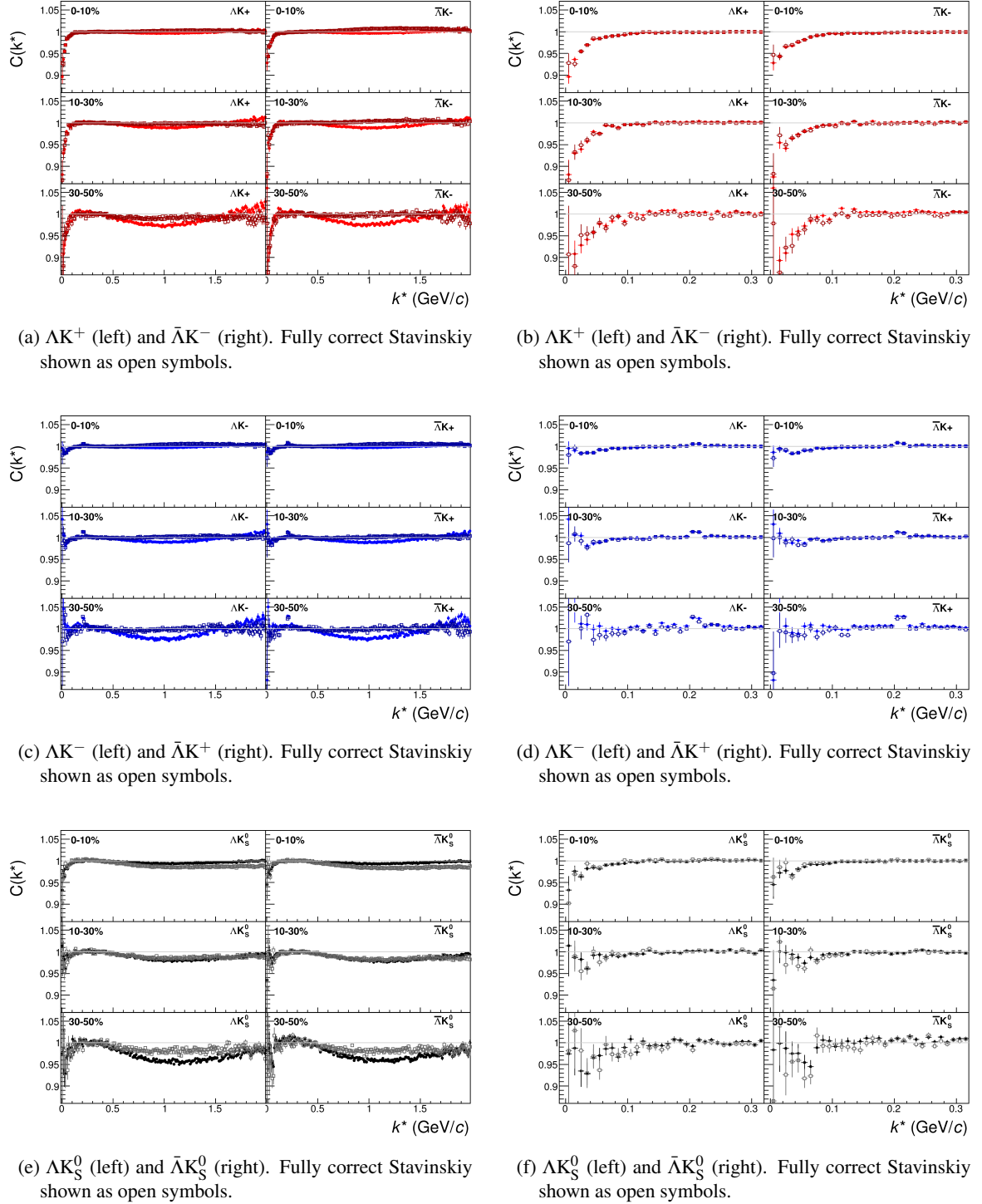


Fig. 15: ΛK and $\bar{\Lambda} \bar{K}$ correlation functions built using the fully correct Stavinskiy method for 0-10%, 10-30%, and 30-50% centralities. In the fully correct method, the pseudo-pairs (same-event pairs with one particle rotated by 180° in the transverse plane) are also run through the pair cuts used in the analysis (an example of an incorrect implementation is shown in Fig. 14). Closed symbols represent correlations built using the normal mixed-event background, while open symbols represent correlations formed using the Stavinskiy same-event pseudo-pairs as a background. Figures in the right column are zoomed-in versions of figures in the left column.

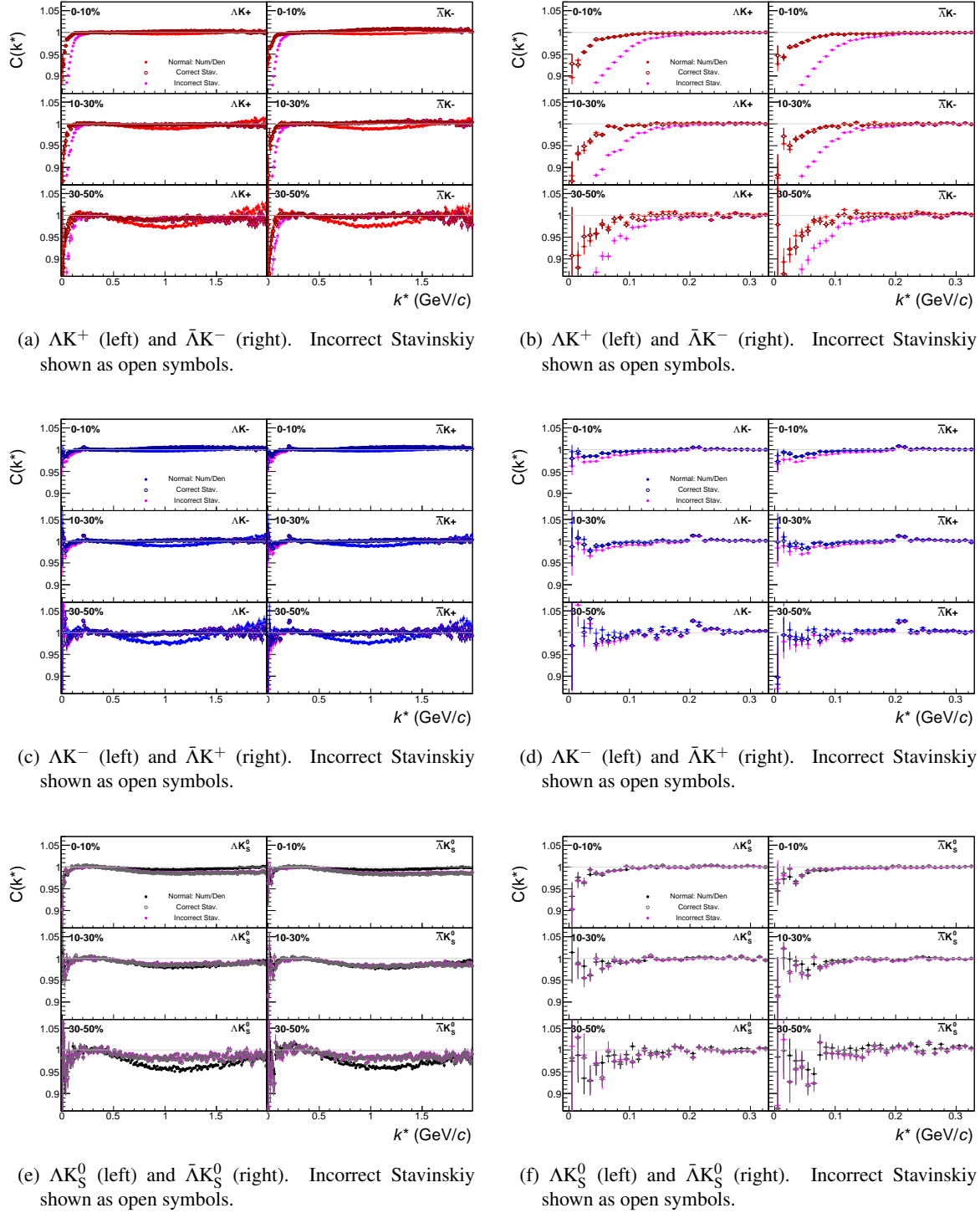


Fig. 16: ΛK and $\bar{\Lambda} \bar{K}$ correlation functions built, both correctly and incorrectly, using the Stavinskiy method for 0-10%, 10-30%, and 30-50% centralities. This figure is the same as Fig. 13, but with results from the incorrect Stavinskiy implementation shown in magenta. The closed, (red, blue, black) symbols represent correlation functions formed using the normal method with mixed-event background pairs. The open, cyan symbols represent correlation functions formed using the correct Stavinskiy method. The closed, magenta symbols represent correlation functions formed using the incorrect Stavinskiy method. In the correct method, the pseudo-pairs (same-event pairs with one particle rotated by 180° in the transverse plane) are also run through the pair cuts used in the analysis; in the incorrect method, they are not. Figures in the right column are zoomed-in versions of figures in the left column.

332 **6 Fitting**

333 **6.1 Model: $\Lambda K_S^0, \Lambda K^\pm, \Xi^- K_S^0$**

334 The two-particle relative momentum correlation function may be written theoretically by the Koonin-
 335 Pratt equation [4, 5]:

$$C(\mathbf{k}^*) = \int S(\mathbf{r}^*) |\Psi_{\mathbf{k}^*}(\mathbf{r}^*)|^2 d^3 \mathbf{r}^* \quad (4)$$

336 where $S(\mathbf{r}^*)$ is the pair source distribution, $\Psi_{\mathbf{k}^*}(\mathbf{r}^*)$ is the two-particle wave-function, and k^* is the
 337 momentum of one particle in the pair rest frame. In the absence of Coulomb effects, and assuming a
 338 spherically Gaussian source of width R , and s-wave scattering, the 1D femtoscopic correlation function
 339 can be calculated analytically using:

$$C(k^*) = 1 + C_{QI}(k^*) + C_{FSI}(k^*) \quad (5)$$

340 C_{QI} describes plane-wave quantum interference:

$$C_{QI}(k^*) = \alpha \exp(-4k^{*2}R^2) \quad (6)$$

341 where $\alpha = (-1)^{2j}/(2j+1)$ for identical particles with spin j , and $\alpha = 0$ for non-identical particles. For
 342 all analyses presented in this note, $\alpha = 0$. C_{FSI} describes the s-wave strong final state interaction between
 343 the particles:

$$\begin{aligned} C_{FSI}(k^*) &= (1 + \alpha) \left[\frac{1}{2} \left| \frac{f(k^*)}{R} \right|^2 \left(1 - \frac{d_0}{2\sqrt{\pi}R} \right) + \frac{2\Re f(k^*)}{\sqrt{\pi}R} F_1(2k^*R) - \frac{\Im f(k^*)}{R} F_2(2k^*R) \right] \\ f(k^*) &= \left(\frac{1}{f_0} + \frac{1}{2} d_0 k^{*2} - ik^* \right)^{-1}; \quad F_1(z) = \int_0^z \frac{e^{x^2-z^2}}{z} dx; \quad F_2(z) = \frac{1-e^{-z^2}}{z} \end{aligned} \quad (7)$$

344 where R is the source size, $f(k^*)$ is the s-wave scattering amplitude, f_0 is the complex scattering length,
 345 and d_0 is the effective range of the interaction.

346 An additional parameter λ is typically included in the femtoscopic fit function to account for the purity
 347 of the pair sample. In the case of no residual correlations (to be discussed in Section 5.4), the fit function
 348 becomes:

$$C(k^*) = 1 + \lambda [C_{QI}(k^*) + C_{FSI}(k^*)] \quad (8)$$

349 **6.2 Model: $\Xi^- K^\pm$**

350 The two-particle correlation function may be written as:

$$C(\mathbf{k}^*) = \sum_S \rho_S \int S(\mathbf{r}^*) |\Psi_{\mathbf{k}^*}^S(\mathbf{r}^*)|^2 d^3 \mathbf{r}^* \quad (9)$$

351 where ρ_S is the normalized emission probability of particles in a state with spin S , $S(\mathbf{r}^*)$ is the pair
 352 emission source distribution (assumed to be Gaussian), and $\Psi_{\mathbf{k}^*}^S(\mathbf{r}^*)$ is the two-particle wave-function
 353 including both strong and Coulomb interactions [6]:

$$\Psi_{\mathbf{k}^*}(\mathbf{r}^*) = e^{i\delta_c} \sqrt{A_c(\eta)} [e^{i\mathbf{k}^*\cdot\mathbf{r}^*} F(-i\eta, 1, i\xi) + f_c(k^*) \frac{\tilde{G}(\rho, \eta)}{r^*}] \quad (10)$$

where $\rho = k^* r^*$, $\eta = (k^* a_c)^{-1}$, $\xi = \mathbf{k}^* \cdot \mathbf{r}^* + k^* r^* \equiv \rho(1 + \cos \theta^*)$, and $a_c = (\mu z_1 z_2 e^2)^{-1}$ is the two-particle Bohr radius (including the sign of the interaction). δ_c is the Coulomb s-wave phase shift, $A_c(\eta)$ is the Coulomb penetration factor, $\tilde{G} = \sqrt{A_c}(G_0 + iF_0)$ is a combination of the regular (F_0) and singular (G_0) s-wave Coulomb functions. $f_c(k^*)$ is the s-wave scattering amplitude:

$$f_c(k^*) = \left[\frac{1}{f_0} + \frac{1}{2} d_0 k^{*2} - \frac{2}{a_c} h(\eta) - ik^* A_c(\eta) \right]^{-1} \quad (11)$$

where, the “h-function”, $h(\eta)$, is expressed through the digamma function, $\psi(z) = \Gamma'(z)/\Gamma(z)$ as:

$$h(\eta) = 0.5[\psi(i\eta) + \psi(-i\eta) - \ln(\eta^2)] \quad (12)$$

In this case, the λ parameter may be included as:

$$C(\mathbf{k}^*) = (1 - \lambda) + \lambda \sum_S \rho_S \int S(\mathbf{r}^*) |\Psi_{\mathbf{k}^*}^S(\mathbf{r}^*)|^2 d^3 \mathbf{r}^* \quad (13)$$

6.3 Momentum Resolution Corrections

Finite track momentum resolution causes the reconstructed momentum of a particle to smear around the true value. This, of course, also holds true for V0 particles. The effect is propagated up to the pairs of interest, which causes the reconstructed relative momentum (k_{Rec}^*) to differ from the true momentum (k_{True}^*). Smearing of the momentum typically will result in a suppression of the signal. More specifically, the smearing will broaden the signal, which would cause a decrease in the extracted radius of the system. The effect of finite momentum resolution can be investigated using the HIJING MC data, for which both the true and reconstructed momenta are available. Figure 15 shows sample k_{True}^* vs. k_{Rec}^* plots for ΛK^\pm 0-10% analyses; Figure 15a was generated using same-event pairs, while Figure 15b was generated using mixed-event pairs (with $N_{\text{mix}} = 5$).

If there are no contaminations in our particle collection, the plots in Figure 15 should be smeared around $k_{\text{True}}^* = k_{\text{Rec}}^*$; this is mostly true in our analyses. However, there are some interesting features of our results which demonstrate a small (notice the log-scale on the z-axis) contamination in our particle collection. The structure around $k_{\text{Rec}}^* = k_{\text{True}}^* - 0.15 \text{ GeV}/c$ is mainly caused by K_S^0 contamination in our $\Lambda(\bar{\Lambda})$ sample. The remaining structure not distributed about $k_{\text{Rec}}^* = k_{\text{True}}^*$ is due to π and e contamination in our K^\pm sample. These contaminations are more visible in Figure 16, which show k_{Rec}^* vs. k_{True}^* plots (for a small sample of the ΛK^\pm 0-10% central analysis), for which the MC truth (i.e. true, known identity of the particle) was used to eliminate misidentified particles in the $K^+(a)$ and $\Lambda(b)$ collections. (NOTE: This is an old figure and is for a small sample of the data. A new version will be generated shortly. It, nonetheless, demonstrates the point well).

Information gained from looking at k_{Rec}^* vs k_{true} can be used to apply corrections to account for the effects of finite momentum resolution on the correlation functions. A typical method (“Ratio” method) involves using the MC HIJING data to build two correlation functions, $C_{\text{Rec}}(k^*)$ and $C_{\text{True}}(k^*)$, using the generator-level momentum (k_{True}^*) and the measured detector-level momentum (k_{Rec}^*). The data is then corrected by multiplying by the ratio, $C_{\text{True}}/C_{\text{Rec}}$, before fitting. This essentially unsmears the data, which then can be compared directly to theoretical predictions and fits. Although this is conceptually simple, there are a couple of big disadvantages to this method. First, HIJING does not incorporate final-state interactions, so weights must be used when building same-event (numerator) distributions. These weights account for the interactions, and, in the absence of Coulomb interactions, can be calculated using Eq. 5. Of course, these weights are valid only for a particular set of fit parameters. Therefore, in the fitting process, during which the fitter explores a large parameter set, the corrections will not remain valid. As

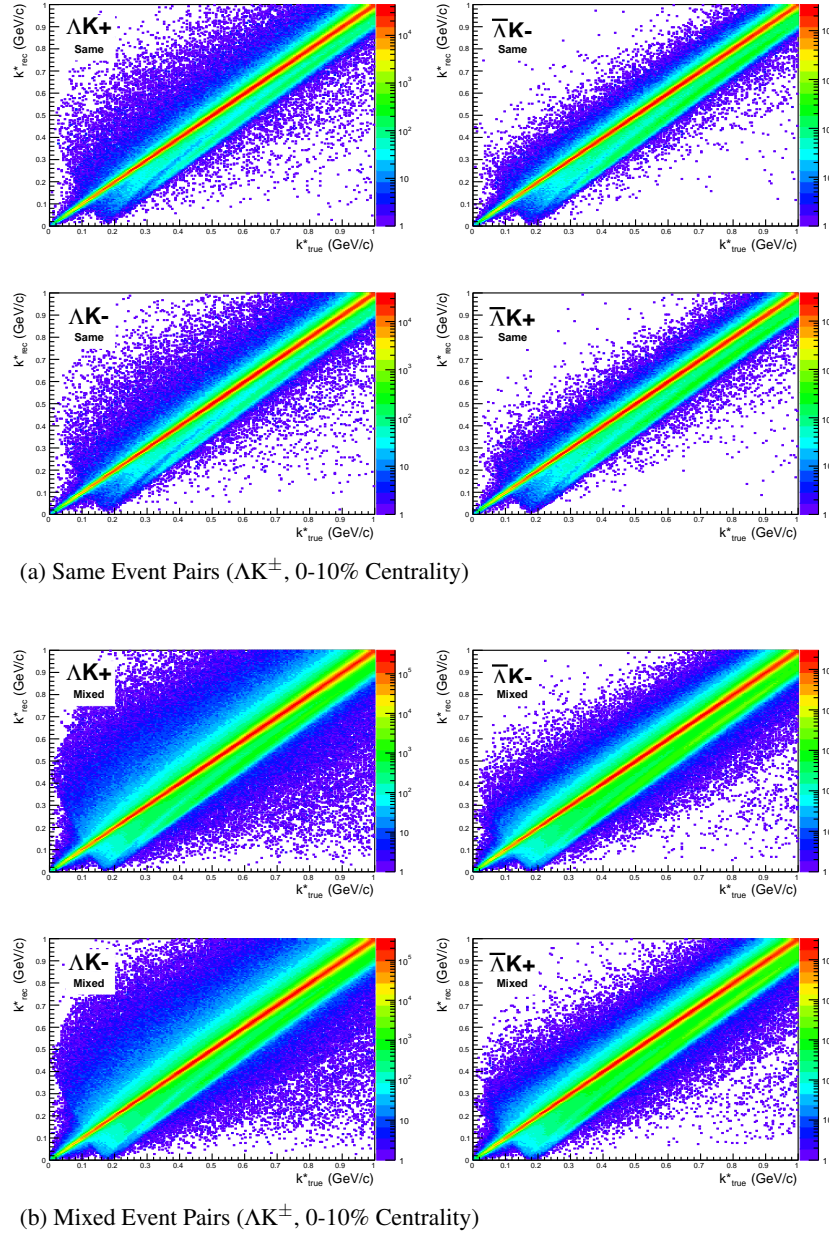
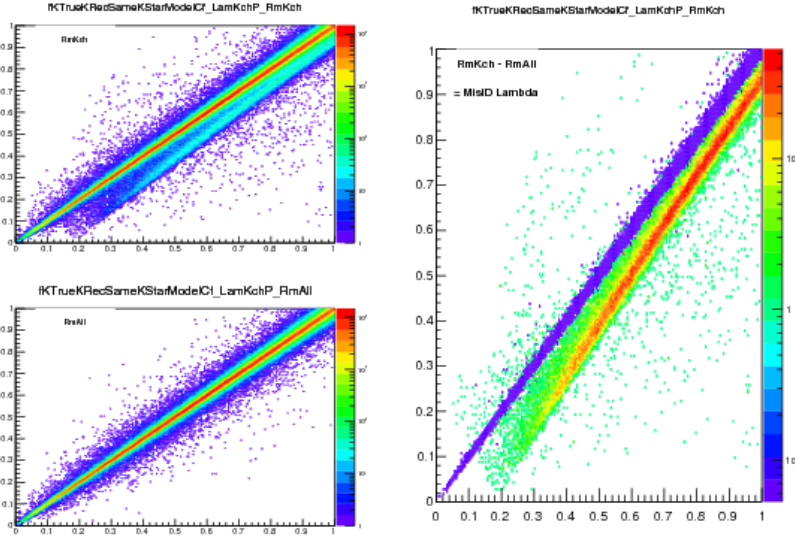
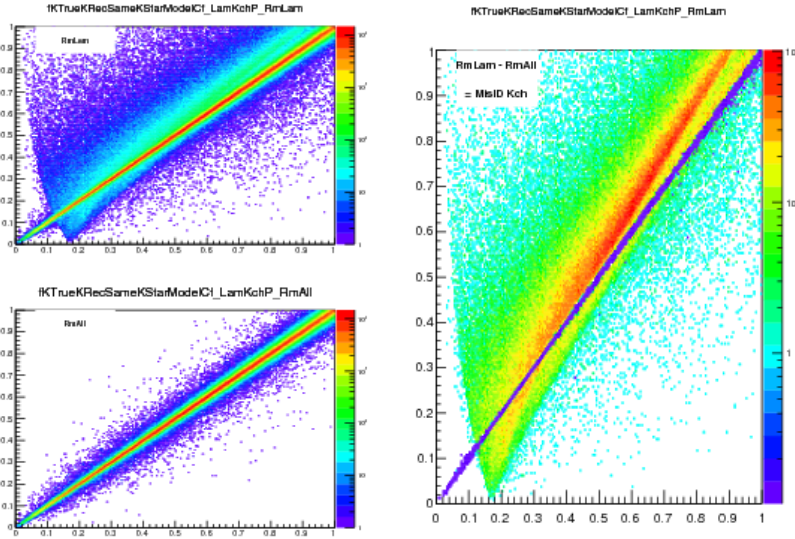


Fig. 17: Sample k_{True}^* vs. k_{Rec}^* plots from MC HIJING events for ΛK^\pm 0-10% analyses. The structure which appears around $k_{\text{Rec}}^* = k_{\text{True}}^* - 0.15 \text{ GeV}/c$ is mainly caused by K_S^0 contamination in our $\Lambda(\bar{\Lambda})$ sample. The remaining structure not distributed about $k_{\text{Rec}}^* = k_{\text{True}}^*$ is due to π and e contamination in our K^\pm sample. These contaminations are more clearly visible in Figure 16

such, applying the momentum resolution correction and fitting becomes a long and drawn out iterative process. An initial parameter set is obtained (through fitting without momentum resolution corrections, theoretical models, or a good guess), then the MC data is analyzed to obtain correlation functions needed to calculate the correction factor, the data is fit using the correction factor, a refined parameter set is extracted, the MC data is analyzed again to obtain the new correction factor, etc. This process continues until the parameter set stabilizes. The second issue concerns statistics. With the MC data available on the grid, we were not able to generate the statistics necessary to use the raw $C_{\text{True}}/C_{\text{Rec}}$ ratio. The ratio was not stable, and when applied to the data, obscured the signal. Attempting to fit the ratio to use to generate the corrections also proved problematic. However, as HIJING does not include final-state interactions, the same-event and mixed-event pairs are very similar (with the exception of things like



(a) (Top Left) All misidentified K^+ excluded. (Bottom Left) All misidentified Λ and K^+ excluded. (Right) The difference of (Top Left) - (Bottom Left), which reveals the contamination in our Λ collection. The structure which appears around $k_{\text{Rec}}^* = k_{\text{True}}^* - 0.15 \text{ GeV}/c$ is mainly caused by K_S^0 contamination in our $\Lambda(\bar{\Lambda})$ sample.



(b) (Top Left) All misidentified Λ excluded. (Bottom Left) All misidentified Λ and K^+ excluded. (Right) The difference of (Top Left) - (Bottom Left), which reveals the contamination in our K^+ collection. The structure not distributed about $k_{\text{Rec}}^* = k_{\text{True}}^*$ is due to π and e^- contamination in our K^\pm sample.

Fig. 18: In the figure, the y-axis = k_{Rec}^* , and the x-axis = k_{True}^* . (Left) k_{Rec}^* vs. k_{True}^* plots for a small sample of the ΛK^+ 0-10% central analysis, MC truth was used to eliminate misidentified particles in the K^+ (a) and Λ (b) collections. (Right) The difference of the top left and bottom left plots. Contaminations in our particle collections are clearly visible. Figure (a) demonstrates a K_S^0 contamination in our Λ collection; Figure (b) demonstrates a π and e^- contamination in our K^\pm collection.

401 energy and momentum conservation, etc). Therefore, one may build the numerator distribution using
 402 mixed-event pairs. This corresponds, more or less, to simply running the weight generator through the
 403 detector framework.

404 A second approach (“Matrix” method) is to use information gained from plots like those in Figure 15,

405 which can be considered response matrices. The response matrix describes quantitatively how each
 406 k_{Rec}^* bin receives contributions from multiple k_{True}^* bins, and can be used to account for the effects of
 407 finite momentum resolution. With this approach, the resolution correction is applied on-the-fly during
 408 the fitting process by propagating the theoretical correlation function (fit) through the response matrix,
 409 according to:

$$C_{\text{Fit}}(k_{\text{Rec}}^*) = \frac{\sum_{k_{\text{True}}^*} M_{k_{\text{Rec}}^*, k_{\text{True}}^*} C_{\text{Fit}}(k_{\text{True}}^*)}{\sum_{k_{\text{True}}^*} M_{k_{\text{Rec}}^*, k_{\text{True}}^*}} \quad (14)$$

410 where $M_{k_{\text{Rec}}^*, k_{\text{True}}^*}$ is the response matrix (Figure 15), $C_{\text{Fit}}(k_{\text{True}}^*)$ is the fit binned in k_{True}^* , and the denominator normalizes the result.

412 Equation 14 describes that, for a given k_{Rec}^* bin, the observed value of $C(k_{\text{Rec}}^*)$ is a weighted average of
 413 all $C(k_{\text{True}}^*)$ values, where the weights are the normalized number of counts in the $[k_{\text{Rec}}^*, k_{\text{True}}^*]$ bin. As
 414 seen in Figure 15, overwhelmingly the main contributions comes from the $k_{\text{Rec}}^* = k_{\text{True}}^*$ bins. Although
 415 the correction is small, it is non-negligible for the low- k^* region of the correlation function.

416 Here, the momentum resolution correction is applied to the fit, not the data. In other words, during
 417 fitting, the theoretical correlation function is smeared just as real data would be, instead of unsmearing
 418 the data. This may not be ideal for the theorist attempting to compare a model to experimental data, but
 419 it leaves the experimental data unadulterated. The current analyses use this second approach to applying
 420 momentum resolution corrections because of two major advantages. First, the MC data must be analyzed
 421 only once, and no assumptions about the fit are needed. Secondly, the momentum resolution correction
 422 is applied on-the-fly by the fitter, delegating the iterative process to a computer instead of the user.

423 The two methods described above, Ratio and Matrix, should reproduce the same results at the parameter
 424 set used to generate the $C_{\text{True}}/C_{\text{Rec}}$ needed for the Ratio method. Figure 17 shows that the two methods
 425 converge as the binning size is decreased.

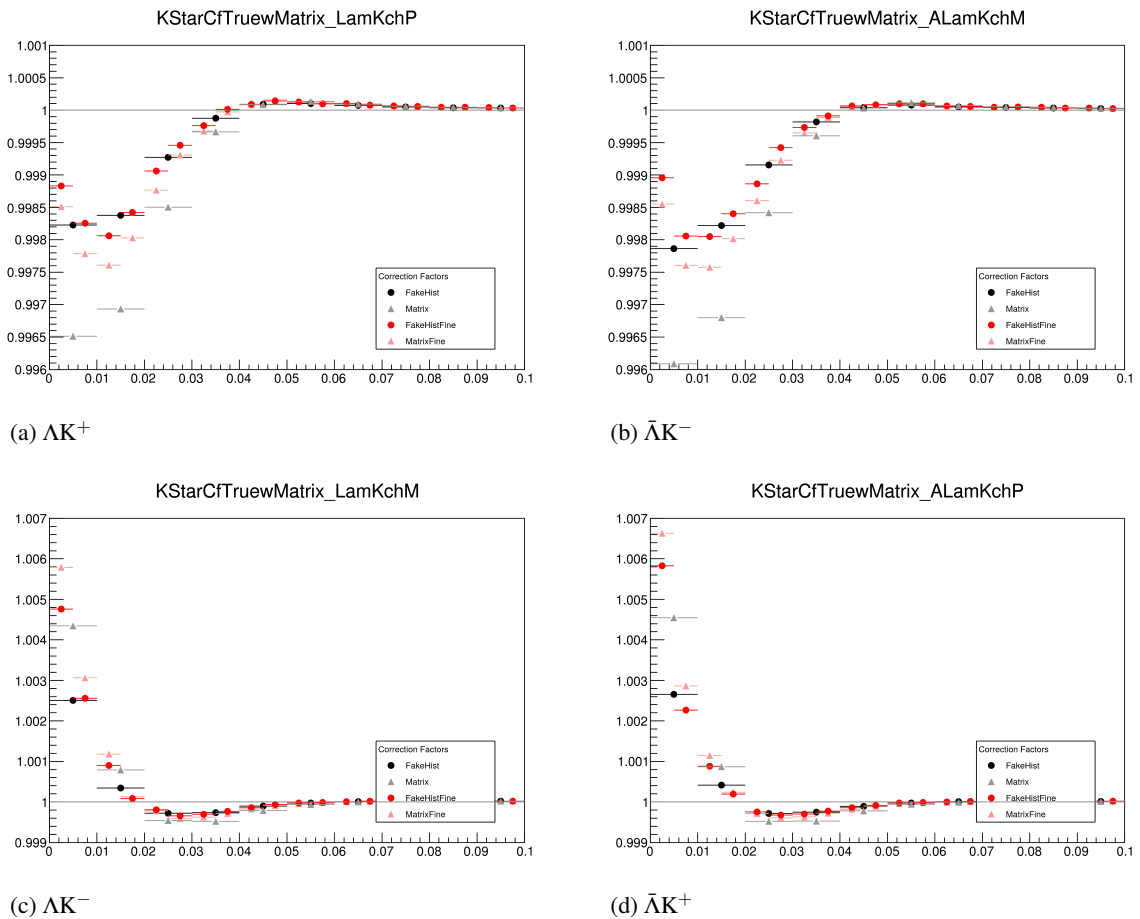


Fig. 19: Comparison of the two methods, Ratio and Matrix, for accounting for momentum resolution effects with HIJING. The Ratio method corresponds to the “FakeHist” histograms (circles), while the Matrix method corresponds to the “Matrix” histograms (triangles). Black shows a course binning, while red shows a finer binning.

426 **6.4 Residual Correlations**

427 The purpose of this analysis is study the interaction and scale of the emitting source of the primary
 428 ΛK pairs. In order to obtain correct results, it is desirable for our particle collections to consist of
 429 primary particles. In practice, this is impossible to achieve; many of our particles are not primary,
 430 but originate as decay products from other resonances. Some of our Λ hyperons decay from Σ^0 , Ξ^0 ,
 431 Ξ^- and $\Sigma^{*(+,-,0)}(1385)$ parents, and some of our K mesons decay from $K^{*(+,-,0)}(892)$ parents. In
 432 these decays, the daughter carries away a momentum very similar to that of its parent. As a result,
 433 the correlations between the particles in the daughter pair will be sensitive to, and dependent upon, the
 434 interaction between the parents. In effect, the correlation between the parents will be visible, although
 435 smeared out, in the daughters' signal. We call this a residual correlation resulting from feed-down. The
 436 contributions from the primary correlation, residual correlations, and fake pairs on the finally measure
 437 data is shown schematically in Figure 18. Residual correlations are important in an analysis when three
 438 criteria are met [7]: i) the parent correlation signal is large, ii) a large fraction of pairs in the sample
 439 originate from the particular parent system, and iii) the decay momenta are comparable to the expected
 440 correlation width in k^* .

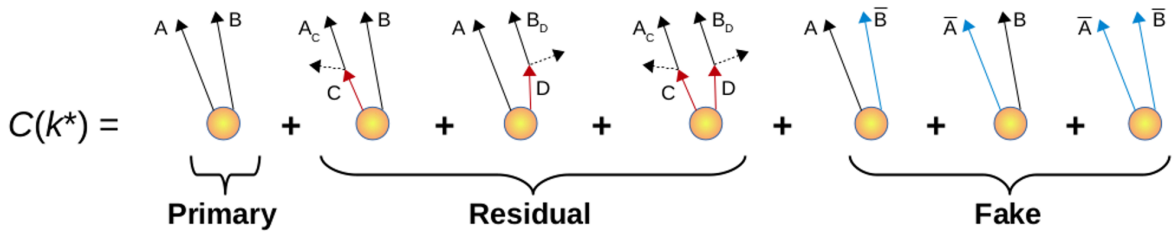


Fig. 20: A schematic representation of the contributions to the finally measured data from the primary correlation, residual correlations, and fake pairs.

441 As it is difficult for us to eliminate these residual correlations in our analyses, we must attempt to account
 442 for them in our fit. The genuine ΛK correlation function may be combined with the contributions from
 443 residual feed-down and misidentified particles to obtain the final, measured correlation function:

$$C_{\text{measured}}(k_{\Lambda K}^*) = 1 + \lambda'_{\Lambda K}[C_{\Lambda K}(k_{\Lambda K}^*) - 1] + \sum_{i,j} \lambda'_{ij}[C_{ij}(k_{\Lambda K}^*) - 1] \quad (15)$$

$$\begin{aligned} \lambda'_{ij} &= \lambda_{\text{Fit}} \lambda_{ij} \\ \sum_{i,j} \lambda'_{ij} &= \lambda_{\text{Fit}} \sum_{i,j} \lambda_{ij} = \lambda_{\text{Fit}} \end{aligned}$$

444 where the ΛK term represents the genuine ΛK correlation, and the i, j terms denote the contributions
 445 from residual feed-down and possible impurities. More specifically, $C_{ij}(k_{\Lambda K}^*)$ is the correlation function
 446 between parents of particle species i and j , expressed in the basis of the relative momentum of the
 447 observed daughter ΛK pairs. The λ parameters serve as weight dictating the strength of the parent
 448 contribution to the daughter pair, and are normalized to unity. The individual λ_{ij} are fixed (and whose
 449 values can be found in Table 5), but the parameter λ_{Fit} is left free. The λ_{Fit} parameter serves as an overall
 450 normalization shared by all contributors.

451 In order to obtain the parent correlation function expressed in the relative momentum of the daughter
 452 pair, one must use a transform matrix. The transform matrix describes the decay kinematics of the parent
 453 system into the daughter, and maps the k^* of the parent pair onto that of the daughter. Using this matrix,
 454 the transformed residual correlation function can be obtained:

$$C_{ij}(k_{\Lambda K}^*) \equiv \frac{\sum_{k_{ij}^*} C_{ij}(k_{ij}^*) T(k_{ij}^*, k_{\Lambda K}^*)}{\sum_{k_{ij}^*} T(k_{ij}^*, k_{\Lambda K}^*)} \quad (16)$$

The transform matrix is generated with the THERMINATOR 2 [8] simulation. It is formed for a given parent pair, ij , by taking all ΛK pairs originating from ij , calculating the relative momentum of the parents (k_{ij}^*) and daughters ($k_{\Lambda K}^*$), and filling a two-dimensional histogram with the values. The transform matrix is essentially an unnormalized probability distribution mapping the k^* of the parent pair to that of the daughter pair when one or both parents decay. An example of such transform matrices can be found in Figures 19 and 20.

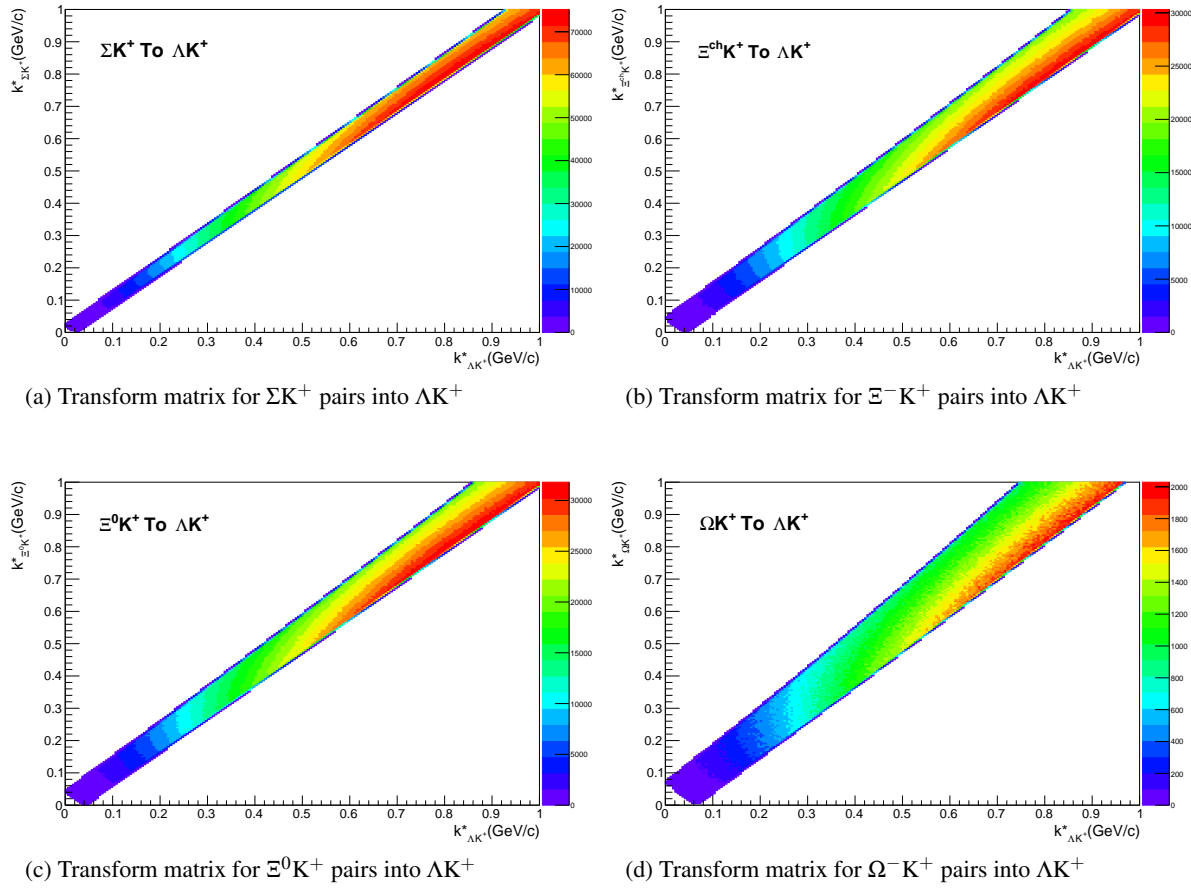


Fig. 21: Sample Transform Matrices generated with THERMINATOR for ΛK^+ Analysis

Femtoscopic analyses are sensitive to the pair emission structure at kinetic freeze-out. Therefore, in the eyes of femtoscopy, any particle born from a resonance decay before last rescattering is seen as primary. For our study, when including three residual contributors, we consider a particle to be primary if its parent has a proper decay length of $c\tau < 10$ fm. When including ten residual contributors, we must reduce this number to $c\tau < 4$ fm for consistency. Moving to ten contributors, we introduce feed-down from Σ^* and K^* resonances, with proper decay lengths of $c\tau \approx 5$ fm and $c\tau \approx 4$ fm, respectively. As these are considered non-primary for the case of ten contributors, so must any resonance with $c\tau > 4$ fm.

As previously stated, the λ parameters dictate the strength of the parent contribution to the daughter pair. Therefore, the λ parameter for parent system AB can be estimated as the total number of ΛK pairs in our

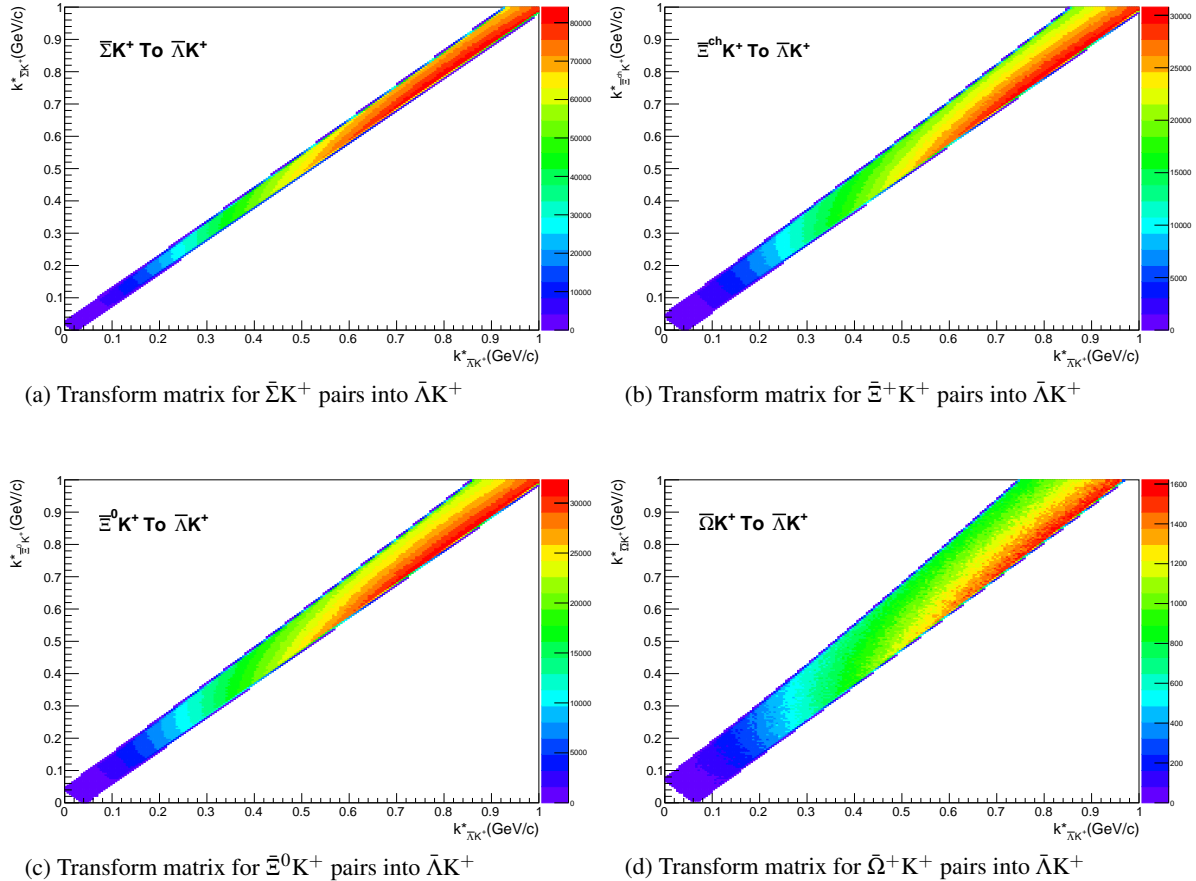


Fig. 22: Sample Transform Matrices generated with THERMINATOR for $\bar{\Lambda}K^+$ Analysis

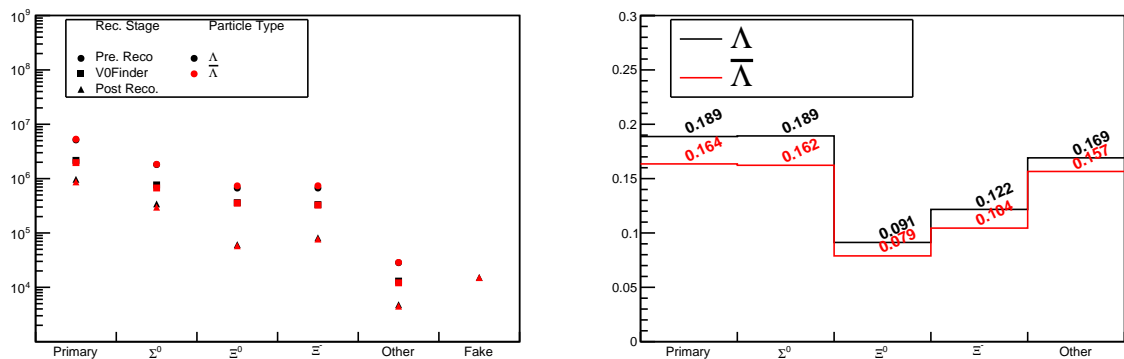
experimental sample originating from AB (N_{AB}) divided by the total number of ΛK pairs (N_{Total}):

$$\lambda_{AB} = \frac{N_{AB}}{N_{Total}} \quad (17)$$

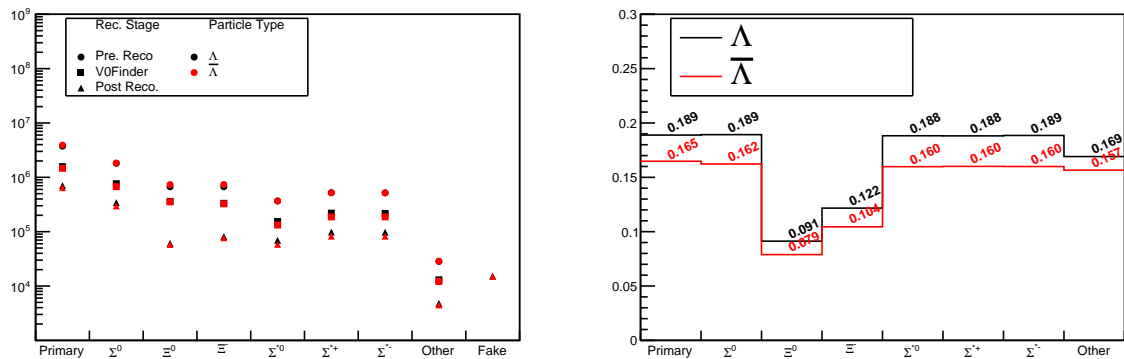
The particle yields can be estimated using THERMINATOR 2 simulation (N_{ij}^{THERM}), while the reconstruction efficiencies (RE_{ij}) are estimated with MC HIJING data, which has been run through GEANT to simulate the detector response (Fig. 21). Thus, the λ parameters are estimated as:

$$\lambda_{AB} = \frac{N_{AB}}{N_{Total}} = \frac{N_{AB}^{THERM} RE_{AB}^{HIJING}}{\sum_{ij} N_{ij}^{THERM} RE_{ij}^{HIJING}} \quad (18)$$

The λ values used can be found in Table 5, for the case of both three and ten residual contributors. In the table, we also list the λ values used for “Other” and “Fakes”. The “Other” category contains pairs which are not primary, and which do not originate from the (3 or 10) residual pairs included in the fit. The “Fakes” category represents pairs that are mistakenly identified as ΛK . To estimate this λ_{Fakes} value, we assumed that the number of fake pairs was equal to the total number of pairs multiplied by the Λ purity (i.e. assuming perfect purity for the kaons); or, more simply, $\lambda_{Fakes} = 1.0 - \text{Purity}(\Lambda)$. For both of these contributors (“Other” and “Fakes”), we assume that these correlations average to unity, and therefore do not contribute to the final correlation function.



(a) Reconstruction Efficiencies (3 Residuals)



(b) Reconstruction Efficiencies (10 Residuals)

Fig. 23: Reconstruction Efficiencies

AK ⁺ residuals		$\bar{\Lambda}K^-$ residuals		AK ⁻ residuals		$\bar{\Lambda}K^+$ residuals		AK _S ⁰ residuals		$\bar{\Lambda}K_S^0$ residuals	
Pair System	λ value	Pair System	λ value	Pair System	λ value	Pair System	λ value	Pair System	λ value	Pair System	λ value
3 Residuals (Max Parent $c\tau_{\text{decay}} = 10 \text{ fm}$)											
AK ⁺	0.527	$\bar{\Lambda}K^-$	0.526	AK ⁻	0.526	$\bar{\Lambda}K^+$	0.527	AK _S ⁰	0.543	$\bar{\Lambda}K_S^0$	0.544
$\Sigma^0 K^+$	0.111	$\bar{\Sigma}^0 K^-$	0.110	$\Sigma^0 K^-$	0.110	$\bar{\Sigma}^0 K^+$	0.111	$\Sigma^0 K_S^0$	0.120	$\bar{\Sigma}^0 K_S^0$	0.120
$\Xi^0 K^+$	0.039	$\bar{\Xi}^0 K^-$	0.035	$\Xi^0 K^-$	0.038	$\bar{\Xi}^0 K^+$	0.036	$\Xi^0 K_S^0$	0.042	$\bar{\Xi}^0 K_S^0$	0.039
$\Xi^- K^+$	0.050	$\bar{\Xi}^+ K^-$	0.046	$\Xi^- K^-$	0.050	$\bar{\Xi}^+ K^+$	0.046	$\Xi^- K_S^0$	0.054	$\bar{\Xi}^+ K_S^0$	0.050
Other	0.226	Other	0.235	Other	0.228	Other	0.233	Other	0.194	Other	0.199
Fakes	0.048	Fakes	0.048	Fakes	0.048	Fakes	0.048	Fakes	0.048	Fakes	0.048
10 Residuals (Max Parent $c\tau_{\text{decay}} = 4 \text{ fm}$)											
AK ⁺	0.180	$\bar{\Lambda}K^-$	0.180	AK ⁻	0.179	$\bar{\Lambda}K^+$	0.181	AK _S ⁰	0.192	$\bar{\Lambda}K_S^0$	0.193
$\Sigma^0 K^+$	0.116	$\bar{\Sigma}^0 K^-$	0.114	$\Sigma^0 K^-$	0.115	$\bar{\Sigma}^0 K^+$	0.116	$\Sigma^0 K_S^0$	0.125	$\bar{\Sigma}^0 K_S^0$	0.124
$\Xi^0 K^+$	0.040	$\bar{\Xi}^0 K^-$	0.037	$\Xi^0 K^-$	0.040	$\bar{\Xi}^0 K^+$	0.037	$\Xi^0 K_S^0$	0.043	$\bar{\Xi}^0 K_S^0$	0.040
$\Xi^- K^+$	0.052	$\bar{\Xi}^+ K^-$	0.047	$\Xi^- K^-$	0.052	$\bar{\Xi}^+ K^+$	0.048	$\Xi^- K_S^0$	0.056	$\bar{\Xi}^+ K_S^0$	0.052
$\Sigma^{*+} K^+$	0.054	$\bar{\Sigma}^{*-} K^-$	0.051	$\Sigma^{*+} K^-$	0.053	$\bar{\Sigma}^{*-} K^+$	0.051	$\Sigma^{*+} K_S^0$	0.058	$\bar{\Sigma}^{*-} K_S^0$	0.055
$\Sigma^{*-} K^+$	0.048	$\bar{\Sigma}^{*+} K^-$	0.050	$\Sigma^{*-} K^-$	0.048	$\bar{\Sigma}^{*+} K^+$	0.050	$\Sigma^{*-} K_S^0$	0.052	$\bar{\Sigma}^{*+} K_S^0$	0.054
$\Sigma^{*0} K^+$	0.048	$\bar{\Sigma}^{*0} K^-$	0.045	$\Sigma^{*0} K^-$	0.048	$\bar{\Sigma}^{*0} K^+$	0.045	$\Sigma^{*0} K_S^0$	0.052	$\bar{\Sigma}^{*0} K_S^0$	0.048
ΛK^{*0}	0.046	$\bar{\Lambda} \bar{K}^{*0}$	0.047	$\Lambda \bar{K}^{*0}$	0.046	$\bar{\Lambda} K^{*0}$	0.047	ΛK^{*0}	0.022	$\bar{\Lambda} K^{*0}$	0.022
$\Sigma^0 K^{*0}$	0.041	$\bar{\Sigma}^0 \bar{K}^{*0}$	0.041	$\Sigma^0 \bar{K}^{*0}$	0.041	$\bar{\Sigma}^0 K^{*0}$	0.041	$\Sigma^0 K^{*0}$	0.019	$\bar{\Sigma}^0 K^{*0}$	0.019
$\Xi^0 K^{*0}$	0.014	$\bar{\Xi}^0 \bar{K}^{*0}$	0.013	$\Xi^0 \bar{K}^{*0}$	0.014	$\bar{\Xi}^0 K^{*0}$	0.013	$\Xi^0 K^{*0}$	0.007	$\bar{\Xi}^0 K^{*0}$	0.006
$\Xi^- K^{*0}$	0.018	$\bar{\Xi}^+ \bar{K}^{*0}$	0.017	$\Xi^- \bar{K}^{*0}$	0.018	$\bar{\Xi}^+ K^{*0}$	0.017	$\Xi^- K^{*0}$	0.009	$\bar{\Xi}^+ K^{*0}$	0.008
Other	0.295	Other	0.310	Other	0.299	Other	0.307	Other	0.318	Other	0.330
Fakes	0.048	Fakes	0.048	Fakes	0.048	Fakes	0.048	Fakes	0.048	Fakes	0.048

Table 6: λ values for the individual components of the AK correlation functions for the case of 3 and 10 residual contributions.

482 In practice, we model the correlation function of the parents (ex. $\Sigma^0 K^+$), and run the correlation function
 483 through the appropriate transform matrix to determine the contribution to the daughter correlation func-
 484 tion (ex. ΛK^+). In an ideal world, we would simply look up the parent interaction in some table, and
 485 input this into our model, and form the parent correlation function, C_{ij} , through the Lednicky equation
 486 (for the case of one or more charge neutral particle in the pair), or via the CoulombFitter machinery
 487 described in Sec.5.2. Unfortunately, the world in which we live is not perfect, such a table does not
 488 exist, and little is known about the interaction between the particles in the residual pairs of this study.
 489 Additionally, introducing a unique set of scattering parameters and radii for each residual system would
 490 introduce a large number of additional fit parameters, for which we do not have many constraints, and
 491 would cause our fitter to be too unconstrained and yield untrustworthy results. Therefore, for this analy-
 492 sis, we assume all residual pairs have the same source size as the daughter pair. Furthermore, we assume
 493 Coulomb-neutral residual pairs share the same scattering parameters as the daughter pair. Therefore, for
 494 Coulomb-neutral pairs, such as $\Sigma^0 K$, and $\Xi^0 K$, $C_{ij}(k_{ij}^*)$ is calculated from Eqn. 5, with the help of Eqn. 7;
 495 $C_{ij}(k_{\Lambda K}^*)$ is then obtained by transforming $C_{ij}(k_{ij}^*)$ with Eq. 16, using the appropriate transform matrix.

496 For residual pairs affected by both the strong and Coulomb interactions, things are a bit more compli-
 497 cated. This is due to the fact that, for the case of both strong and Coulomb interaction, we no longer
 498 have a nice analytical form with which to fit. Generating a correlation function including both is also
 499 time consuming, as described further in Sec.5.2. This increase in formation time is not an issue in gen-
 500 erating single correlation functions, however, it does become a problem when including the method in
 501 the fit process, where thousands of generated correlation functions are needed (the parallelization of the
 502 process across a large number of GPU cores, to drastically decrease run-time, is currently underway).
 503 Therefore, when modeling $\Xi^- K^\pm$ residual correlations, we use the experimental $\Xi^- K^\pm$ data; in this case,
 504 there is no need to make any assumptions about scattering parameters or source sizes. The downside is
 505 that, especially in the 30-50% centrality bin, the statistics are low and error bars large. For the other
 506 cases, we assume the strong interaction is negligible, and generate the parent correlation assuming a
 507 Coulomb-only scenario (see Sec.5.2 for more details). This approximation is well justified here as a
 508 Coulomb-only description of the system describes, reasonably well, the broad features of the $\Xi^{ch} K^{ch}$
 509 correlation; the strong interaction is necessary for the fine details. However, as these correlations are
 510 run through a transform matrix, which largely flattens out and fine details, a Coulomb-only description
 511 should be sufficient.

512 In practice, the Coulomb-only scenario is achieved by first building a large number of Coulomb-only
 513 correlations for various radii and λ parameter values, and interpolating from this grid during the fitting
 514 process. This allows us to generate the correlations functions with the speed needed to converge on
 515 fit results within a reasonable amount of time. We find consistent results between using the ΞK data
 516 and the Coulomb-only interpolation method. When quantifying the $\Xi^- K^\pm$ residual contribution, the
 517 experimental $\Xi^- K^\pm$ data is always used. When the number of residual pairs used is increased to 10,
 518 so that contributors such as $\Sigma^{*+} K^-$ enter the picture, the Coulomb-only interpolation method is used.
 519 In other words, the ΞK experimental data is only used to model the ΞK residual contribution, all other
 520 charged pairs are treated with the Coulomb-only interpolation method.

521 Two examples of how very different transform matrices can alter a correlation function are shown in
 522 Figures 22 and 23 below. These figures were taken using parameter values obtained from fits to the data.
 523 In the top left corner of the figures, the input correlation function (closed symbols) is shown together
 524 with the output, transformed, correlation function (open symbols). In the bottom left, the transformed
 525 correlation is shown by itself (with zoomed y-axis). This is especially helpful when the λ parameter is
 526 very small, in which case the contribution in the top left can look flat, but the zoomed in view in the
 527 bottom left shows the structure. The right two plots in each figure show the transform matrix without
 528 (top right) and with (bottom right) a log-scale on the z-axis. Note, more examples of these transforms
 529 can be found in Sec. 9.

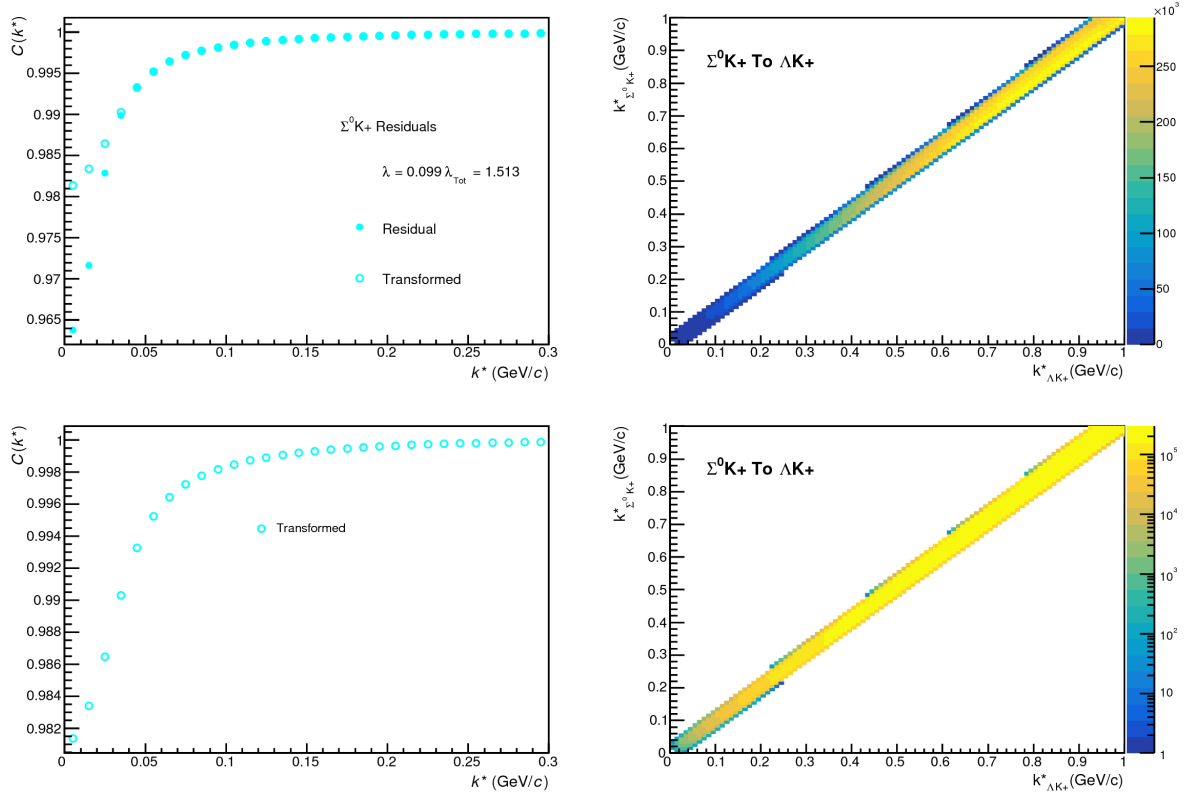


Fig. 24: $\Sigma^0 \text{K}^+$ Transform. These figures were taken using parameter values obtained from fits to the data. In the top left corner of the figures, the input correlation function (closed symbols) is shown together with the output, transformed, correlation function (open symbols). In the bottom left, the transformed correlation is shown by itself. The right two plots in each figure show the transform matrix without (top right) and with (bottom right) a log-scale on the z-axis.

Concerning the radii of the residual parent pairs, it was suggested that these should be set to smaller values than those of the daughter pair. In the interest of minimizing the number of parameters in the fitter, we tested this by introducing an m_T -scaling of the parents' radii. The motivation for this scaling comes from the approximate m_T -scaling of the radii observed in 30. To achieve this scaling, we assume the radii follow an inverse-square-root distribution: $R_{AB} = \alpha m_T^{-1/2}$. Then, it follows that we should scale the parent radii as:

$$R_{AB} = R_{\Lambda K} \left(\frac{m_{T,AB}}{m_{T,\Lambda K}} \right)^{-1/2} \quad (19)$$

The values of m_T for each pair system were taken from THERMINATOR. As the fitter dances around parameter space and selects a new radius for the ΛK system, the radii of the residuals is simply the ΛK radius scaled by the appropriate factor, given above (Eq.19). In the end, this scaling factor made no significant difference in our fit results, so this complication is excluded from our final results. Note that this is not surprising, as the most extreme scaling factor was, in the case of using 10 residual systems, between ΛK^+ with $m_{T,\Lambda K^+} \approx 1.4 \text{ GeV}/c^2$ and $\Xi^- K^{*0}$ with $m_{T,\Xi^- K^{*0}} \approx 1.8 \text{ GeV}/c^2$, resulting in a scale factor of ≈ 0.9 .

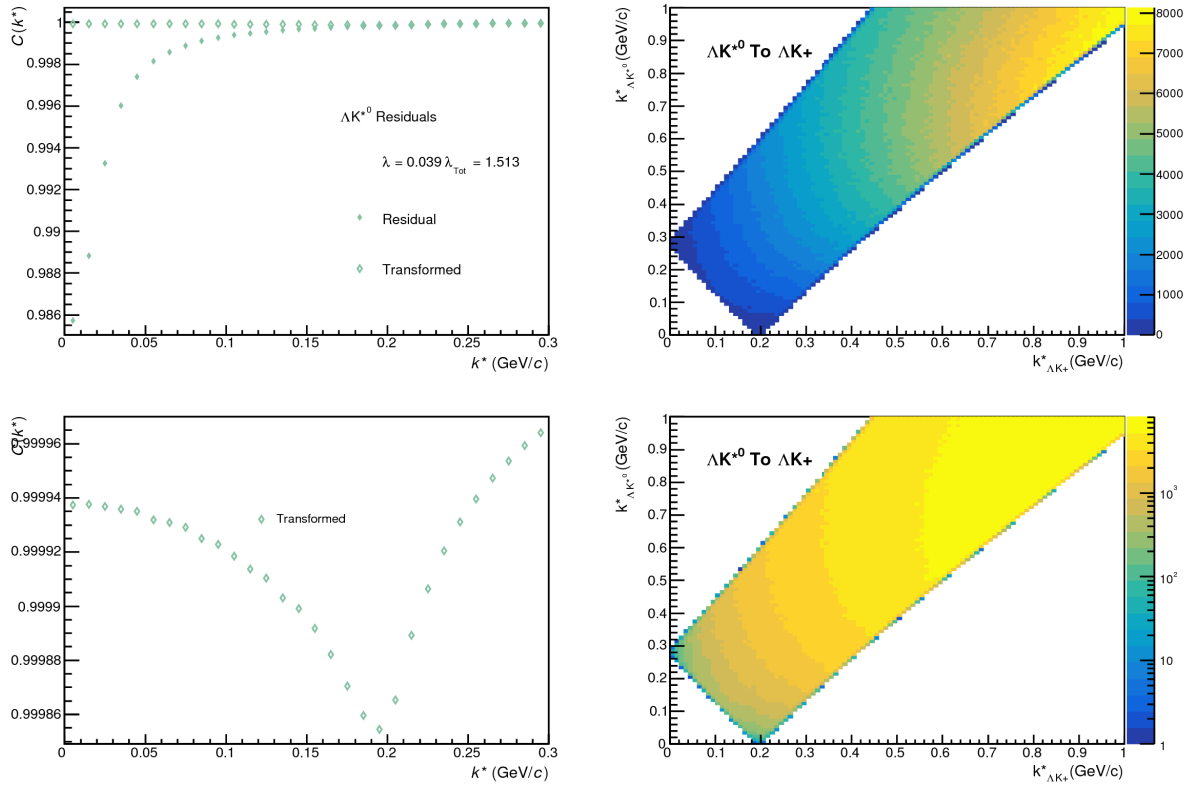


Fig. 25: ΛK^0 Transform. These figures were taken using parameter values obtained from fits to the data. In the top left corner of the figures, the input correlation function (closed symbols) is shown together with the output, transformed, correlation function (open symbols). In the bottom left, the transformed correlation is shown by itself. The right two plots in each figure show the transform matrix without (top right) and with (bottom right) a log-scale on the z-axis.

543 **6.5 Non-Flat Background**

544 We observe a significant non-femtoscopic, non-flat, background in all of our correlations at large k^* .
 545 This background increases with decreasing centrality, is the same amongst all ΛK^\pm pairs, and is more
 546 pronounced in the ΛK_S^0 system, as can be seen in Fig. 24. Figure 25a shows that THERMINATOR 2
 547 simulation does a good job of describing the difference in backgrounds between ΛK^\pm and ΛK_S^0 .

548 Before beginning, it is important to note that the difference in ΛK^\pm and ΛK_S^0 backgrounds is due mainly
 549 to the difference in kinematic cuts, not due to any interesting physics. Figure 25b shows that, for THER-
 550 MINATOR simulation, when restrictions are imposed on the p_T of the K_S^0 to more closely match the
 551 K^\pm cuts, the backgrounds align much better. Therefore, we conclude that the difference in background
 552 between ΛK^\pm and ΛK_S^0 observed in our experimental data is simply due to a difference in kinematic cuts
 553 between K^\pm and K_S^0 particles.

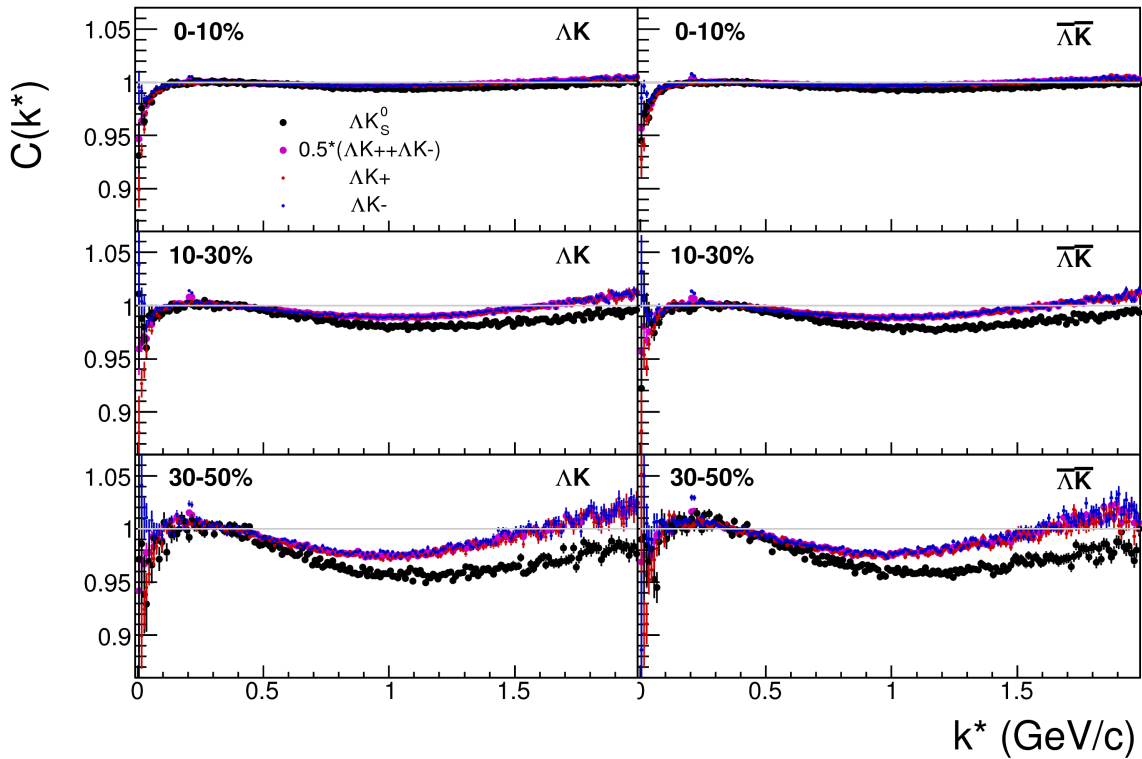


Fig. 26: A comparison on the non-femtoscopic backgrounds observed in our our ΛK experimental data.

544 It is suggested that this background effect is due primarily to particle collimation associated with elliptic
 545 flow [9]. More specifically, these backgrounds result from mixing events with unlike event-plane angles
 546 (Ψ_{EP}). As explained in [9], when elliptic flow is present, all particles are more likely to be emitted
 547 in a specific direction (in-plane), as opposed to a perpendicular direction. Therefore, the difference in
 548 momenta for pairs of particles tends to be smaller, compared to the case of no flow. In the case of mixed-
 549 event pairs, the two events used do not share an event-plane, and therefore there is no collimation effect
 550 in the pairs from flow. As a result, pairs with larger momentum are more likely when mixed-events
 551 are used (in the denominator of the correlation function), causing the correlation function to dip below
 552 unity. In general, the observation of the correlation function below unity, at a given k^* , means it is more
 553 probable to find a pair at that k^* when the daughters are taken from mixed-events, as compared to when
 554 they are taken from the same event. This same reasoning suggests that the background should lead to an
 555 enhancement at low- k^* . The enhancement at high- k^* ($k^* \gtrsim 1.5$ GeV/c) does not result from the collective
 556 flow of the system. We are not certain what causes this enhancement, but typical suspects are jet-like

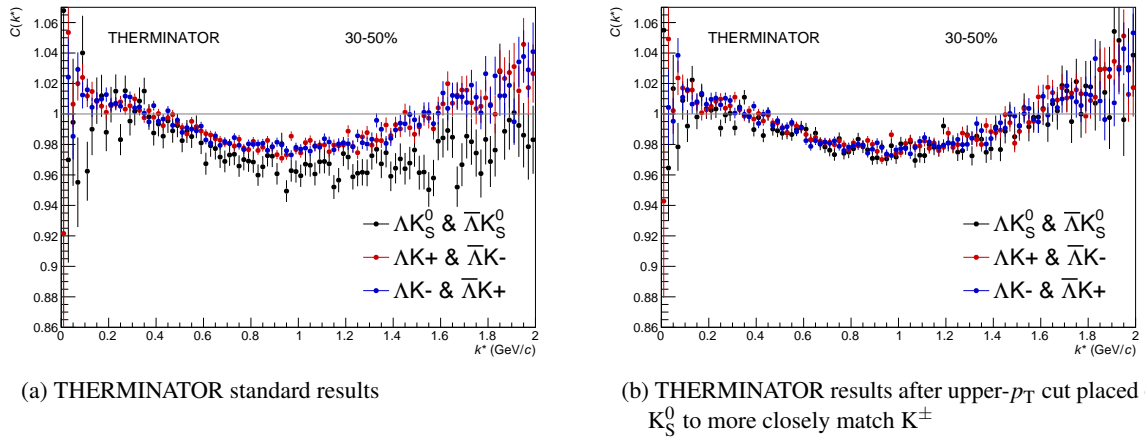


Fig. 27: THERMINATOR 2 simulation for ΛK^+ (red), ΛK^- (blue), and ΛK_S^0 (black). In 25a, we show the standard THERMINATOR 2 results. THERMINATOR 2 does a good job describing qualitatively the different between the ΛK^\pm and ΛK_S^0 backgrounds. In 25b, an upper- p_T cut was placed on the K_S^0 particles to more closely match the K^\pm kinematic cuts. After this tweak, the ΛK^\pm and ΛK_S^0 backgrounds agree much better.

567 correlations and resonance decays.

568 We can split our correlation functions into three main regions. First, the low- k^* region ($k^* \lesssim 0.3$ GeV/c)
 569 contains the femtoscopic correlations, as well as a likely enhancement from the background. The
 570 intermediate- k^* region ($0.3 \lesssim k^* \lesssim 1.5$ GeV/c) contains a suppression from the background. Finally,
 571 the high- k^* region ($k^* \gtrsim 1.5$ GeV/c) contains an enhancement with unknown origin.

572 The issue here is that we need to know the behavior of the non-femtoscopic background in the low-
 573 k^* region, but we only cleanly observe it in the region further out where there is no femtoscopic signal.
 574 Unfortunately, we cannot simply rotate each event to artificially align their event-planes and rid ourselves
 575 of this mixing effect, as our azimuthal angle acceptance is not perfectly uniform, and we have only finite
 576 event-plane resolution. With better resolution, one could simply bin events in Ψ_{EP} and only mix events
 577 within a given bin. We pursued this direction, and observed a slight decrease in the background; however,
 578 going to finer binning, we saw no additional reduction in the background, signaling that we had reached
 579 the limits dictated by the resolution. In the end, we are forced to model the background to include it into
 580 our fit.

581 THERMINATOR 2 simulation has been shown to reproduce the background features in a πK analysis
 582 [9]. After issuing each simulated event a random Ψ_{EP} ¹, we found THERMINATOR 2 did an exceptional
 583 job of describing our data. Furthermore, the simulation showed the non-femtoscopic background affects
 584 the correlation function as a separable scale factor (Fig 27, discussed below). Figure 26 shows the
 585 THERMINATOR 2 simulation (gold) together with experimental data (red, blue, or black). The figure
 586 also shows a 6th-order polynomial fit to the simulation (gold), as well as the fit polynomial scaled to
 587 match the data (red, blue, black).

588 Figure 27 shows three different correlation function generated using THERMINATOR 2 simulation (“Cf
 589 w/o Bgd (A)”, “Cf w. Bgd (B)”, “Bgd(C)”), as well as two histograms describing the relation between
 590 the three (“Ratio (B/C)”, “1+Diff(B-C)”). “Cf w/o Bgd (A)” shows a correlation function with a femto-
 591 scopic correlation, but without background. When THERMINATOR 2 is run without randomizing event
 592 planes, and therefore having all events share a common event plane, no background is observed, as ex-
 593 pected. The femtoscopic correlation effect was introduced by assuming a set of scattering parameters for

¹default was for all events to share a common event plane

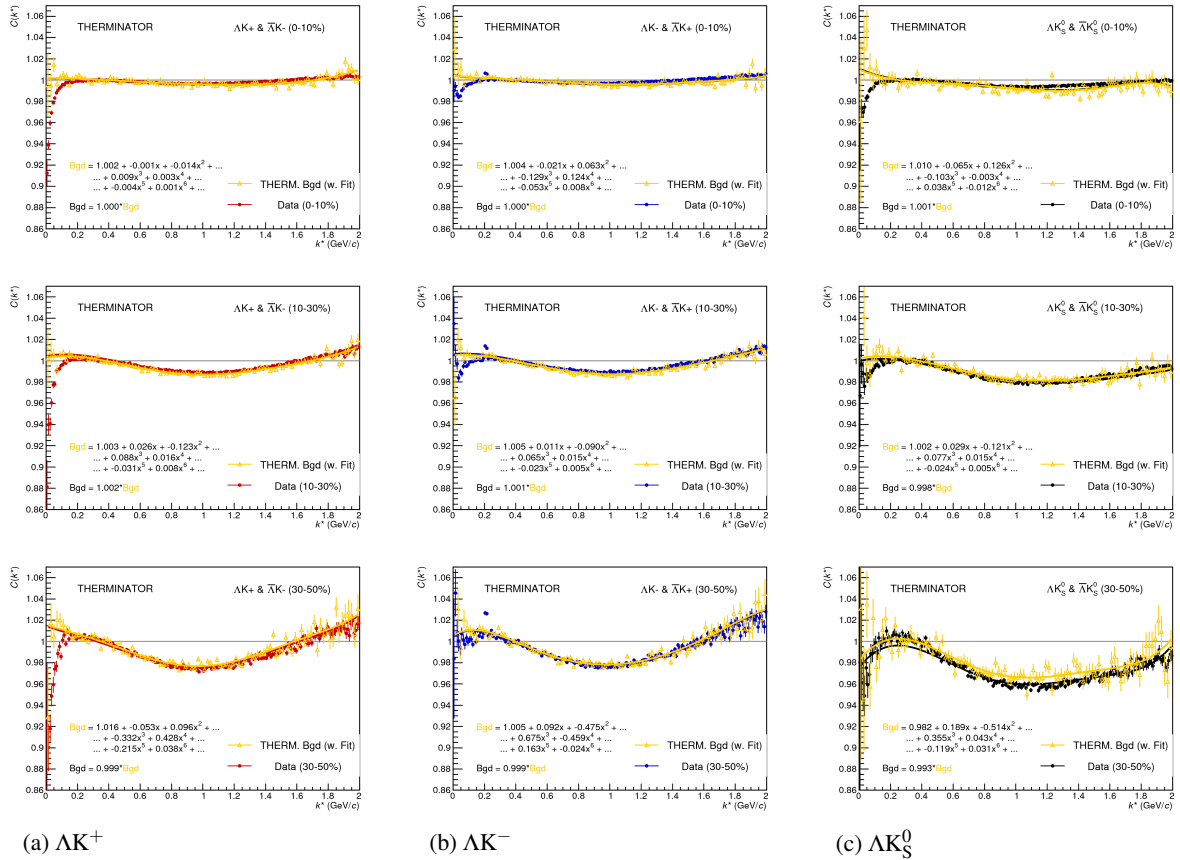


Fig. 28: THERMINATOR 2 simulation (gold) together with experimental data (red, blue, or black). The left column shows results for ΛK^+ (26a), middle for ΛK^- (26b), and right for ΛK_S^0 (26c). A 6th-order polynomial fit to the simulation is shown as a solid gold line, and whose fit parameters are printed on the lower left of each plot. This polynomial is scaled to match the experimental data; the value of this scale is printed in the lower left corner of each plot. The polynomial fit with scale factor applied is drawn in a color matching the experimental data (red, blue, black).

the system, and weighting the numerators appropriately. The second correlation, "Cf w. Bgd (B)", shows a correlation function with both a femtoscopic correlation and a background (most closely matches our situation in experiment). To generate the background, each event was given a random event-plane angle, as is given to us in experiment. To generate the femtoscopic correlation, the same numerator weighting procedure was used. Finally, "Bgd (C)", shows a correlation function with a non-femtoscopic background, but no femtoscopic correlation, i.e. background only. This is generated just as "Cf w. Bgd (B)", with randomized event planes, but unit weights are used when filling the numerators, so no femtoscopic effects are included.

The main point of Fig. 27 is that the black points match the blue (and purple) points; or, equivalently:

$$C_{fw/oBgd} = \frac{C_{fw.Bgd}}{Bgd} \rightarrow C_{theory} = \frac{C_{exp}}{F_{Bgd}} \rightarrow C_{exp} = C_{theory} \cdot F_{Bgd} \quad (20)$$

i.e. THERMINATOR 2 simulation shows the non-femtoscopic background affects the correlation function as a separable scale factor. We expect this behavior to be roughly the same in the experimental data.

The description by THERMINATOR 2 of the non-femtoscopic backgrounds in the ΛK^\pm systems is re-

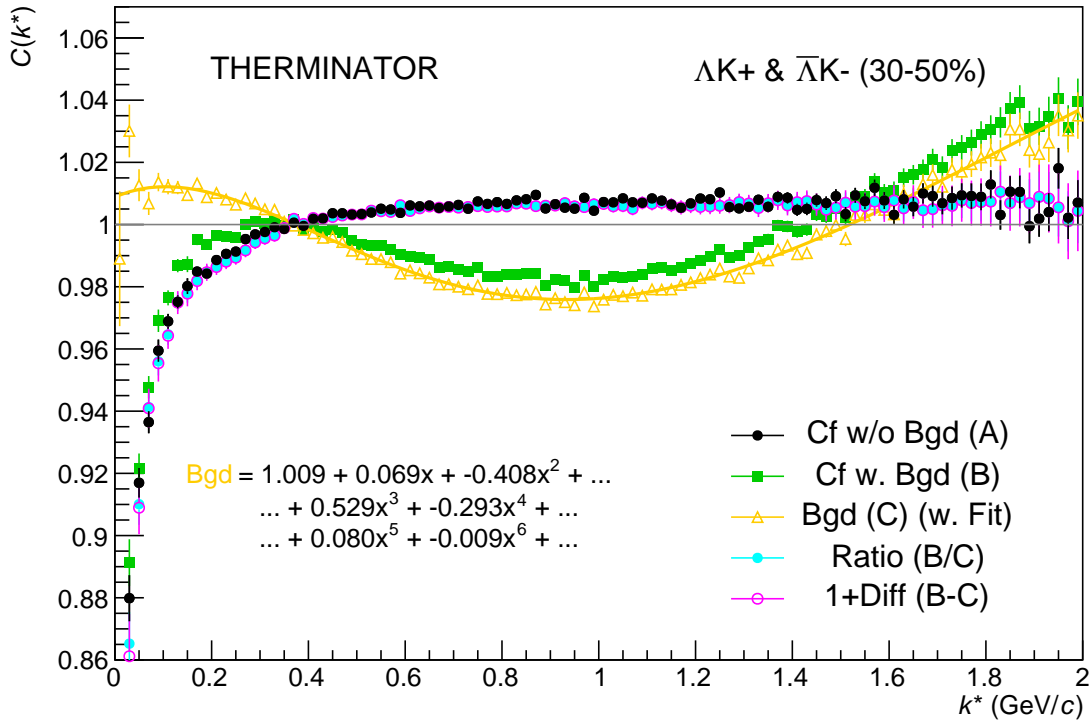


Fig. 29: Correlation with background decomposition with THERMINATOR. "Cf w/o Bgd (A)" shows a correlation function with a femtoscopic correlation, but without background. "Cf w. Bgd (B)", shows a correlation function with both a femtoscopic correlation and a background (most closely matches our situation in experiment). "Bgd (C)", shows a correlation function with a non-femtoscopic background, but no femtoscopic correlation, i.e. background only.

markable, and can be used in a quantitative fashion to help fit the data. More specifically, the non-femtoscopic backgrounds were modeled by (6th-)order polynomial fits to THERMINATOR 2 simulation for the ΛK^\pm analyses; one polynomial for each centrality class. The form of each polynomial was set before use with the experimental data, by fitting to the THERMINATOR 2 simulation, shown in Fig. 26. At the time of the fit, the polynomial used to correct each correlation function could only be adjusted by a simple scale factor to best match the data.

The description of the ΛK_S^0 is good at a qualitative level, but not quantitatively good enough to be utilized in our fit. As such, we use a linear form to model the background in the ΛK_S^0 system. The background for each correlation function was fixed before use in the signal region by fitting a linear form to the region $0.6 < k^* < 0.9 \text{ GeV}/c$. In all cases, the non-femtoscopic background correction was applied as a scale factor.

An alternative approach to treating the non-femtoscopic background is to instead attempt to eliminate it. The background may be effectively reduced by forming the reference distribution ($B(k^*)$) with the "Stavinskiy method". With the Stavinskiy method, mixed-event pairs are not used for the reference distribution; instead, same-event pseudo-pairs, formed by rotating one particle in a real pair by 180° in the transverse plane, are used. This rotation rids the pairs of any femtoscopic correlation, while maintaining correlations due to elliptic flow (and other suitably symmetric contributors). The effect on our ΛK correlation functions can be seen in the appendix, in Sec. 4.2.

Figure 28 demonstrates the use of the Stavinskiy method with THERMINATOR 2. In the figure, unit

weights were used for all numerators, so no femtoscopic signal is included, only background effects. The black points show an ideal, experimentally unreachable, situation of aligning all of the event-plane angles. With THERMINATOR 2, when the event-planes are aligned, the background signal is killed. The green points show the case of random event-plane angles, a situation more closely matching that of experiment. The purple points shown the affect of applying the Stavinskiy method to the case of random event-planes. The figure shows that this method effectively kills the non-flat background (i.e. the procedure takes the green points to the purple). Finally, the blue points show the effect of applying the Stavinskiy method when all of the event-planes are aligned. This shows that the Stavinskiy method does not introduce any signal to an already flat background.

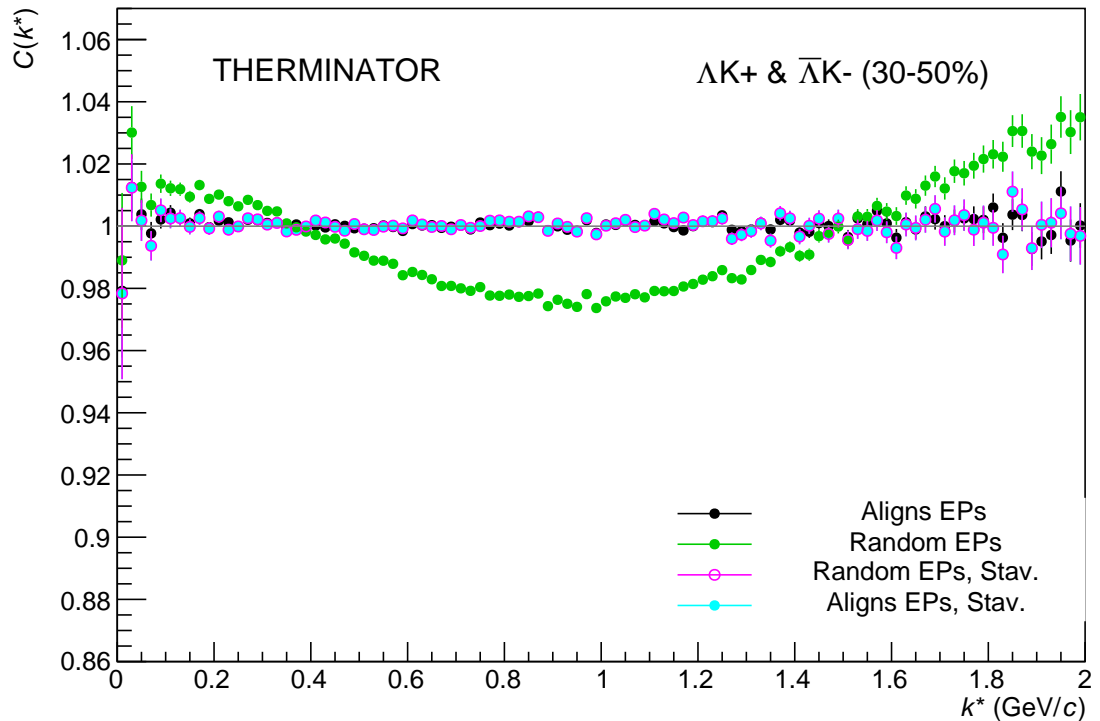


Fig. 30: The use of the Stavinskiy method with THERMINATOR 2. Unit weights were used for all numerators, so no femtoscopic signal is included, only background effects. The black points show an ideal, experimentally unreachable, situation of aligning all of the event-plane angles. The green points show the experimental situation of random event-plane angles. The purple points shown the affect of applying the Stavinskiy method to the case of random event-planes. Finally, the blue points show the effect of applying the Stavinskiy method when all of the event-planes are aligned.

635 6.6 LednickyFitter

The code developed to fit the data is called “LednickyFitter”, and utilizes the ROOT TMinuit implementation of the MINUIT fitting package. In short, given a function with a number of parameters, the fitter explores the parameter space searching for the minimum of the function. In this implementation, the function to be minimized should represent the difference between the measured and theoretical correlation functions. However, a simple χ^2 test is inappropriate for fitting correlation functions, as the ratio of two Poisson distributions does not result in a Poisson distribution. Instead, a log-likelihood fit function of the following form is used [3]:

$$\chi^2_{PML} = -2 \left[A \ln \left(\frac{C(A+B)}{A(C+1)} \right) + B \ln \left(\frac{A+B}{B(C+1)} \right) \right] \quad (21)$$

where A is the experimental signal distribution (numerator), B is the experimental background distribution (denominator), and C is the theoretical fit correlation function. Therefore, we use Eq. 21 as the statistic quantifying the quality of the fit. The parameters of the fit are: λ , R , f_0 ($\Re f_0$ and $\Im f_0$ separately), d_0 , and normalization N .

With our procedure, we are able to share parameters between different analyses and fit all simultaneously. A given pair and its conjugate (e.g. ΛK^+ and $\bar{\Lambda} K^-$) always share scattering parameters ($\Re f_0$, $\Im f_0$, d_0). However, the three distinct analyses (ΛK^+ , ΛK^- , and ΛK_S^0) are assumed to have scattering parameters unique from each other. We assume the pair emission source for a given centrality class is similar between all analyses; therefore, for each centrality, all ΛK analyses share a common radius parameter. We assume the same is true for the overall normalization λ parameters in Eq. 16. Finally, each correlation function has a unique normalization parameter.

All correlation functions were normalized in the range $0.32 < k^* < 0.40$ GeV/c, and fit in the range $0.0 < k^* < 0.30$ GeV/c. For the ΛK^- analysis, the region $0.19 < k^* < 0.23$ GeV/c was excluded from the fit to exclude the bump caused by the Ω^- resonance. For each pair system, we account for contributions from three residual contributors, as discussed in Sec. 5.4, and whose individual λ values are listed in Table 5 (the cases of zero and ten residual contributors were also investigated, but the case of three contributors was deemed most reasonable). We account for effects of finite track momentum resolution, as outlined in Sec. 5.3. The non-femtoscopic backgrounds are modeled using the THERMINATOR 2 simulation for the ΛK^\pm analyses, and with a linear form for the ΛK_S^0 system, as described in Sec. 5.5. In general, corrections are applied to the fit function, the raw data is never touched.

To summarize, the complete fit function is constructed as follows:

1. The uncorrected, primary, correlation function, $C_{\Lambda K}(k_{\text{True}}^*)$, is constructed using Eqns. 5 and 7
2. The correlation functions describing the parent systems which contribute residually are obtained using:
 - Eqns. 5 and 7 for the case of Coulomb-neutral pairs
 - $\Xi^- K^\pm$ experimental data for $\Xi^- K^\pm$ contributions
 - a Coulomb-only curve, with the help of Appendix ??, for other pairs including the Coulomb interaction
3. The residual contributions to the ΛK correlation function is found by running each parent correlation function through the appropriate transform matrix, via Eq.16
4. The primary and residual correlations are combined, via Eq.15 with Tab. 5, to form $C'_{Fit}(k_{\text{True}}^*)$
5. The correlation function is corrected to account for momentum resolution effects using Eq. 14, to obtain $C'_{Fit}(k_{\text{Rec}}^*)$
6. Finally, the non-flat background correction, $F_{\text{Bgd}}(k_{\text{Rec}}^*)$ is applied, and the final fit function is obtained, $C_{\text{Fit}}(k_{\text{Rec}}^*) = C'_{\text{Fit}}(k_{\text{Rec}}^*) * F_{\text{Bgd}}(k_{\text{Rec}}^*)$

Figures 45, 46, and 47 (31, 32, and 33, or 38, 39, and 40), in Section 7, show experimental data with fits for all studied centralities for $\Lambda K_S^0(\bar{\Lambda} K_S^0)$, $\Lambda K^+(\bar{\Lambda} K^-)$, and $\Lambda K^-(\bar{\Lambda} K^+)$, respectively. In the figures, the black solid line represents the “raw” fit, i.e. not corrected for momentum resolution effects nor non-flat

background. The green line shows the fit to the non-flat background. The purple points show the fit after momentum resolution, non-flat background, and residual correlations (if applicable) corrections have been applied. The extracted fit values with uncertainties are also printed on the figures.

6.7 Coulomb Fitter

When fitting the $\Xi^-(\bar{\Xi}^+)K^\pm$ results, it is necessary to include both strong and Coulomb effects. In this case, Equation 5 is no longer valid, and, in fact, there is no analytical form with which to fit. We therefore must take a more basic approach, and integrate out Eq.4 by hand. To achieve this, one has two options. The first option is to numerically integrate Eq.4. The second option is to simulate a large sample of particle pairs, calculate the wave function describing the interaction, and average to obtain the integral. Having no experience with either of these options, we elected the latter of simulating pairs. The code developed to achieve this functionality is called “CoulombFitter”. Currently, in order to generate the statistics needed for a stable fit, we find that $\sim 10^4$ simulated pairs per 10 MeV bin are necessary. The nature of this process means that the “CoulombFitter” takes much longer to run than the “LednickyFitter” of Section 5.1.

Unfortunately, with this analysis, we are not sensitive to, and therefore not able to distinguish between, the iso-spin singlet and triplet states. We proceed with our analysis, but the results must be interpreted as iso-spin averaged scattering parameters.

As stated before, to generate a fit correlation function, we must simulate a large number of pairs, calculate the wave-function, and average Ψ^2 over all pairs in a given k^* bin. Essentially, we calculate Equation 9 by hand:

$$\begin{aligned} C(\mathbf{k}^*) &= \sum_S \rho_S \int S(\mathbf{r}^*) |\Psi_{\mathbf{k}^*}^S(\mathbf{r}^*)|^2 d^3\mathbf{r}^* \\ &\longrightarrow C(|\mathbf{k}^*|) \equiv C(k^*) = \sum_S \rho_S \langle |\Psi^S(\mathbf{k}_i^*, \mathbf{r}_i^*)|^2 \rangle_i \\ &\longrightarrow C(k^*) = \lambda \sum_S \rho_S \langle |\Psi^S(\mathbf{k}_i^*, \mathbf{r}_i^*)|^2 \rangle_i + (1 - \lambda) \end{aligned} \quad (22)$$

where $\langle \rangle_i$ represents an average over all pairs in a given k^* bin.

In summary, for a given k^* bin, we must draw $N_{pairs} \sim 10^4$ pairs, and for each pair:

- 703 1. Draw a random \mathbf{r}^* vector according to our Gaussian source distribution $S(\mathbf{r}^*)$
- 704 2. Draw a random \mathbf{k}^* vector satisfying the $|\mathbf{k}^*|$ restriction of the bin
 - 705 – We draw from real k^* vectors obtained from the data
 - 706 – However, we find that drawing from a distribution flat in k^* gives similar results
- 707 3. Construct the wave-function Ψ

After all pairs for a given k^* bin are simulated and wave-functions obtained, the results are averaged to give the fit result.

Construction of the wave-functions, Equation 10, involves a number of complex functions not included in standard C++ or ROOT libraries (namely, $h(\eta)$, $\tilde{G}(\rho, \eta)$), and $F(-i\eta, 1, i\xi)$. These functions were even difficult to find and implement from elsewhere. Our solution was to embed a Mathematica kernel into our C++ code to evaluate these functions. However, having Mathematica work on-the-fly with the fitter was far too time consuming (fitter would have taken days, maybe weeks to finish). Our solution

715 was to use Mathematica to create matrices representing these functions for different parameter values.
 716 During fitting, these matrices were then interpolated and the results used to build the wave-functions.
 717 This method decreased the running time dramatically, and we are not able to generate results in under ~
 718 1 hour. This process will be explained in more detail in future versions of the note.

7 Systematic Errors

720 In order to understand the systematic uncertainties of our data, the analysis code was run many times
 721 using slightly different values for a number of important cuts, and the results were compared. To quantify
 722 the systematic errors on the data, all correlation functions built using all varied cut values were bin-by-
 723 bin averaged, and the resulting variance of each bin was taken as the systematic error. The cuts included
 724 in the systematic study, as well as the values used in the variations, are shown in Tab. 6 (ΛK_S^0) and Tab.
 725 7 (ΛK^\pm). Note, the central value corresponds to that used in the analysis.

726 Similarly, the fit parameters extracted from all of these correlation functions were averaged, and the
 727 resulting variances were taken as the systematic errors for the fit parameters. As with the systematic
 728 errors on the data, this was performed for all varied cut values. Additionally, a systematic analysis
 729 was done on our fit method through varying our k^* fit range, as well as varying our modeling of the
 730 non-femtoscopic background. Our choice of k^* fit range was varied by $\pm 25\%$. As previously stated,
 731 the non-femtoscopic backgrounds are modeled using the THERMINATOR 2 simulation for the ΛK^\pm
 732 analyses, and with a linear form for the ΛK_S^0 system. To study the contribution of this choice to our
 733 systematic errors, we modeled the backgrounds of all of our systems by fitting to the data with a with a
 734 linear, quadratic, and Gaussian form. Additionally, we modeled the backgrounds of all systems with a
 735 polynomial fit to the THERMINATOR simulation, scaled to match the data. The resulting uncertainties
 736 in the extracted parameter sets were combined with our uncertainties arising from our particle and pair
 737 cuts.

7.1 Systematic Errors: ΛK_S^0

7.1.1 Particle and Pair Cuts

740 The cuts included in the systematic study, as well as the values used in the variations, are listed below.
 741 Note, the central value corresponds to that used in the analysis.

ΛK_S^0 systematics	
DCA to PV $\Lambda(\bar{\Lambda})$	< [4, 5, 6] mm
DCA to PV K_S^0	< [2, 3, 4] mm
DCA $\Lambda(\bar{\Lambda})$ Daughters	< [3, 4, 5] mm
DCA K_S^0 Daughters	< [2, 3, 4] mm
$\cos(\theta_{PA}) \Lambda(\bar{\Lambda})$ to PV	> [0.9992, 0.9993, 0.9994]
$\cos(\theta_{PA}) K_S^0$ to PV	> [0.9992, 0.9993, 0.9994]
DCA to PV of $p(\bar{p})$ Daughter of $\Lambda(\bar{\Lambda})$	> [0.5, 1, 2] mm
DCA to PV of $\pi^-(\pi^+)$ Daughter of $\Lambda(\bar{\Lambda})$	> [2, 3, 4] mm
DCA to PV of π^+ Daughter of K_S^0	> [2, 3, 4] mm
DCA to PV of π^- Daughter of K_S^0	> [2, 3, 4] mm
Δr of Like-Charge Daughters	> [5, 6, 7] cm

Table 7: ΛK_S^0 systematics. In the table, the shorthand used is as follows: PA = pointing angle; PV = primary vertex; DCA = distance of closest approach; Δr = average separation

742 **7.1.2 Non-Flat Background**

743 We fit our non-flat background with a linear function. To study the contribution of this choice to our sys-
 744 tematic errors, we also fit with a quadratic and Gaussian form. The resulting uncertainties are combined
 745 with the uncertainties arising from our particle cuts.

746 **7.1.3 Fit Range**

747 Our choice of k^* fit range was varied by $\pm 25\%$. The resulting uncertainties in the extracted parameter
 748 sets were combined with our uncertainties arising from our particle and pair cuts.

749 **7.2 Systematic Errors: ΛK^\pm**

750 **7.2.1 Particle and Pair Cuts**

751 The cuts included in the systematic study, as well as the values used in the variations, are listed below.
 752 Note, the central value corresponds to that used in the analysis.

ΛK^\pm systematics	
DCA $\Lambda(\bar{\Lambda})$ to PV	< [4, 5, 6] mm
DCA $\Lambda(\bar{\Lambda})$ Daughters	< [3, 4, 5] mm
$\cos(\theta_{PA}) \Lambda(\bar{\Lambda})$ to PV	> [0.9992, 0.9993, 0.9994]
DCA to PV of $p(\bar{p})$ Daughter of $\Lambda(\bar{\Lambda})$	> [0.5, 1, 2] mm
DCA to PV of $\pi^-(\pi^+)$ Daughter of $\Lambda(\bar{\Lambda})$	> [2, 3, 4] mm
Δr of $\Lambda(\bar{\Lambda})$ Daughter with Same Charge as K^\pm	> [7, 8, 9] cm
DCA to PV in Transverse Plane of K^\pm	< [1.92, 2.4, 2.88]
DCA to PV in Longitudinal Direction of K^\pm	< [2.4, 3.0, 3.6]

Table 8: ΛK^\pm systematics. In the table, the shorthand used is as follows: PA = pointing angle; PV = primary vertex; DCA = distance of closest approach; Δr = average separation.

753 **7.2.2 Non-Flat Background**

754 We fit our non-flat background with a linear function. To study the contribution of this choice to our sys-
 755 tematic errors, we also fit with a quadratic and Gaussian form. The resulting uncertainties are combined
 756 with the uncertainties arising from our particle cuts.

757 **7.2.3 Fit Range**

758 Our choice of k^* fit range was varied by $\pm 25\%$. The resulting uncertainties in the extracted parameter
 759 sets were combined with our uncertainties arising from our particle and pair cuts.

760 **7.3 Systematic Errors: ΞK^\pm**

761 **7.3.1 Particle and Pair Cuts**

762 The cuts included in the systematic study, as well as the values used in the variations, are listed below.
 763 Note, the central value corresponds to that used in the analysis.

$\Xi^- K^\pm$ systematics

$\Xi^- K^\pm$ systematics	
DCA to PV $\Xi(\bar{\Xi})$	< [2, 3, 4] mm
DCA $\Xi(\bar{\Xi})$ Daughters	< [2, 3, 4] mm
$\cos(\theta_{PA}) \Xi(\bar{\Xi})$ to PV	> [0.9991, 0.9992, 0.9993]
$\cos(\theta_{PA}) \Lambda(\bar{\Lambda})$ to $\Xi(\bar{\Xi})$ DV	> [0.9992, 0.9993, 0.9994]
DCA to PV bachelor π	> [0.5, 1, 2] mm
DCA to PV $\Lambda(\bar{\Lambda})$	> [1, 2, 3] mm
DCA $\Lambda(\bar{\Lambda})$ Daughters	< [3, 4, 5] mm
DCA to PV of $p(\bar{p})$ Daughter of $\Lambda(\bar{\Lambda})$	> [0.5, 1, 2] mm
DCA to PV of $\pi^-(\pi^+)$ Daughter of $\Lambda(\bar{\Lambda})$	> [2, 3, 4] mm
$\Delta\mathbf{r}$ of $\Lambda(\bar{\Lambda})$ Daughter and K^\pm with like charge	> [7, 8, 9] cm
$\Delta\mathbf{r}$ of Bachelor π and K^\pm with like charge	> [7, 8, 9] cm
DCA to PV in Transverse Plane of K^\pm	< [1.92, 2.4, 2.88]
DCA to PV in Longitudinal Direction of K^\pm	< [2.4, 3.0, 3.6]

Table 9: $\Xi^- K^\pm$ systematics. In the table, the shorthand used is as follows: PA = pointing angle; PV = primary vertex; DV = decay vertex; DCA = distance of closest approach; $\Delta\mathbf{r}$ = average separation.

764 **8 Results and Discussion**

765 **8.1 Results: ΛK_S^0 and ΛK^\pm**

766 In the following sections, we present results assuming (i) three residual contributors (Sec. 7.1.1), (ii) ten
767 residual contributors (Sec. 7.1.2), and (iii) no residual correlations (Sec. 7.1.3).

768 For the results shown, unless otherwise noted, the following hold true: All correlation functions were
769 normalized in the range $0.32 < k^* < 0.40$ GeV/c, and fit in the range $0.0 < k^* < 0.30$ GeV/c. For the ΛK^-
770 and $\bar{\Lambda} K^+$ analyses, the region $0.19 < k^* < 0.23$ GeV/c was excluded from the fit to exclude the bump
771 caused by the Ω^- resonance. The non-femtoscopic backgrounds for the ΛK^+ and ΛK^- systems were
772 modeled by a (6th-order polynomial fit to THERMINATOR simulation, while those for the ΛK_S^0 were
773 fit with a simple linear form. The $\Lambda K^+(\bar{\Lambda} K^-)$ radii are shared with $\Lambda K^-(\bar{\Lambda} K^+)$, while the $\Lambda K_S^0(\bar{\Lambda} K_S^0)$
774 radii are unique. In the figures showing experimental correlation functions with fits, the black solid line
775 represents the primary (ΛK) correlation's contribution to the fit. The green line shows the fit to the non-
776 flat background. The purple points show the fit after all residuals' contributions have been included, and
777 momentum resolution and non-flat background corrections have been applied.

778 Before beginning, I first collect a summary of my final results in Figure 29. In the summary plot, we
779 show the extracted scattering parameters in the form of a $\Im f_0$ vs $\Re f_0$ plot, which includes the d_0 values
780 to the right side. We also show the λ vs. radius parameters for all three of our studied centrality bins.
781 In Fig. 29, three residual contributors were used. For the ΛK_S^0 results shown in the figure, the ΛK_S^0
782 and $\bar{\Lambda} K_S^0$ analyses were fit simultaneously across all centralities (0-10%, 10-30%, 30-50%); scattering
783 parameters and a single λ parameter were shared amongst all, the radii were shared amongst results
784 of like-centrality, and each has a unique normalization parameter. For the ΛK^\pm results shown, all four
785 pair combinations were fit simultaneously ($\Lambda K^+, \bar{\Lambda} K^-, \Lambda K^-, \bar{\Lambda} K^+$) across all centralities. Scattering
786 parameters were shared between pair-conjugate systems (i.e. a parameter set describing ΛK^+ & $\bar{\Lambda} K^-$,
787 and a separate set describing ΛK^- & $\bar{\Lambda} K^+$). For each centrality, a radius and λ parameters were shared
788 between all pairs. Each analysis has a unique normalization parameter.

789 **8.1.1 3 Residual Correlations Included in Fit**

790 Figure 29 nicely collects and summarizes all of our extracted fit parameters for the case of 3 included
 791 residual contributors. Figure 30 presents our extracted fit radii, along with those of other systems pre-
 792 viously analyzed by ALICE [10], as a function of pair transverse mass (m_T). Figures 31, 32, and 33
 793 show the experimental correlation functions with fits, assuming 3 residual contributors, for all studied
 794 centralities for ΛK_S^0 with $\bar{\Lambda} K_S^0$, ΛK^+ with $\bar{\Lambda} K^-$, and ΛK^- with $\bar{\Lambda} K^+$, respectively. The parameter sets
 795 extracted from the fits can be found in Tables 13 and 14.

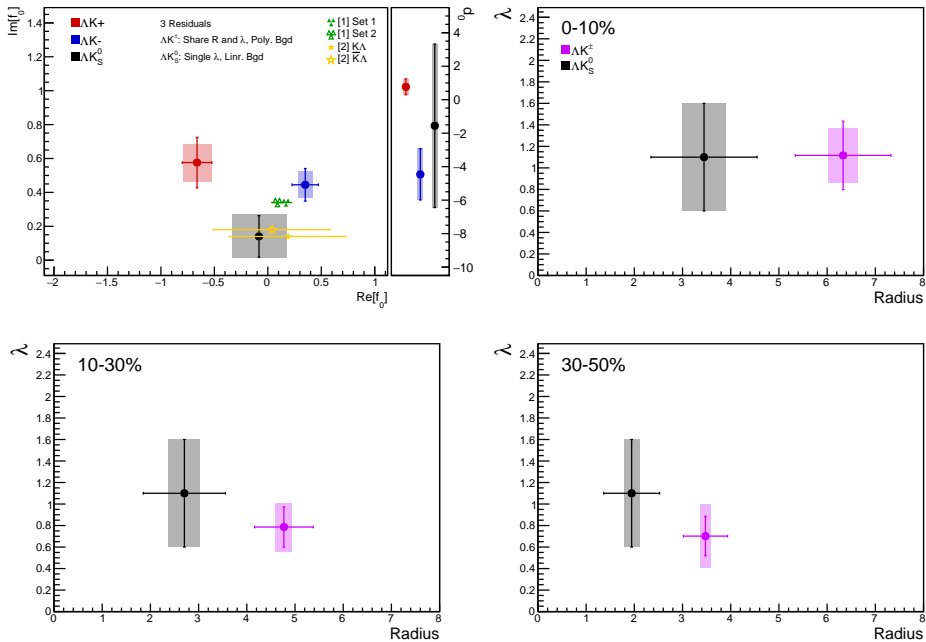


Fig. 31: Extracted scattering parameters for the case of 3 residual contributors for all of our ΛK systems. [Top Left]: $\Im f_0$ vs. $\Re f_0$, together with d_0 to the right. [Top Right (Bottom Left, Bottom Right)]: λ vs. Radius for the 0-10% (10-30%, 30-50%) bin. The green [11] and yellow [12] points show theoretical predictions made using chiral perturbation theory.

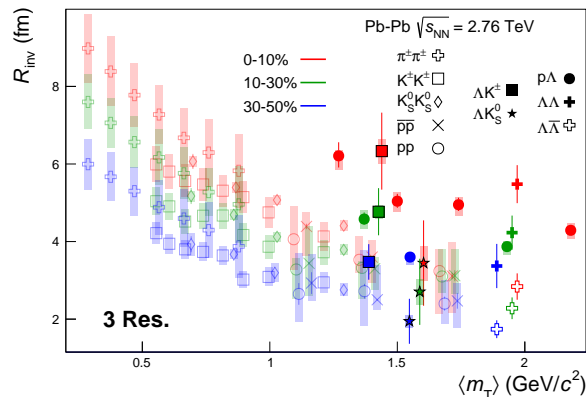


Fig. 32: 3 residual correlations in ΛK fits. Extracted fit R_{inv} parameters as a function of pair transverse mass (m_T) for various pair systems over several centralities. The ALICE published data [10] is shown with transparent, open symbols. The new ΛK results are shown with opaque, filled symbols. In the left, the ΛK^+ (with its conjugate pair) results are shown separately from the ΛK^- (with its conjugate pair) results. In the right, all ΛK^\pm results are averaged.

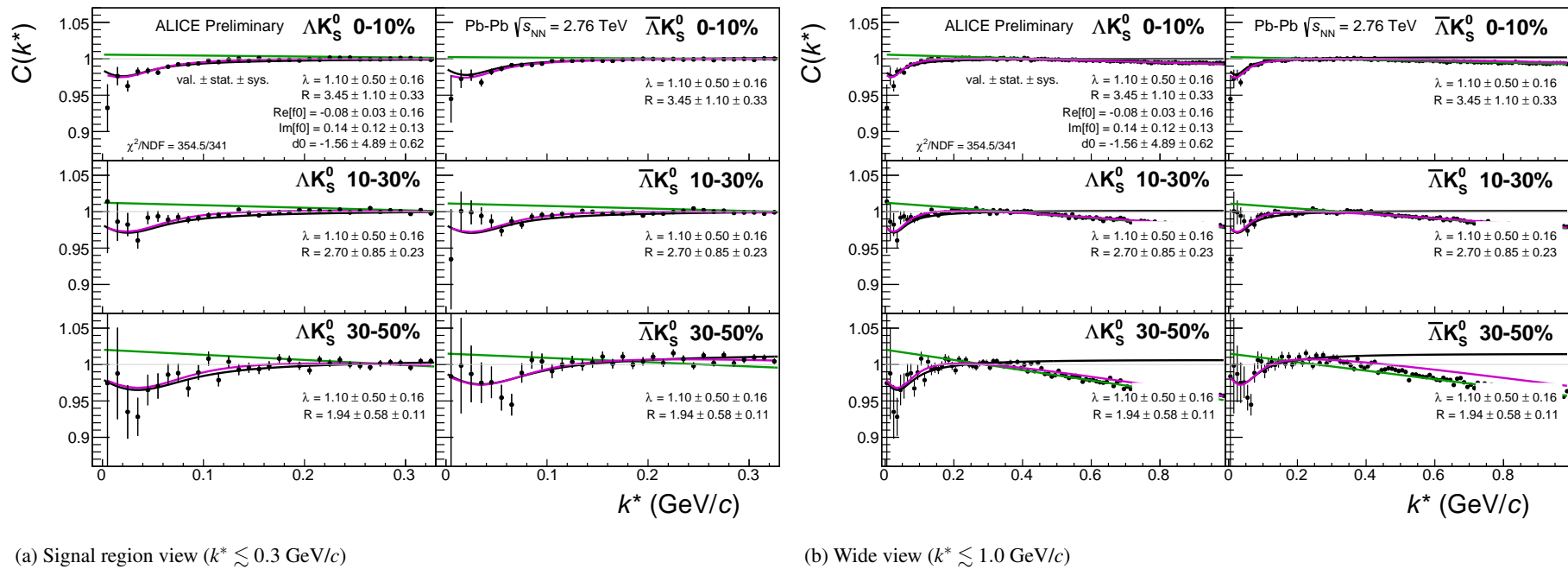


Fig. 33: Fits, with 3 residual correlations included, to the ΛK_S^0 (left) and $\bar{\Lambda} K_S^0$ (right) data for the centralities 0-10% (top), 10-30% (middle), and 30-50% (bottom). The lines represent the statistical errors, while the boxes represent the systematic errors. A single λ parameter is shared amongst all. Each analysis has a unique normalization parameter. The radii are shared between analyses of like centrality, as these should have similar source sizes. The scattering parameters ($\Im f_0$, $\Re f_0$, d_0) are shared amongst all. The background is modeled by a (6th-)degree polynomial fit to THERMINATOR simulation. The black solid line represents the primary (AK) correlation's contribution to the fit. The green line shows the fit to the non-flat background. The purple points show the fit after all residuals' contributions have been included, and momentum resolution and non-flat background corrections have been applied. The extracted fit values with uncertainties are printed.

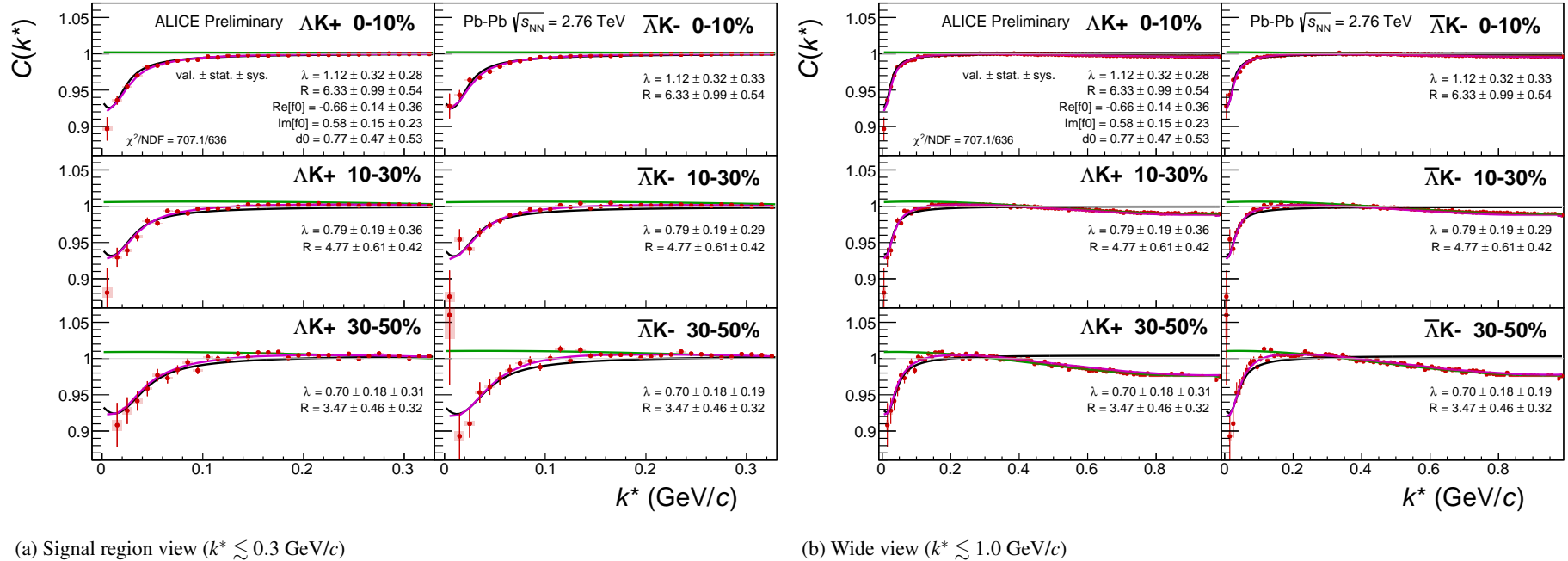


Fig. 34: Fits, with 3 residual correlations included, to the ΛK^+ (left) and $\bar{\Lambda} K^-$ (right) data for the centralities 0-10% (top), 10-30% (middle), and 30-50% (bottom). The lines represent the statistical errors, while the boxes represent the systematic errors. All ΛK^\pm analyses are fit simultaneously across all centralities (0-10%, 10-30%, 30-50%). Scattering parameters ($\Im f_0$, $\Re f_0$, d_0) are shared between pair-conjugate systems (i.e. a parameter set describing the ΛK^+ & $\bar{\Lambda} K^-$ system, and a separate set describing the ΛK^- & $\bar{\Lambda} K^+$ system). For each centrality, a radius and λ parameters are shared between all pairs (ΛK^+ , $\bar{\Lambda} K^-$, ΛK^- , $\bar{\Lambda} K^+$). Each analysis has a unique normalization parameter. The background is modeled by a (6th-degree polynomial fit to THERMINATOR simulation. The black solid line represents the primary (ΛK) correlation's contribution to the fit. The green line shows the fit to the non-flat background. The purple points show the fit after all residuals' contributions have been included, and momentum resolution and non-flat background corrections have been applied. The extracted fit values with uncertainties are printed.

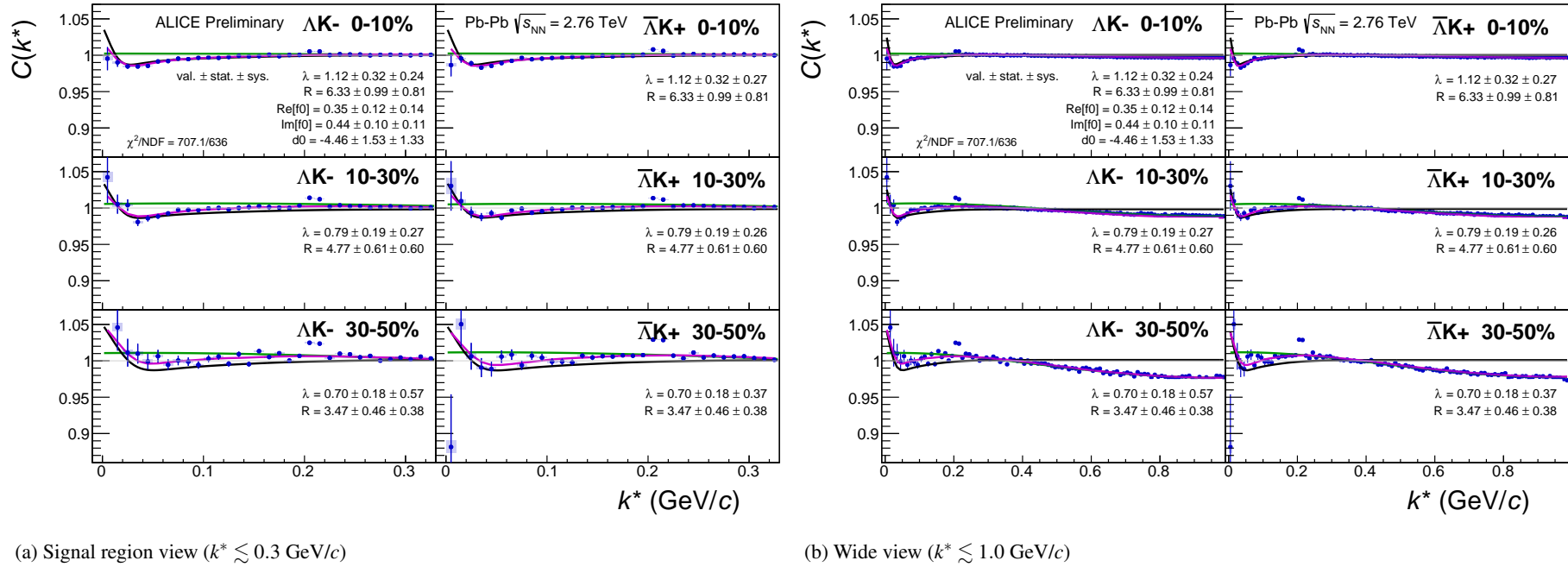


Fig. 35: Fits, with 3 residual correlations included, to the ΛK^- (left) with $\bar{\Lambda} K^+$ (right) data for the centralities 0-10% (top), 10-30% (middle), and 30-50% (bottom). The lines represent the statistical errors, while the boxes represent the systematic errors. All ΛK^\pm analyses are fit simultaneously across all centralities (0-10%, 10-30%, 30-50%). Scattering parameters ($\Im f_0$, $\Re f_0$, d_0) are shared between pair-conjugate systems (i.e. a parameter set describing the ΛK^+ & $\bar{\Lambda} K^-$ system, and a separate set describing the ΛK^- & $\bar{\Lambda} K^+$ system). For each centrality, a radius and λ parameters are shared between all pairs (ΛK^+ , $\bar{\Lambda} K^-$, ΛK^- , $\bar{\Lambda} K^+$). Each analysis has a unique normalization parameter. The background is modeled by a (6th-)degree polynomial fit to THERMINATOR simulation. The black solid line represents the “raw” fit, i.e. not corrected for momentum resolution effects nor non-flat background. The green line shows the fit to the non-flat background. The purple points show the fit after momentum resolution and non-flat background corrections have been applied. The extracted fit values with uncertainties are printed.

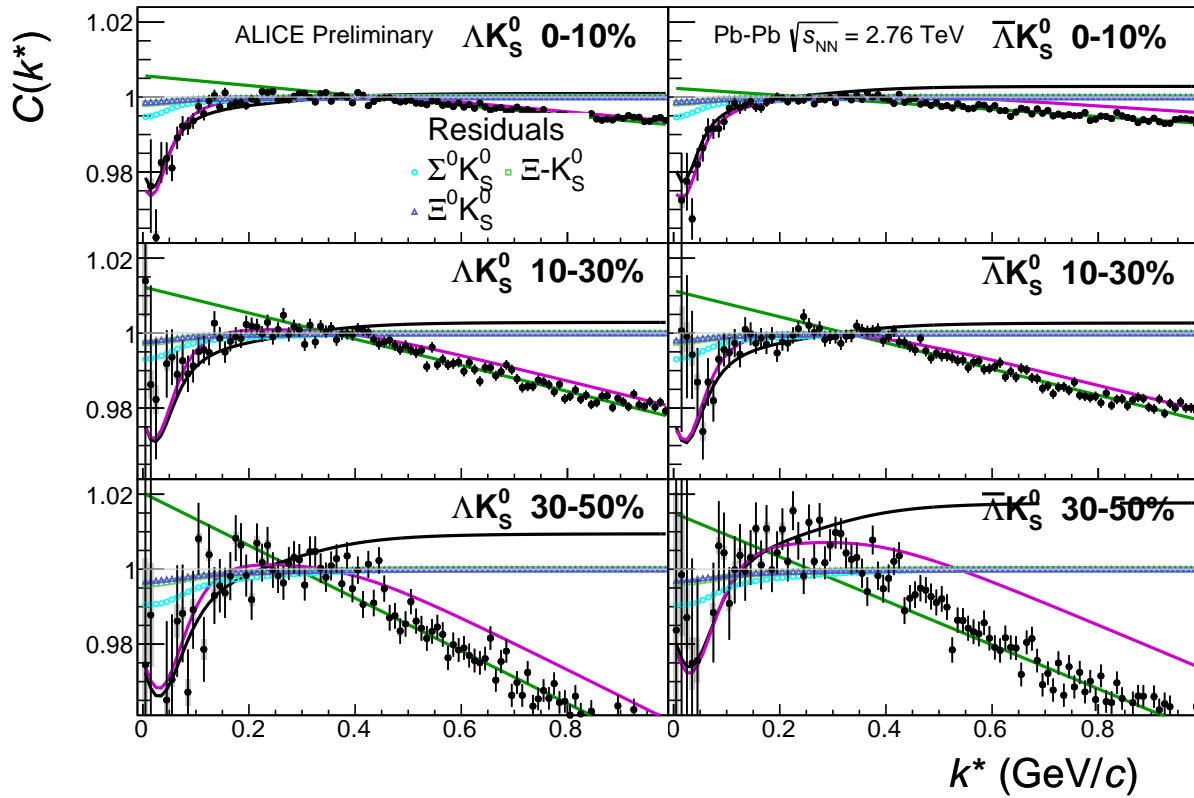


Fig. 36: Fits, with 3 residual correlations included and shown, to the ΛK_s^0 (left) and $\bar{\Lambda} K_s^0$ (right) data for the centralities 0-10% (top), 10-30% (middle), and 30-50% (bottom). The three parent pairs used for the residual correction to the ΛK_s^0 ($\bar{\Lambda} K_s^0$) fit are $\Sigma^0 K_s^0$, $\Xi^0 K_s^0$, and $\Xi^- K_s^0$ ($\bar{\Sigma}^0 K_s^0$, $\bar{\Xi}^0 K_s^0$, and $\bar{\Xi}^+ K_s^0$).

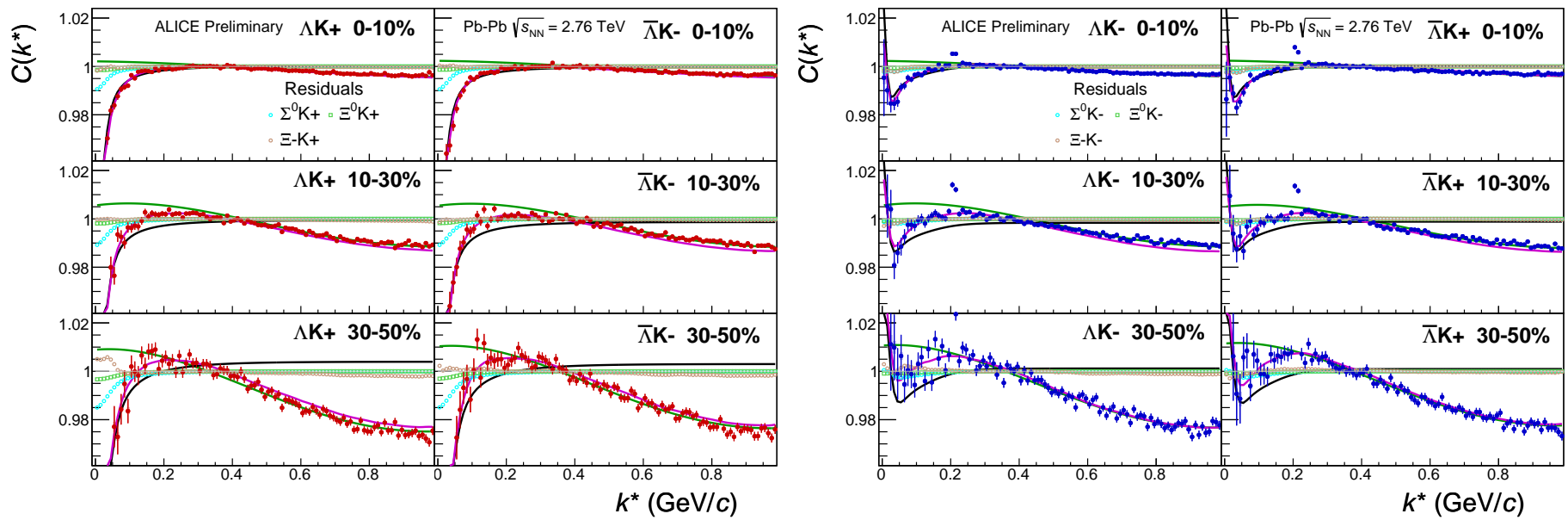


Fig. 37: Fits, with 3 residual correlations included and shown, to the ΛK^+ & $\bar{\Lambda} K^-$ (left) and ΛK^- & $\bar{\Lambda} K^+$ (right) data for the centralities 0-10% (top), 10-30% (middle), and 30-50% (bottom). The three parent pairs used for the residual correction to the $\Lambda K^+(\bar{\Lambda} K^-)$ fit are $\Sigma^0 K^+$, $\Xi^0 K^+$, and $\Xi^- K^+$ ($\bar{\Sigma}^0 K^-$, $\bar{\Xi}^0 K^-$, and $\bar{\Xi}^+ K^-$).

		Fit Results $\Lambda(\bar{\Lambda})K_S^0$				
System	Centrality	Fit Parameters				
		λ	R	$\mathbb{R}f_0$	$\mathbb{I}f_0$	d_0
$\Lambda K_S^0 \& \bar{\Lambda} K_S^0$	0-10%	1.10 ± 0.50 (stat.) ± 0.50 (sys.)	3.45 ± 1.10 (stat.) ± 0.45 (sys.)	-0.08 ± 0.03 (stat.) ± 0.25 (sys.)	0.14 ± 0.12 (stat.) ± 0.13 (sys.)	-1.56 ± 4.89 (stat.) ± 3.53 (sys.)
	10-30%		2.70 ± 0.85 (stat.) ± 0.32 (sys.)			
	30-50%		1.94 ± 0.58 (stat.) ± 0.16 (sys.)			

Table 10: Fit Results $\Lambda(\bar{\Lambda})K_S^0$, with 3 residual correlations included. Each pair is fit simultaneously with its conjugate (ie. ΛK_S^0 with $\bar{\Lambda} K_S^0$) across all centralities (0-10%, 10-30%, 30-50%), for a total of 6 simultaneous analyses in the fit. A single λ parameter is shared amongst all. Each analysis has a unique normalization parameter. The radii are shared between analyses of like centrality, as these should have similar source sizes. The scattering parameters ($\mathbb{R}f_0$, $\mathbb{I}f_0$, d_0) are shared amongst all. The background is fit with a linear form in the range $0.6 < k^* < 0.9$ GeV/c. The fit is done on the data with only statistical error bars. The errors marked as “stat.” are those returned by MINUIT. The errors marked as “sys.” are those which result from my systematic analysis (as outlined in Section 6).

		Fit Results $\Lambda(\bar{\Lambda})K^\pm$				
System	Centrality	Fit Parameters				
		λ	R	$\mathbb{R}f_0$	$\mathbb{I}f_0$	d_0
$\Lambda K^+ \& \bar{\Lambda} K^-$	0-10%	1.12 ± 0.32 (stat.) ± 0.25 (sys.)	6.33 ± 0.99 (stat.) ± 0.31 (sys.)	-0.66 ± 0.14 (stat.) ± 0.13 (sys.)	0.58 ± 0.15 (stat.) ± 0.11 (sys.)	0.77 ± 0.47 (stat.) ± 1.66 (sys.)
	10-30%	0.79 ± 0.19 (stat.) ± 0.23 (sys.)	4.77 ± 0.61 (stat.) ± 0.17 (sys.)			
$\Lambda K^+ \& \bar{\Lambda} K^-$	30-50%	0.70 ± 0.18 (stat.) ± 0.30 (sys.)	3.47 ± 0.46 (stat.) ± 0.10 (sys.)	0.35 ± 0.12 (stat.) ± 0.07 (sys.)	0.44 ± 0.10 (stat.) ± 0.08 (sys.)	-4.46 ± 1.53 (stat.) ± 1.36 (sys.)

Table 11: Fit Results $\Lambda(\bar{\Lambda})K^\pm$, with 3 residual correlations included. All ΛK^\pm analyses are fit simultaneously across all centralities (0-10%, 10-30%, 30-50%). Scattering parameters ($\mathbb{R}f_0$, $\mathbb{I}f_0$, d_0) are shared between pair-conjugate systems (i.e. a parameter set describing the $\Lambda K^+ \& \bar{\Lambda} K^-$ system, and a separate set describing the $\Lambda K^- \& \bar{\Lambda} K^+$ system). For each centrality, a radius and λ parameters are shared between all pairs ($\Lambda K^+, \bar{\Lambda} K^-, \Lambda K^-, \bar{\Lambda} K^+$). Each analysis has a unique normalization parameter. The background is modeled by a (6th-)degree polynomial fit to THERMINATOR simulation. The fit is done on the data with only statistical error bars. The errors marked as “stat.” are those returned by MINUIT. The errors marked as “sys.” are those which result from my systematic analysis (as outlined in Section 6).

796 **8.1.2 10 Residual Correlations Included in Fit**

797 Figure 36 nicely collects and summarizes all of our extracted fit parameters for the case of 10 included
 798 residual contributors. Figure 37 presents our extracted fit radii, along with those of other systems pre-
 799 viously analyzed by ALICE [10], as a function of pair transverse mass (m_T). Figures 38, 39, and 40
 800 show the experimental correlation functions with fits, assuming 10 residual contributors, for all studied
 801 centralities for ΛK_S^0 with $\bar{\Lambda} K_S^0$, ΛK^+ with $\bar{\Lambda} K^-$, and ΛK^- with $\bar{\Lambda} K^+$, respectively. The parameter sets
 802 extracted from the fits can be found in Tables 11 and 12.

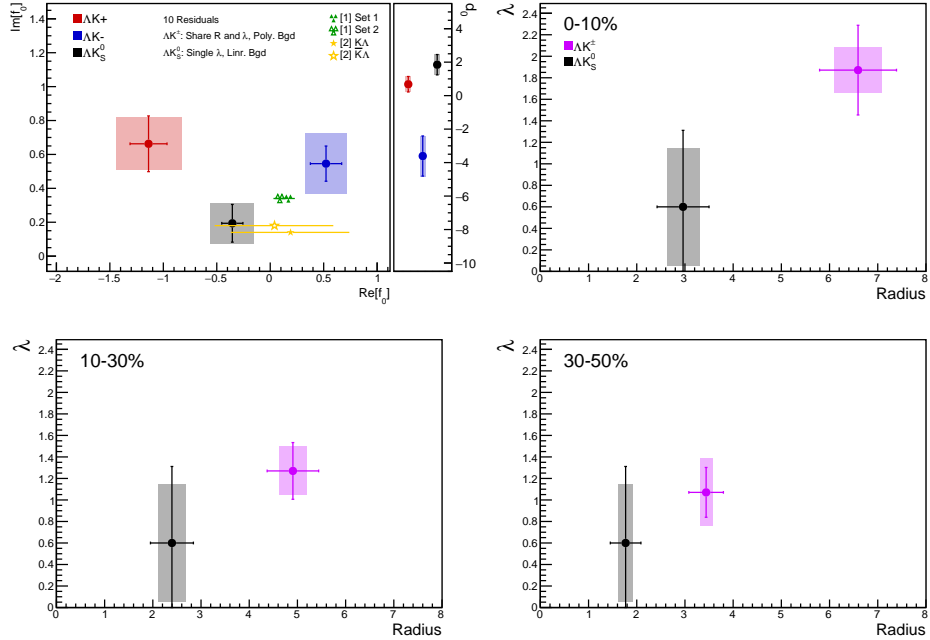


Fig. 38: Extracted scattering parameters for the case of 10 residual contributors for all of our ΛK systems. [Top Left]: $\Im f_0$ vs. $\Re f_0$, together with d_0 to the right. [Top Right (Bottom Left, Bottom Right)]: λ vs. Radius for the 0-10% (10-30%, 30-50%) bin. The green [11] and yellow [12] points show theoretical predictions made using chiral perturbation theory.

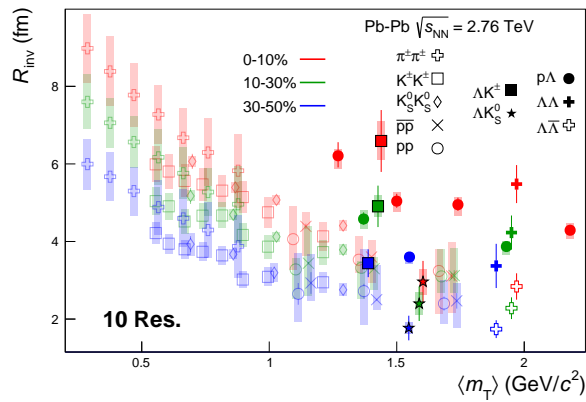


Fig. 39: 10 residual correlations in ΛK fits. Extracted fit R_{inv} parameters as a function of pair transverse mass (m_T) for various pair systems over several centralities. The ALICE published data [10] is shown with transparent, open symbols. The new ΛK results are shown with opaque, filled symbols. In the left, the ΛK^+ (with its conjugate pair) results are shown separately from the ΛK^- (with its conjugate pair) results. In the right, all ΛK^\pm results are averaged.

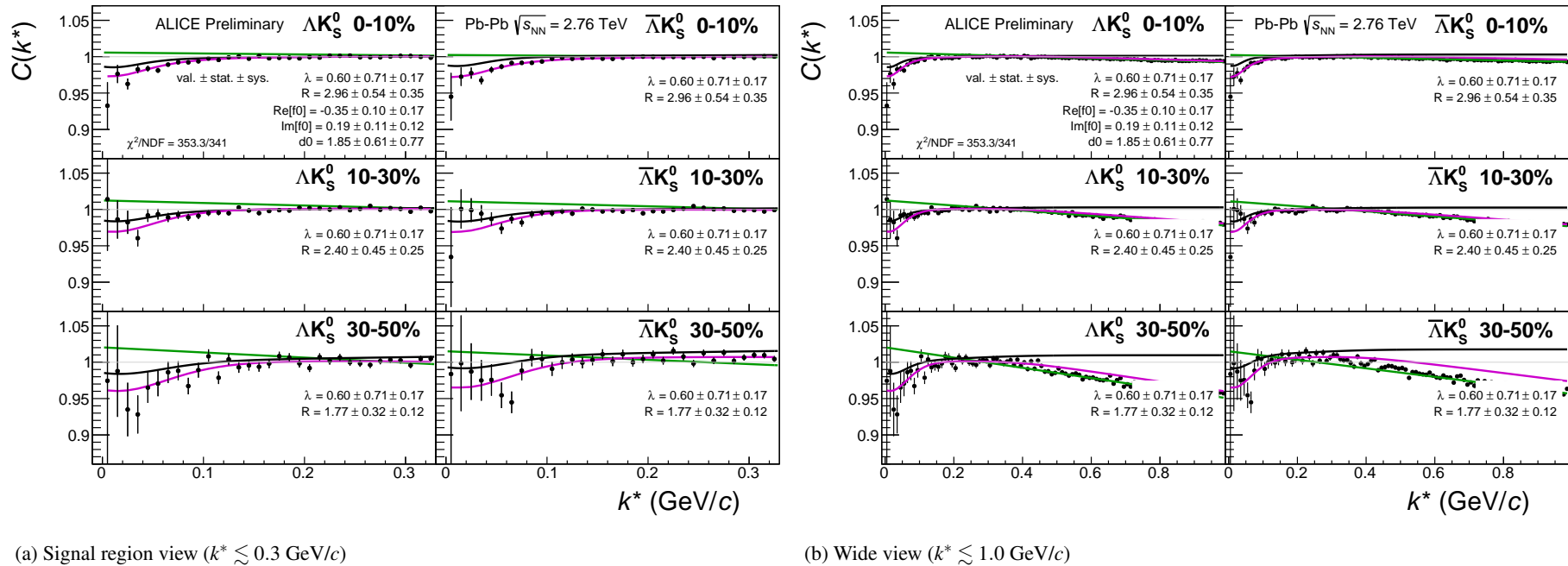


Fig. 40: Fits, with 10 residual correlations included, to the ΛK_s^0 (left) and $\bar{\Lambda} K_s^0$ (right) data for the centralities 0-10% (top), 10-30% (middle), and 30-50% (bottom). The lines represent the statistical errors, while the boxes represent the systematic errors. A single λ parameter is shared amongst all. Each analysis has a unique normalization parameter. The radii are shared between analyses of like centrality, as these should have similar source sizes. The scattering parameters ($\Im f_0$, $\Re f_0$, d_0) are shared amongst all. The background is modeled by a (6th-degree polynomial fit to THERMINATOR simulation. The black solid line represents the primary (ΛK) correlation's contribution to the fit. The green line shows the fit to the non-flat background. The purple points show the fit after all residuals' contributions have been included, and momentum resolution and non-flat background corrections have been applied. The extracted fit values with uncertainties are printed.

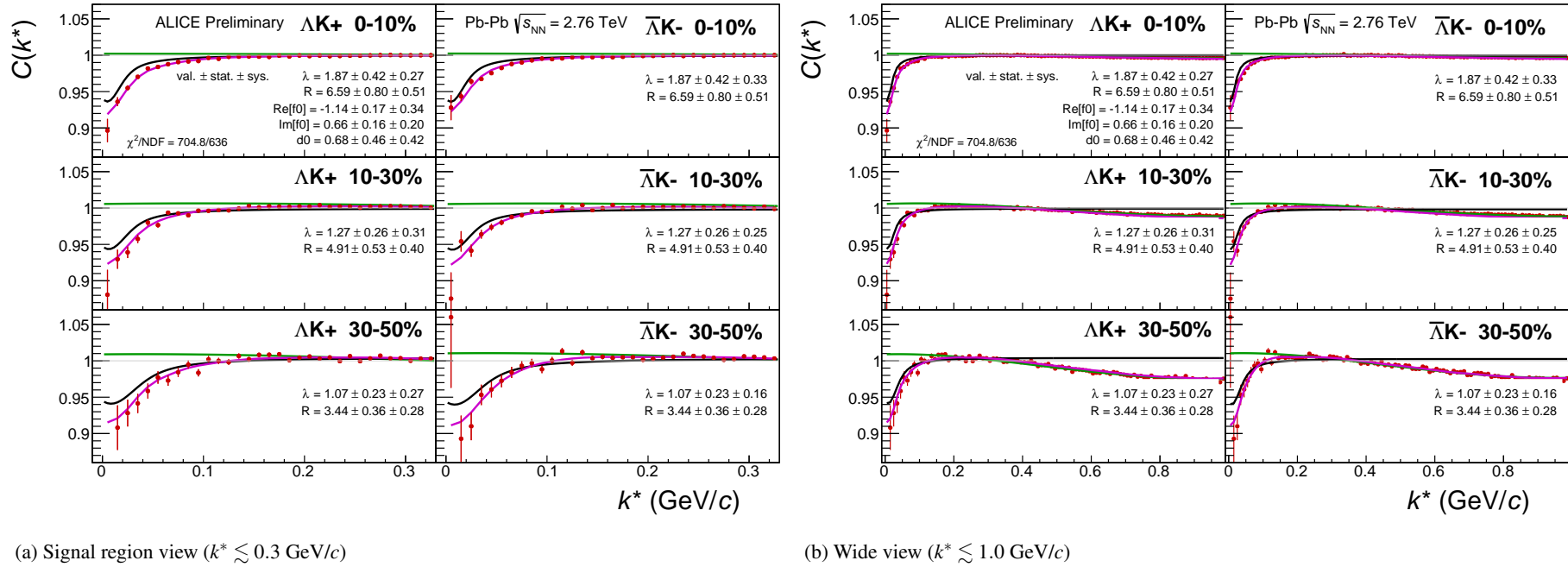


Fig. 41: Fits, with 10 residual correlations included, to the ΛK^+ (left) and $\bar{\Lambda} K^-$ (right) data for the centralities 0-10% (top), 10-30% (middle), and 30-50% (bottom). The lines represent the statistical errors, while the boxes represent the systematic errors. All ΛK^\pm analyses are fit simultaneously across all centralities (0-10%, 10-30%, 30-50%). Scattering parameters ($\Re f_0$, $\Im f_0$, d_0) are shared between pair-conjugate systems (i.e. a parameter set describing the ΛK^+ & $\bar{\Lambda} K^-$ system, and a separate set describing the ΛK^- & $\bar{\Lambda} K^+$ system). For each centrality, a radius and λ parameters are shared between all pairs (ΛK^+ , $\bar{\Lambda} K^-$, ΛK^- , $\bar{\Lambda} K^+$). Each analysis has a unique normalization parameter. The background is modeled by a (6th-degree polynomial fit to THERMINATOR simulation. The black solid line represents the primary (ΛK) correlation's contribution to the fit. The green line shows the fit to the non-flat background. The purple points show the fit after all residuals' contributions have been included, and momentum resolution and non-flat background corrections have been applied. The extracted fit values with uncertainties are printed.

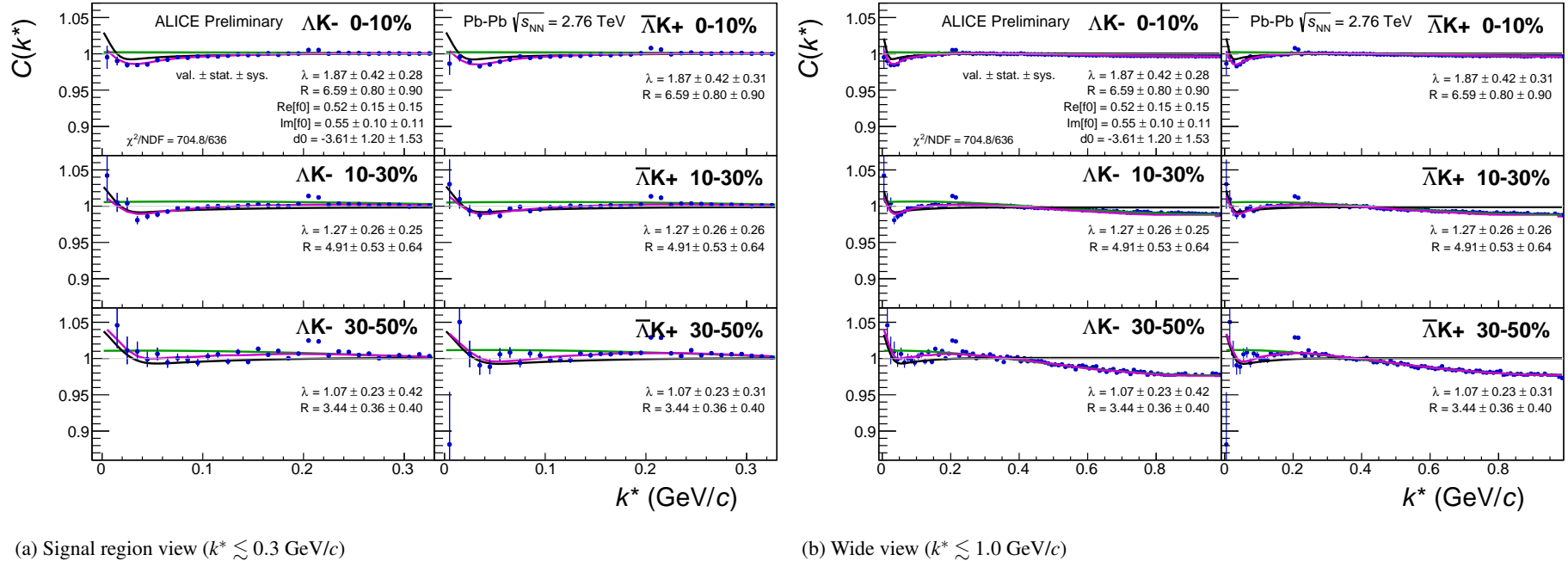


Fig. 42: Fits, with 10 residual correlations included, to the ΛK^- (left) with $\bar{\Lambda} K^+$ (right) data for the centralities 0-10% (top), 10-30% (middle), and 30-50% (bottom). The lines represent the statistical errors, while the boxes represent the systematic errors. All ΛK^\pm analyses are fit simultaneously across all centralities (0-10%, 10-30%, 30-50%). Scattering parameters ($\Im f_0$, $\Re f_0$, d_0) are shared between pair-conjugate systems (i.e. a parameter set describing the ΛK^+ & $\bar{\Lambda} K^-$ system, and a separate set describing the ΛK^- & $\bar{\Lambda} K^+$ system). For each centrality, a radius and λ parameters are shared between all pairs (ΛK^+ , $\bar{\Lambda} K^-$, ΛK^- , $\bar{\Lambda} K^+$). Each analysis has a unique normalization parameter. The background is modeled by a (6th-degree polynomial fit to THERMINATOR simulation. The black solid line represents the primary (ΛK) correlation's contribution to the fit. The green line shows the fit to the non-flat background. The purple points show the fit after all residuals' contributions have been included, and momentum resolution and non-flat background corrections have been applied. The extracted fit values with uncertainties are printed.

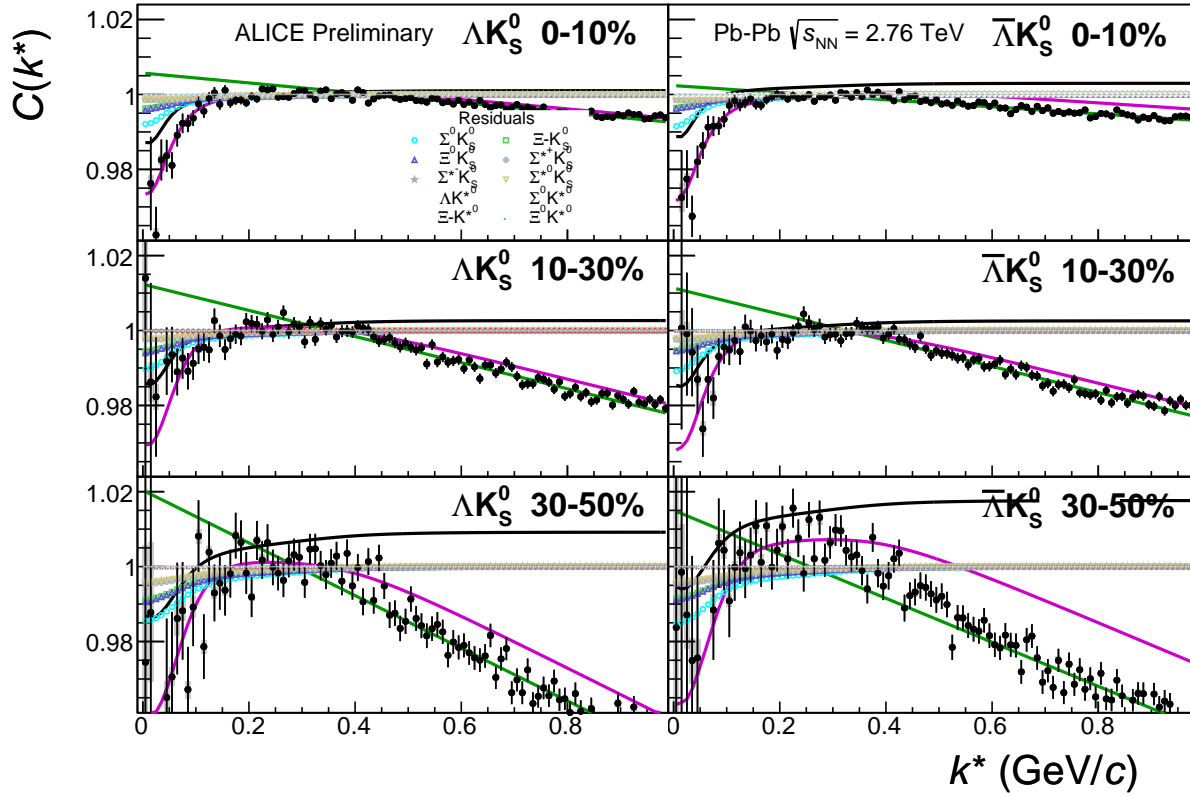
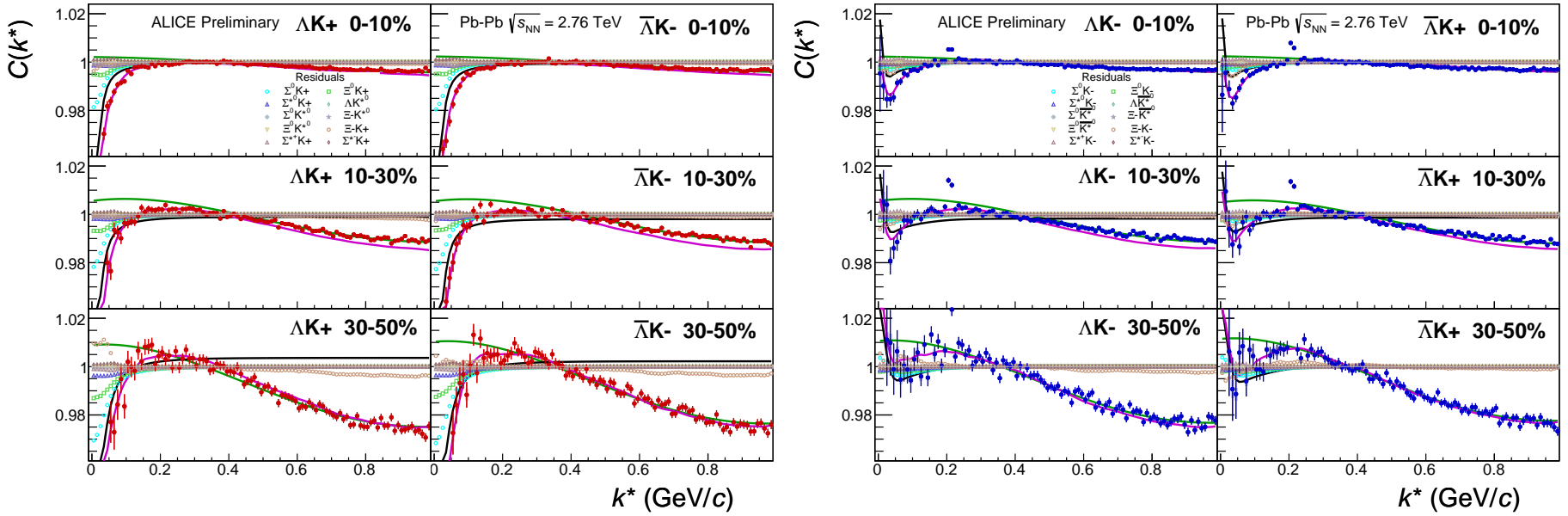


Fig. 43: Fits, with 10 residual correlations included and shown, to the ΛK_s^0 (left) and $\bar{\Lambda} K_s^0$ (right) data for the centralities 0-10% (top), 10-30% (middle), and 30-50% (bottom). The ten parent pairs used for the residual correction to the ΛK_s^0 ($\bar{\Lambda} K_s^0$) fit are $\Sigma^0 K_s^0$, $\Xi^0 K_s^0$, $\Xi^- K_s^0$, $\Sigma^{*(+,-,0)} K_s^0$, ΛK^{*0} , $\Sigma^0 K^{*0}$, $\Xi^- K^{*0}$, and $\Xi^+ K_s^0$ ($\bar{\Sigma}^0 K_s^0$, $\bar{\Xi}^0 K_s^0$, $\Xi^+ K_s^0$, $\bar{\Sigma}^{*(+,-,0)} K_s^0$, $\bar{\Lambda} K^{*0}$, $\bar{\Sigma}^0 K^{*0}$, $\bar{\Xi}^0 K^{*0}$, and $\Xi^+ \bar{K}^{*0}$).



(a) ΛK^+ ($\bar{\Lambda} K^-$) fits with residual contributions shown for the centralities 0-10% (top), 10-30% (middle), and 30-50% (bottom)

(b) ΛK^- ($\bar{\Lambda} K^+$) fits with residual contributions shown for the centralities 0-10% (top), 10-30% (middle), and 30-50% (bottom)

Fig. 44: Fits, with 10 residual correlations included and shown, to the ΛK^+ & $\bar{\Lambda} K^-$ (left) and ΛK^- & $\bar{\Lambda} K^+$ (right) data for the centralities 0-10% (top), 10-30% (middle), and 30-50% (bottom). The ten parent pairs used for the residual correction to the ΛK^+ ($\bar{\Lambda} K^-$) fit are $\Sigma^0 K^+$, $\Xi^0 K^+$, $\Xi^- K^+$, $\Sigma^{*(+,-,0)} K^+$, ΛK^{*0} , $\Sigma^0 K^{*0}$, $\Xi^0 K^{*0}$, and $\Xi^- K^{*0}$ ($\bar{\Sigma}^0 K^-$, $\bar{\Xi}^0 K^-$, $\bar{\Xi}^+ K^-$, $\bar{\Sigma}^{*(+,-,0)} K^-$, $\bar{\Lambda} K^{*0}$, $\bar{\Sigma}^0 \bar{K}^{*0}$, $\bar{\Xi}^0 \bar{K}^{*0}$, and $\bar{\Xi}^+ \bar{K}^{*0}$).

Fit Results $\Lambda(\bar{\Lambda})K_S^0$						
System	Centrality	Fit Parameters				
		λ	R	$\mathbb{R}f_0$	$\mathbb{I}f_0$	d_0
$\Lambda K_S^0 \text{ & } \bar{\Lambda} K_S^0$	0-10%			$2.96 \pm 0.54 \text{ (stat.)} \pm 0.33 \text{ (sys.)}$		
	10-30%	$0.60 \pm 0.71 \text{ (stat.)} \pm 0.54 \text{ (sys.)}$	$2.40 \pm 0.45 \text{ (stat.)} \pm 0.29 \text{ (sys.)}$	$-0.35 \pm 0.10 \text{ (stat.)} \pm 0.21 \text{ (sys.)}$	$0.19 \pm 0.11 \text{ (stat.)} \pm 0.12 \text{ (sys.)}$	$1.85 \pm 0.61 \text{ (stat.)} \pm 2.68 \text{ (sys.)}$
	30-50%		$1.77 \pm 0.32 \text{ (stat.)} \pm 0.15 \text{ (sys.)}$			

Table 12: Fit Results $\Lambda(\bar{\Lambda})K_S^0$, with 10 residual correlations included. Each pair is fit simultaneously with its conjugate (ie. ΛK_S^0 with $\bar{\Lambda} K_S^0$) across all centralities (0-10%, 10-30%, 30-50%), for a total of 6 simultaneous analyses in the fit. A single λ parameter is shared amongst all. Each analysis has a unique normalization parameter. The radii are shared between analyses of like centrality, as these should have similar source sizes. The scattering parameters ($\mathbb{R}f_0$, $\mathbb{I}f_0$, d_0) are shared amongst all. The background is fit with a linear form in the range $0.6 < k^* < 0.9 \text{ GeV}/c$. The fit is done on the data with only statistical error bars. The errors marked as “stat.” are those returned by MINUIT. The errors marked as “sys.” are those which result from my systematic analysis (as outlined in Section 6).

Fit Results $\Lambda(\bar{\Lambda})K^\pm$						
System	Centrality	Fit Parameters				
		λ	R	$\mathbb{R}f_0$	$\mathbb{I}f_0$	d_0
$\Lambda K^+ \text{ & } \bar{\Lambda} K^-$	0-10%	$1.87 \pm 0.42 \text{ (stat.)} \pm 0.21 \text{ (sys.)}$	$6.59 \pm 0.80 \text{ (stat.)} \pm 0.49 \text{ (sys.)}$	$-1.14 \pm 0.17 \text{ (stat.)} \pm 0.31 \text{ (sys.)}$	$0.66 \pm 0.16 \text{ (stat.)} \pm 0.15 \text{ (sys.)}$	$0.68 \pm 0.46 \text{ (stat.)} \pm 0.53 \text{ (sys.)}$
	10-30%	$1.27 \pm 0.26 \text{ (stat.)} \pm 0.23 \text{ (sys.)}$	$4.91 \pm 0.53 \text{ (stat.)} \pm 0.28 \text{ (sys.)}$			
$\Lambda K^+ \text{ & } \bar{\Lambda} K^-$	30-50%	$1.07 \pm 0.23 \text{ (stat.)} \pm 0.32 \text{ (sys.)}$	$3.44 \pm 0.36 \text{ (stat.)} \pm 0.13 \text{ (sys.)}$	$0.52 \pm 0.15 \text{ (stat.)} \pm 0.19 \text{ (sys.)}$	$0.55 \pm 0.10 \text{ (stat.)} \pm 0.18 \text{ (sys.)}$	$-3.61 \pm 1.20 \text{ (stat.)} \pm 1.02 \text{ (sys.)}$

Table 13: Fit Results $\Lambda(\bar{\Lambda})K^\pm$, with 10 residual correlations included. All ΛK^\pm analyses are fit simultaneously across all centralities (0-10%, 10-30%, 30-50%). Scattering parameters ($\mathbb{R}f_0$, $\mathbb{I}f_0$, d_0) are shared between pair-conjugate systems (i.e. a parameter set describing the $\Lambda K^+ \text{ & } \bar{\Lambda} K^-$ system, and a separate set describing the $\Lambda K^- \text{ & } \bar{\Lambda} K^+$ system). For each centrality, a radius and λ parameters are shared between all pairs ($\Lambda K^+, \bar{\Lambda} K^-, \Lambda K^-, \bar{\Lambda} K^+$). Each analysis has a unique normalization parameter. The background is modeled by a (6th-degree polynomial fit to THERMINATOR simulation. The fit is done on the data with only statistical error bars. The errors marked as “stat.” are those returned by MINUIT. The errors marked as “sys.” are those which result from my systematic analysis (as outlined in Section 6).

803 **8.1.3 No Residual Correlations Included in Fit**

804 Figure 43 nicely collects and summarizes all of our extracted fit parameters for the case of no included
 805 residual contributors. Figure 44 presents our extracted fit radii, along with those of other systems pre-
 806 viously analyzed by ALICE [10], as a function of pair transverse mass (m_T). Figures 45, 46, and 47
 807 show the experimental correlation functions with fits, assuming no residual contributors, for all studied
 808 centralities for ΛK_S^0 with $\bar{\Lambda} K_S^0$, ΛK^+ with $\bar{\Lambda} K^-$, and ΛK^- with $\bar{\Lambda} K^+$, respectively. The parameter sets
 809 extracted from the fits can be found in Tables 13 and 14.

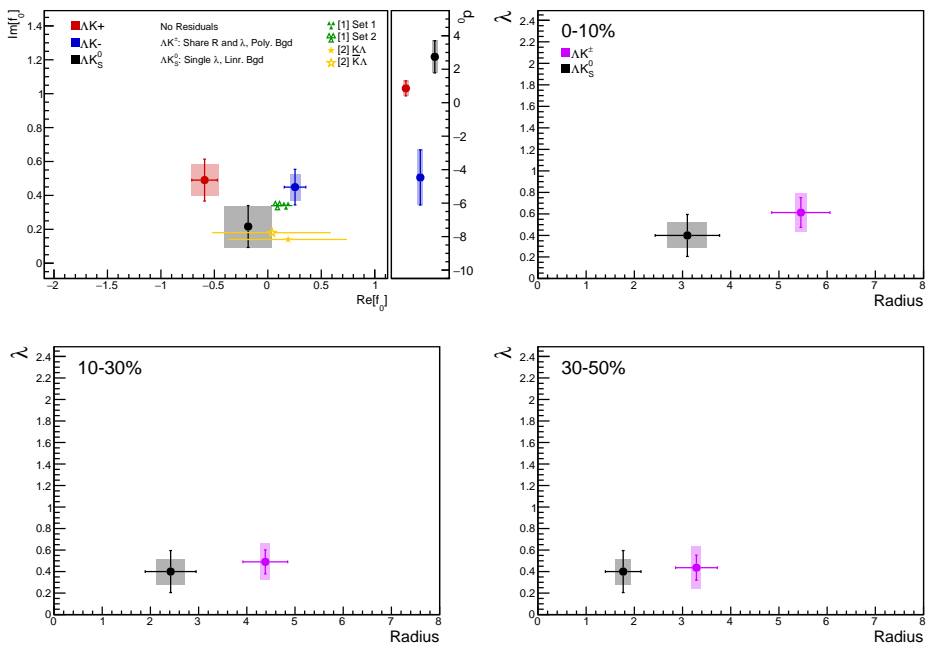


Fig. 45: Extracted scattering parameters for the case of NO residual contributors for all of our ΛK systems. [Top Left]: $\Im f_0$ vs. $\Re f_0$, together with d_0 to the right. [Top Right (Bottom Left, Bottom Right)]: λ vs. Radius for the 0-10% (10-30%, 30-50%) bin. The green [11] and yellow [12] points show theoretical predictions made using chiral perturbation theory.

810 Figure 44 shows extracted R_{inv} parameters as a function of transverse mass (m_T) for various pair systems
 811 over several centralities. The published ALICE data [10] is shown with transparent, open symbols. The
 812 new ΛK results are shown with opaque, filled symbols. The radii shown an increasing size with increas-
 813 ing centrality, as is expected from the simple geometric picture of the collisions. The radii decrease
 814 in size with increasing m_T , and we see an approximate scaling of the radii with transverse mass, as is
 815 expected in the presence of collective flow in the system.

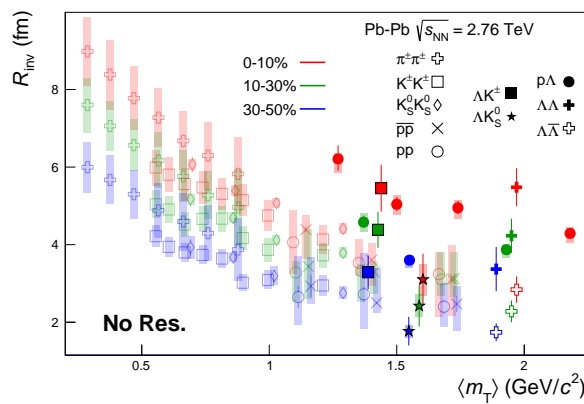


Fig. 46: No residual correlations in ΛK fits. Extracted fit R_{inv} parameters as a function of pair transverse mass (m_T) for various pair systems over several centralities. The ALICE published data [10] is shown with transparent, open symbols. The new ΛK results are shown with opaque, filled symbols. In the left, the ΛK^+ (with its conjugate pair) results are shown separately from the ΛK^- (with its conjugate pair) results. In the right, all ΛK^\pm results are averaged.

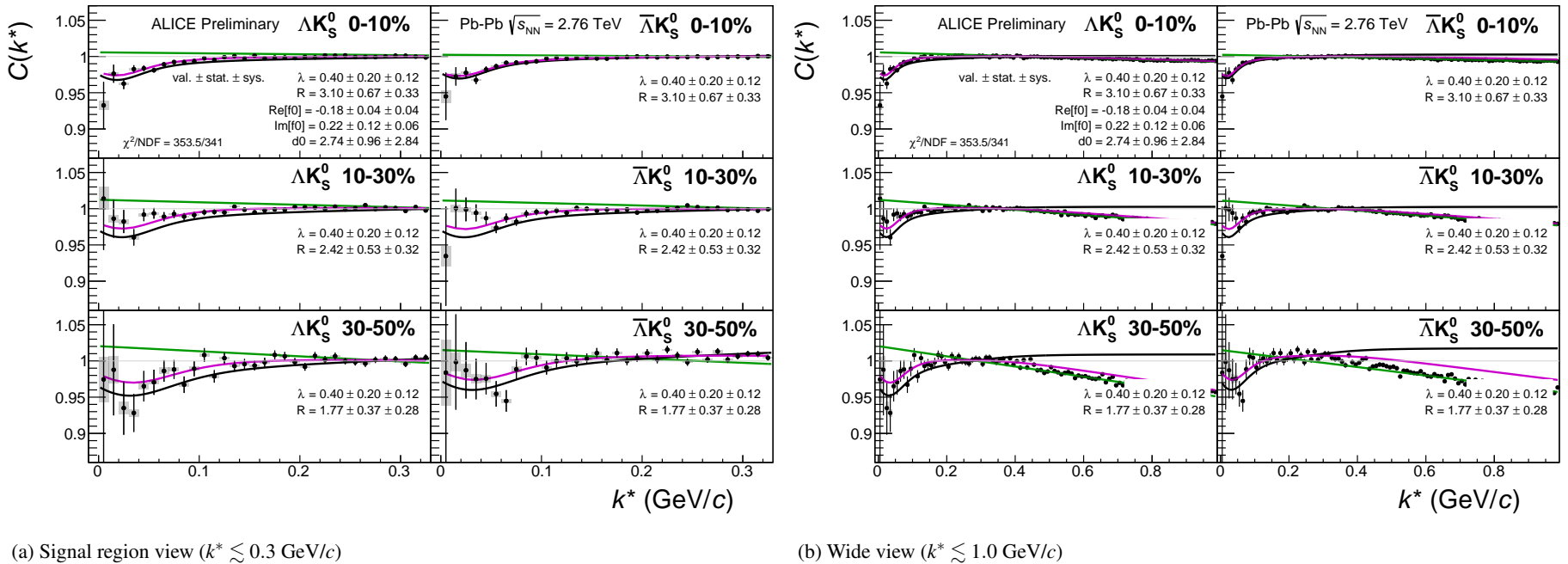
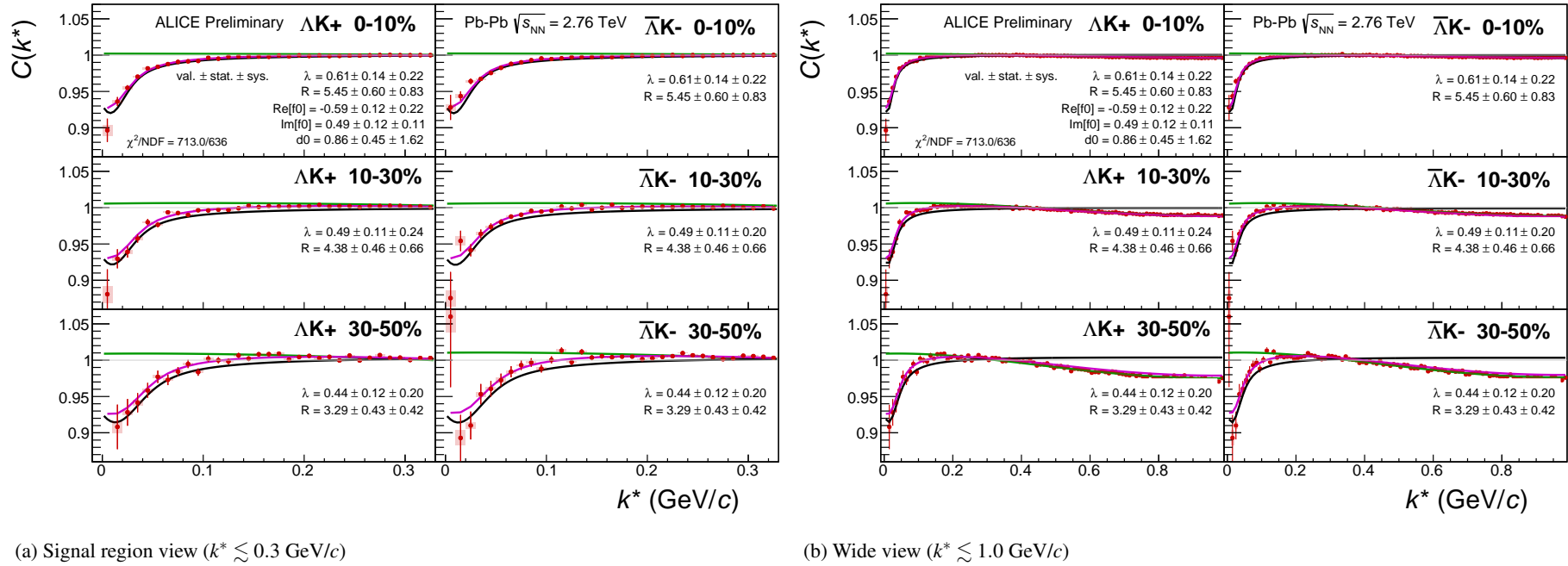


Fig. 47: Fits, with NO residual correlations included, to the ΛK_s^0 (left) and $\bar{\Lambda} K_s^0$ (right) data for the centralities 0-10% (top), 10-30% (middle), and 30-50% (bottom). The lines represent the statistical errors, while the boxes represent the systematic errors. A single λ parameter is shared amongst all. Each analysis has a unique normalization parameter. The radii are shared between analyses of like centrality, as these should have similar source sizes. The scattering parameters ($\Re f_0$, $\Im f_0$, d_0) are shared amongst all. The background is modeled by a (6th-)degree polynomial fit to THERMINATOR simulation. The black solid line represents the “raw” primary fit, i.e. not corrected for momentum resolution effects nor non-flat background. The green line shows the fit to the non-flat background. The purple points show the fit after momentum resolution and non-flat background corrections have been applied. The extracted fit values with uncertainties are printed.



(a) Signal region view ($k^* \lesssim 0.3 \text{ GeV}/c$)

(b) Wide view ($k^* \lesssim 1.0 \text{ GeV}/c$)

Fig. 48: Fits to the ΔK^+ (left) and $\bar{\Delta} K^-$ (right) data for the centralities 0-10% (top), 10-30% (middle), and 30-50% (bottom). The lines represent the statistical errors, while the boxes represent the systematic errors. All ΔK^\pm analyses are fit simultaneously across all centralities (0-10%, 10-30%, 30-50%). Scattering parameters ($\Im f_0$, $\Re f_0$, d_0) are shared between pair-conjugate systems (i.e. a parameter set describing the ΔK^+ & $\bar{\Delta} K^-$ system, and a separate set describing the ΔK^- & $\bar{\Delta} K^+$ system). For each centrality, a radius and λ parameters are shared between all pairs (ΔK^+ , $\bar{\Delta} K^-$, ΔK^- , $\bar{\Delta} K^+$). Each analysis has a unique normalization parameter. The background is modeled by a (6th-)degree polynomial fit to THERMINATOR simulation. The black solid line represents the “raw” primary fit, i.e. not corrected for momentum resolution effects nor non-flat background. The green line shows the fit to the non-flat background. The purple points show the fit after momentum resolution and non-flat background corrections have been applied. The extracted fit values with uncertainties are printed.

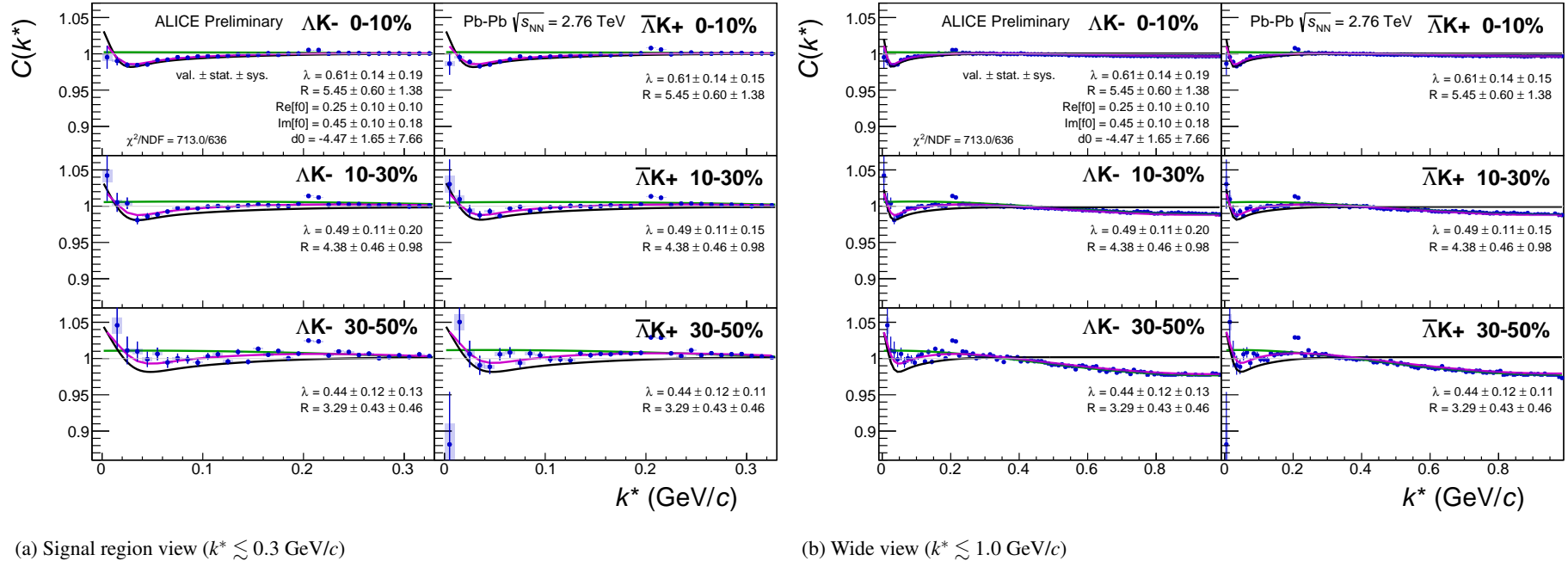


Fig. 49: Fits, with NO residual correlations included, to the ΛK^- (left) with $\bar{\Lambda} K^+$ (right) data for the centralities 0-10% (top), 10-30% (middle), and 30-50% (bottom). The lines represent the statistical errors, while the boxes represent the systematic errors. All ΛK^\pm analyses are fit simultaneously across all centralities (0-10%, 10-30%, 30-50%). Scattering parameters ($\Im f_0$, $\Re f_0$, d_0) are shared between pair-conjugate systems (i.e. a parameter set describing the ΛK^+ & $\bar{\Lambda} K^-$ system, and a separate set describing the ΛK^- & $\bar{\Lambda} K^+$ system). For each centrality, a radius and λ parameters are shared between all pairs (ΛK^+ , $\bar{\Lambda} K^-$, ΛK^- , $\bar{\Lambda} K^+$). Each analysis has a unique normalization parameter. The background is modeled by a (6th-)degree polynomial fit to THERMINATOR simulation. The black solid line represents the “raw” primary fit, i.e. not corrected for momentum resolution effects nor non-flat background. The green line shows the fit to the non-flat background. The purple points show the fit after momentum resolution and non-flat background corrections have been applied. The extracted fit values with uncertainties are printed.

Fit Results $\Lambda(\bar{\Lambda})K_S^0$						
System	Centrality	Fit Parameters				
		λ	R	$\mathbb{R}f_0$	$\mathbb{I}f_0$	d_0
$\Lambda K_S^0 \text{ & } \bar{\Lambda} K_S^0$	0-10%			$3.10 \pm 0.67 \text{ (stat.)} \pm 0.41 \text{ (sys.)}$		
	10-30%	$0.40 \pm 0.20 \text{ (stat.)} \pm 0.12 \text{ (sys.)}$	$2.42 \pm 0.53 \text{ (stat.)} \pm 0.29 \text{ (sys.)}$	$-0.18 \pm 0.04 \text{ (stat.)} \pm 0.22 \text{ (sys.)}$	$0.22 \pm 0.12 \text{ (stat.)} \pm 0.12 \text{ (sys.)}$	$2.74 \pm 0.96 \text{ (stat.)} \pm 1.28 \text{ (sys.)}$
	30-50%		$1.77 \pm 0.37 \text{ (stat.)} \pm 0.16 \text{ (sys.)}$			

Table 14: Fit Results $\Lambda(\bar{\Lambda})K_S^0$, with no residual correlations included. Each pair is fit simultaneously with its conjugate (ie. ΛK_S^0 with $\bar{\Lambda} K_S^0$) across all centralities (0-10%, 10-30%, 30-50%), for a total of 6 simultaneous analyses in the fit. A single λ parameter is shared amongst all. Each analysis has a unique normalization parameter. The radii are shared between analyses of like centrality, as these should have similar source sizes. The scattering parameters ($\mathbb{R}f_0$, $\mathbb{I}f_0$, d_0) are shared amongst all. The background is fit with a linear form in the range $0.6 < k^* < 0.9 \text{ GeV}/c$. The fit is done on the data with only statistical error bars. The errors marked as “stat.” are those returned by MINUIT. The errors marked as “sys.” are those which result from my systematic analysis (as outlined in Section 6).

Fit Results $\Lambda(\bar{\Lambda})K^\pm$						
System	Centrality	Fit Parameters				
		λ	R	$\mathbb{R}f_0$	$\mathbb{I}f_0$	d_0
$\Lambda K^+ \text{ & } \bar{\Lambda} K^-$	0-10%	$0.61 \pm 0.14 \text{ (stat.)} \pm 0.18 \text{ (sys.)}$	$5.45 \pm 0.60 \text{ (stat.)} \pm 0.12 \text{ (sys.)}$	$-0.59 \pm 0.12 \text{ (stat.)} \pm 0.13 \text{ (sys.)}$	$0.49 \pm 0.12 \text{ (stat.)} \pm 0.09 \text{ (sys.)}$	$0.86 \pm 0.45 \text{ (stat.)} \pm 1.63 \text{ (sys.)}$
	10-30%	$0.49 \pm 0.11 \text{ (stat.)} \pm 0.17 \text{ (sys.)}$	$4.38 \pm 0.46 \text{ (stat.)} \pm 0.10 \text{ (sys.)}$			
$\Lambda K^+ \text{ & } \bar{\Lambda} K^-$	30-50%	$0.44 \pm 0.12 \text{ (stat.)} \pm 0.20 \text{ (sys.)}$	$3.29 \pm 0.43 \text{ (stat.)} \pm 0.10 \text{ (sys.)}$	$0.25 \pm 0.10 \text{ (stat.)} \pm 0.05 \text{ (sys.)}$	$0.45 \pm 0.10 \text{ (stat.)} \pm 0.08 \text{ (sys.)}$	$-4.47 \pm 1.65 \text{ (stat.)} \pm 1.60 \text{ (sys.)}$

Table 15: Fit Results $\Lambda(\bar{\Lambda})K^\pm$, with no residual correlations included. All ΛK^\pm analyses are fit simultaneously across all centralities (0-10%, 10-30%, 30-50%). Scattering parameters ($\mathbb{R}f_0$, $\mathbb{I}f_0$, d_0) are shared between pair-conjugate systems (i.e. a parameter set describing the $\Lambda K^+ \text{ & } \bar{\Lambda} K^-$ system, and a separate set describing the $\Lambda K^- \text{ & } \bar{\Lambda} K^+$ system). For each centrality, a radius and λ parameters are shared between all pairs ($\Lambda K^+, \bar{\Lambda} K^-, \Lambda K^-, \bar{\Lambda} K^+$). Each analysis has a unique normalization parameter. The background is modeled by a (6th-degree polynomial fit to THERMINATOR simulation. The fit is done on the data with only statistical error bars. The errors marked as “stat.” are those returned by MINUIT. The errors marked as “sys.” are those which result from my systematic analysis (as outlined in Section 6).

816 **8.1.4 Fit Method Comparisons**

817 In Figure 48, we show extracted fit parameters for the case of $\Lambda K^+(\bar{\Lambda}K^-)$ sharing radii with $\Lambda K^-(\bar{\Lambda}K^+)$.
 818 The figure shows results for three different treatments of the non-femtoscopic background: a polynomial
 819 fit to THERMINATOR 2 simulation to model the background (circles), a linear fit to the data to model
 820 the background (squares), and the Stavinskiy method (crosses).

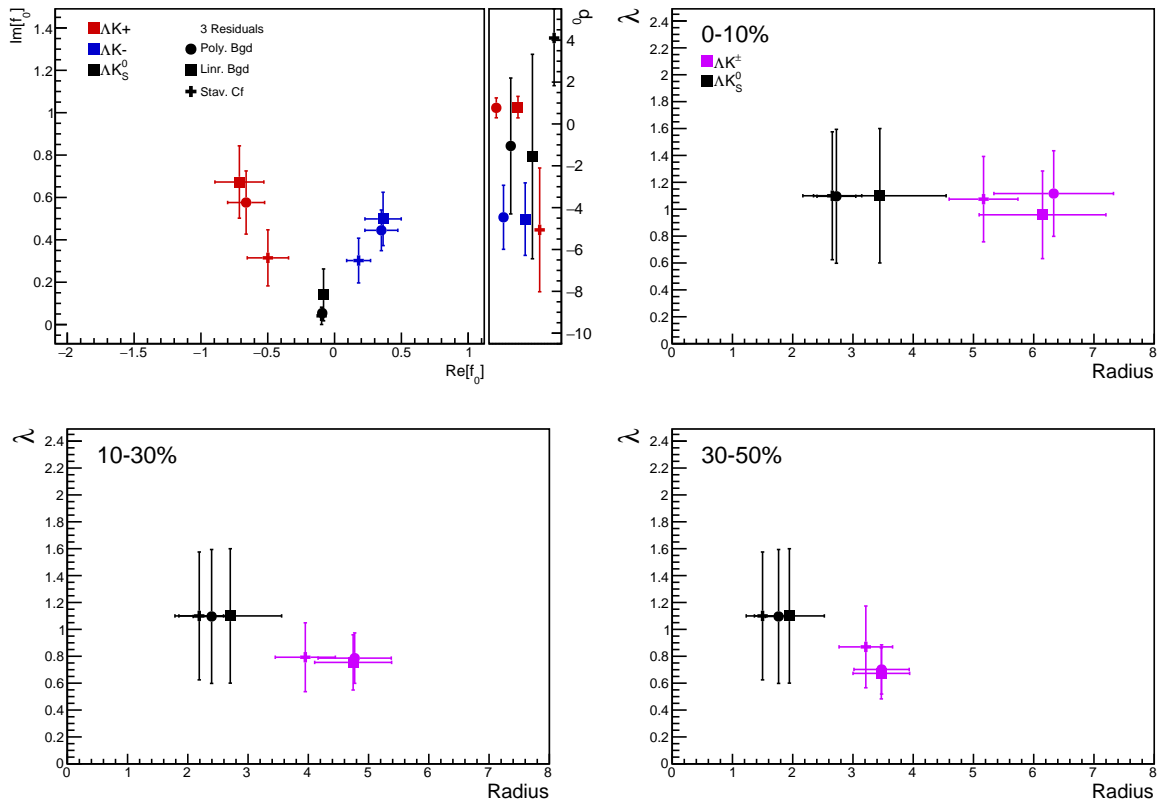


Fig. 50: Compare Fit Parameters: Background treatment: Extracted fit results for all of our $\Lambda(\bar{\Lambda})K^\pm$ systems across all studied centrality bins (0-10%, 10-30%, 30-50%). The $\Lambda K^+(\bar{\Lambda}K^-)$ and $\Lambda K^-(\bar{\Lambda}K^+)$ systems share both a radius and a λ parameter for each centrality bin (i.e. 3 total radius parameters, 3 total λ parameters). The figure shows results for three different treatments of the non-femtoscopic background: a polynomial fit to THERMINATOR 2 simulation to model the background (circles), a linear fit to the data to model the background (squares), and the Stavinskiy method (crosses). The green [11] and yellow [12] points show theoretical predictions made using chiral perturbation theory.

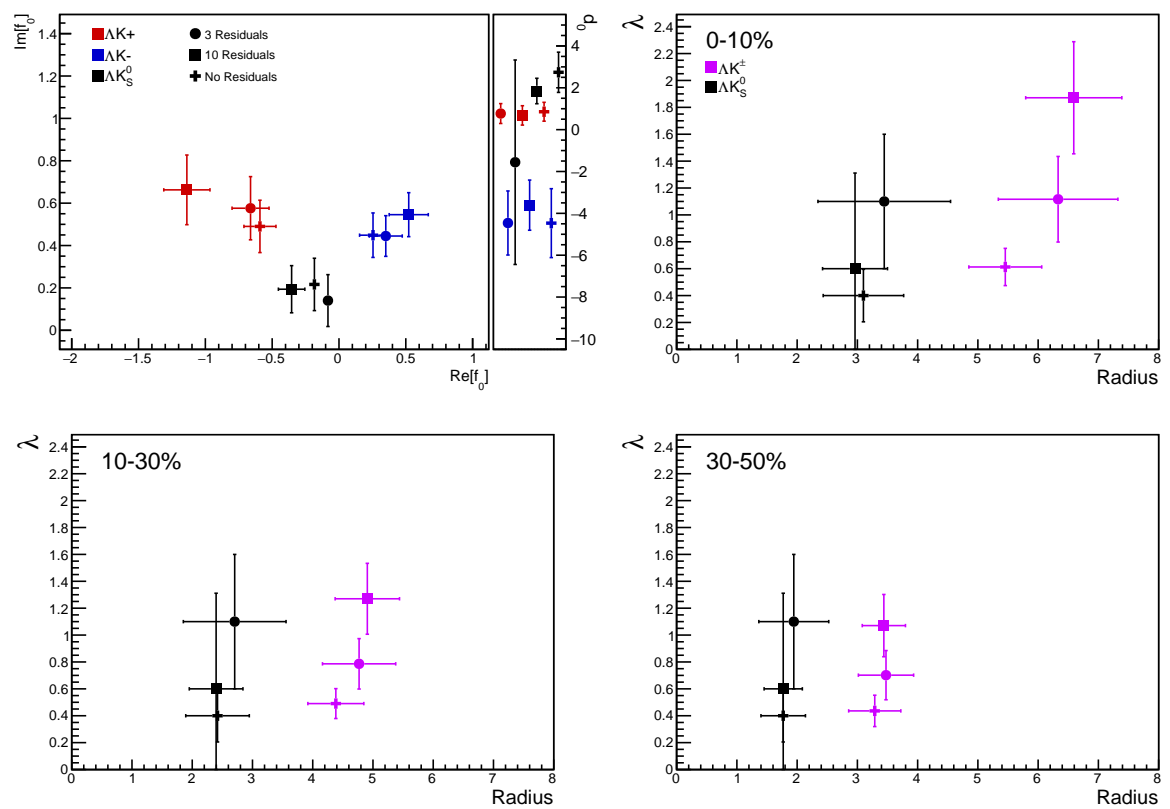


Fig. 51: Compare Fit Parameters: Number of residuals: Results shown for the case of 3 (+), 10 (X), and no (circles) residual contributors.

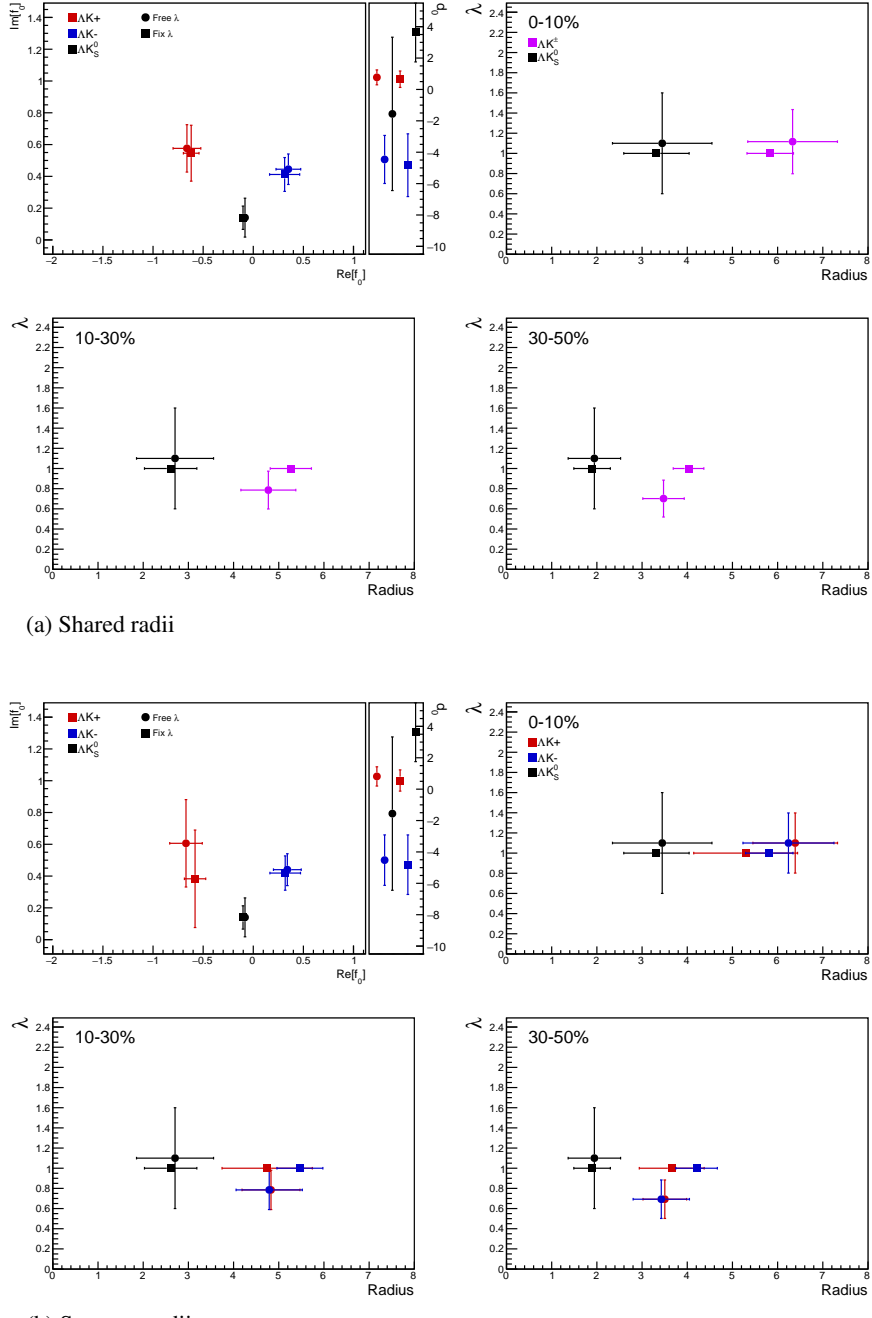


Fig. 52: Compare Fit Parameters: Free vs fixed λ : Results shown for λ parameters left free (filled symbols) and fixed to 1 (open symbols). In the top plot (50a), the ΔK^+ and ΔK^- analyses share radii, whereas in the bottom (50b) they have unique radii.

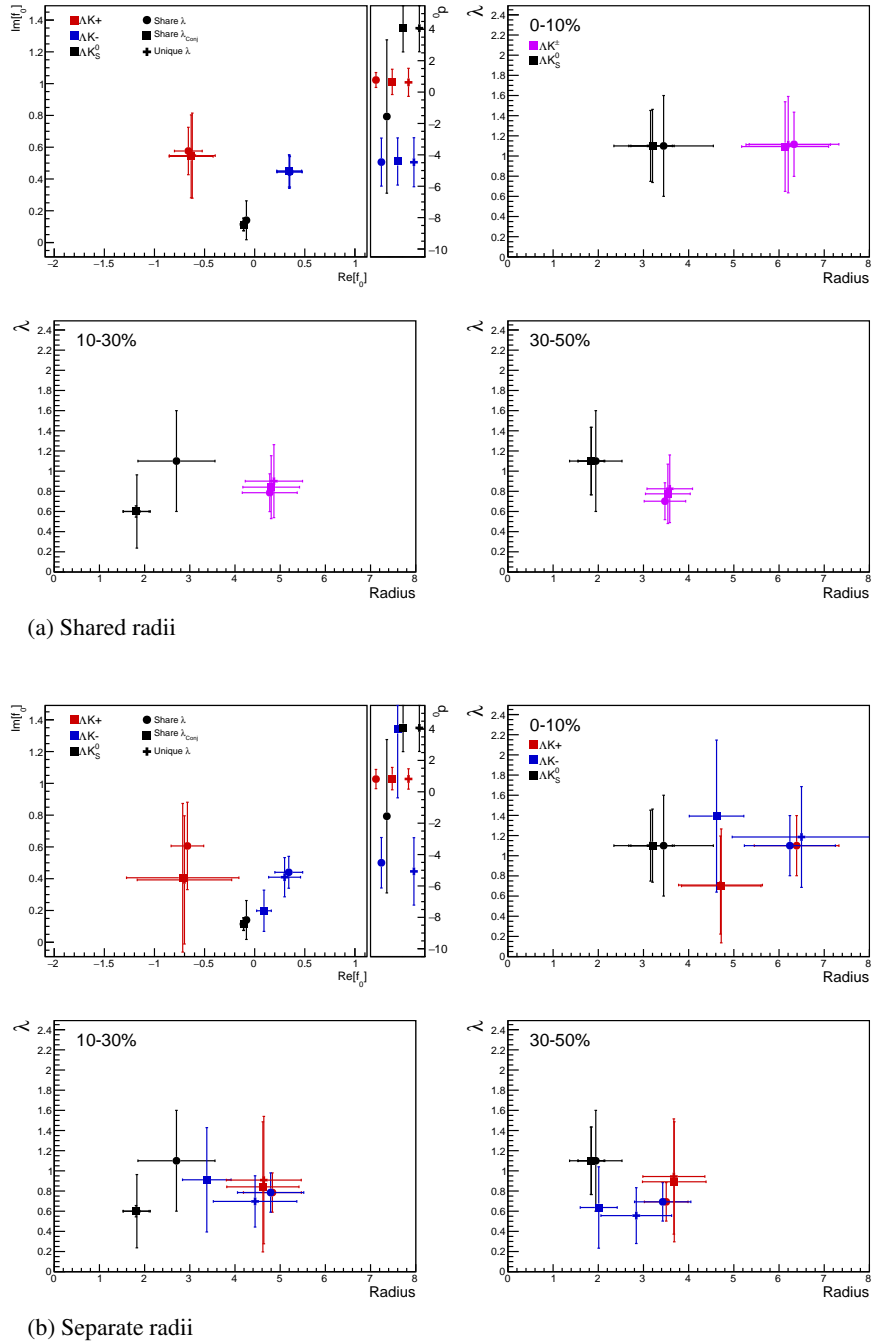
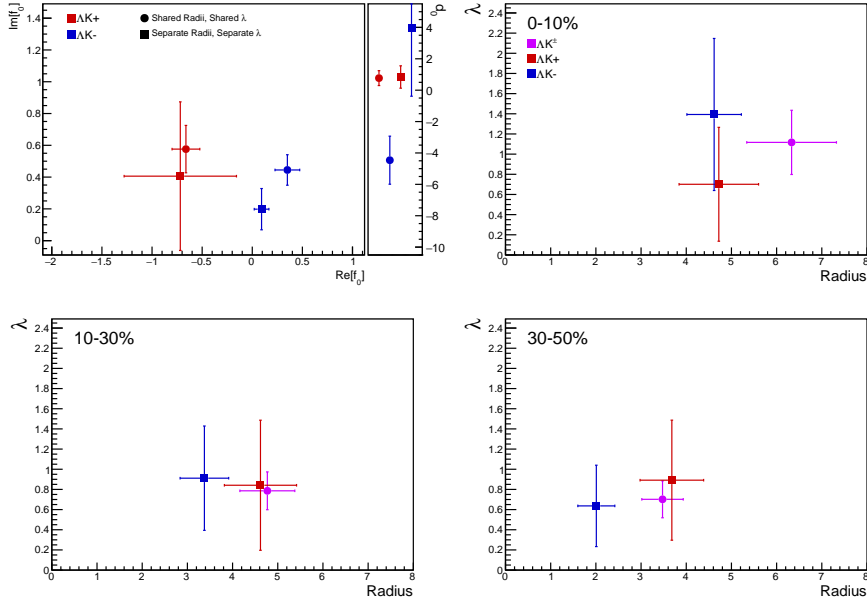
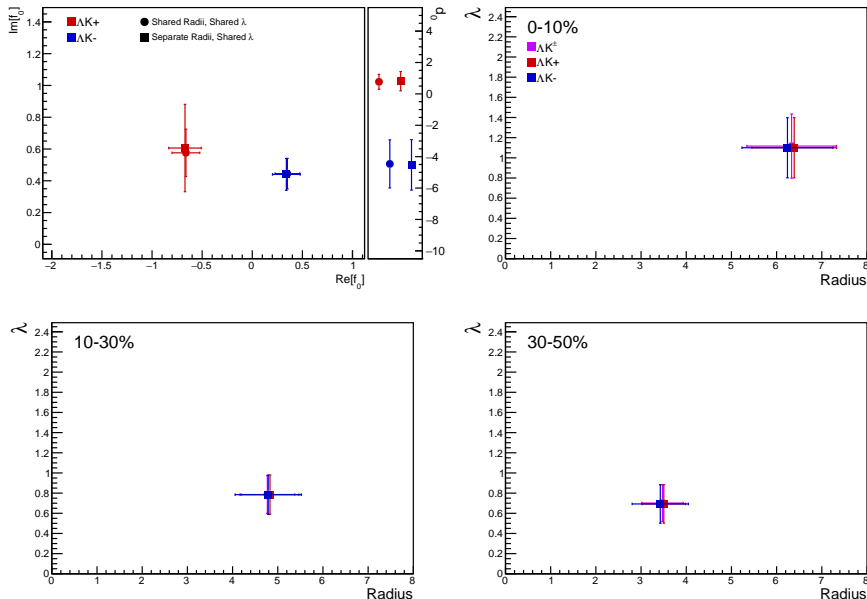


Fig. 53: Compare Fit Parameters: Shared vs unique λ : Results shown for different sharing of the λ parameters between analyses and systems. In the top (51a), the ΛK^+ and ΛK^- analyses share radii, whereas in the bottom (51b), they do not. “Share λ ” (circles) is the case where a single λ is shared amongst all analyses for a given centrality bin (i.e., in 51a, 3 radius parameters and 3 λ parameters). “Share λ_{Conj} ” (squares) means that conjugate pairs (ex. ΛK^+ and $\bar{\Lambda} K^-$) share a λ parameter for each centrality. This corresponds to 6 total λ parameters (for each of the 3 centrality bins, the $\Lambda K^+(\bar{\Lambda} K^-)$ receives a unique λ , as does $\Lambda K^-(\bar{\Lambda} K^+)$). Finally, in “Unique λ ” (+), each analysis received its own unique λ parameter. This corresponds to 12 λ parameters (for each of the 3 centrality bins, each ΛK^+ , $\bar{\Lambda} K^-$, ΛK^- , and $\bar{\Lambda} K^+$ receives a unique λ).



(a) Shared radii



(b) Separate radii

Fig. 54: Compare Fit Parameters: Shared vs. Separate Radii: Results shown for the case of radii being shared between ΛK^+ and ΛK^- (circles) vs not shared (squares). In (a), when the radii are not shared between ΛK^+ and ΛK^- , neither are the λ parameters. In (b), the λ parameters are always shared between ΛK^+ and ΛK^-

821 **8.1.5 Discussion of m_T -Scaling**

822 It is clear from the results presented in the previous sections, that the ΛK systems do not conform to the
 823 approximate m_T -scaling of the pair source sizes. At first thought, this may appear to be a troubling result;
 824 the approximate scaling is an observed consequence of the collective behavior of the soft (low- p_T) sector
 825 of the produced system. The Λ and K particles certainly participate in the collective expansion of the
 826 QGP medium, so why do their extracted femtoscopic radii not behave as expected? To get straight to the
 827 point: the ΛK systems are (obviously) comprised on non-identical particles, each with its own and unique
 828 single particle source. Each source is, in general, unique in both its overall size, and in its space-time po-
 829 sition within the produced medium. The hydrodynamic nature of the medium produces the approximate
 830 m_T -scaling with respect to these single-particle sources, not the pair sources. The combination of these
 831 effects, when probing correlations between non-identical particle pairs, leads to extracted radii falling
 832 outside of the (identical particle femtoscopy) m_T -scaling trend. Figure 53 (which contains the same data
 833 as Fig.30), shows again the R_{inv} vs m_T plot, but also highlights (with arrows) the approximate individual
 834 $\langle m_T \rangle$ values of the single particle distributions. The grey circles show how single particle sizes change
 835 with m_T .

836 Taking a close look at Fig. 53, one can see that the previously published data (transparent points) are
 837 for identical particle analyses only. For these cases, the pair source, probed through femtoscopy, is
 838 comprised of two identical sources laying on top of each other. The extracted femtoscopic radii are
 839 related to the single particle source sizes by a factor of $\sqrt{2}$, and of course follow the m_T -scaling trend.
 840 The other (unpublished) non-identical particle femtoscopy study ($p\Lambda$) included in the figure, also shows
 841 radii deviating from the m_T -scaling band. Drawing a comparison with the $\Lambda\bar{\Lambda}$ study shown in Fig. 30
 842 is a bit more complicated; the $\Lambda\bar{\Lambda}$ system, although containing non-identical particles, does contain a
 843 particle with its antiparticle, for which annihilation could conceivably alter the pair source distribution.
 844 It would be more surprising if the non-identical analyses did happen to conform to the scaling; although,
 845 this could occur for a non-identical analysis in which the particles have similar masses as well as similar
 846 m_T distributions. For the case presented here, the result differing from m_T -scaling is not surprising.

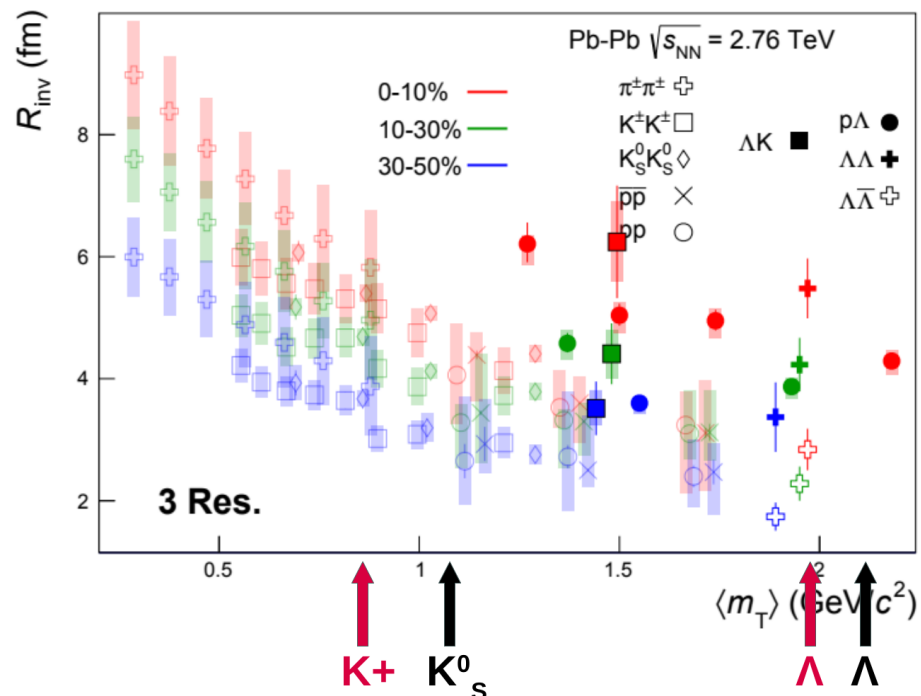


Fig. 55: Same as Fig. 30, but with the individual m_T values for the single particle distributions identified. The grey circles show how the single particle sizes are expected to change with m_T .

I will also briefly point out that it is not automatically clear where a non-identical study should be placed on such a R_{inv} vs m_T plot. Each single particle distribution has a well-defined $\langle m_T \rangle$, which, to a large extent, determines the single particle region of homogeneity. When combining two sources with different spatio-temporal characteristics, originating from particles of different m_T , how should one define the pair m_T ? A simple mathematical expression for the pair m_T is easy to come up with, but that's not exactly what I'm hinting at here. With respect to this m_T -scaling picture, the m_T value dictates the source size, and one desires the same for non-identical particles. However, do the two unequal sized sources both contribute equally to the extracted femtoscopic size? Or does the larger (smaller) source more closely dictate the femtoscopic signal? If the contribution is equal, then it seems natural to simply more-or-less average the two, single particle, m_T values. If the contribution is unequal, then there should be introduced some sort of weighting in the pair m_T calculation reflecting this fact. In any case, in our study we use the most straightforward definition of pair m_T , defined as:

$$m_{T,\text{pair}}^2 = \left(\frac{m_{\text{inv}}}{2}\right)^2 + \left(\frac{1}{2}|\mathbf{p}_{T,1} + \mathbf{p}_{T,2}|\right)^2 \quad (23)$$

Many times, the equation for non-identical particle pair m_T is defined with the average mass replacing $m_{\text{inv}}/2$. However, the above Eq. 23 is more directly analogous to the single particle m_T :

$$m_T^2 = m^2 + \mathbf{p}_T^2 = (p^0)^2 - (p^3)^2 \quad (24)$$

as, Eq. 23 may be rewritten as:

$$\begin{aligned} m_{T,\text{pair}}^2 &= (K^0)^2 - (K^3)^2 \\ K^\mu &\equiv \frac{1}{2}(p_1^\mu + p_2^\mu) \end{aligned} \quad (25)$$

Identical particle femtoscopic studies are able to probe only the size of the emitting region, or, more precisely, the second moments of the emission function. In addition to this, non-identical particle studies are able to measure the relative emission shifts, the first moments of the emission function. One method to extract information about the emission asymmetries in the system is via a spherical decomposition of the correlation function. With this method, one can draw a wealth of information from just a few components of the decomposition. More specifically, the C_{00} component is similar to the 1D correlation functions typically studied, and probes the overall size of the source. The $\Re C_{11}$ component probes the asymmetry in the system; a non-zero value reveals the asymmetry.

In Fig. 54 we show results for the C_{00} and $\Re C_{11}$ components from the spherical decomposition of our ΛK^+ system in the 0-10% centrality bin (red circles). Results from a number of other components within the decomposition, as well as for our ΛK_S^0 and ΛK^- systems, are contained in 9.2. Along with the experimental data in Fig. 54, we have also included results from THERMINATOR simulation for an impact parameter of $b = 2$ fm (gold stars). As THERMINATOR does not include any final state effects, we assumed scattering parameters $(\Re f_0, \Im f_0, d_0) = (-1.16, 0.51, 1.08)$ and weighted the numerator pairs with $|\Psi|^2$, as discussed previously. As seen in the figure, the C_{00} signal is similar to that observed in our one-dimensional study. The $\Re C_{11}$ component shows a clear deviation from zero, and the negative value signifies that the Λ particles are, on average, emitted further out and/or earlier than the K mesons.

Fig. 55 shows a closer look at the THERMINATOR simulation, whose spherical harmonic decomposition was shown along with the data in Fig. 54. The top left of Fig. 55a shows a fit to the one-dimensional correlation function from THERMINATOR. The scattering parameters are known precisely here, as they served as the weights used in the simulation, and are kept constant in the fit. We are interested in looking

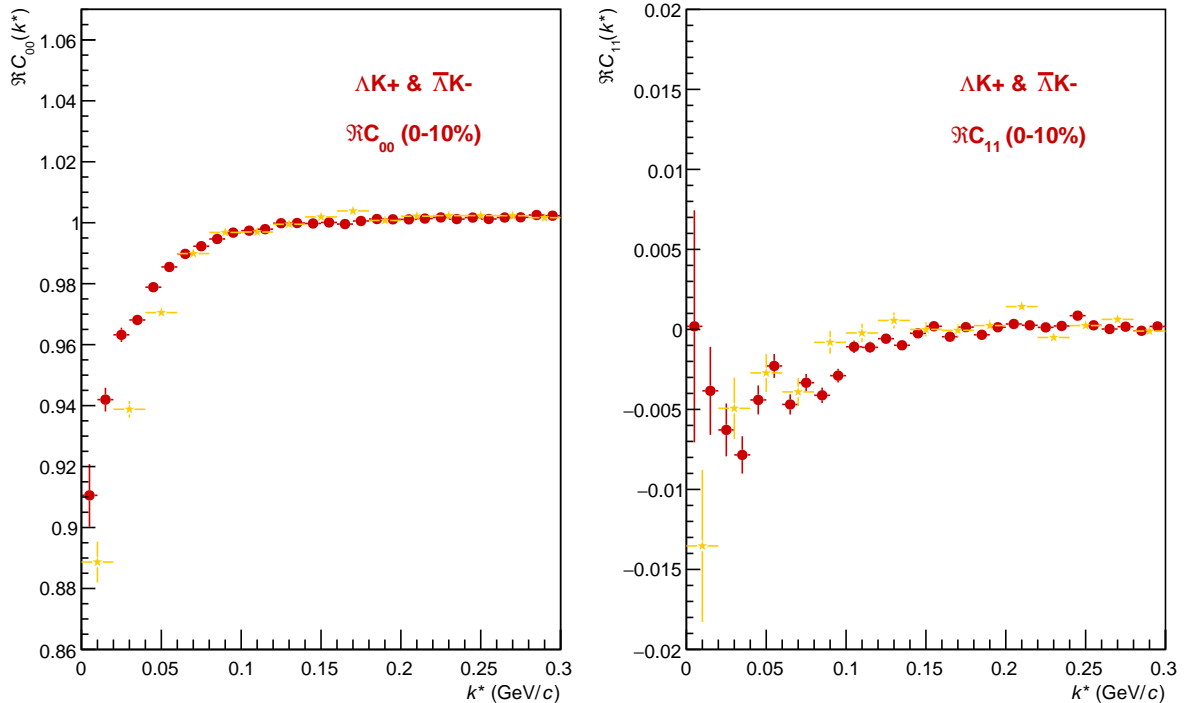
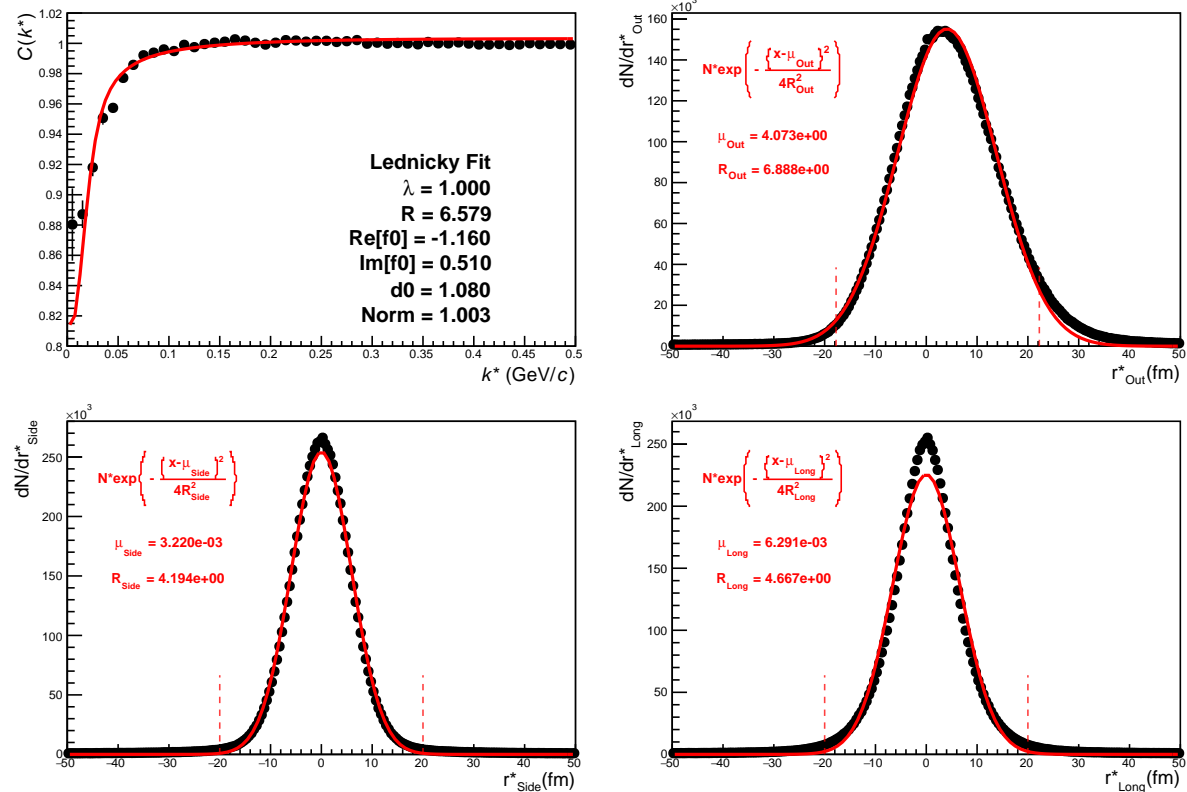


Fig. 56: C_{00} (left) and $\Re C_{11}$ (right) components of a spherical harmonic decomposition of the ΛK^+ correlation function for the 0-10% centrality bin. The C_{00} component is similar to the 1D correlation functions typically studied, and probes the overall size of the source. The $\Re C_{11}$ component probes the asymmetry in the system; a non-zero value reveals the asymmetry

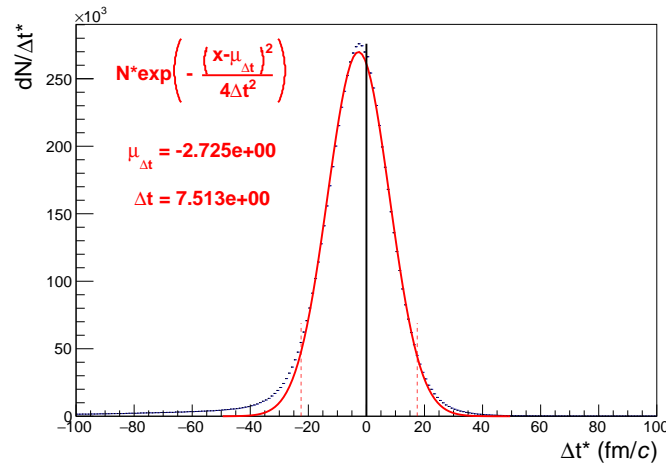
at the extracted one-dimensional source size here, so the λ parameter is also fixed at unity. The other three plots in Fig. 55a show the source distribution in the out (top right), side (bottom left), and long (bottom right) directions (all in the PRF). The source distributions have all been fitted with a Gaussian form, the result of which is printed within the respective plot. One immediately sees a significant shift in the out direction, $\mu_{\text{out}} \approx 4$ fm, and negligible shift in the other two directions, $\mu_{\text{side}} \approx \mu_{\text{long}} \approx 0$ fm. The figure demonstrates that, within the THERMINATOR model, the Λ is, on average, emitted further out than its K partner. Finally, Fig. 55b shows the distribution of the relative time of emittance, again in the PRF. The figure shows that the Λ is, on average, emitted earlier than its K partner.

We end this section with a brief look at how a spatial separation of the single particle sources affects the radii extracted from a femtoscopic analysis. To achieve this, we use THERMINATOR in a similar fashion as described above, but with one important difference. Instead of taking the source information from THERMINATOR, we instead draw the source from a pre-determined Gaussian distribution. In all cases, we take $R_{\text{out}} = R_{\text{side}} = R_{\text{long}} = 5$ fm, and $\mu_{\text{side}} = \mu_{\text{long}} = 0$ fm. Figure 56 shows an example of results obtained from THERMINATOR following this procedure, where $\mu_{\text{out}} = 3$ fm.

In Figure 57, we show results for the case of $\mu_{\text{out}} = 1$ fm, $\mu_{\text{out}} = 3$ fm, and $\mu_{\text{out}} = 6$ fm. In this figure, we do not show the side and long distributions, as they appear identical to those shown in Fig. 56. The figure demonstrates that as the separation μ_{out} increases, so do the extracted femtoscopic radii.

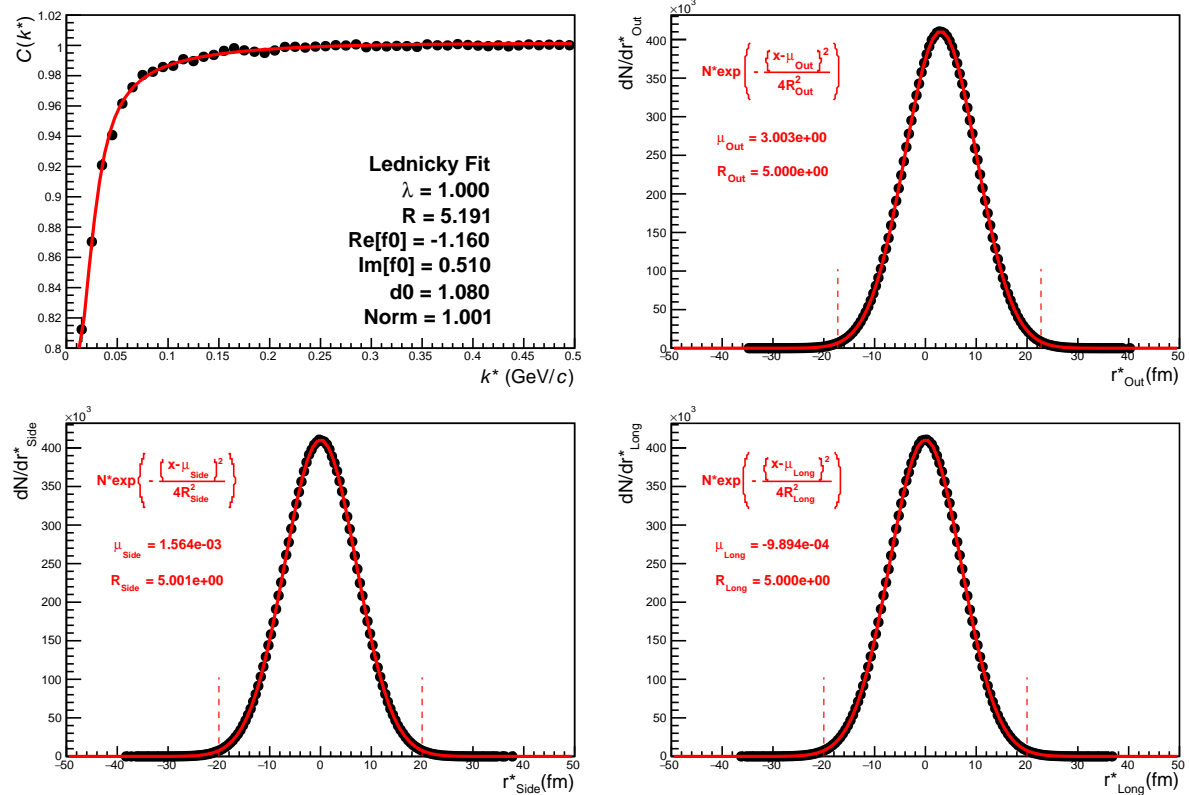
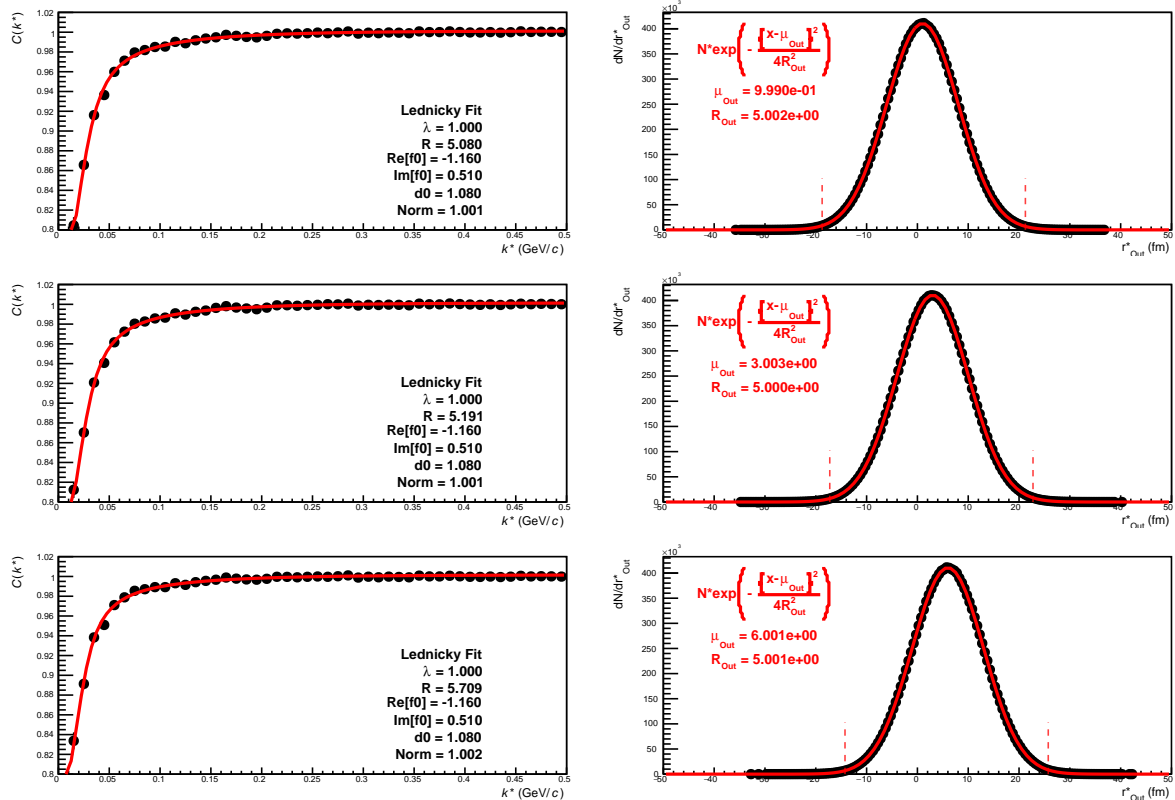


(a) Caption 1



(b) Caption 2

Fig. 57: Long Overall

**Fig. 58:** Long Caption**Fig. 59:** Long Caption

8.2 Results: ΞK^\pm

Even without any fits to the data, the fact that the $\Xi^- K^+$ data dips below unity (Fig. 58) is exciting, as this cannot occur purely from a Coulomb interaction. We hope that this dip signifies that we are able to peer through the overwhelming contribution from the Coulomb interaction to see the effects arising from the strong interaction.

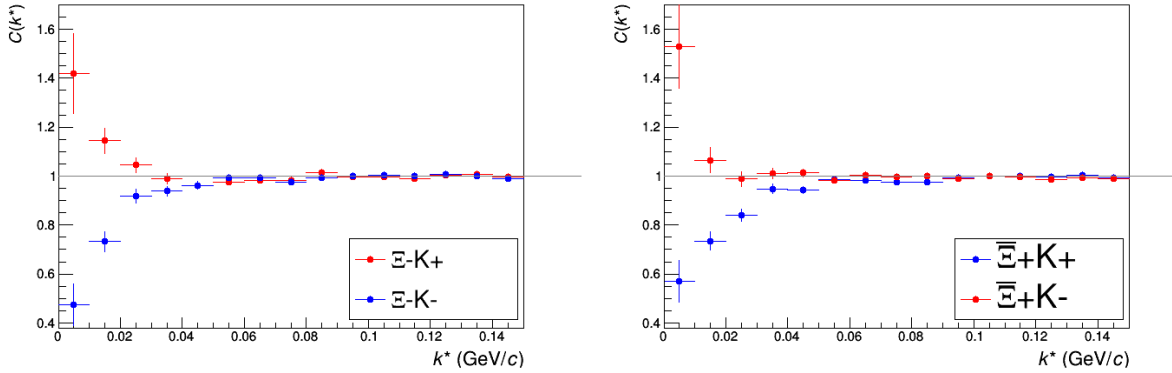


Fig. 60: ΞK^\pm Results for 0-10% Centrality. (Left) $\Xi^- K^+$ and $\Xi^- K^-$ (Right) $\Xi^+ K^+$ and $\Xi^+ K^-$

Figure 59 demonstrates graphically, that the $\Xi^- K^+$ results cannot be described by solely the Coulomb interaction. In this figure, we present the data along with a Coulomb-only band. The Coulomb-only band is spanned by two Coulomb-only curves, whose parameters are given in the figure. The Coulomb-only curves were generated using a technique identical to the generation of the fit function, described in Sec. 5.2, except, of course, with the nuclear scattering parameters all set to zero. The Coulomb-only curves change monotonically with varying λ or varying radius parametres, therefore, any curves built with parameter sets intermediate to those use in the Coulomb-only band will be contained in the band.

Including the strong interaction into the simulation can change, sometimes dramatically, the resulting correlation function, as shown in Figure 60. In the figure, the solid line represents a Coulomb-only curve, i.e. a simulated correlation function with the strong interaction turned off. The dashed lines represent a full simulation, including both the strong and Coulomb interactions. The two dashed lines differ only in the real part of the assumed scattering length: positive in Set 1, and negative in Set 2. In the top figure, for the $\Xi^- K^+$ simulation, we see that parameter set 2, with a negative real part of the scattering length, causes the simulated curve to dip below unity, as is seen in the data. If there is a parallel to be drawn between this analysis and the ΛK analysis, we expect to see similar effects in the ΛK^+ system and the $\Xi^- K^+$ systems. In these systems, we could have an $s\bar{s}$ annihilation picture. Or, another possible way of thinking about these systems is in terms of net strangeness. The ΛK^+ system has $S=0$, while the ΛK^- has $S=-2$. The $\Xi^- K^+$ has $S=-1$, while the $\Xi^- K^-$ has $S=-3$.

The author was asked to perform a global Coulomb-only fit to the data, to ensure that the system truly could not be described simply by the Coulomb interaction. In other words, in the fit, the strong force was turned off, and the $\Xi^- K^+$, $\Xi^+ K^-$, $\Xi^- K^-$, $\Xi^+ K^+$ systems all share one single radius parameter, while the pair and conjugate pair systems share a λ parameter. The results of this fit are shown in Figures 61 and 62. In Fig. 61, there was a lower limit of 0.1 fm placed on the radius parameter, and the radius parameter was initialized to 3 fm (as seems reasonable, when considering the transverse mass of the system and looking at Fig. 30). As is shown in the results, the radius parameter reached this unrealistic lower bound of 0.1 fm. In Fig. 62, the parameters were all unbounded, and the radius parameter was initialized to 10 fm. In this case, the radius parameters remain high, and end at an unrealistic value of 10.84 fm. In both cases, the λ parameters are too low. From these figures, we conclude that a global Coulomb-only fit is not suitable for the data.

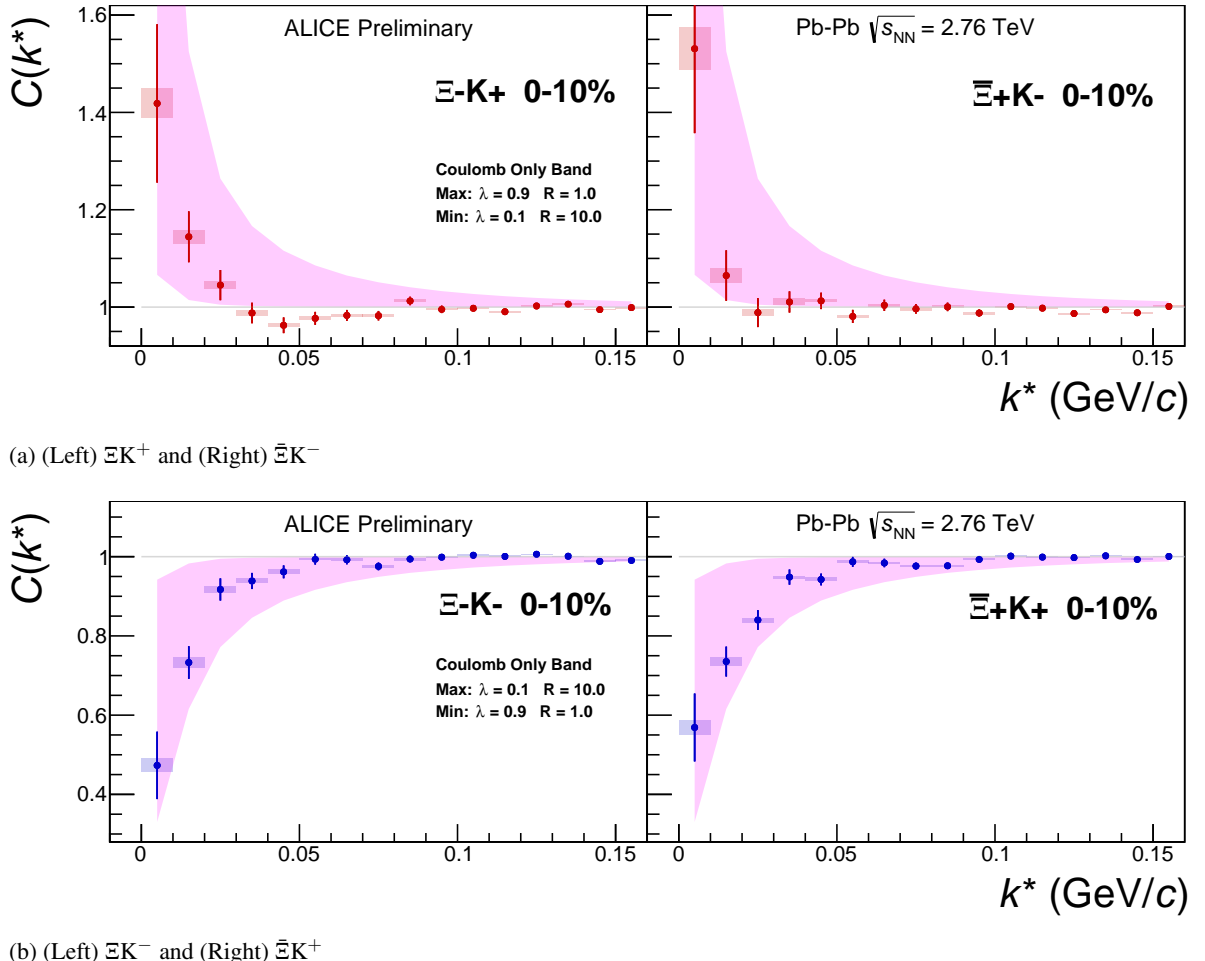


Fig. 61: ΞK^\pm data with Coulomb-only bands for the 0-10% centrality bin. The Coulomb-only bands span two sets of Coulomb-only curves: (1) $\lambda = 0.9$, $R = 1.0$ fm and (2) $\lambda = 0.1$, $R = 10.0$ fm. The Coulomb-only curves are simulated correlation functions for the respective pair system assuming only a Coulomb interaction, i.e. ignoring the strong interaction. The Coulomb-only curves change monotonically with varying λ and varying R , therefore, any intermediate parameter set will fall within this Coulomb-only band.

934 Although the global Coulomb-only fit failed, it is possible that a Coulomb-only fit performed on $\Xi^- K^+$
 935 and $\bar{\Xi}^+ K^-$ separately from $\Xi^- K^-$ and $\bar{\Xi}^+ K^+$ could be suitable. The result of such fits are shown in
 936 Figures 63 and 64. Figure 63, shows that the fit is not able to describe the dip in the $\Xi^- K^+$ data below
 937 unity. Of course, this is obviously true for an attractive Coulomb-only fit. The radius parameter of
 938 8.43 fm extracted from this fit is unrealistically large. In Figure 64 shows the Coulomb-only fit can
 939 described the $\Xi^- K^-$ data reasonable well; although the extracted radius of 3.73 fm is somewhat larger
 940 than expected.

9 To Do

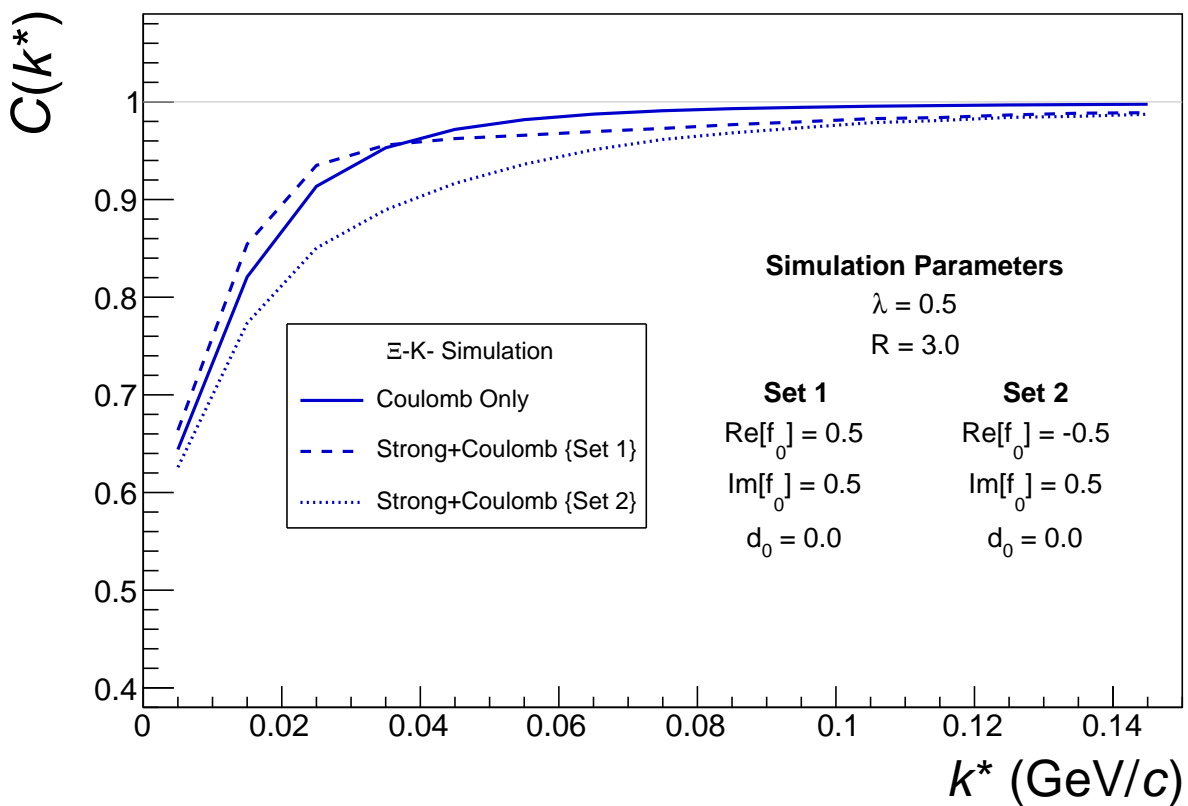
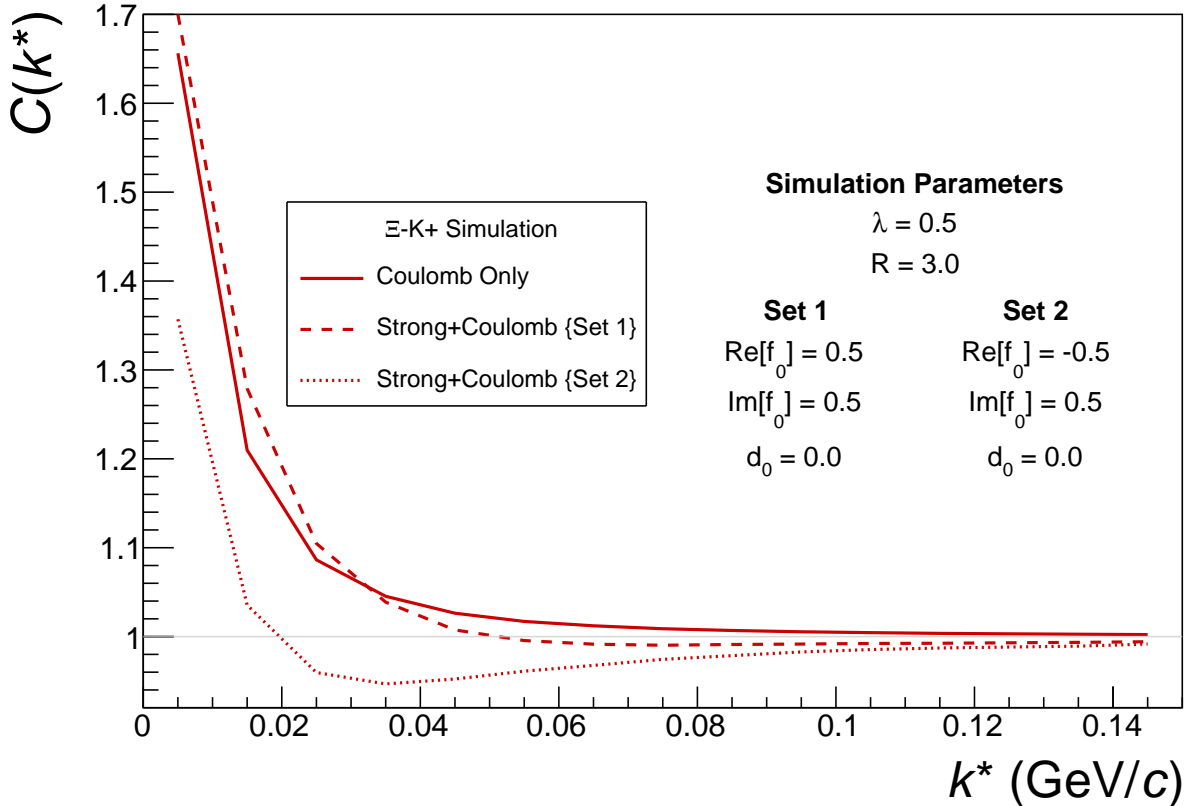
(b) ΞK^- and $\bar{\Xi} K^+$ simulation

Fig. 62: Effect on the Coulomb-only curve of including the strong interaction for ΞK^\pm systems. The solid line represents a Coulomb-only curve, i.e. a simulated correlation function with the strong interaction turned off. The dashed lines represent a full simulation, including both the strong and Coulomb interactions. The two dashed lines differ only in the real part of the assumed scattering length: positive in Set 1, and negative in Set 2.

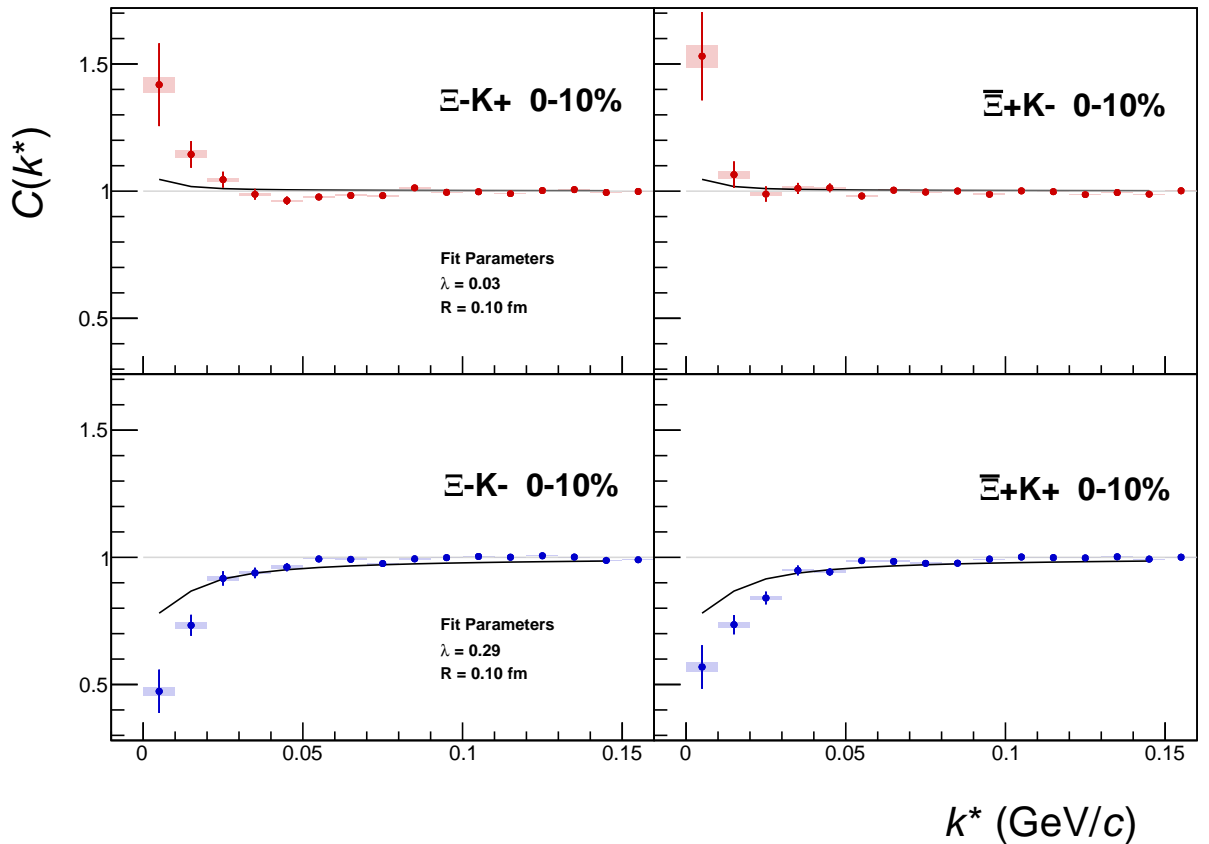


Fig. 63: ΞK^\pm Global Coulomb-only fit (Set 1) for 0-10% centrality. In this fit, there was a lower limit of 0.1 fm placed on the radius parameter, and the radius parameter was initialized to 3 fm (as seems reasonable, when considering the transverse mass of the system and looking at Fig. 30). As is shown in the results, the radius parameter reached this unrealistic lower bound of 0.1 fm. Also, the extracted λ parameters are too low.

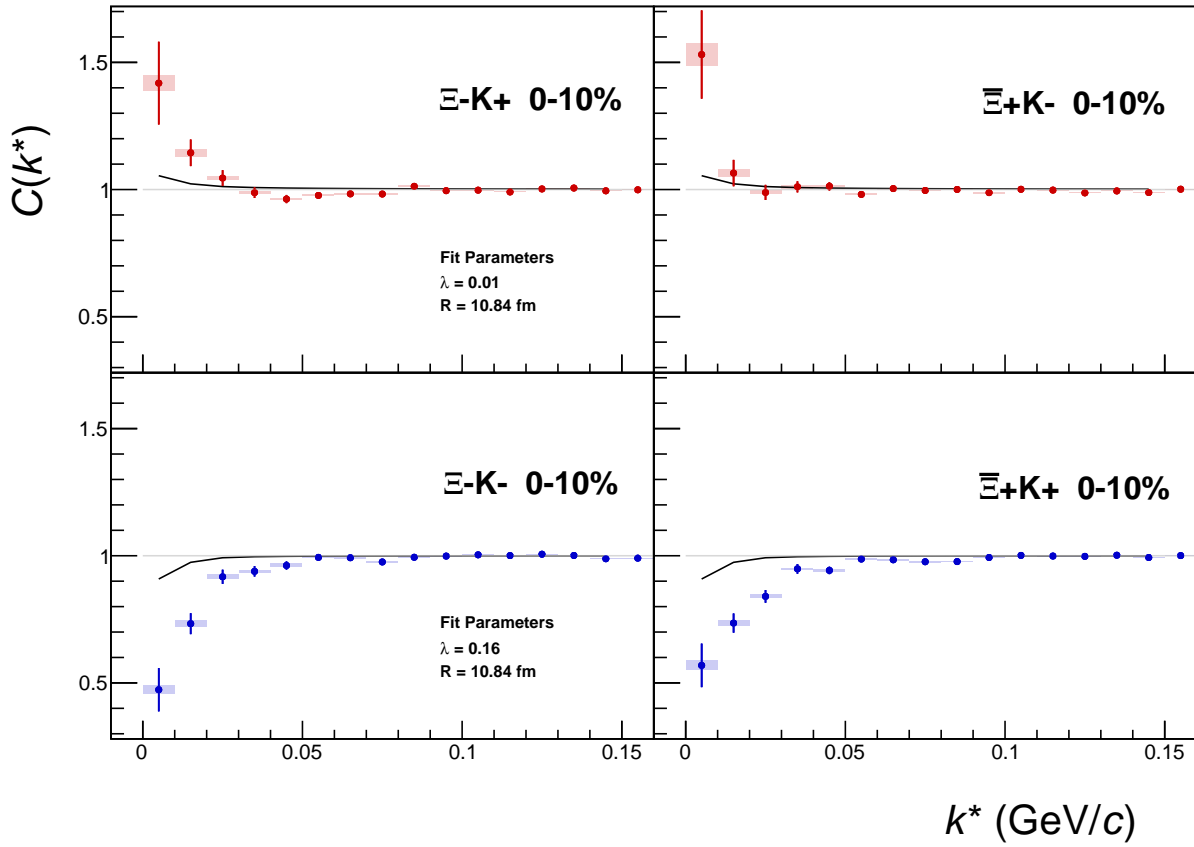


Fig. 64: ΞK^\pm Global Coulomb-only fit (Set 2) for 0-10% centrality. In this fit, the parameters were all unbounded, and the radius parameter was initialized to 10 fm. In this case, the radius parameters remain high, and ends at an unrealistic value of 10.84 fm. Also, the extracted λ parameters are too low.

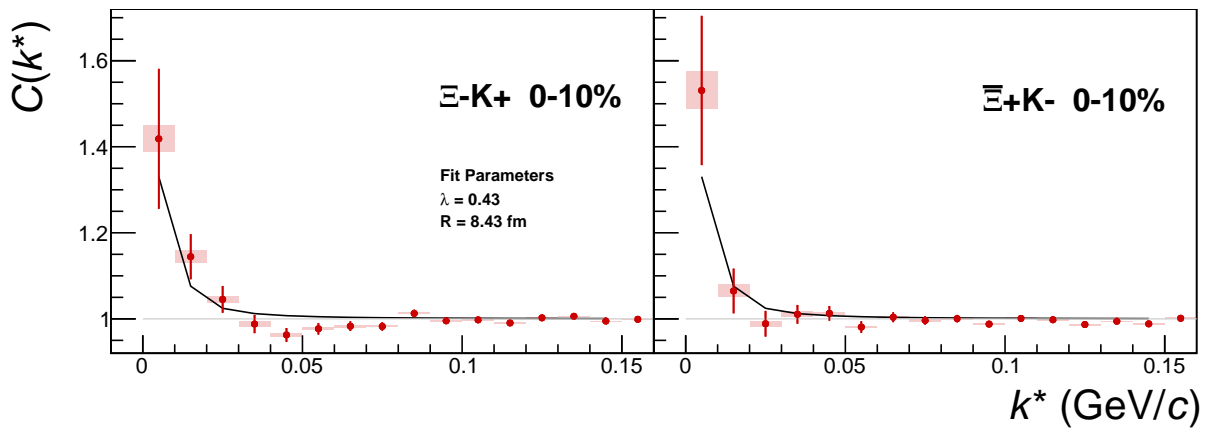


Fig. 65: $\Xi\text{-}K^+$ Coulomb-only fit for 0-10% centrality

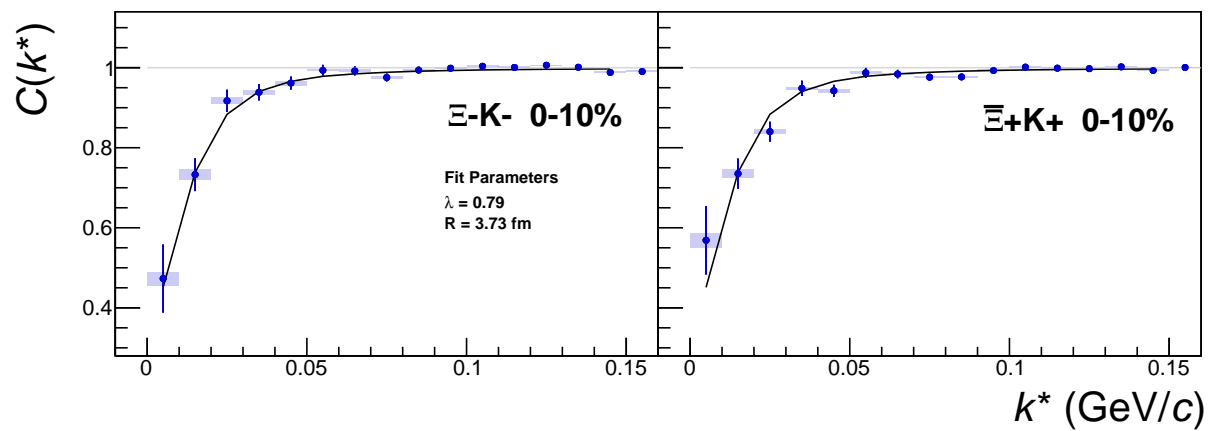


Fig. 66: $\Xi^- K^-$ Coulomb-only fit for 0-10% centrality

942 **10 Additional Figures**

943 **10.1 Residuals**

944 **10.1.1 ΛK^+ Residuals**

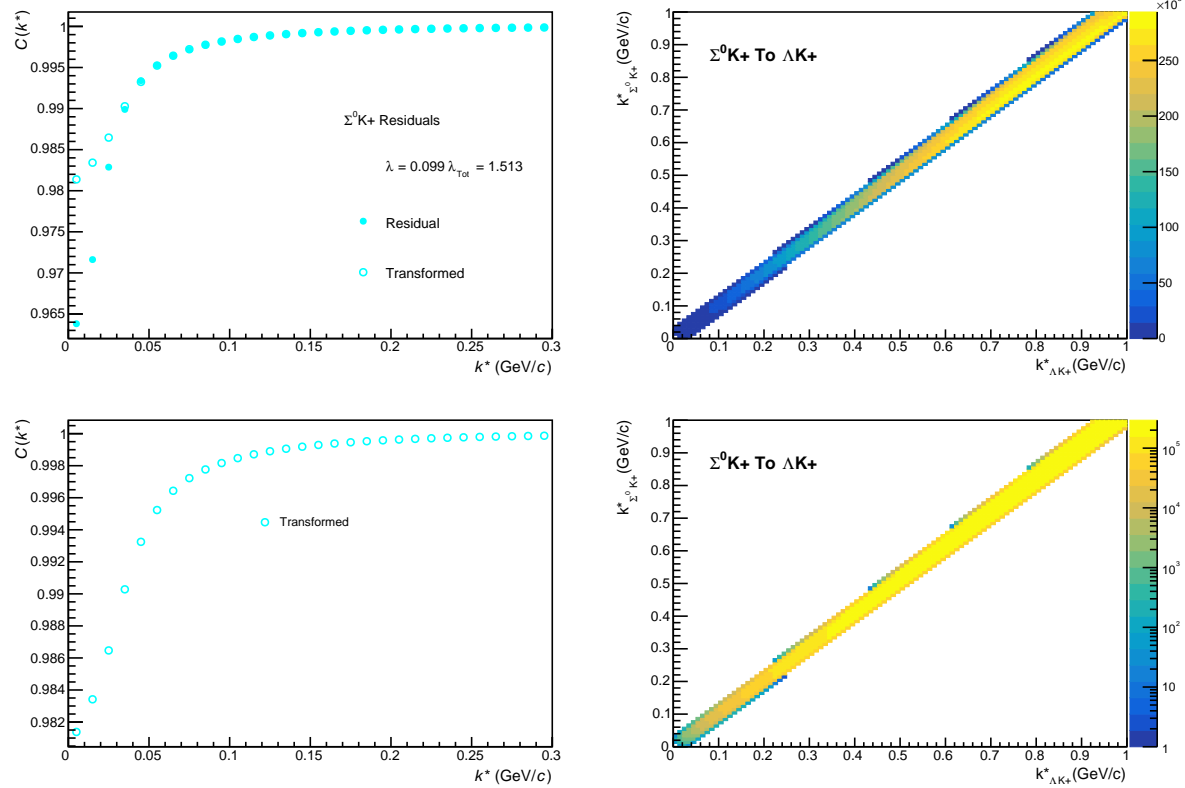
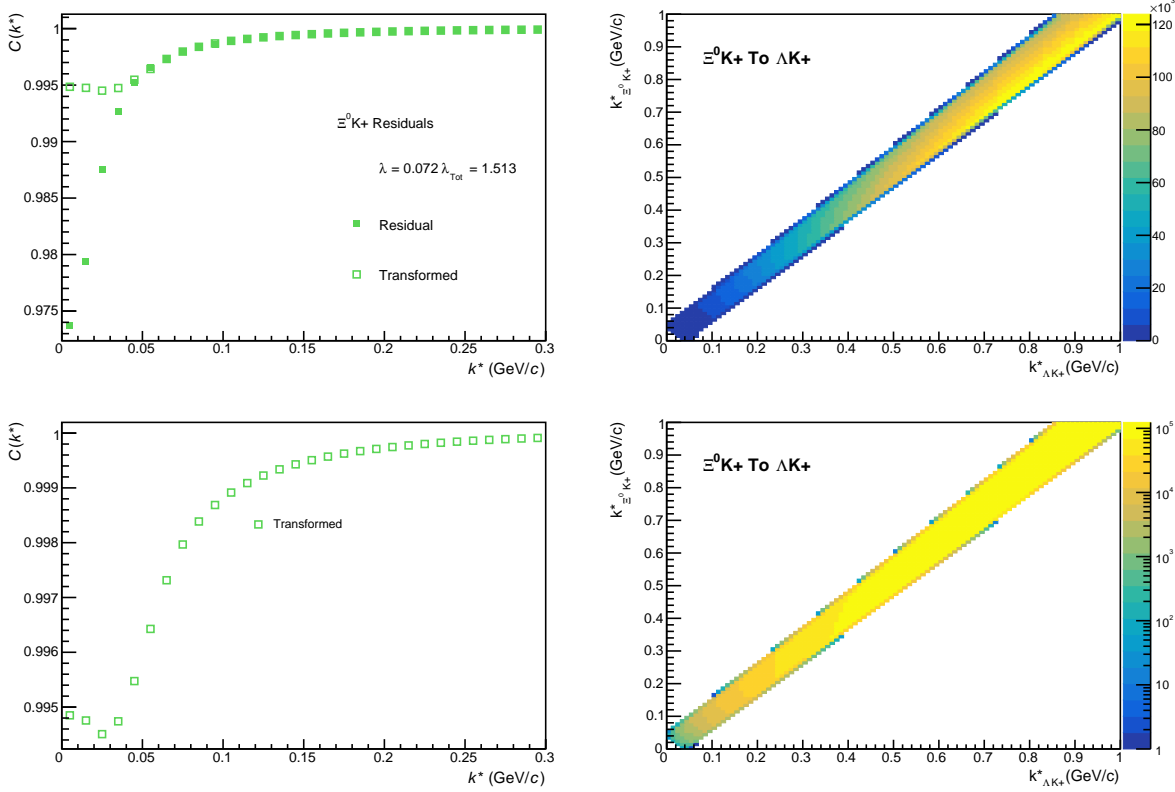
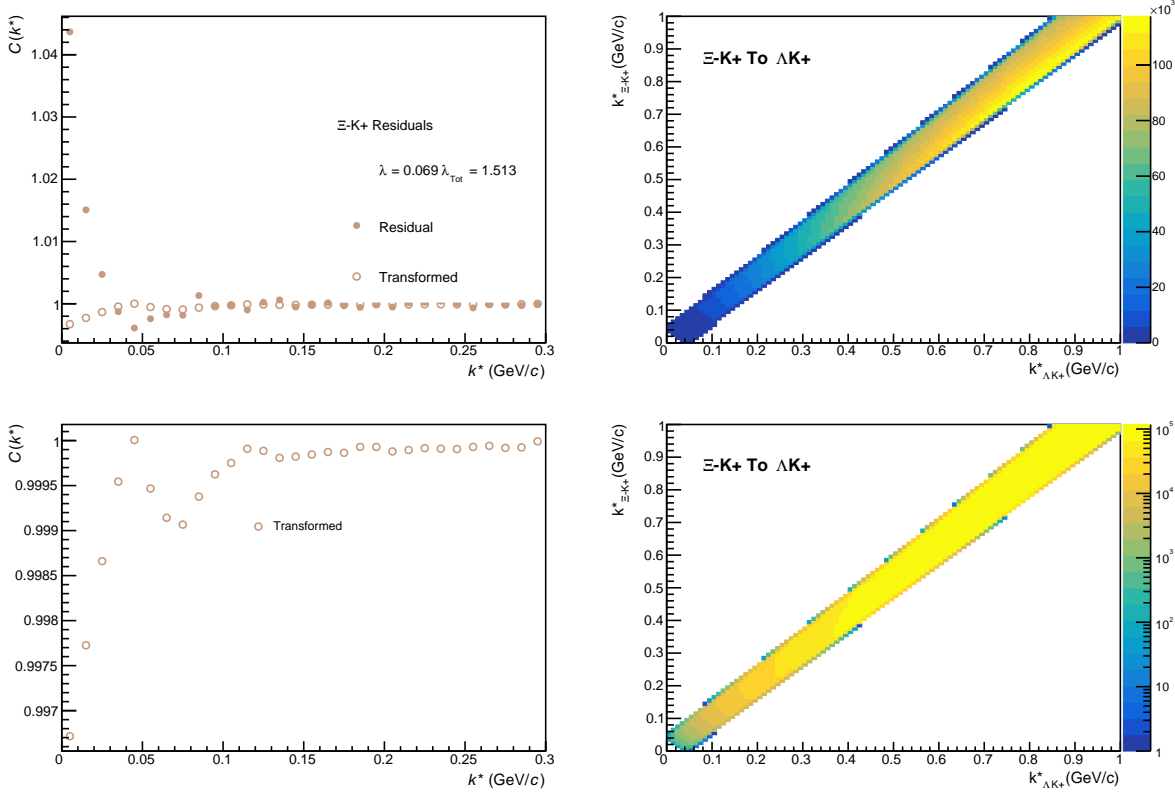


Fig. 67: Residuals: $\Sigma^0 K^+$ to ΛK^+ (0-10% Centrality)


Fig. 68: Residuals: $\Xi^0 K^+$ to ΛK^+ (0-10% Centrality)

Fig. 69: Residuals: $\Xi^- K^+$ to ΛK^+ (0-10% Centrality)

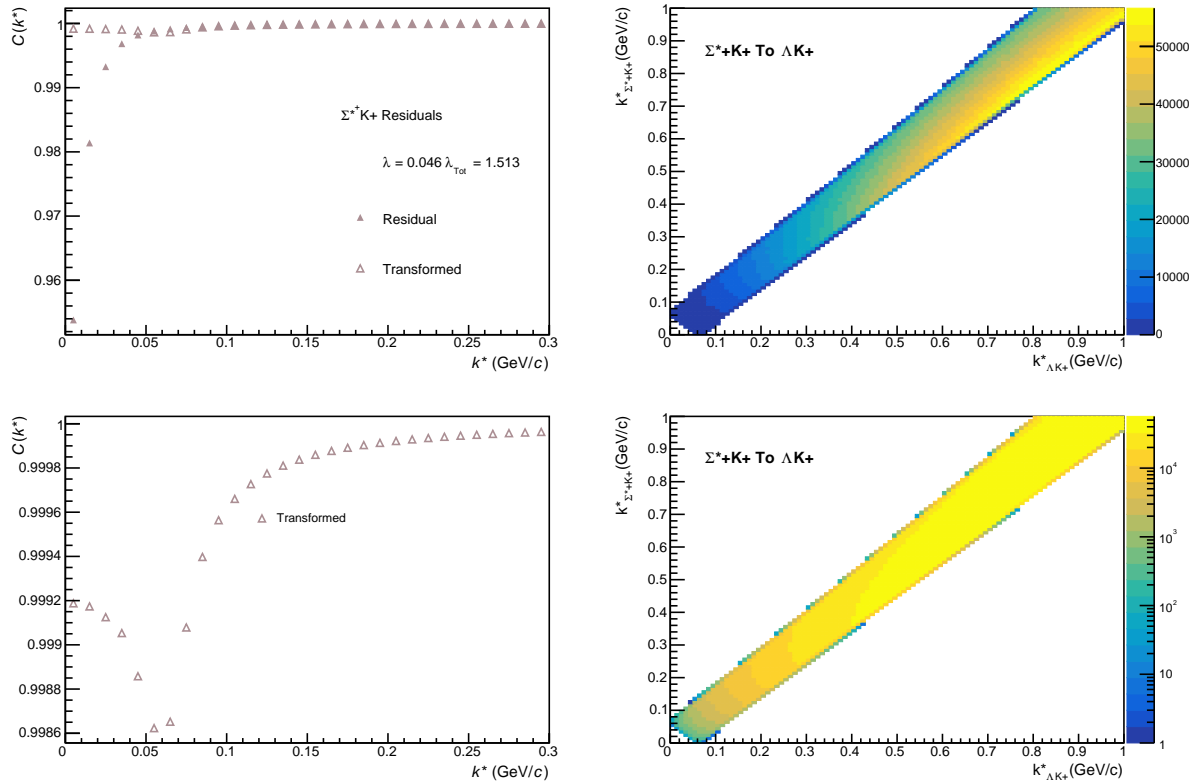


Fig. 70: Residuals: $\Sigma^+ K^+$ to ΛK^+ (0-10% Centrality)

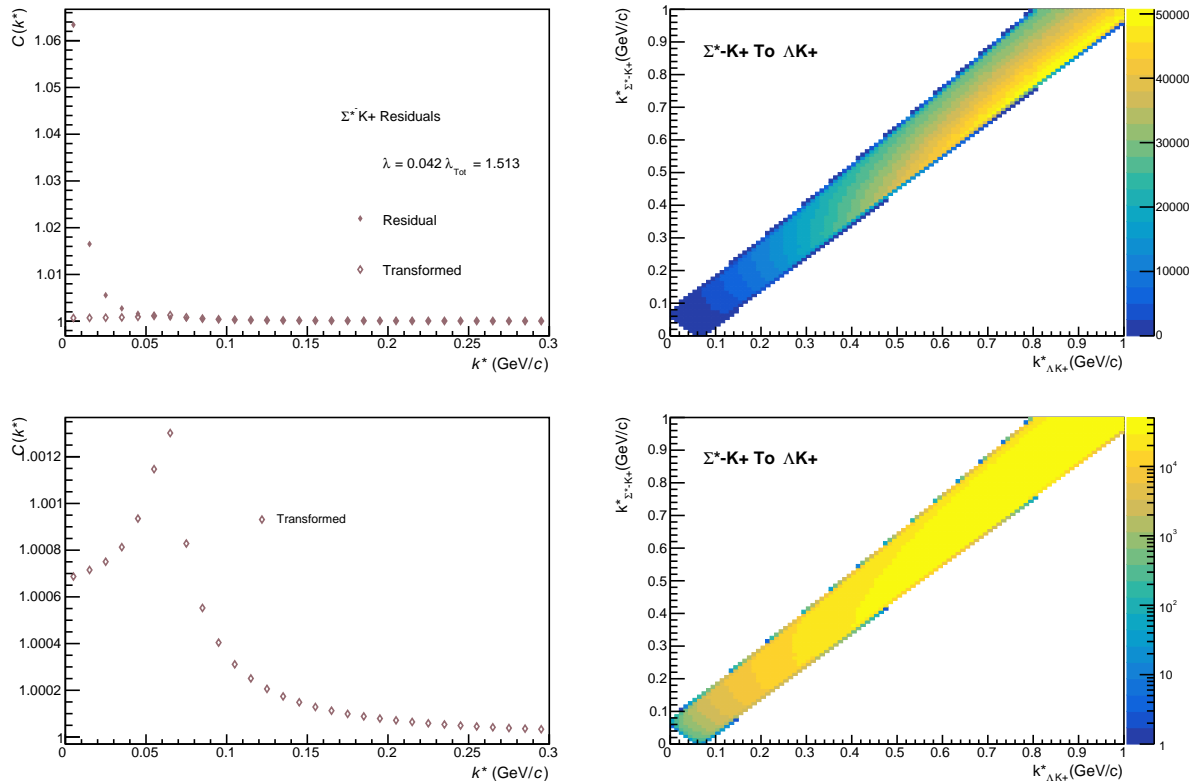
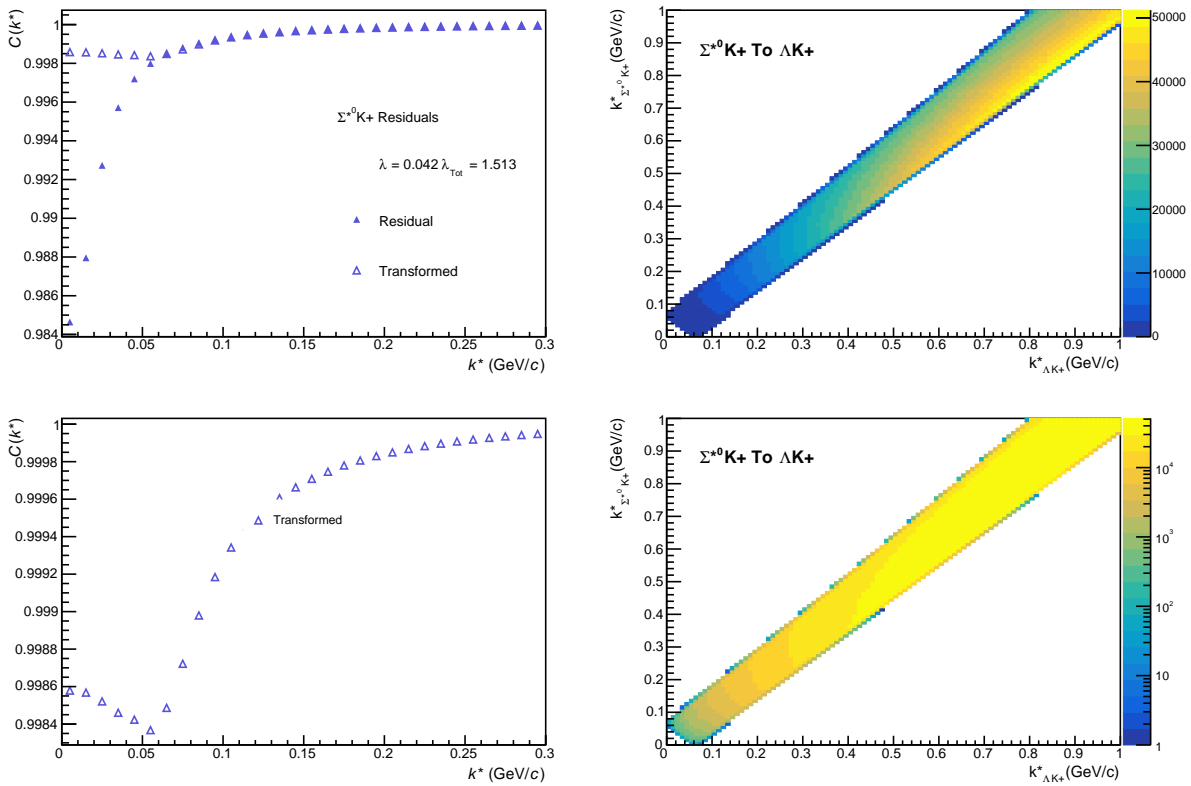
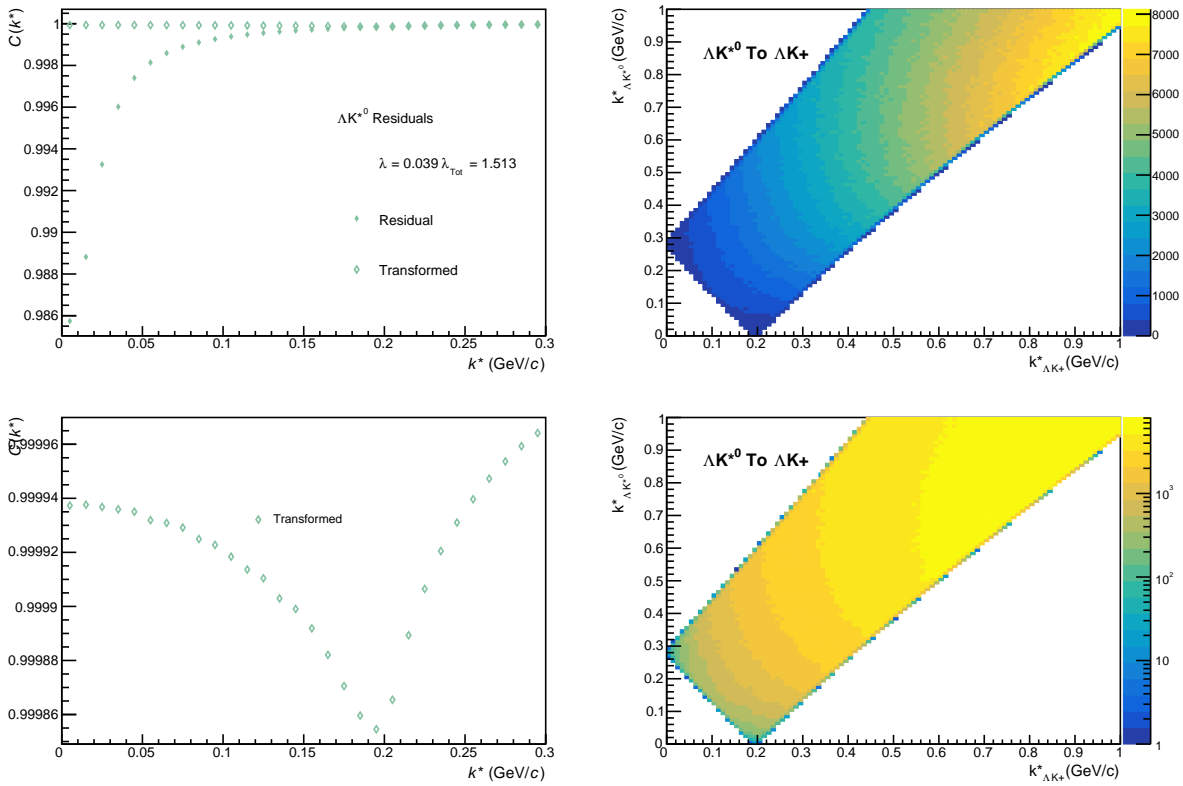


Fig. 71: Residuals: $\Sigma^- K^+$ to ΛK^+ (0-10% Centrality)


 Fig. 72: Residuals: $\Sigma^{*0} K^+$ to ΛK^+ (0-10% Centrality)

 Fig. 73: Residuals: ΛK^{*0} to ΛK^+ (0-10% Centrality)

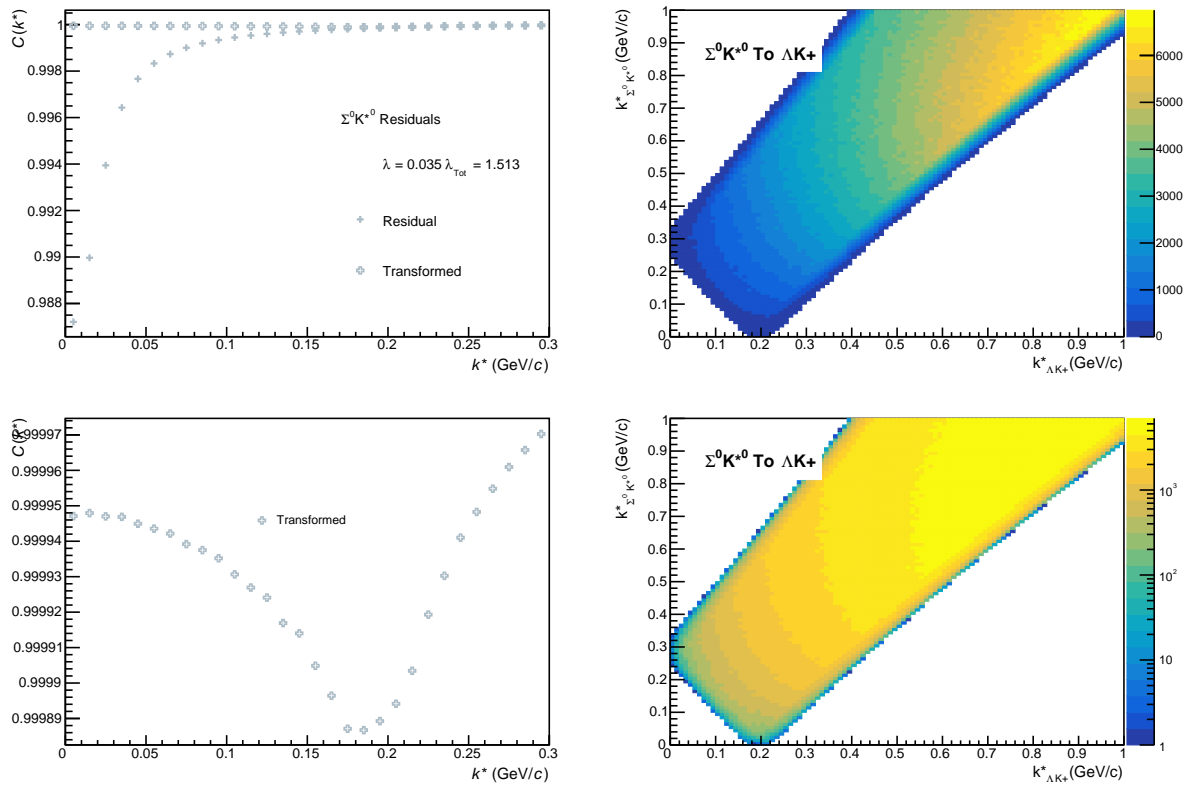


Fig. 74: Residuals: $\Sigma^0 K^{*0}$ to ΛK^+ (0-10% Centrality)

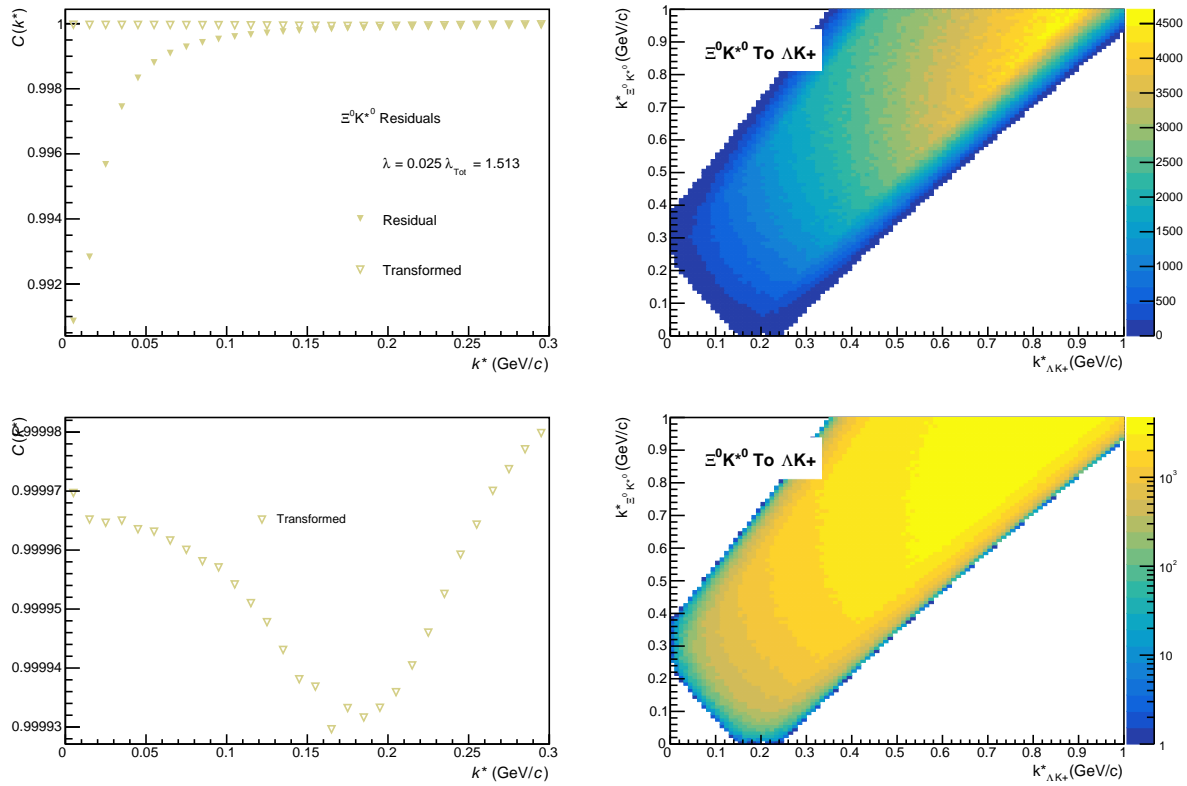


Fig. 75: Residuals: $\Xi^0 K^{*0}$ to ΛK^+ (0-10% Centrality)

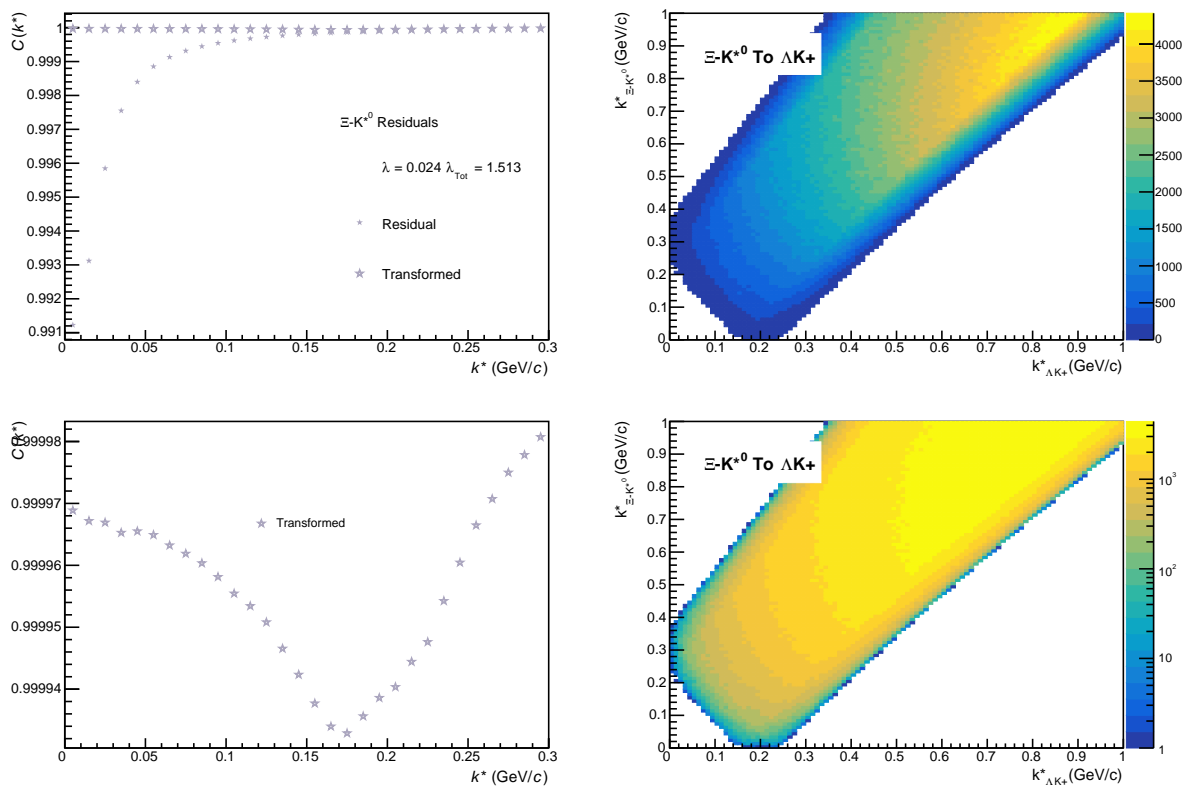


Fig. 76: Residuals: $\Xi\text{-}K^{*0}$ to ΛK^+ (0-10% Centrality)

945 **10.1.2 ΛK^- Residuals**

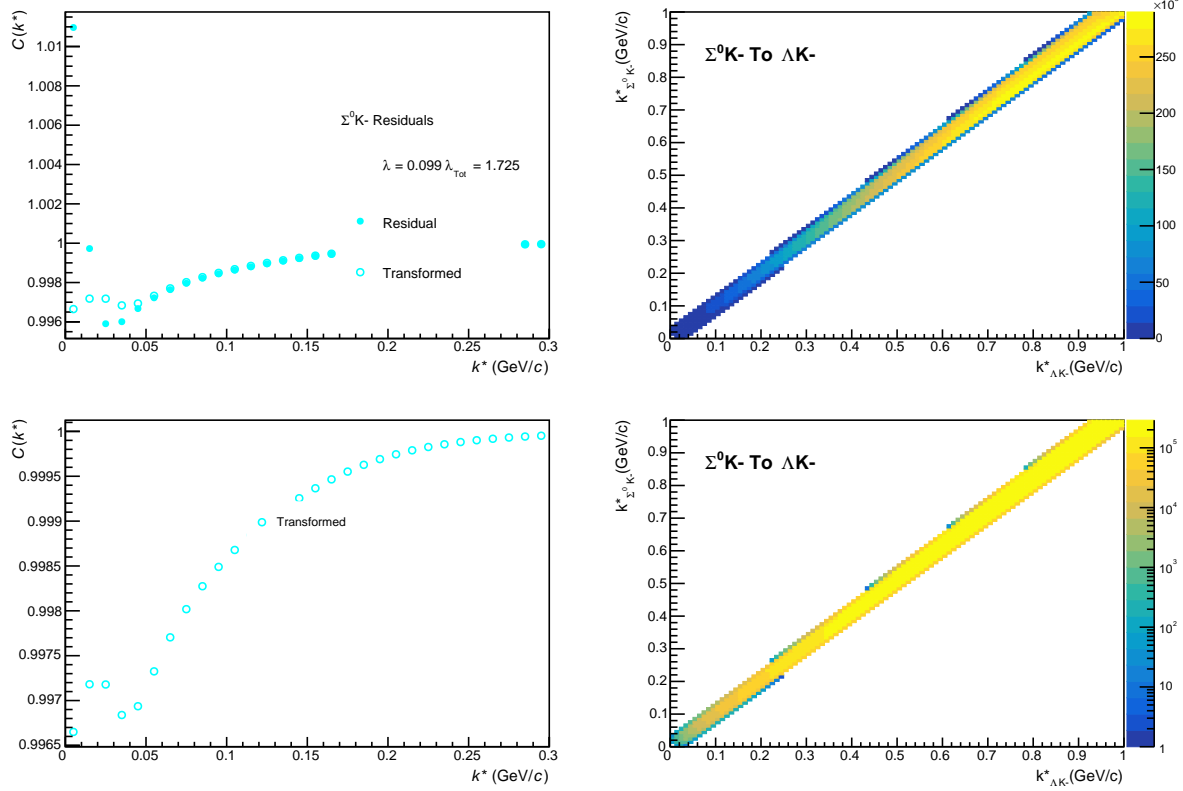
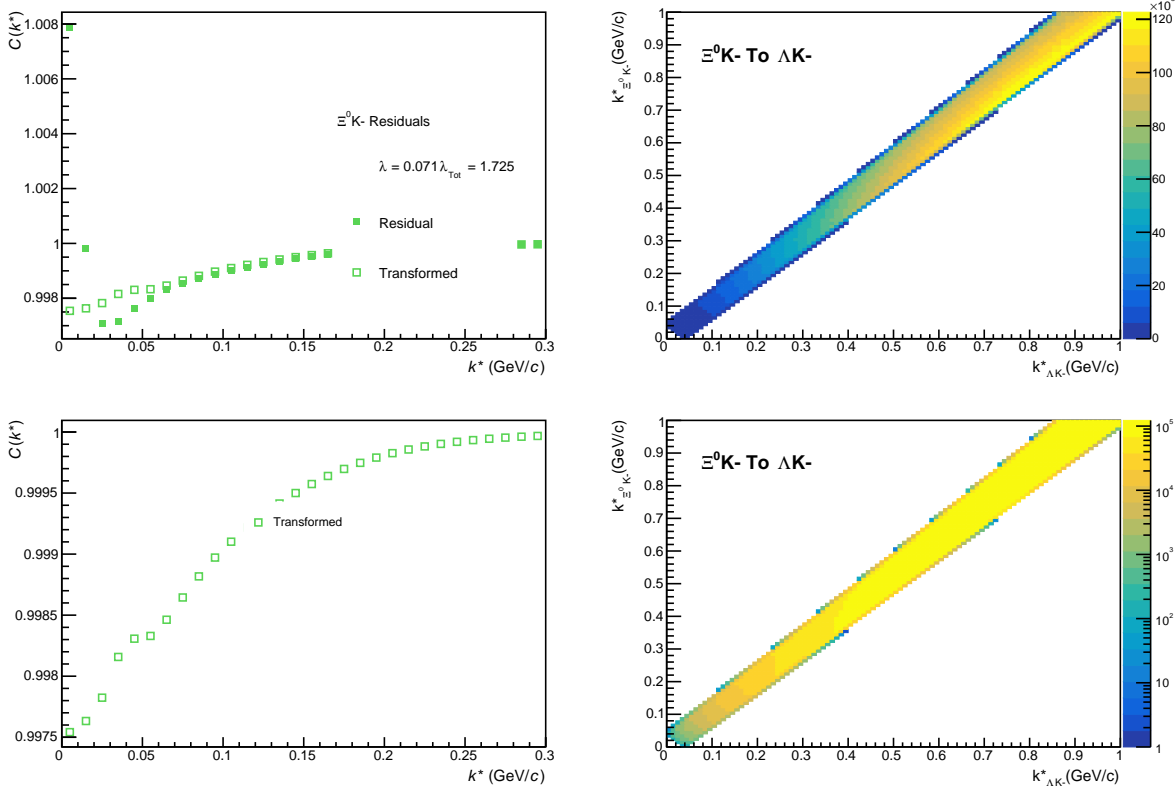
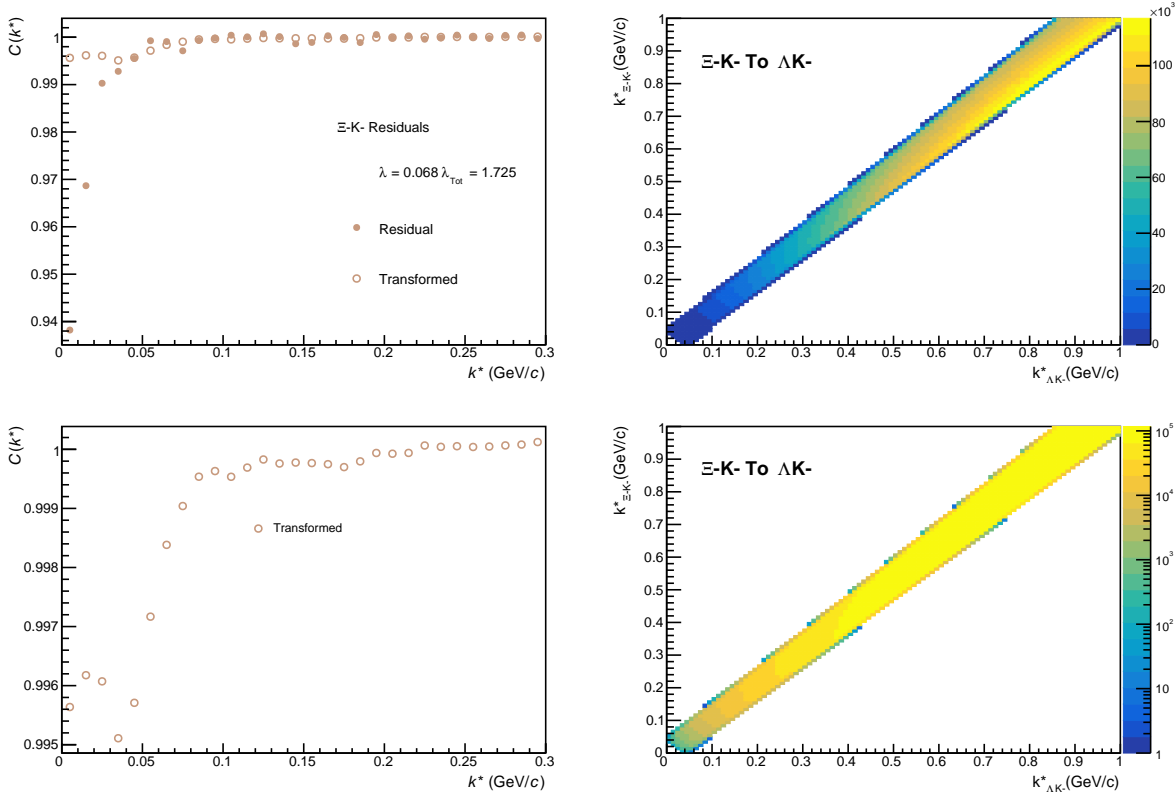


Fig. 77: Residuals: $\Sigma^0 K^-$ to ΛK^- (0-10% Centrality)


Fig. 78: Residuals: $\Xi^0 K^-$ to ΛK^- (0-10% Centrality)

Fig. 79: Residuals: $\Xi^- K^-$ to ΛK^- (0-10% Centrality)

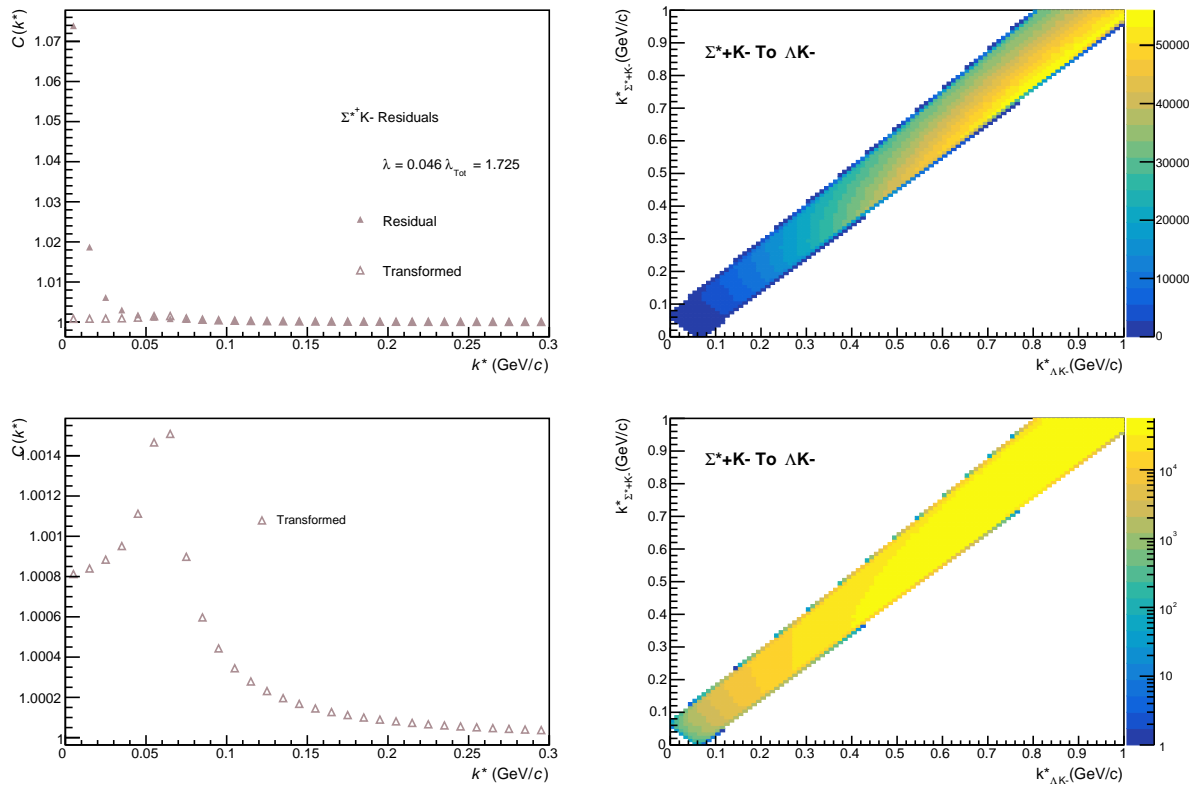


Fig. 80: Residuals: $\Sigma^* + K^-$ to ΛK^- (0-10% Centrality)

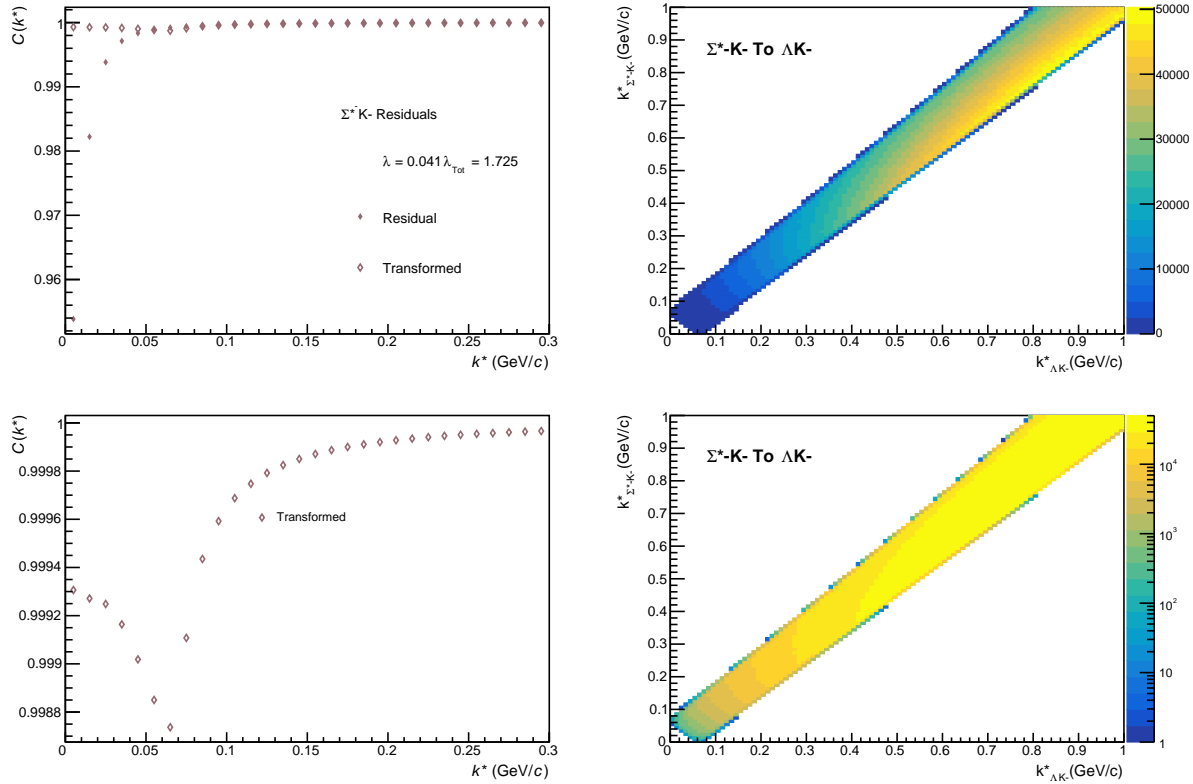
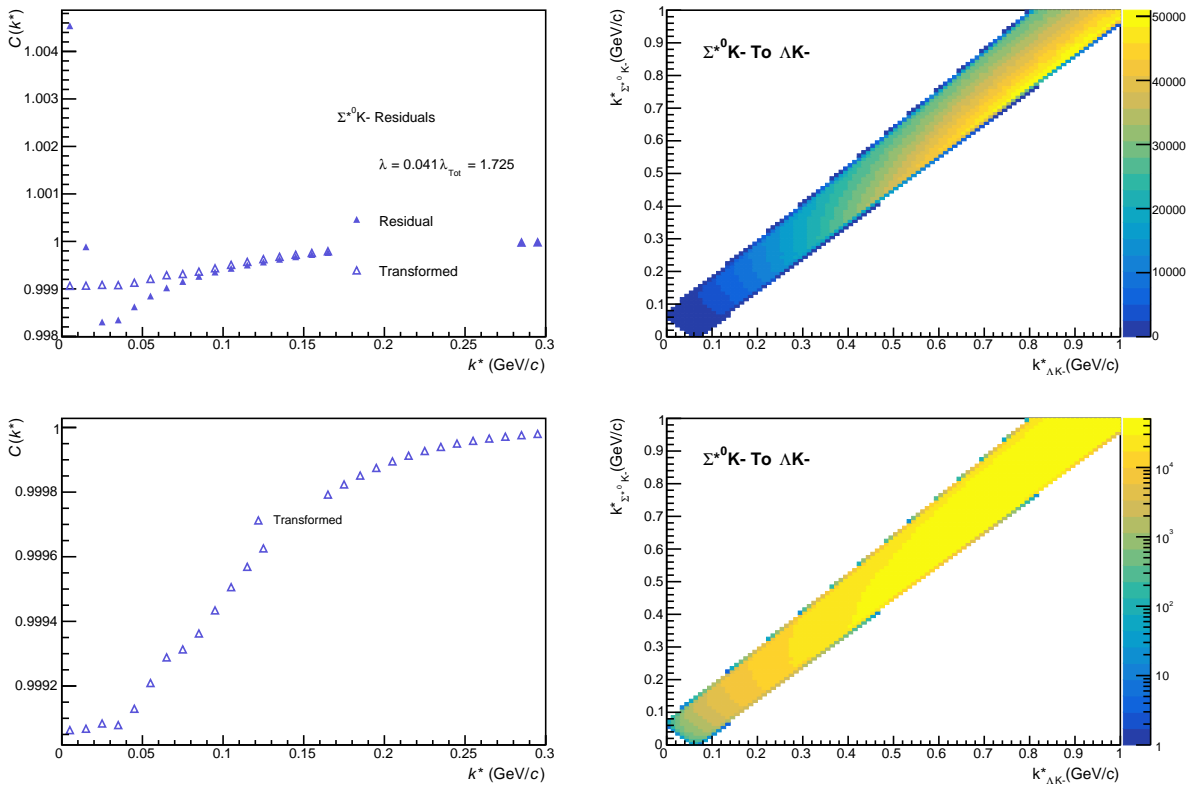
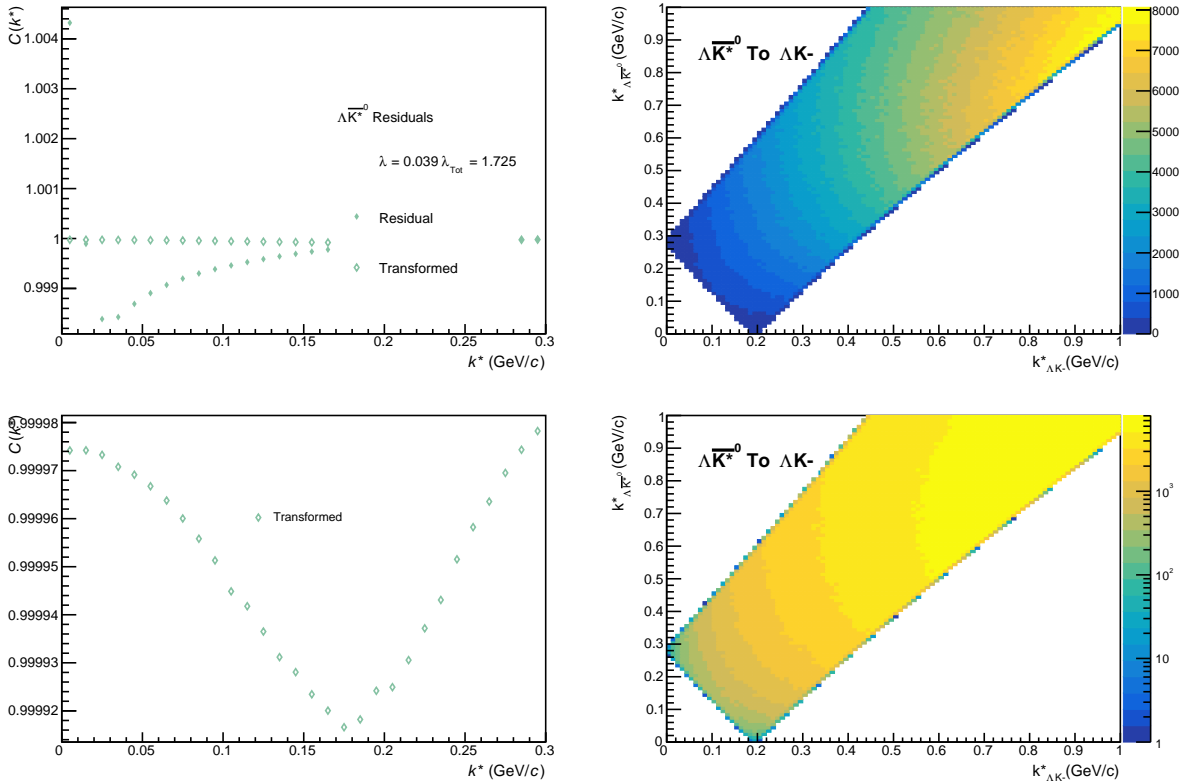


Fig. 81: Residuals: $\Sigma^* - K^-$ to ΛK^- (0-10% Centrality)


Fig. 82: Residuals: $\Sigma^{*0} K^-$ to ΛK^- (0-10% Centrality)

Fig. 83: Residuals: $\Lambda \bar{K}^{*0}$ to ΛK^- (0-10% Centrality)

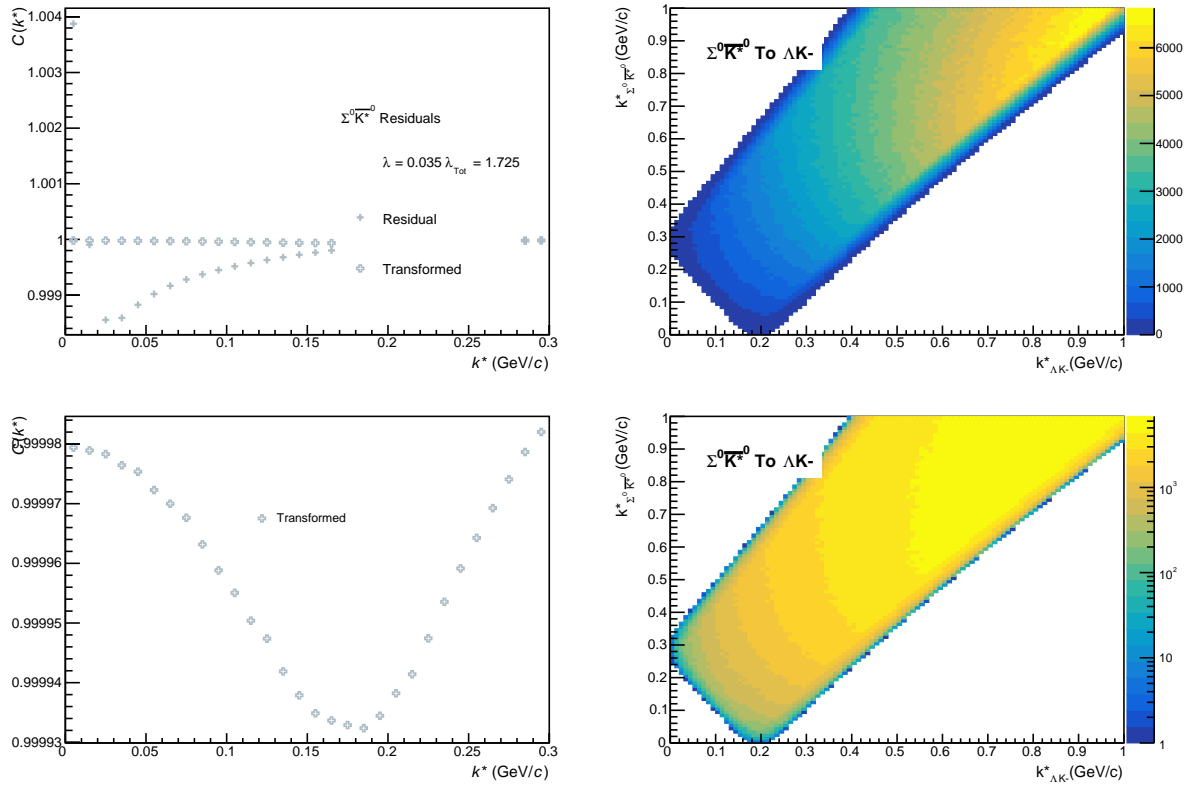


Fig. 84: Residuals: $\Sigma^0 \bar{K}^{*0}$ to ΛK^- (0-10% Centrality)

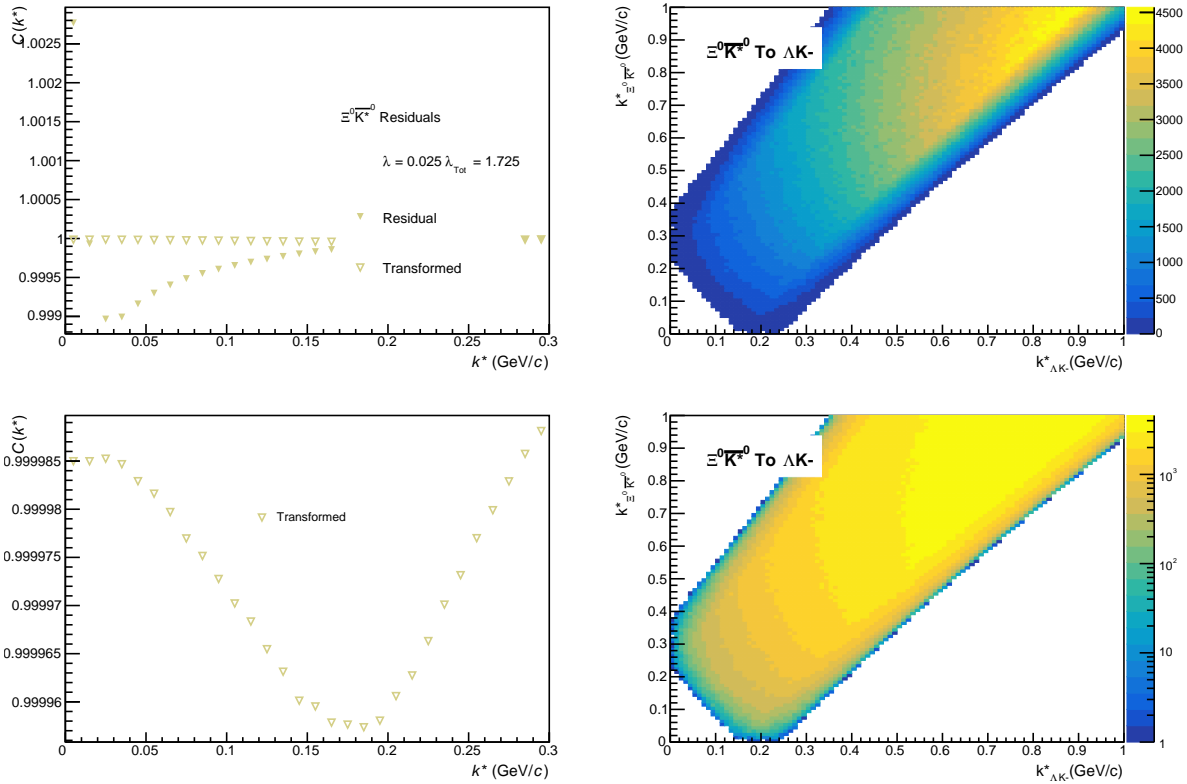


Fig. 85: Residuals: $\Xi^0 \bar{K}^{*0}$ to ΛK^- (0-10% Centrality)

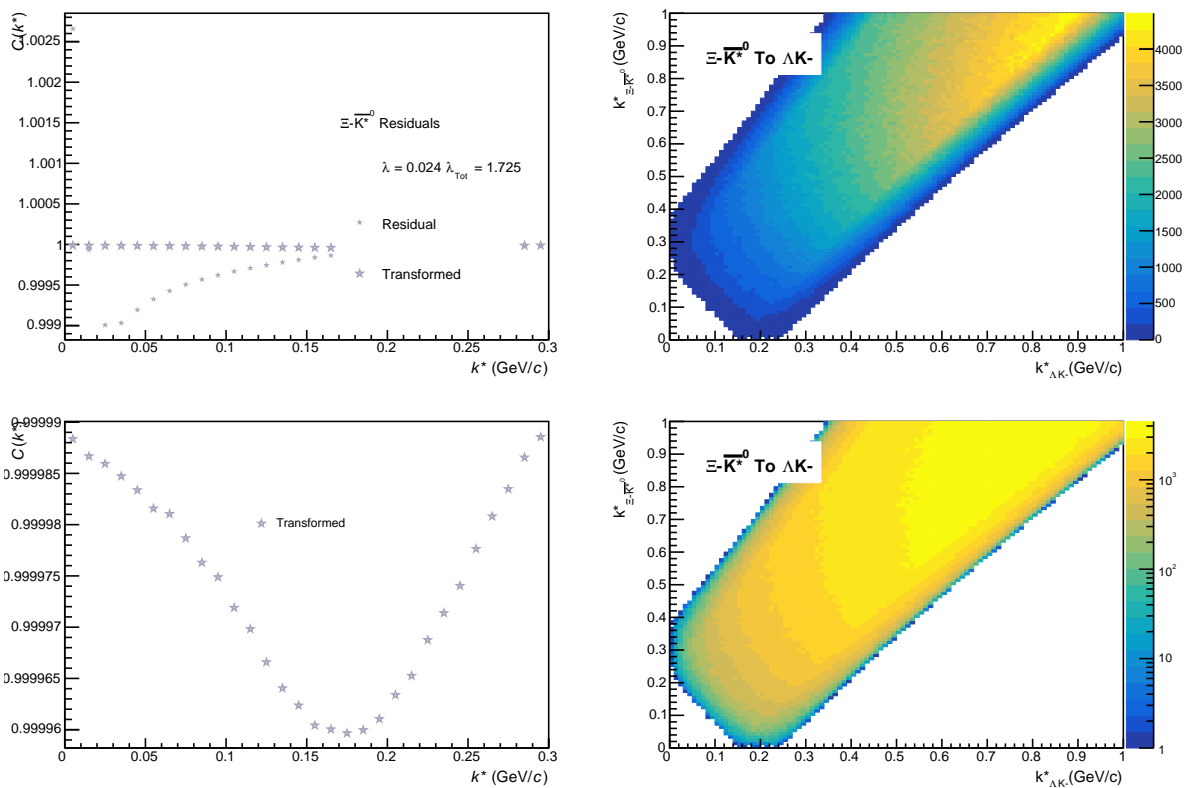


Fig. 86: Residuals: $\Xi-\bar{K}^{*0}$ to ΛK^- (0-10% Centrality)

946 **10.1.3 ΛK_S^0 Residuals**

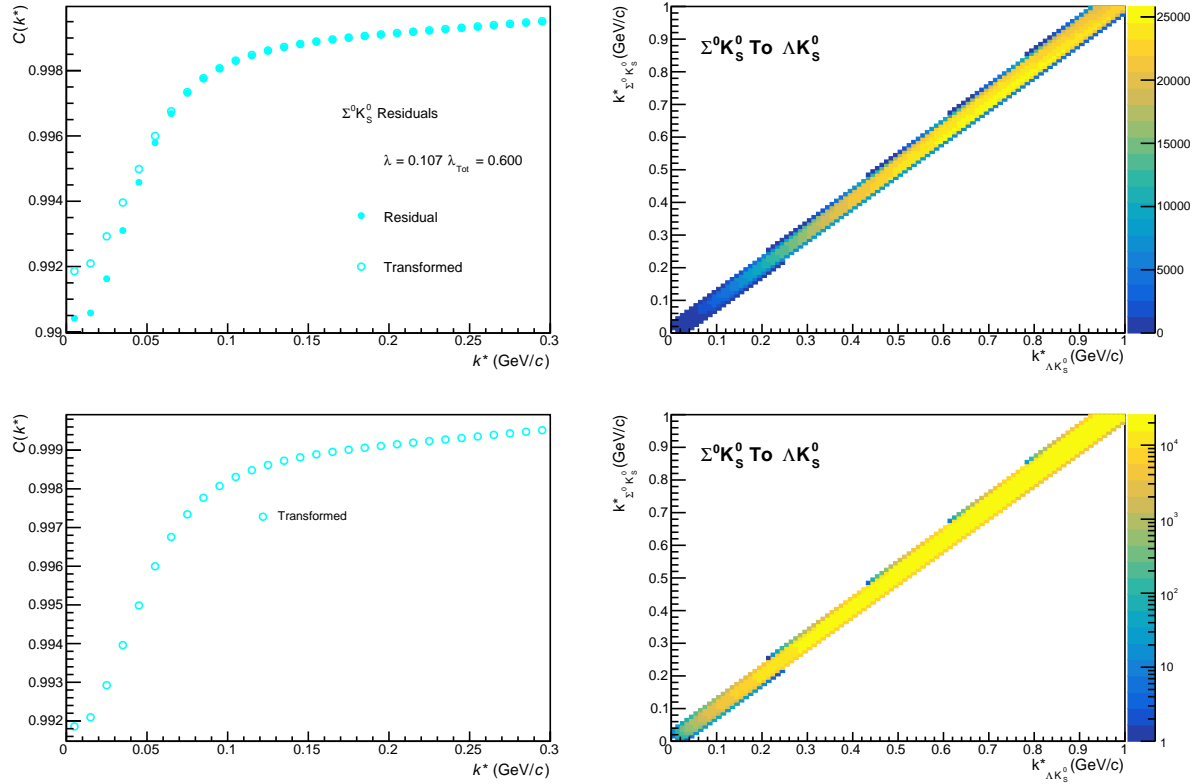


Fig. 87: Residuals: $\Sigma^0 K_S^0$ to ΛK_S^0 (0-10% Centrality)

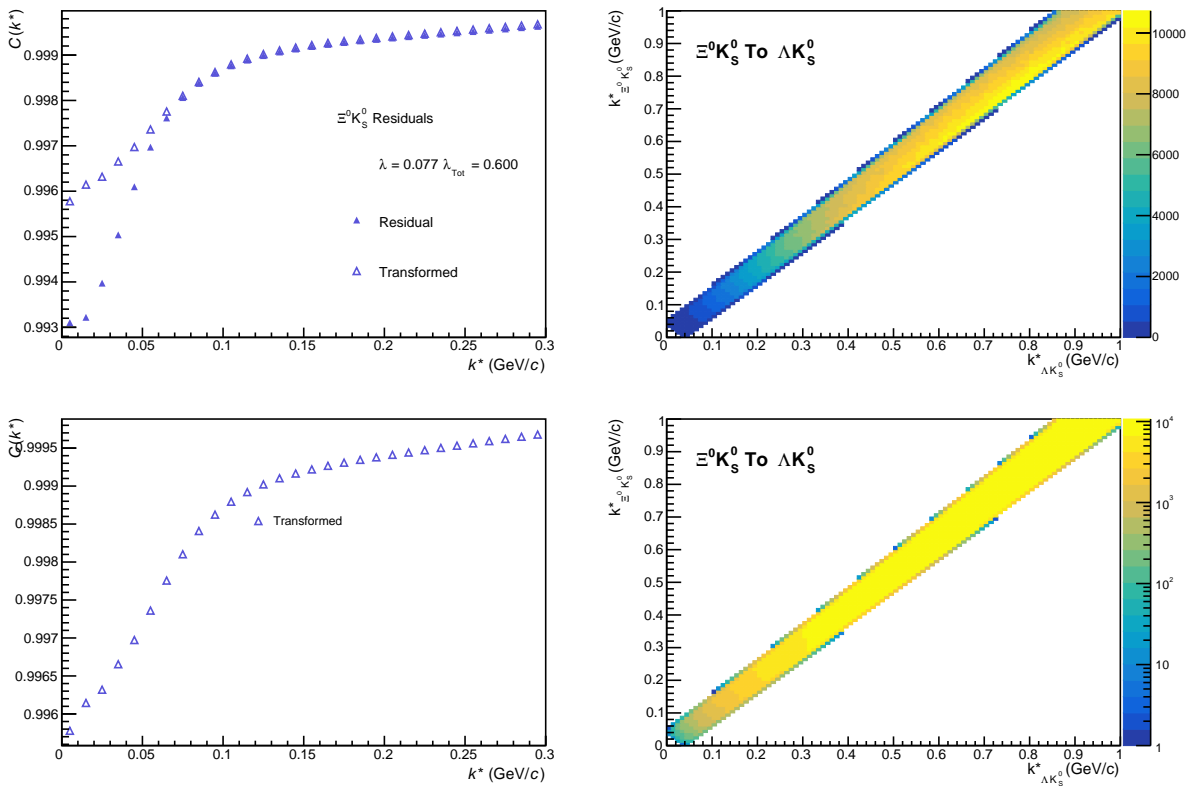


Fig. 88: Residuals: $\Xi^0 K_S^0$ to ΛK_S^0 (0-10% Centrality)

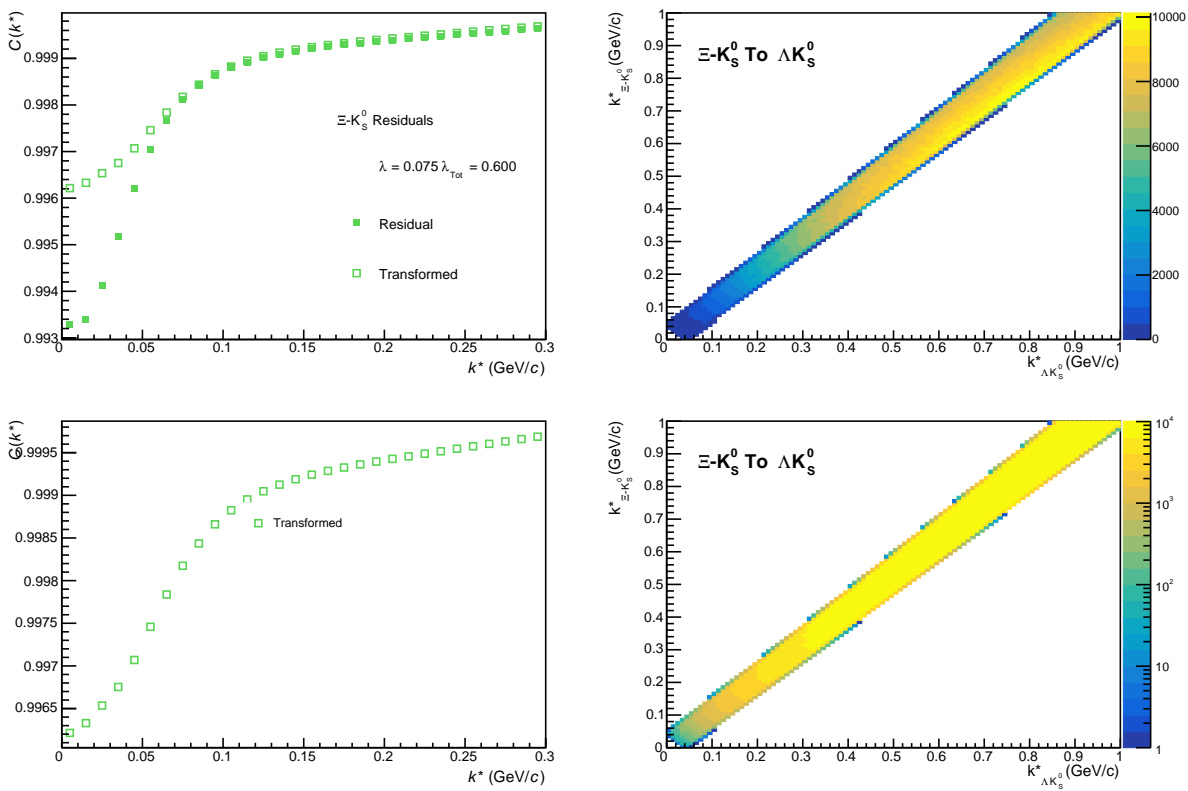


Fig. 89: Residuals: $\Xi^- K_S^0$ to ΛK_S^0 (0-10% Centrality)

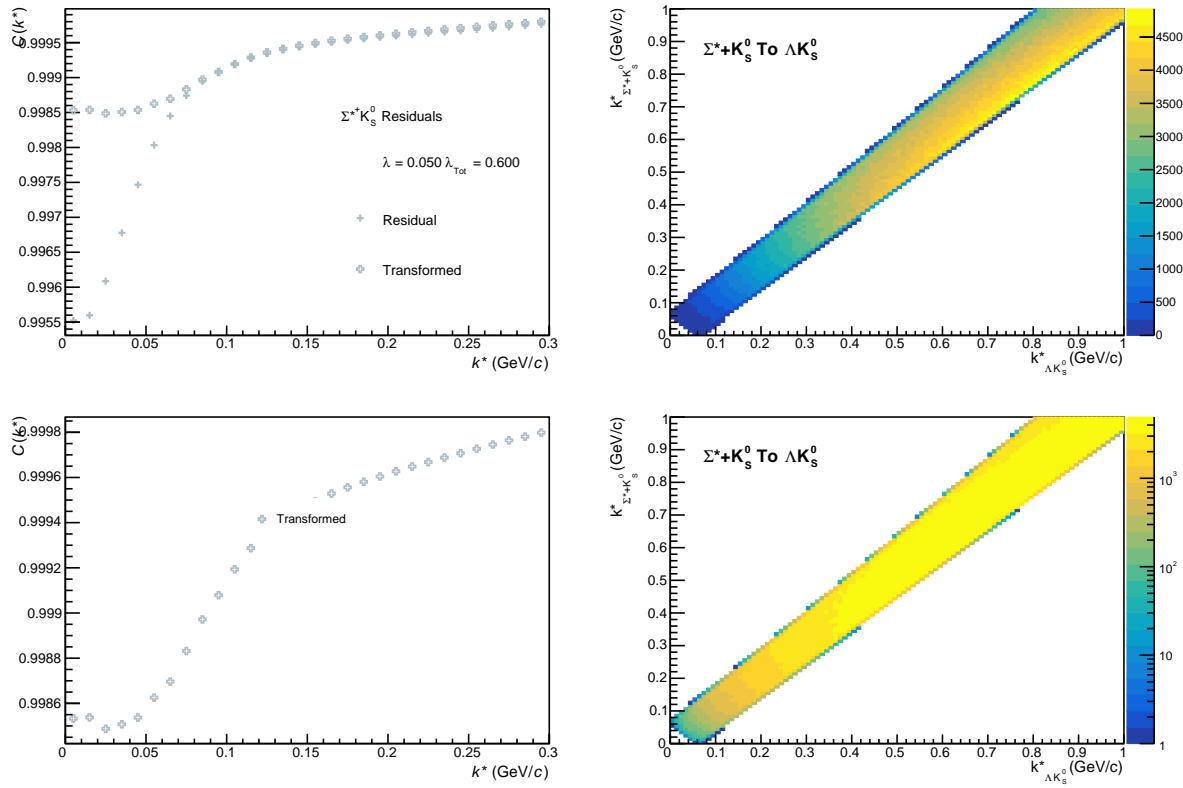


Fig. 90: Residuals: $\Sigma^*+K_S^0$ to ΛK_S^0 (0-10% Centrality)

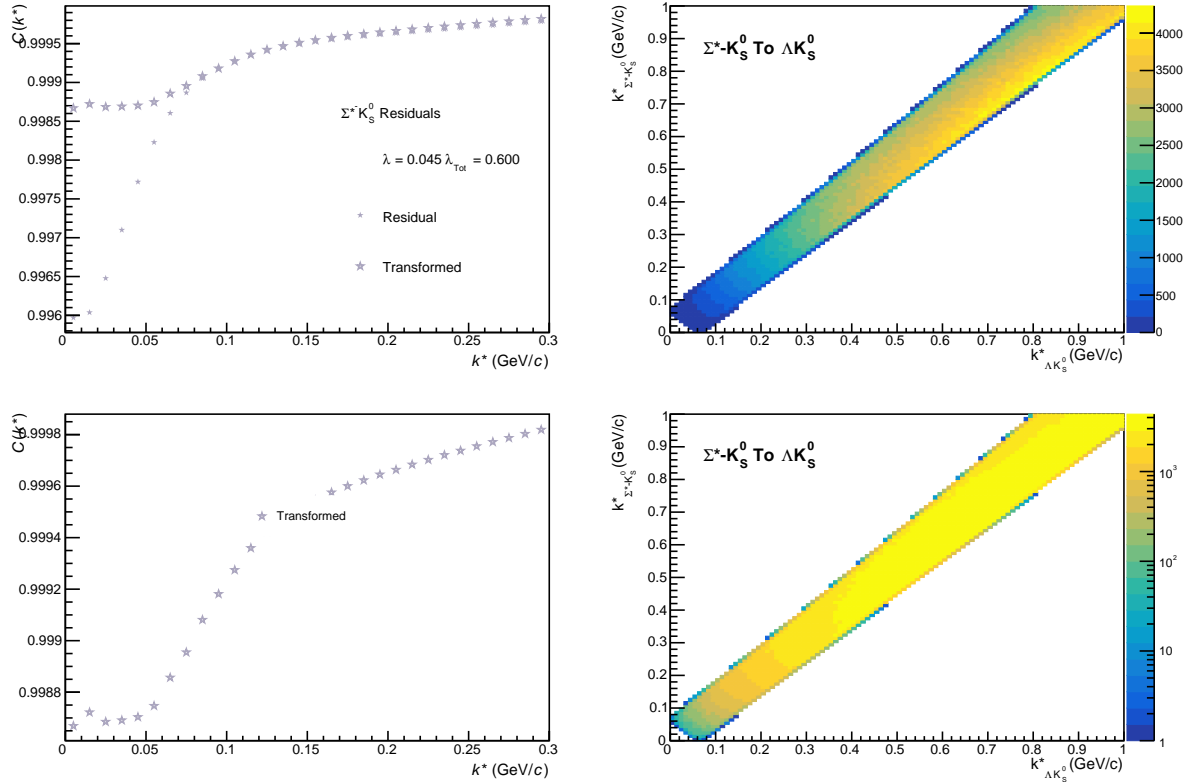
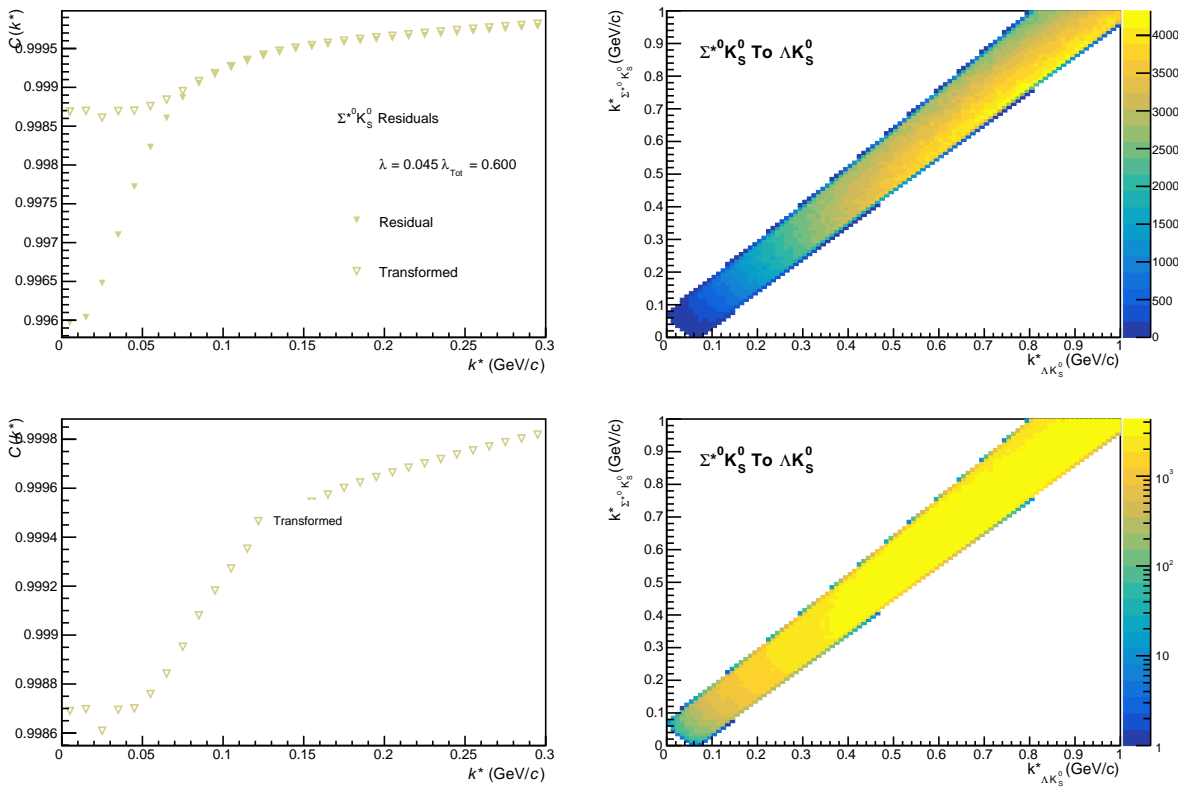
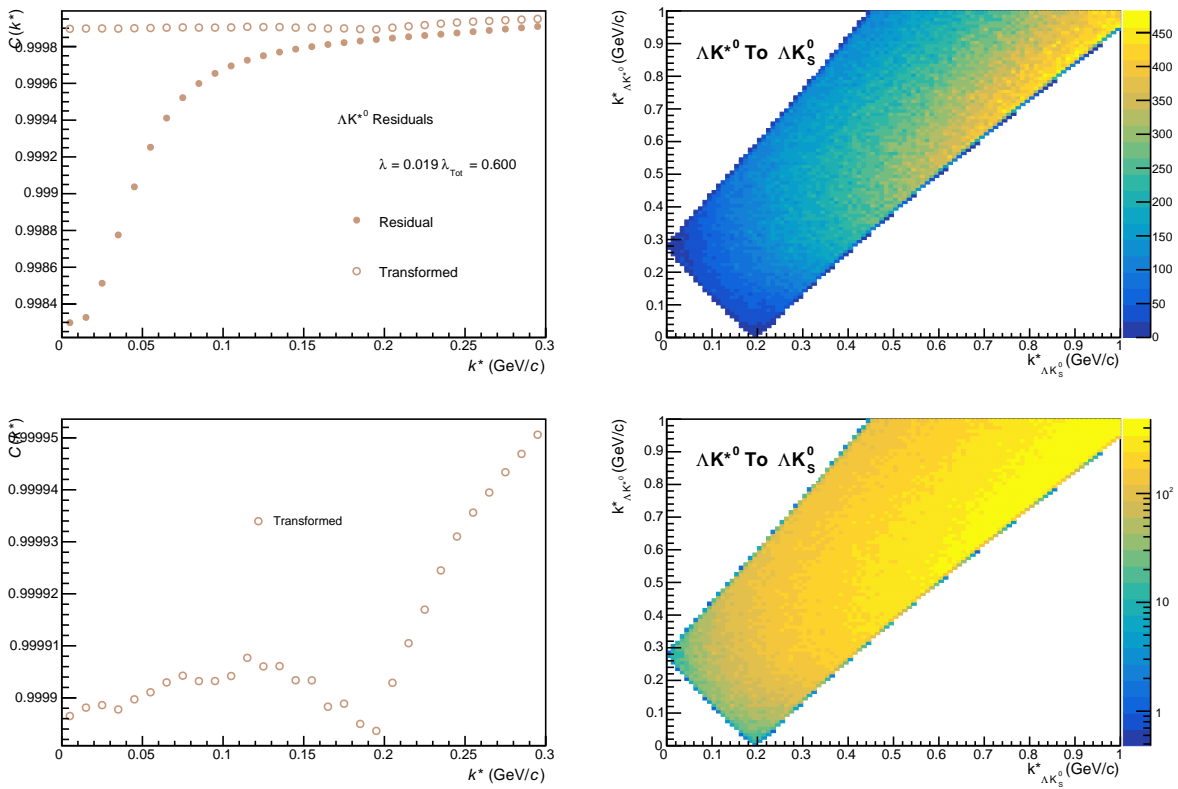
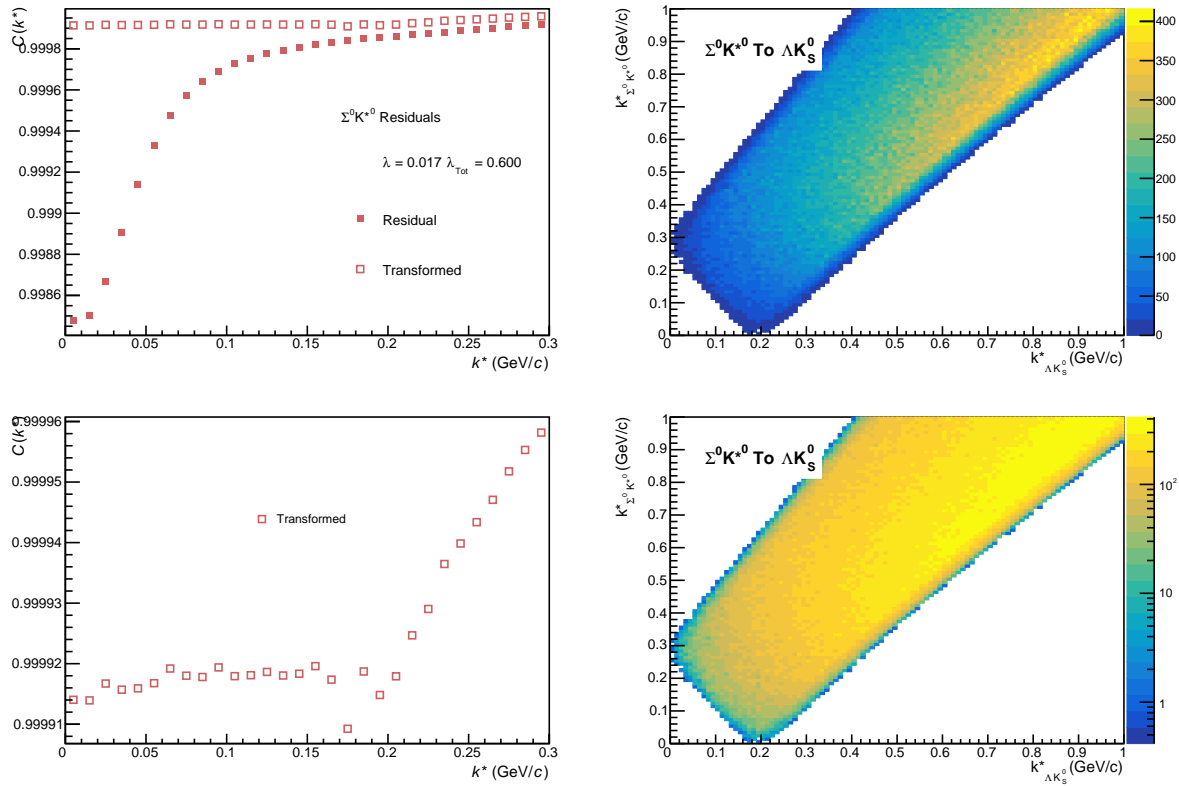
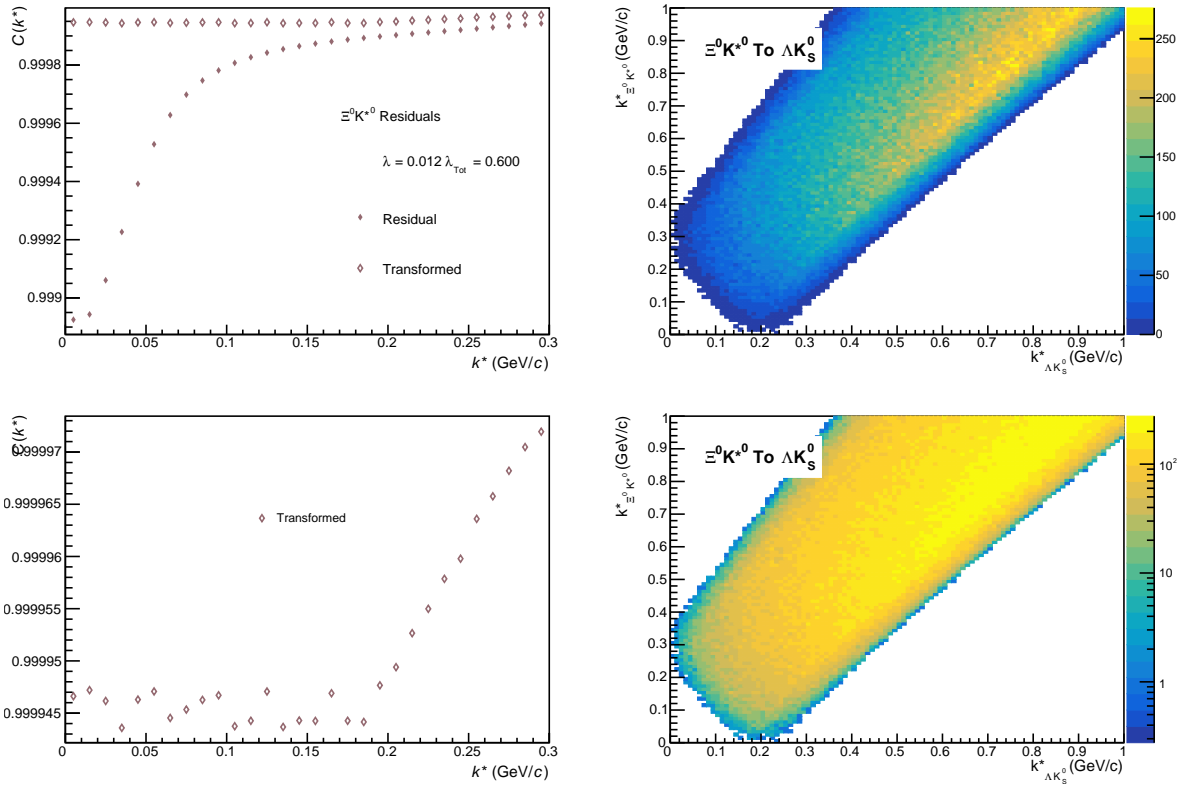


Fig. 91: Residuals: $\Sigma^*-K_S^0$ to ΛK_S^0 (0-10% Centrality)


Fig. 92: Residuals: $\Sigma^{*0} K_S^0$ to ΛK_S^0 (0-10% Centrality)

Fig. 93: Residuals: ΛK^{*0} to ΛK_S^0 (0-10% Centrality)

Fig. 94: Residuals: $\Sigma^0 K^{*0}$ to ΛK_S^0 (0-10% Centrality)Fig. 95: Residuals: $\Xi^0 K^{*0}$ to ΛK_S^0 (0-10% Centrality)

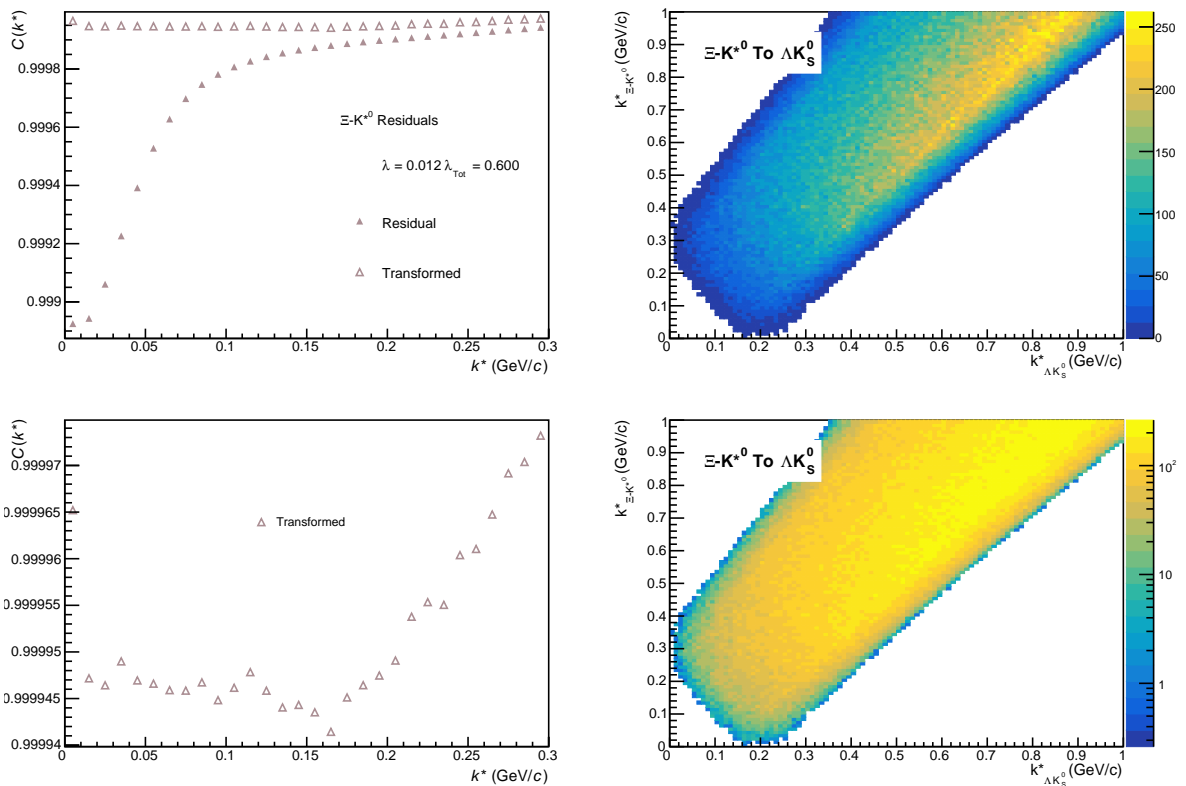


Fig. 96: Residuals: $\Xi \rightarrow K^* \Lambda K_S^0$ (0-10% Centrality)

947 **10.2 Spherical Harmonics**

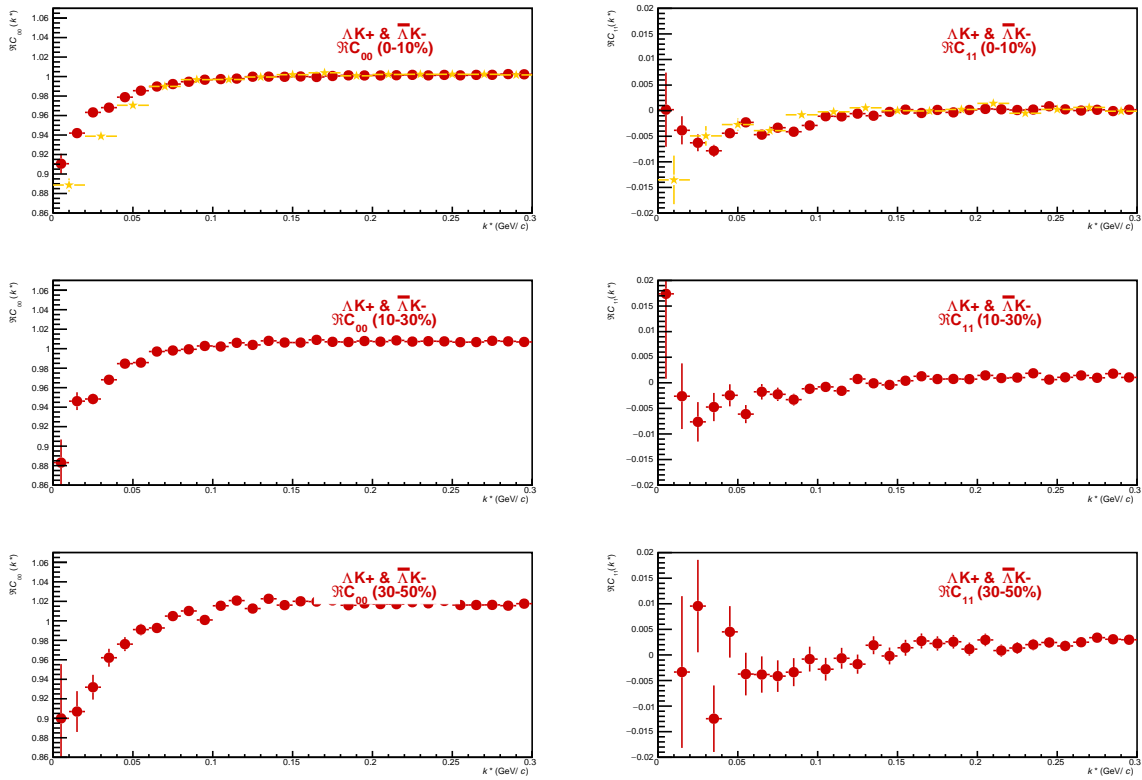


Fig. 97: C_{00} (left) and $\Im C_{11}$ (right) components of a spherical harmonic decomposition of the ΛK^+ correlation function for the 0-10% (top), 10-30% (middle), and 30-50% (bottom) centrality bins

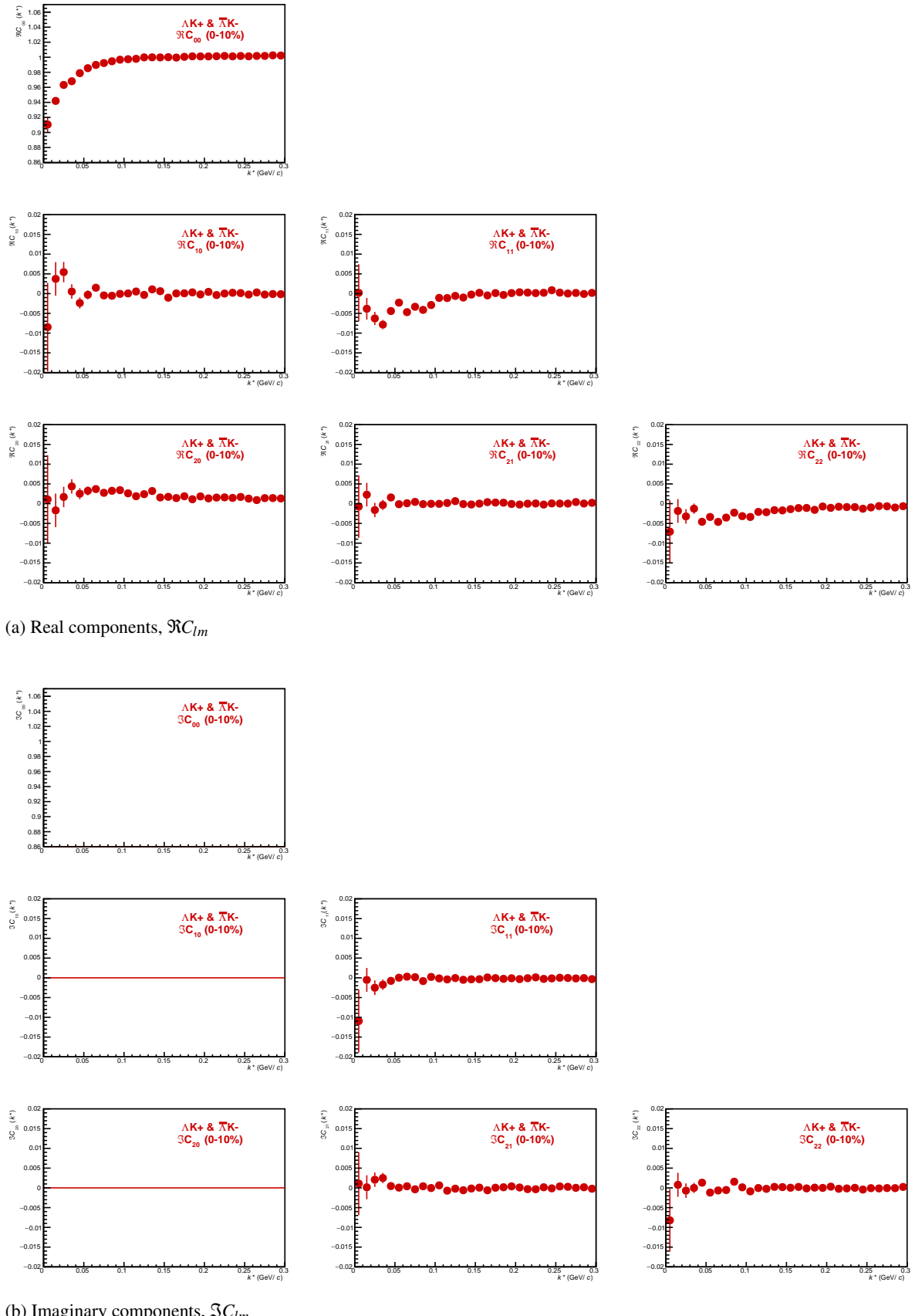


Fig. 98: First six components ($C_{00}, C_{10}, C_{11}, C_{20}, C_{21}, C_{22}$) of the spherical harmonic decomposition of the ΛK^+ correlation function for the 0-10% centrality bin. Note, $\Im C_{00}$, $\Im C_{10}$, and $\Im C_{20}$ are zero by definition.

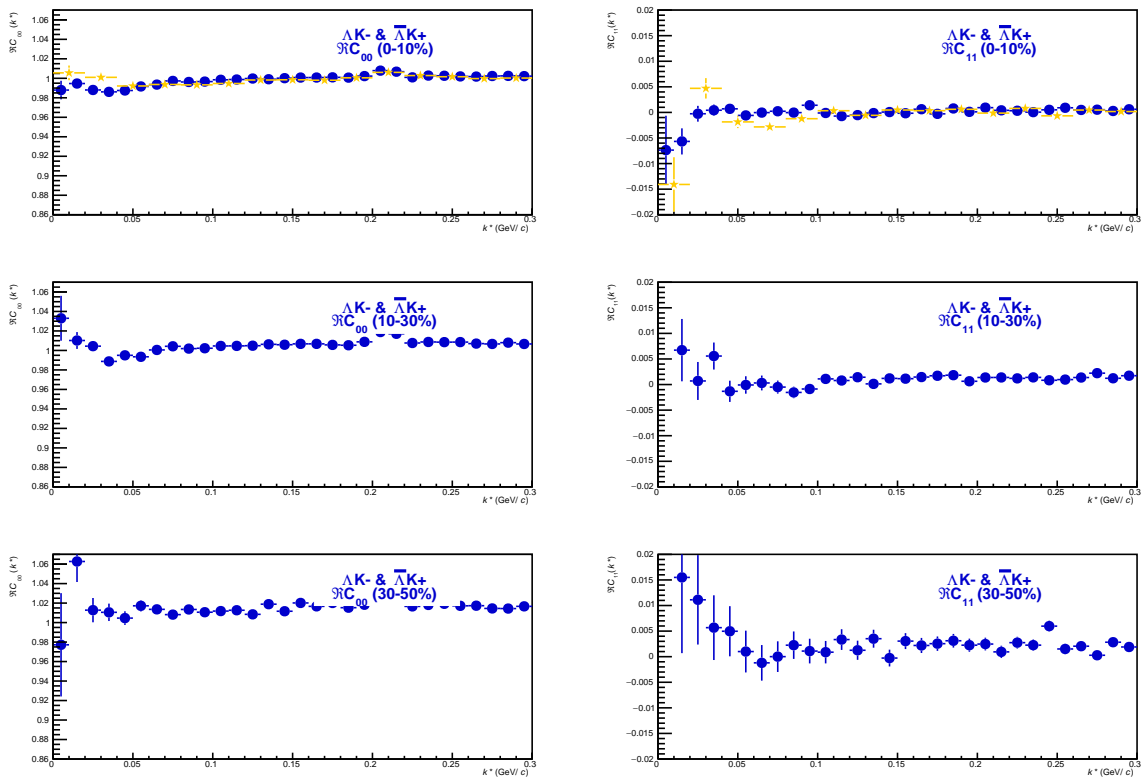


Fig. 99: C_{00} (left) and $\Re C_{11}$ (right) components of a spherical harmonic decomposition of the ΛK^- correlation function for the 0-10% (top), 10-30% (middle), and 30-50% (bottom) centrality bins

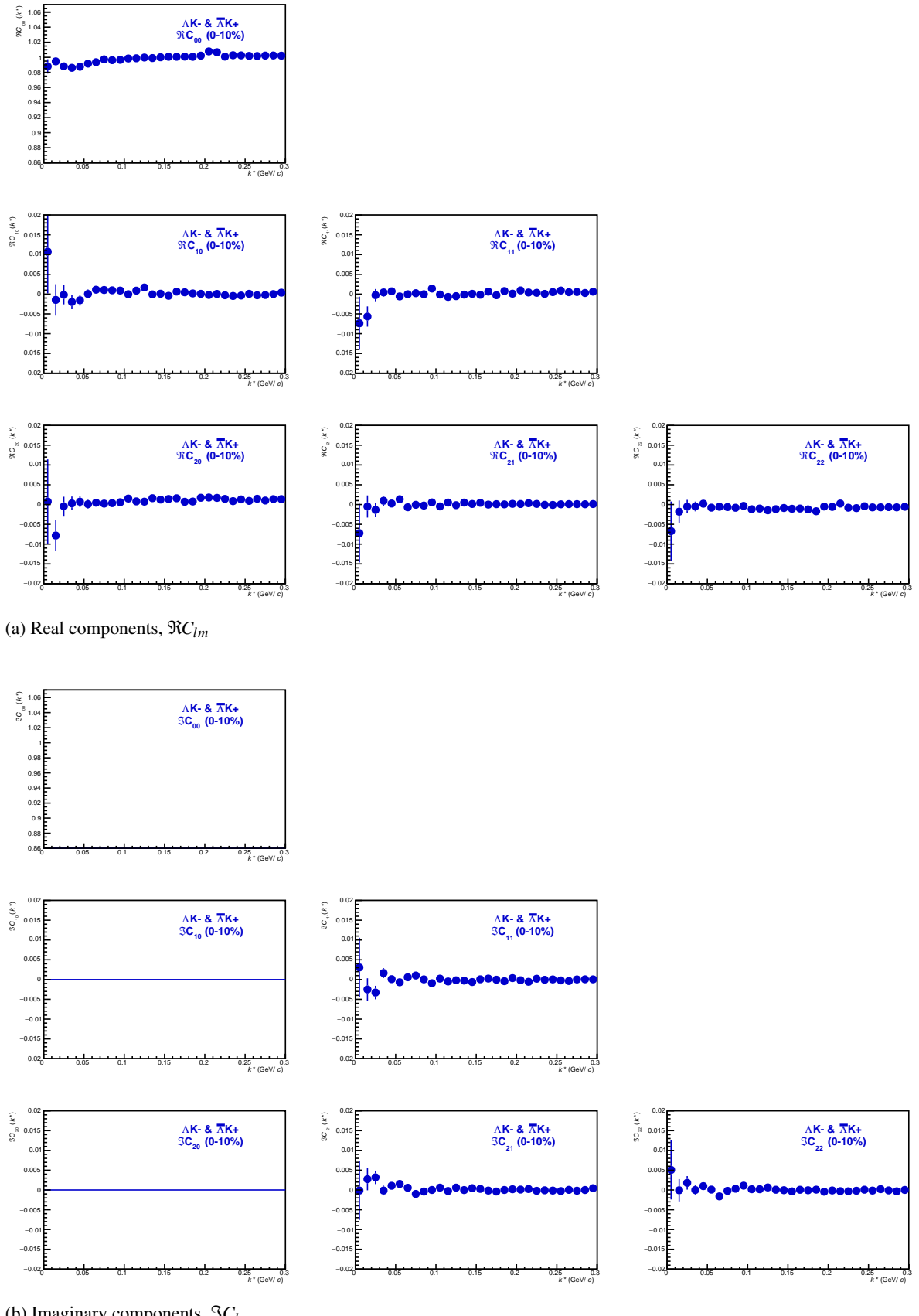


Fig. 100: First six components ($C_{00}, C_{10}, C_{11}, C_{20}, C_{21}, C_{22}$) of the spherical harmonic decomposition of the ΛK^- correlation function for the 0-10% centrality bin. Note, $\Im C_{00}$, $\Im C_{10}$, and $\Im C_{20}$ are zero by definition.

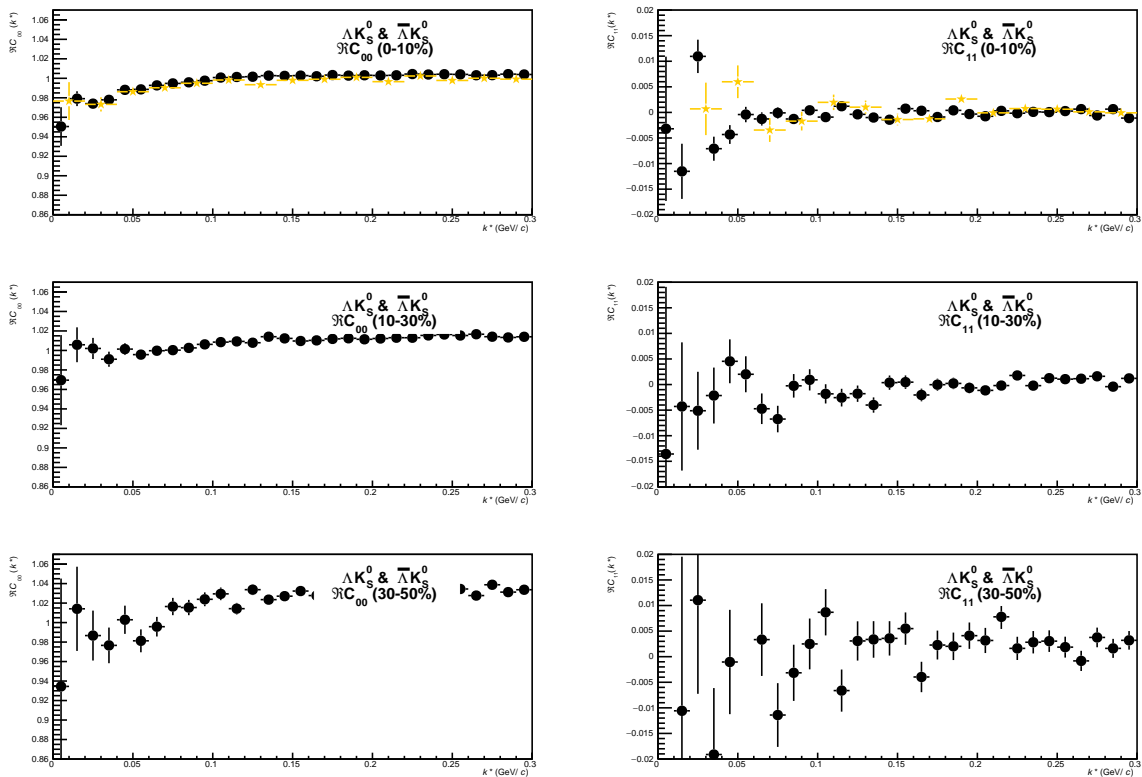


Fig. 101: C_{00} (left) and $\Re C_{11}$ (right) components of a spherical harmonic decomposition of the ΛK_S^0 correlation function for the 0-10% (top), 10-30% (middle), and 30-50% (bottom) centrality bins

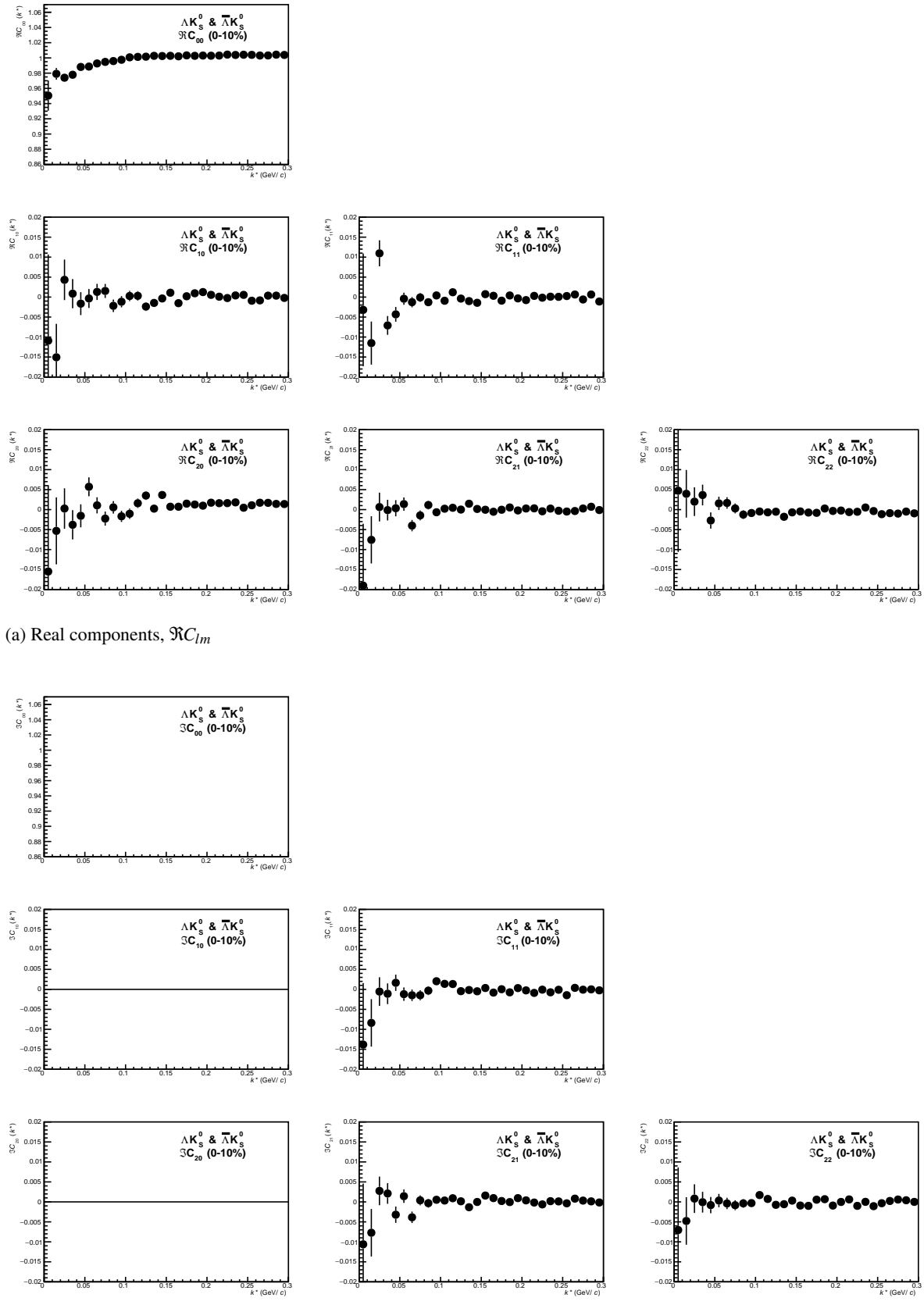


Fig. 102: First six components ($C_{00}, C_{10}, C_{11}, C_{20}, C_{21}, C_{22}$) of the spherical harmonic decomposition of the ΛK_S^0 correlation function for the 0-10% centrality bin. Note, $\Im C_{00}$, $\Im C_{10}$, and $\Im C_{20}$ are zero by definition.

References

- [1] R. Lednický and V. L. Lyuboshitz. *Sov. J. Nucl. Phys.*, 35:770, 1982.
- [2] C. Patrignani et al. Review of Particle Physics. *Chin. Phys.*, C40(10):100001, 2016.
- [3] Michael Annan Lisa, Scott Pratt, Ron Soltz, and Urs Wiedemann. Femtoscopy in relativistic heavy ion collisions. *Ann. Rev. Nucl. Part. Sci.*, 55:357–402, 2005.
- [4] S. E. Koonin. Proton Pictures of High-Energy Nuclear Collisions. *Phys. Lett.*, B70:43–47, 1977.
- [5] S. Pratt, T. Csorgo, and J. Zimanyi. Detailed predictions for two pion correlations in ultrarelativistic heavy ion collisions. *Phys. Rev.*, C42:2646–2652, 1990.
- [6] Richard Lednický. Finite-size effects on two-particle production in continuous and discrete spectrum. *Phys. Part. Nucl.*, 40:307–352, 2009.
- [7] Adam Kisiel, Hanna Zbroszczyk, and Maciej Szymaski. Extracting baryon-antibaryon strong interaction potentials from $p\bar{\Lambda}$ femtoscopic correlation functions. *Phys. Rev.*, C89(5):054916, 2014.
- [8] Mikolaj Chojnacki, Adam Kisiel, Wojciech Florkowski, and Wojciech Broniowski. THERMINATOR 2: THERMal heavy IoN generATOR 2. *Comput. Phys. Commun.*, 183:746–773, 2012.
- [9] A Kisiel. Non-identical particle correlation analysis in the presence of non-femtoscopic correlations. *Acta Physica Polonica B*, 48:717, 04 2017.
- [10] Jaroslav Adam et al. One-dimensional pion, kaon, and proton femtoscopy in Pb-Pb collisions at $\sqrt{s_{NN}} = 2.76$ TeV. *Phys. Rev.*, C92(5):054908, 2015.
- [11] Yan-Rui Liu and Shi-Lin Zhu. Meson-baryon scattering lengths in HB chi PT. *Phys. Rev.*, D75:034003, 2007.
- [12] Maxim Mai, Peter C. Bruns, Bastian Kubis, and Ulf-G. Meißner. Aspects of meson-baryon scattering in three and two-flavor chiral perturbation theory. *Phys. Rev.*, D80:094006, 2009.